

ABSTRACT

MAHONEY, KELLY M. Momentum Transport in Mesoscale Convective Systems. (Under the direction of Dr. Gary Lackmann).

The transport of horizontal momentum by vertical motions within a mesoscale convective system (MCS) affects storm dynamics, sensible weather, and the connection between the system and its surrounding environment. Earlier works have examined this process for a number of purposes, but understanding of its significance to both MCS motion and the generation of convectively-driven surface winds remains incomplete. This study describes the convective momentum transport (CMT) process both qualitatively and quantitatively; this is pursued through the analysis of quasi-idealized numerical simulations. Momentum budgets illustrate that the motion of a numerically-simulated MCS is significantly impacted by CMT within the MCS. Vertical advection of the perturbation wind is found to contribute largely to the momentum field at the leading edge of the cold pool, which is the region in which the resulting accelerated winds drive system motion. Results also show that the pressure gradient acceleration and, to a lesser degree the vertical advection of the background environmental wind, contribute to the acceleration of rear-to-front-directed momentum in the middle- to rearward portions of the storm, thereby generating and reinforcing transport of the perturbation flow into the cold pool and accelerating the MCS.

The second part of this dissertation uses a series of experimental simulations to examine the sensitivity of CMT, MCS motion, and surface wind speed generation to environmental humidity and microphysical processes. Results reveal modest changes in MCS motion, but marked differences in the generation of convectively-driven surface winds. Drier air at mid-levels increases descent within the trailing stratiform region and enhances CMT; this slightly increases average MCS speed by $\sim 1 \text{ ms}^{-1}$, but produces a much larger number of severe surface winds. CMT is also shown to be a contributing factor to the occurrence of severe surface winds produced via the favorable superpositioning of a descending rear inflow jet and the low-level circulation associated with gust front mesovortices. The potential for a descending rear inflow jet to cause

strong surface winds at locations away from the leading edge of the gust front is discussed as well. While such surface wind patterns may occur in a variety of storm environments, it is shown that the additional downward motion imparted by decreasing the relative humidity of the mid-levels leads to additional acceleration through CMT and contributes to an increase in occurrence of strong to severe surface winds. Reducing evaporation yields the most marked decrease in both MCS motion and strength of surface wind speeds, followed by the removal of melting and sublimation, respectively. The challenge of completely isolating the contribution of “cold pool dynamics” (i.e., density current propagation) from “CMT-forced” MCS motion is also discussed.

Avenues for future work are outlined, with a focus on adding or improving the representation of CMT in existing cumulus parameterization schemes, incorporating CMT into conceptual models of both MCS motion and severe surface wind generation, and further exploring of the sensitivity of CMT to a greater variety of storm environments and kinematic profiles.

Momentum Transport in Mesoscale Convective Systems

by
Kelly Marie Mahoney

A dissertation submitted to the Graduate Faculty of
North Carolina State University
in partial fulfillment of the
requirements for the degree of
Doctor of Philosophy

Marine, Earth, and Atmospheric Sciences

Raleigh, North Carolina

August 2009

APPROVED BY:

Gary M. Lackmann
Chair of Advisory Committee

Anantha R. Aiyer

Matthew D. Parker

Sandra E. Yuter

BIOGRAPHY

Kelly Mahoney was born in Baltimore, Maryland and grew up in Ellicott City, Maryland. She first became interested in the weather during a run-in with Hurricane Bertha on a family beach vacation, and shortly thereafter began learning all that she could about meteorology. She came to NC State in the fall of 1999 with the help of a Park Scholarship and completed her Bachelor's degree in 2003, graduating summa cum laude with a major in Meteorology and a minor in Spanish. During her time as an undergraduate, Kelly was an active participant in groups and activities such as Hope for the Homeless and WKNC radio, as well as both the NC State Student and Central North Carolina chapters of the American Meteorological Society (AMS). She was also fortunate enough to be able to fill her college summers storm-chasing, interning at WBAL-TV and WRAL-TV, and doing undergraduate research.

Kelly happily accepted an offer to stay at NC State for graduate school in 2003 and received an AMS graduate fellowship for her first year of study. She was fortunate enough to be able to do her Master's research under the CSTAR project, collaborating with National Weather Service forecasters to examine the effects of upstream convection on downstream precipitation forecasts. Her PhD research was motivated by this earlier work, and she began her dissertation research on the motion of mesoscale convective systems in the fall of 2005. During her graduate school years, Kelly also stayed busy by participating in the Preparing the Professoriate program, serving on the AMS Weather and Forecasting committee, forecasting for Progress Energy, and remaining active with the Graduate Student Association. Upon graduation, Kelly accepted a postdoctoral fellowship with UCAR's Climate Prediction and Application Program to investigate climate change and water resource issues in the western United States.

ACKNOWLEDGEMENTS

Support for this research was received from the National Science Foundation (ATM-0603760) awarded to North Carolina State University.

I would like to express my deep gratitude to my advisor and committee members, Drs. Gary Lackmann, Matt Parker, Sandra Yuter, and Anantha Aiyyer. Their advice and suggestions on developing and improving my research are appreciated tremendously. In particular I would like to thank my advisor, Dr. Lackmann for his patience and constant willingness to help, teach, advise, mentor, support and challenge me.

There are a number of professional friends and mentors that I have been fortunate to come to know throughout my graduate career as well. While it would be impossible to name them all here, I would like to acknowledge Chuck Doswell, Eve Grunfest, Sethu Raman, Russ Schumacher, Julie Demuth, Jack Kain, Mike Coniglio, and Steve Weiss for helpful advice, mentorship, encouragement, and offered opportunities over the years.

I have also been very fortunate to work with a wonderful group of people in the Forecasting Lab, and I gratefully acknowledge its members (both past and present) for everything from collaboration on research and technical issues to friendship and support. Gratitude is extended to Briana Gordon and Adam Baker in particular for managing to make me laugh through even the most stressful of days. A special thanks also goes to Mike Brennan for the years of research help and patience in the Forecasting Lab, and the ongoing friendship and support outside of it.

Finally, I would like to express my most sincere gratitude to my family and friends. First, thank you to my parents, Bill and Gina, and to my brother Billy for unconditional love, support, laughs, and reality-checks. Thanks especially to my parents for instilling in me from the beginning a deep appreciation for learning and education. Thank you to my husband, Scott Jackson, for his limitless and unwavering support and encouragement. The valuable friendships that I've been able to count on over the past few years has also been a huge source of strength for me as well, so thank you to everyone who I've been able to call a friend – your love, support, and understanding has meant more to me than I can possibly express. Thank you, all.

TABLE OF CONTENTS

List of Tables	vii
List of Figures	viii
1. Introduction and background	
1.1 Motivation.....	1
1.2 Background.....	5
1.2.1 Previous related research.....	5
1.2.2 MCS momentum transport.....	6
1.2.3 Momentum transport and near-surface thunderstorm wind gusts.....	7
1.2.3.1 Convectively-driven windstorms.....	7
1.2.3.2 CMT as a possible mechanism for surface wind gust generation in MCSs.....	9
1.3 Summary.....	10
2. Methodology	
2.1 Quasi-idealized modeling approach.....	15
2.1.1 Model set-up and initial conditions.....	15
2.1.2 Neglect of the Coriolis force and the use of homogeneous initial conditions.....	17
2.2 Momentum budget methodology.....	18
2.3 Sensitivity experiments: Model set-up.....	20
2.3.1 Control.....	21
2.3.2 Dry mid-levels.....	21
2.3.3 Reduced evaporation.....	22
2.3.4 No melting.....	22
2.3.5 No sublimation.....	23
3. The role of momentum transport in the motion of a quasi-idealized MCS	
3.1 MCS simulation analysis.....	31
3.1.1 MCS structure	31
3.1.2 MCS motion.....	32

3.2 CMT in the simulated MCS	35
3.2.1 Observational analysis.....	36
3.2.2 Momentum budget analysis.....	36
3.3 Synthesis of role of CMT in MCS motion.....	41
3.4 Synthesis and forecast implications.....	42
4. Sensitivity of CMT and MCS to changes in environmental humidity and model microphysics	
4.1 Motivation.....	60
4.2. Background/previous research.....	62
4.3 Sensitivity tests.....	64
4.3.1 Control	64
4.3.2 Dry mid-levels.....	64
4.3.2.1 DRYM hypotheses.....	64
4.3.2.2 DRYM results.....	65
4.3.3 Reduced evaporation.....	66
4.3.3.1 REVP hypotheses.....	66
4.3.3.2 REVP results.....	67
4.3.4 No melting.....	67
4.3.4.1 NMLT hypotheses.....	67
4.3.4.2 NMLT results.....	68
4.3.5 No sublimation.....	69
4.3.5.1 NSUB hypotheses.....	69
4.3.5.2 NSUB results.....	69
4.4 MCS speed comparisons.....	70
4.4.1 Groundspeed comparisons.....	70
4.4.2 Theoretical cold pool speed comparison.....	71
4.4.3 CTRL vs. DRYM momentum budget comparison.....	73
4.5 Synthesis and summary of results.....	76

5. CMT and strong surface winds produced by MCS outflow

5.1 Sensitivity of severe surface wind production to environmental humidity and microphysical cooling processes.....	132
5.1.1 Severe surface wind definition/terminology.....	132
5.1.2 Comparison of occurrence of severe surface wind speeds in sensitivity experiments.....	133
5.2 Association of CMT, mesovortices, and severe surface wind gust generation.....	134
5.2.1 Superpositioning of the RIJ and mesovortices.....	134
5.2.2 CMT and severe surface wind generation within mesovortices.....	137
5.3 CMT and severe surface winds in the TSR.....	140
5.3.1. CTRL.....	141
5.3.2 DRYM.....	143
5.3.3 REVP, NMLT, NSUB.....	146
5.4 Summary.....	147

6. Concluding remarks

6.1 Summary of results.....	179
6.2 Potential for forecast application of findings.....	181
6.2.1 CP scheme implementation.....	181
6.2.2 Corfidi vectors.....	185
6.2.3 Potential incorporation of CMT into a surface wind gust forecast parameter.....	187
6.3 Summary of ideas for future work.....	190

References.....	195
------------------------	------------

Appendices	213
-------------------------	------------

Appendix A	214
-------------------------	------------

Appendix B	224
-------------------------	------------

Appendix C	235
-------------------------	------------

LIST OF TABLES

Table 2.1	WRF model set-up and parameterization.....	29
Table 2.2	Sensitivity simulation details.....	30
Table 4.1	Table 2 from Yang and Houze (1995), summarizing storm speed, storm orientation, and rear-to-front flow structure for each sensitivity experiment	130
Table A.1.	Summary of Quasi-idealized and Idealized simulations experiment.....	223

LIST OF FIGURES

Figure 1.1	Schematic of hypothesized momentum transport mechanism in an idealized MCS. Based on Houze et al. (1989), where outermost dotted outline represents cloud outline, inner shaded solid contours represent radar reflectivity, and shaded area at surface represents the cold pool. Bold “L” denotes approximate area of midlevel mesolow; thick downward-sloping arrow shows rear-to-front flow, and dashed upward-sloping arrow shows front-to-rear flow branch. Dashed arrow denotes “c”, the accelerated speed at which the cold pool and MCS move.....12
Figure 1.2	Figure 1.2: From Corfidi (1996): Conceptual model of MCS movement (V_{MBE}) as the vector sum of the mean flow in the cloud layer (V_{CL}) and the propagation component (V_{PROP}). Angles ϕ and ψ are used to calculate V_{MBE} given observed values of V_{CL} and V_{LLJ}13
Figure 1.3	Conceptual model of a microburst hypothesized to explain ground-damage patterns, with three stages of development shown. From Wakimoto (2001), based on a figure from Fujita (1985).....14
Figure 2.1	Initial background state (F00) for idealized MCS simulation. (a) 500-hPa geopotential height (m, contours), and wind (shaded as in color bar at left, m/s). Inner (1-km gridspacing) WRF domain outlined in thick black box, and cross-section in (b) shown by dashed line, (b) north (right) - south (left) cross-section as shown in (a), isentropes (K, solid contours, interval 5K starting at 300K) and isotachs (knots, dashed contours, interval 7m/s), (c) surface-based CAPE (shaded as in legend at left, J/kg) and surface-based convective inhibition (CIN, contours, interval 1 J/kg) over WRF model domain at initial time (F00).....24
Figure 2.2	(a) Initial sounding shape used to initialize the quasi-idealized MCS simulation (at (35°lat; -95°lon)). Temperature (°C, solid line), dewpoint (°C, dashed line), wind barbs in knots at right. Compared to other initial soundings used or found by past studies: (b) Weisman and Klemp (1982) initial sounding (c) Bluestein and Jain (1985) composite sounding; (d) Houze et al. (1990) mean sounding; and (e) Parker and Johnson (2000) initial sounding.....25
Figure 2.3	Initial (F00) 1000-hPa temperature (°C, every 0.5°C as indicated at right) for quasi-idealized MCS simulation.....26

Figure 2.4	Simulated composite reflectivity (dBZ) at F09 in simulations (a) with Coriolis and horizontally heterogeneous initial conditions, and (b) without Coriolis and horizontally homogeneous initial conditions. Black lines denote cross-sections depicted in panels (c) and (d); (c) east-west vertical cross-section along line shown in Fig. 2.3a at F09, averaged in an along-line direction in 40-km segments. Cold pool (shaded as shown beginning at $T' = -2^{\circ}\text{C}$), negative (positive) geopotential height perturbation in solid (dashed) contours m^2s^{-2} ; and simulated reflectivity (dBZ, black contours as labeled, every 10dBZ beginning at 20 dBZ). (d) As in (c) except for No-Coriolis run taken along black line shown in Fig. 2.3b.....27
Figure 2.5	Comparison of initial sounding shape used to initialize the quasi-idealized MCS simulation (at 35°lat ; -95°lon) for (a) CTRL simulation, and (b) DRYM (dry mid-levels) simulation. Temperature ($^{\circ}\text{C}$, solid line), dewpoint ($^{\circ}\text{C}$, dashed line), wind barbs in knots at right.....28
Figure 3.1	Simulated composite reflectivity (dBZ, shaded as indicated at right) and cold pool outline ($T'=-2^{\circ}\text{C}$ at 0 m (black, solid)), at (a) F03, (b) F06, (c) F09, and (d) F12. Lines A-A', B-B', and C-C' in (b) - (d) depict cross-sections shown in subsequent figures; distance (km) as denoted by scale legend.43
Figure 3.2	Hourly precipitation (mm, shaded as indicated at right) ending at (a) F03, (b) F06, (c) F09, and (d) F12.....44
Figure 3.3	(a) East-west cross-section along line A-A' as in Fig. 3.1 at F06, averaged in an along-line direction in 40-km segments. Cold pool (shaded as shown beginning at $T' = -2^{\circ}\text{C}$), magnitude of total perturbation wind ($(u'^2 + v'^2)^{1/2}$, ms^{-1}) and simulated reflectivity (dBZ, gray dotted contour, 20 dBZ). Black arrows show ground-relative perturbation flow in the x-z plane scaled as shown by reference vector in lower left corner; (b) as in (a), except solid (dashed) contours represent negative (positive) pressure perturbation in hPa; (c) as in (a) except along B-B' as in Fig. 3.1c at F09; (d) as in (b) except along B-B' as in Fig. 3.1c at F09.....45
Figure 3.4	Figure 3.4: (a) Low-level (2-m) temperature perturbation from initial environment (K, shaded as in legend at right), divergence (black contours, $-5 \times 10^{-4} \text{ s}^{-1}$ interval, starting at $-5 \times 10^{-4} \text{ s}^{-1}$) at 10 m, and composite reflectivity (dashed, interval 10dBZ, starting at 20dBZ) at F06; (b) as in (a) but valid at F09.....46
Figure 3.5	Speed of MCS (ms^{-1} , solid), average of gridpoint maximum wind speed in the lowest 3 km of the cold pool (ms^{-1} , large dashed), average mean cloud-

	bearing wind (from 900 – 200 hPa, ms^{-1} , small dashed), and theoretical cold pool speed c (ms^{-1} , thin solid).....	47
Figure 3.6	(a) Total wind speed (ms^{-1}) along line C-C' shown in Fig. 3.1d and panel f (shaded, according to legend at right) and simulated reflectivity (contours, interval 10dBZ, starting at 20dBZ) at F04; (b) as in (a) except for F06; (c) as in (a) except for F08; (d) as in (a) except for F10; (e) as in (a) except for F12; (f) cross-section C-C' (black dashed) and simulated composite reflectivity at times F06 and F09 as labeled and shaded as in Fig. 3.1	48
Figure 3.7	(a) East-west cross-section through leading edge of MCS along line A-A' at F06 (as shown in Fig. 3.1b) showing cold pool (T' , blue contours, -2°C intervals starting at -4°C), and downward momentum flux (shaded as in legend at right) and simulated radar reflectivity (black contours, 10dBZ intervals starting at 20dBZ); (b) downward momentum flux at 800 m at F09 (m^2s^{-2}), $T'=-2^\circ\text{C}$ at 0 m (black, solid), (c) as in (b) but for $-d/dz(uw)$, where positive values denote convergence (ms^{-2}), (d) as in (b) except at the 2000-m level, (e) as in (d) except at the 2000-m level.	49
Figure 3.8	a) Simulated reflectivity (dBZ, shaded, as in legend at right), $T'=-2^\circ\text{C}$ at 0 m (black, solid), and the vector sum of the u- and v-tendency (TEN) terms from Eqns. (2.2) and (2.3) (vectors, $\text{ms}^{-1}\text{h}^{-1}$, scaled as shown by reference vector in lower left corner) at 800 m at F06; b) as in a) except vectors show VA term, c) as in a) except vectors show HA, d) as in a) except vectors show COR term, e) as in a) except vectors show PGA term, f) as in a) except vectors show RES.	50
Figure 3.9	Cross-sections of momentum budget terms along line A-A' (shown in Fig. 3.1b) at F06: (a) u (m/s, shaded as in legend at right) and TEN_x ($\text{ms}^{-1}\text{h}^{-1}$, positive (negative) values in solid (dashed) contours), and 30-dBZ contour (dotted) of simulated reflectivity; (b) as in (a) except PGA_x ; (c) as in (b) except HAu_x ; (d) as in (a) except VAu' ; (e) as in (a) except VAu	51
Figure 3.10	Volume-averaged momentum budget terms as labeled in key for times F05 – F11 for the (a) leading volume and (b) trailing volume (<i>note different scales of y-axes</i>).....	52
Figure 3.11	Cross-section of u (shaded, m/s as in legend at right), and w (m/s, positive(negative) black solid (dashed) contours) at F09 along B-B' as in Fig. 3.1c. Solid (dashed) box outlines volumes $\text{VOL}_{\text{leading}}$ ($\text{VOL}_{\text{trailing}}$), and simulated reflectivity contour of 30dBZ (dotted).	53

Figure 3.12	TEN _x in VOL _{leading} (solid, ms ⁻¹ h ⁻¹) and x-component of MCS acceleration (dashed, ms ⁻¹ h ⁻¹) vs. time (x-axis, hours).	54
Figure 3.13	a) VOL _{leading} (light gray) and VOL _{trailing} (dark gray) at F06, b) momentum budget term averages as labeled over VOL _{leading} at F06 in ms ⁻¹ h ⁻¹ , c) as in b) but for VOL _{trailing} , d) as in a) but for F09, e) as in b) but for F09, f) as in c) but for F09.	55
Figure 3.14	Figure 3.14: a) Height (y-axis, m) vs. time (x-axis, sec) of average trajectory of 50 parcels originating at RIJ-level at F06; b) PGA (short dashed, ms ⁻² , values on left y-axis), acceleration (d V /dt, long dashed, ms ⁻² , values on left y-axis), and wind speed (V , solid, ms ⁻¹ , values on y-axis at right) for time period t = 25200s (F07:00) to t=34200s (F09:30) only. Dotted box in panel b) denotes period of acceleration from t = 25200s to t = 30300s.	56
Figure 3.15	Schematic of relative contributions of momentum budget terms PGA, VA processes to CMT as indicated by black arrows (thickness of arrows an approximate indication of relative magnitude of terms, and dashed boxes show general locations of VOL _{leading} and VOL _{trailing}).	57
Figure 4.1	Conceptual model of a squall line with trailing stratiform region, from Houze et al. (1989). “L” (“H”) denotes areas of low (high) pressure; arrows shows major flow branches and circulations. Box indicates “secondary” low pressure area described in text.	82
Figure 4.2	Simulated composite reflectivity (dBZ, shaded as indicated at right) and cold pool outline (T’=-2°C at 0 m (black, solid)), for CTRL run at (a) F03, (b) F06, (c) F09, and (d) F12. Lines CTRL_A-CTRL_A’ and CTRL_B-CTRL_B’ in (b) and (c) depict cross-sections shown in subsequent figures.	83
Figure 4.3	Simulated composite reflectivity (dBZ, shaded as indicated at right) and cold pool outline (T’=-2°C at 0 m (black, solid)), for DRYM run at (a) F03, (b) F06, (c) F09, and (d) F12. Lines DRYM_A-DRYM_A’ and DRYM_B-DRYM_B’ in (b) and (c) depict cross-sections shown in subsequent figures.	84
Figure 4.4	Groundspeed of MCS (ms ⁻¹) for CTRL simulation (blue) and DRYM simulation (red).	85
Figure 4.5	(a) East-west along-line averaged (in 40-km segments) cross-section along line CTRL_B-CTRL_B’ as in Fig. 4.2c at F09. Cold pool (shaded as	

shown beginning at $T' = -2^\circ\text{C}$), solid (dashed) contours represent negative (positive) pressure perturbation in hPa magnitude of total perturbation wind $((u'^2 + v'^2)^{1/2}, \text{ms}^{-1})$, and simulated reflectivity (dBZ, purple contour, 20 dBZ); (b) as in (a) except for DRYM simulation taken along DRYM_B-DRYM_B' as in Fig. 4.3c. Distance of cross-sections 175-km.....86

- Figure 4.6 East-west cross-section along-line averaged (in 40-km segments) along line CTRL_B-CTRL_B' as in Fig. 4.2c at F09. (a) Cold pool (shaded as shown beginning at $T' = -2^\circ\text{C}$), magnitude of total perturbation wind $((u'^2 + v'^2)^{1/2}, \text{ms}^{-1})$ and simulated reflectivity (dBZ, dotted contour, 20 dBZ). Black arrows show ground-relative perturbation flow in the x-z plane scaled as shown by reference vector in lower left corner; (b) as in (a) except for DRYM simulation taken along DRYM_B-DRYM_B' as in Fig. 4.3c.....87
- Figure 4.7 Cross-sections as in Fig. 4.6 except showing (a) buoyancy (ms^{-2} , shaded as shown) and simulated reflectivity (dBZ, black contours, every 10 dBZ starting at 20 dBZ); (b) as in (a) except for DRYM simulation. Values shaded in light green and cooler colors $< 0 \text{ms}^{-2}$. Buoyancy calculated according to $B = \theta_v' / \theta_v - q_h$88
- Figure 4.8 a) CTRL at F09: convective gridpoints (blue) and stratiform gridpoints (red) according to criteria described in text. Box denotes boundaries of areas in which stratiform gridcells are averaged within in images at right. (b); b) CFAD of CTRL vertical velocity w , at F09 for boxed blue stratiform area in (a). Bin size is 0.1ms^{-1} and plot is contoured as indicated by shading and key at bottom; c) as in a) except for DRYM simulation; d) as in d) except for DRYM simulation.....89
- Figure 4.9 As in Fig. 4.8 except b) and d) display microphysical scheme heating tendency (Ks^{-1}) with bin size $.00025 \text{Ks}^{-1}$90
- Figure 4.10 As in Fig. 4.8 except b) and d) display the magnitude of the perturbation wind speed $((u'^2 + v'^2)^{1/2}, \text{ms}^{-1})$, bin size 1ms^{-1}91
- Figure 4.11 Row a) CTRL along-line averaged (in 40-km segments) vertical cross-sections through leading edge at most bowing segment showing cold pool (T' , blue contours, -2°C intervals starting at -4°C), and downward momentum flux (m^2s^{-2} , shaded as in legend at right) and simulated radar reflectivity (black contours, 10dBZ intervals starting at 20dBz) from F09 – F12 as labeled; row b) as in a) except for DRYM.....92

Figure 4.12	As in Fig. 4.11 except vertical velocity, w (ms^{-1} , shaded as indicated at right), magnitude of total wind speed ($((u^2 + v^2)^{1/2}$, ms^{-1} black contours every 5ms^{-1} starting at 20ms^{-1}), and simulated reflectivity (dBZ, purple contour, 20 dBZ).....	93
Figure 4.13	Simulated composite reflectivity (dBZ, shaded as indicated at right) and cold pool outline ($T'=-2^\circ\text{C}$ at 0 m (black, solid)), for REVP run at (a) F03, (b) F06, (c) F09, and (d) F12. Line REVP_A-REVP_A' in (c) depicts cross-section shown in subsequent figures.	94
Figure 4.14	As in Fig. 4.5 except comparing CTRL and REVP simulations.....	95
Figure 4.15	As in Fig. 4.6 except comparing CTRL and REVP simulations.....	96
Figure 4.16	As in Fig. 4.7 except comparing CTRL and REVP simulations. (Back edge of system abrupt due to orientation of cross-section REVP_A – REVP_A' through along-line averaged data.)	97
Figure 4.17	As in Fig. 4.8 except comparing CTRL and REVP simulations.....	98
Figure 4.18	As in Fig. 4.9 except comparing CTRL and REVP simulations.....	99
Figure 4.19	As in Fig. 4.10 except magnitude of full wind field, comparing CTRL and REVP simulations.....	100
Figure 4.20	Simulated composite reflectivity (dBZ, shaded as indicated at right) and cold pool outline ($T'=-2^\circ\text{C}$ at 0 m (black, solid)), for NMLT run at (a) F03, (b) F06, (c) F09, and (d) F12. Line NMLT_A-NMLT_A' in (c) depicts cross-section shown in subsequent figures.....	101
Figure 4.21	As in Fig. 4.5 except comparing CTRL and NMLT simulations.....	102
Figure 4.22	As in Fig. 4.6 except comparing CTRL and NMLT simulations.....	103
Figure 4.23	As in Fig. 4.7 except comparing CTRL and NMLT simulations.....	104
Figure 4.24	As in Fig. 4.12 except comparing CTRL and NMLT simulations.....	105
Figure 4.25	Vertical cross-sections as in Fig. 4.24, showing cold pool ($T' = -2^\circ\text{C}$, blue contours), hydrometeor mixing ratios (contours as labeled $\times 10^{-4}$, gkg^{-1}) for graupel (burgundy contours), cloud ice (purple), rain (green contours and fill), and snow (pink contours and fill) in CTRL (row A) and NMLT (row B) simulations.....	106

Figure 4.26	As in Fig. 4.8 except comparing CTRL and NMLT simulations.....	107
Figure 4.27	As in Fig. 4.9 except comparing CTRL and NMLT simulations.....	108
Figure 4.28	As in Fig. 4.19 except comparing CTRL and NMLT simulations.....	109
Figure 4.29	As in Fig. 4.11 except comparing CTRL and NMLT simulations.....	110
Figure 4.30	Simulated composite reflectivity (dBZ, shaded as indicated at right) and cold pool outline ($T'=-2^{\circ}\text{C}$ at 0 m (black, solid)), for NSUB run at (a) F03, (b) F06, (c) F09, and (d) F12. Line NSUB_A-NSUB_A' in (c) depicts cross-section shown in subsequent figures.....	111
Figure 4.31	As in Fig. 4.5 except comparing CTRL and NSUB simulations.....	112
Figure 4.32	As in Fig. 4.6 except comparing CTRL and NSUB simulations.....	113
Figure 4.33	As in Fig. 4.7 except comparing CTRL and NMLT simulations.....	114
Figure 4.34	As in Fig. 4.12 except comparing CTRL and NSUB simulations.....	115
Figure 4.35	Vertical cross-sections as in Fig. 4.34, showing cold pool ($T'=-2^{\circ}\text{C}$, blue contour), hydrometeor mixing ratios (contours as labeled $\times 10^{-4}$, gkg^{-1}) for graupel (burgundy), cloud ice (purple), rain (green contours and fill), and snow (pink contours and fill) in CTRL (row A) and NSUB (row B) simulations.....	116
Figure 4.36	As in Fig. 4.8 except comparing CTRL and NSUB simulations.....	117
Figure 4.37	As in Fig. 4.9 except comparing CTRL and NSUB simulations.....	118
Figure 4.38	As in Fig. 4.19 except comparing CTRL and NSUB simulations.....	119
Figure 4.39	As in Fig. 4.11 except comparing CTRL and NSUB simulations.....	120
Figure 4.40	Comparison of MCS groundspeeds (ms^{-1}) for CTRL (dark blue), DRYM (red), REVP (green), NMLT (purple), NSUB (light blue).....	121
Figure 4.41	a) Comparison of MCS groundspeeds (ms^{-1}); b) theoretical cold pool speed (ms^{-1}) as calculated according to c_{full} in Eqn (4.1); c) theoretical cold pool speed (ms^{-1}) as calculated according to c_{buoy_only} in Eqn (4.2) for	

	CTRL (dark blue), DRYM (red), REVP (green), NMLT (purple), NSUB (light blue).....	122
Figure 4.42	a) Cross-section of u (shaded, ms^{-1} as in legend at right), and w (ms^{-1} , positive(negative) black solid (dashed) contours) at F09 along CTRL_B-CTRL_B' as in Fig. 4.2c. Solid (dashed) box outlines volumes $\text{VOL}_{\text{leading}}$ ($\text{VOL}_{\text{trailing}}$), and simulated reflectivity contour of 30dBZ (dotted); b) as in a) except for DRYM.....	123
Figure 4.43	a) Volume-averaged momentum budget terms ($\text{ms}^{-1}\text{h}^{-1}$) for CTRL as labeled in key for times F05 – F11 for $\text{VOL}_{\text{leading}}$; b) as in a) but for $\text{VOL}_{\text{trailing}}$; c) as in a) except for DRYM; d) as in b) except for DRYM (note different y-axis scales between $\text{VOL}_{\text{leading}}$ and $\text{VOL}_{\text{trailing}}$).....	124
Figure 4.44	(a) East-west cross-section along line CTRL_B-CTRL_B' as in Fig. 4.2c at F09. Cold pool (blue contour, $T' = -2^\circ\text{C}$), total wind magnitude (ms^{-1} , shaded as indicated), VAu' (30-min averaged quantity, $\text{ms}^{-1}\text{h}^{-1}$, black contours starting 1 $\text{ms}^{-1}\text{h}^{-1}$), $\text{VA}\bar{u}$ (30-min averaged quantity, $\text{ms}^{-1}\text{h}^{-1}$, red contours starting at 1 $\text{ms}^{-1}\text{h}^{-1}$), ; (b) as in (a) except for DRYM simulation taken along DRYM_B-DRYM_B' as in Fig. 4.3c. Distance of cross-sections 175 km.	125
Figure 4.45	a) Momentum budget term averages ($\text{ms}^{-1}\text{h}^{-1}$) as labeled over for CTRL $\text{VOL}_{\text{leading}}$ at F05, b) as in a) but for $\text{VOL}_{\text{trailing}}$, c) as in a) but for DRYM, d) as in b) but for DRYM.	126
Figure 4.46	a) Momentum budget term averages ($\text{ms}^{-1}\text{h}^{-1}$) as labeled over for CTRL $\text{VOL}_{\text{leading}}$ at F09, b) as in a) but for $\text{VOL}_{\text{trailing}}$, c) as in a) but for DRYM, d) as in b) but for DRYM.	127
Figure 4.47	a) As in Fig. 4.8a except for F06; b) as in Fig. 4.8c except for F06; c) CFAD of $\text{VA}\bar{u}$ (bin size .0005 $\text{ms}^{-1}\text{s}^{-1}$); d) as in c) except for VAu' , e) as in c) except for $ \text{VAu}' + \text{VAv}' $; f) as in c) except for DRYM; g) as in d) except for DRYM; h) as in e) except for DRYM.....	128
Figure 4.48	As in Fig. 4.47 except for F09.	129
Figure 5.1	a) Total number of gridpoints with 10-m wind magnitude $> 25.7\text{ms}^{-1}$ vs. time (hours) on x-axis; b) total number of gridpoints with 10-m wind magnitude $> 25.7\text{ms}^{-1}$ for entire simulation; c) as in a) except normalized by storm area (number of gridcells with simulated composite reflectivity $> 30\text{dBZ}$); d) as in b) except for normalized values in c).....	149

Figure 5.2	a) CTRL cold pool ($T' = -2^{\circ}\text{C}$, light and dark blue for times as labeled, areas of gridcell 10-m wind magnitude $> 25.7\text{ms}^{-1}$ (red, shaded); b) as in a) except for DRYM; c) as in Fig. 5.1c except comparing CTRL and DRYM only; d) as in Fig. 5.1d except comparing CTRL and DRYM only.....150
Figure 5.3	Mesovortex generation mechanisms from Atkins and St. Laurent (2009b). a) Cyclonic-only genesis; b) cyclonic-anticyclonic mesovortex couplet genesis. See Atkins and St. Laurent (2009b) for further detail.151
Figure 5.4	Damaging wind generation mechanism (right) from descending rear-inflow jet (RIJ) and gust front mesovortex superposition versus non-damaging mesovortices (left) from Atkins and St. Laurent (2009a).....152
Figure 5.5	CTRL simulation at F10, a) 10-m winds (ms^{-1} , shaded as indicated at right), and 400-m absolute vorticity (black contours, every $0.5 \times 10^{-2} \text{ s}^{-1}$), black lines and labels denote cross-sections used in subsequent figures. b) – e) As in a) but zoomed-in panels in areas indicated by corresponding black boxes in a). Numbers identify individual mesovortices discussed in text.....153
Figure 5.6	10-m winds (vectors and fill), 400-m vort (red), 400-m $w < 0$ (black): CTRL simulation 10-m winds (ms^{-1} , shaded as indicated at right and shown by vectors; reference vector in lower-left), 400-m absolute vorticity (red contours, every $0.5 \times 10^{-2} \text{ s}^{-1}$), 400-m $w < 0$ (ms^{-1} , black contours, at -0.5, -1, and -2 ms^{-1}) at F10 for a) MV1 a) MV2, c) MV3, and d) MV4.....154
Figure 5.7	East-west vertical cross sections of CTRL at F10 for areas indicated in Fig. 5.5. Total wind magnitude (ms^{-1} , shaded as indicated), cold pool ($T' = -2^{\circ}\text{C}$, black contour), and absolute vorticity (red contours, every $0.5 \times 10^{-2} \text{ s}^{-1}$) for CTRL at F10 for a) MV1 a) MV2, c) MV3, and d) MV4.155
Figure 5.8	As in Fig. 5.7 except for along shortened cross-sections as labeled and shown in Fig. 5.5. Vectors show total wind magnitude (ms^{-1}) according to reference vector in lower left.....156
Figure 5.9	Cross-sections as shown in Fig. 5.7. Buoyancy (ms^{-2} , shaded as shown), total hydrometeor mixing ratios [(of snow, rain, graupel) red contours as labeled $\times 10^{-4}$, gkg^{-1}], isotachs of total wind (interval 5ms^{-1} starting at 20ms^{-1} , blue contours), and $w < 0$ (interval 1ms^{-1} , black contours, starting at -1ms^{-1}). PD1 and PD2 denote collocation of hydrometeor maxima and

	downdrafts; BD1 and BD2 denote regions of buoyancy minima and downdrafts in the TSR.....	157
Figure 5.10	Magnitude of 10-m wind field (ms^{-1} , shaded), absolute vorticity (at 400 m, every $0.5 \cdot 10^{-2} \text{ s}^{-1}$, thick red contours), VAV' (i.e., $\text{VAu}' + \text{VAV}'$) (at 400 m, magnitude in black contours every $5 \text{ m}^{\text{s}^{-1}}\text{h}^{-1}$ beginning at 10, vectors according to reference vector), and $\text{VA}\bar{u}$ (at 400 m, every $1 \text{ ms}^{-1}\text{h}^{-1}$ beginning at 1, thin green dashed contours) at F10 for CTRL simulation for a) MV1 a) MV2, c) MV3, and d) MV4. X's marks maxima of VAV' as discussed in text.....	158
Figure 5.11	East-west cross-sections along lines indicated in Fig. 5.5a at F10. Cold pool (blue contour, $T' = -2^\circ\text{C}$), total wind magnitude (ms^{-1} , shaded as indicated), VAu' ($\text{ms}^{-1}\text{h}^{-1}$, black contours starting $1 \text{ ms}^{-1}\text{h}^{-1}$), $\text{VA}\bar{u}$ ($\text{ms}^{-1}\text{h}^{-1}$, red contours starting at $1 \text{ ms}^{-1}\text{h}^{-1}$) for a) MV1 a) MV2, c) MV3, and d) MV4.....	159
Figure 5.12	From simulation analyzed in Chapter 3 (as in Fig. 3.14): Composite parcel height (red line, m, values on y-axis at left) and wind speed ($ V $, solid, ms^{-1} , values on y-axis at right) vs. time (x-axis, sec) of average trajectory of 50 parcels originating at RIJ-level for time period $t = 25200\text{s}$ (F07:00) to $t=34200\text{s}$ (F09:30).....	160
Figure 5.13	CTRL cold pool boundary ($T' = -2^\circ\text{C}$, contours), areas of gridcell 10-m wind magnitude $> 25.7\text{ms}^{-1}$ (shaded) for times F0600 – F0640 where colors denote different times as labeled in upper right.....	161
Figure 5.14	Total wind magnitude (ms^{-1} , shaded as indicated), cold pool ($T' = -2^\circ\text{C}$, black contour), and $w < 0$ (black contours, 0.5, -1, -2, -3, -4 and -5 ms^{-1}) at F06 along line CTRL_C – CTRL_C' in Fig. 5.13. A, B, and C denote specific downdrafts discussed in text.....	162
Figure 5.15	As in Fig. 5.14 except wind vectors omitted and times F0600 – F0640 shown as labeled.....	163
Figure 5.16	As in Fig. 5.11 except along line CTRL_C – CTRL_C' for F0600 – F0640 as labeled.....	164
Figure 5.17	CTRL cold pool (blue contour, $T' = -2^\circ\text{C}$), total wind magnitude (ms^{-1} , shaded as indicated, vectors according to reference vector in lower left), VAu' ($\text{ms}^{-1}\text{h}^{-1}$, black contours starting $1 \text{ ms}^{-1}\text{h}^{-1}$), $\text{VA}\bar{u}$ ($\text{ms}^{-1}\text{h}^{-1}$, red contours starting at $1 \text{ ms}^{-1}\text{h}^{-1}$).....	165

Figure 5.18	DRYM occurrences of grid cell 10-m wind magnitude $> 25.7\text{ms}^{-1}$ (red) for times F0700 – F1155.....	166
Figure 5.19	As in Fig. 5.13 except for DRYM from F0700 – F0740 as labeled in upper right.....	167
Figure 5.20	As in Fig. 5.16 except along line DRYM_C – DRYM_C' and for F0700 – F0740 as labeled.....	168
Figure 5.21	As in Fig. 5.17 except for DRYM at F0730.....	169
Figure 5.22	DRYM cold pool (blue contour, $T' = -2^{\circ}\text{C}$), total wind magnitude (ms^{-1} , shaded as indicated), $w < 0$ (ms^{-1} , black contours starting 0.5ms^{-1}) along line DRYM_C – DRYM_C' from F0700 – F0740 as labeled.....	170
Figure 5.23	As in Fig. 5.22 except for F0735 only.....	171
Figure 5.24	a) CTRL at F09: wind magnitude at 5 km AGL (ms^{-1} , shaded as indicated), $w < 0$ (ms^{-1} , orange contours every 1ms^{-1} beginning at -1ms^{-1}), simulated reflectivity (dBZ, black contours, every 10 dBZ starting at 20 dBZ), and red box denoting area plotted in CFAD in (b); b) CFAD of microphysical heating tendency, h diabatic (Ks^{-1}), at F09 for CTRL area denoted in (a). Bin size is $.01\text{Ks}^{-1}$ and plot is contoured as indicated by shading and key at bottom; c) as in a) except for DRYM simulation; d) as in d) except for DRYM simulation.....	172
Figure 5.25	a) CTRL at F09: wind magnitude at 5 km AGL (ms^{-1} , shaded as indicated), $w < 0$ (ms^{-1} , orange contours every 1ms^{-1} beginning at -1ms^{-1}), simulated reflectivity (dBZ, black contours, every 10 dBZ starting at 20 dBZ), and red box denoting area plotted in CFAD in (b); b) CFAD of vertical velocity, w at F09 for CTRL area denoted in (a). Bin size is 0.25ms^{-1} and plot is contoured as indicated by shading and key at bottom; c) as in a) except for DRYM simulation; d) as in d) except for DRYM simulation.....	173
Figure 5.26	As in Fig. 5.25 except b) and d) display the magnitude of the perturbation wind speed $((u'^2 + v'^2)^{1/2}, \text{ms}^{-1})$, bin size 1ms^{-1}	174
Figure 5.27	As in Fig. 5.25 except b) and d) display VAV' bin size $.01\text{ms}^{-1} \text{s}^{-1}$	175
Figure 5.28	As in Fig. 5.25 except b) and d) display $VA\bar{u}$ bin size $.01\text{ms}^{-1} \text{s}^{-1}$	176
Figure 5.29	As in Fig. 5.2a,b except for a) REVP, b) NMLT, and c) NSUB.....	177

Figure 5.30	a) as in Fig. 5.29b, black box shows area of severe winds shown in b); b) 10-m AGL total wind magnitude (ms^{-1} , shaded as indicated), column-total hydrometeor concentration (black contours as labeled $\times 10^{-4}$, gkg^{-1}); c) vertical cross-section shown by black line in b), cold pool (blue contour, $T' = -2^\circ\text{C}$), total wind magnitude (ms^{-1} , shaded as indicated, vectors according to reference vector in lower left), and hydrometeor mixing ratios (contours as labeled $\times 10^{-4}$, gkg^{-1}) for graupel (orange), cloud ice (light purple), rain (green), and snow (pink).....178
Figure 6.1	a) Schematic of “before”-MCS region (red) and “after”-MCS region (blue) used for averages shown in b); b) SKEW-T showing “before”-MCS area-averaged temperature and dewpoint profiles (red, right and left, respectively) and “after”-MCS area-averaged temperature and dewpoint profiles (red, right and left, respectively), with average wind fields shown at right in knots.....192
Figure 6.2	a) Original Corfidi vector technique, with MCS core motion (thick dotted arrow) expressed as the vector sum of 1) advection of cells by the mean cloud-layer wind (arrow pointing to upper right) and 2) cell propagation directed into the low-level jet (arrow pointing to bottom of page). MCS centroid is depicted by the cross symbol [from Corfidi (2003), after Corfidi et al. (1996)], and b) updated Corfidi technique showing (top) upwind and (bottom) downwind versions of the vector technique to forecast short-term motion of upwind-developing systems (MCS motion given by thick red arrows) and downwind-developing systems (MCS motion given by thick green arrow at bottom of figure), respectively. Vector lengths are proportional to wind speed; MCS centroids are denoted by the cross symbol [from Corfidi (2003)].....193
Figure 6.3	Corfidi vectors at F09 (vectors, reference vectors as indicated in lower left) and vector magnitude (ms^{-1} , shaded as indicated) calculated according to a) Corfidi (2003), and b) Corfidi et al. (1996). Single thick black arrow represents “observed” mean vector motion of CTRL MCS.....194
Figure A.1	Initial soundings for Q-I (red and green lines) and Idealized simulation (blue lines, plotted underneath red/green) taken near center of domain near trigger.....216
Figure A.2	Simulated composite reflectivity (dBZ, shaded as indicated) for a) Quasi-idealized simulation at F03; b) Idealized simulation at F03; c) as in a) except at F06; d) as in b) except at F06.....217

Figure A.3	As in A.2 except at F09 in a) and b) and at F12 in c) and d).....	218
Figure A.4	a) Vertical cross-section of simulated composite reflectivity (dBZ, black contours) at F06 averaged in an along-line direction in 40-km segments in simulations showing cold pool (shaded as shown beginning at $T' = -2^{\circ}\text{C}$), negative (positive) pressure perturbation in solid (dashed) contours (hPa); and simulated reflectivity (dBZ, black contours as labeled, every 10dBZ beginning at 20 dBZ) for the a) quasi-idealized simulation, and b) idealized simulation.....	219
Figure A.5	a) Quasi-idealized simulated reflectivity at F06 with black line indicating cross-section in other panels; b) as in a) except for Idealized simulation; c) cold pool shaded as shown, simulated reflectivity (black contours), and PGA_x from Eqn 2.2 ($\text{ms}^{-1}\text{h}^{-1}$, positive (negative) values in purple solid (pink dashed) contours), d) as in c) except for Idealized; e) as in c) except VAu' ; f) as in e) except for Idealized; g) as in c) except $\text{VA}\bar{u}$; h) as in g) except for Idealized.....	220
Figure A.6	Volume-averaged momentum budget terms as labeled in key for times F05 – F11 for the a) quasi-idealized leading volume and b) idealized simulation leading volume; c) as in a) except for trailing volume (<i>note different scales of y-axes</i>); d) as in c) except for idealized simulation....	221
Figure A.7	Speed of MCS (ms^{-1}) from quasi-idealized simulation (solid) and idealized simulation (dashed).....	222
Figure B.1	Simulated composite reflectivity (dBZ, shaded as indicated at left) for a) CTRL at F03, b) FAST at F03, c) CTRL at F06, and d) FAST at F06....	226
Figure B.2	Simulated composite reflectivity (dBZ, shaded as indicated at left) for a) CTRL at F09, b) FAST at F09, c) CTRL at F12, and d) FAST at F12...	227
Figure B.3	a) Outline of 30-dBZ simulated composite reflectivity at each hour in different color for a) CTRL, and b) FAST. c) Table comparing average speed of CTRL and FAST.....	228
Figure B.4	Initial u-wind profiles (ms^{-1}) for a) CTRL, b) FAST-ULJ, and c) FAST-LLJ.....	229
Figure B.5	Simulated composite reflectivity (dBZ, shaded as indicated at left) at F09 for a) CTRL, b) FAST-LLJ, c) FAST-ULJ. d) Comparison of system groundspeeds (ms^{-1}) as labeled.	230

Figure B.6	(a) East-west cross-section taken in center of MCS apex at F06 showing cold pool (shaded as shown beginning at $T' = -4^{\circ}\text{C}$) and magnitude of total perturbation wind $((u'^2 + v'^2)^{1/2}, \text{ms}^{-1}$, black contours) for a)CTRL, b) FAST-ULJ, and c) FAST-LLJ. Black arrows show ground-relative flow in the x-z plane scaled as shown by reference vector in lower left corner.....	231
Figure B.7	Initial soundings for a) CTRL, b) SLLJ, and c) FtR-LLJ.....	232
Figure B.8	Simulated composite reflectivity (dBZ, shaded as indicated at left) for at F09 for a) CTRL, b) SLLJ, and c) FtR-LLJ.....	233
Figure B.9	As in Fig. B.8 except at F12.....	234
Figure C.1	Simulated composite reflectivity (dBZ, shaded as indicated at right) at F03 for (a) CTRL run (b) REVP, and (c) IEVP.....	236
Figure C.2	As in Fig. C.1 except at F06.....	237
Figure C.3	As in Fig. C.1 except at F09.....	238
Figure C.4	As in Fig. C.1 except at F12.....	239
Figure C.5	Comparison of initial sounding shape used to initialize the quasi-idealized MCS simulation (at $35^{\circ}\text{lat}; -95^{\circ}\text{lon}$) for (a) CTRL simulation, and (b) MOIM (moist mid-levels) simulation. Temperature ($^{\circ}\text{C}$, solid line), dewpoint ($^{\circ}\text{C}$, dashed line), wind barbs in knots at right.....	240
Figure C.6	Simulated composite reflectivity (dBZ, shaded as indicated at right) at F03 for (a) CTRL run (b) DRYM, and (c) MOIM.....	241
Figure C.7	As in Fig. C.6 except at F06.....	242
Figure C.8	As in Fig. C.6 except at F09.....	243
Figure C.9	As in Fig. C.6 except at F12.....	244

Chapter 1

Introduction and Background

1.1 Motivation

A mesoscale convective system (MCS) is defined by the American Meteorological Society as “an ensemble of convective cells producing a contiguous region of precipitation on the order of 100 km or more,” and the motivations for studying such systems are numerous and diverse. From a societal impact standpoint, MCSs are the main producers of precipitation in many regions of the world and are thus critical to agricultural and human needs. Yet such systems are also capable of producing severe weather in the form of strong surface winds, hail, and tornadoes, as well as lightning and flash floods; Ashley and Mote (2005) discuss individual derecho-producing MCSs that have each resulted in human casualties, injuries, and property damages exceeding \$500 million. Research-driven motivation also stems from the myriad research questions that extend beyond simply identifying the causes and immediate effects of such systems; the general study of MCSs intertwines nearly all spatial and temporal scales and atmospheric science sub-disciplines. That is, from microscale processes of turbulence and mixing to synoptic scale interactions, and extending to longer-term global climate feedbacks, MCSs offer research challenges to dynamists, cloud physicists, observationalists, forecasters, and numerical modelers.

The particular investigation presented here aims to improve understanding of the processes that drive MCS motion and low-level flow dynamics. MCS motion is often the combined result of several physical processes that occur on different temporal and spatial scales, and forecasting such feedbacks remains a challenge to human forecasters and numerical weather prediction (NWP) models alike (e.g., Corfidi 2003). The causes and dynamics of MCS motion are of importance to both researchers seeking to improve dynamical understanding of these systems, as well as to operational forecasters aiming to improve forecast accuracy of the timing and intensity of associated precipitation and

severe weather (e.g., Merritt and Fritsch 1984; Corfidi 2003). A large body of past research has explored various mechanisms by which these systems move (e.g., cold pools, gravity waves), and the goal of this investigation is to provide an in-depth assessment of a process that may also significantly affect MCS motion and associated sensible weather: the vertical transport and adjustment of horizontal momentum within an MCS.

Figure 1 conceptually illustrates aspects of the convective momentum transport (CMT) process, using an adaptation of the Houze et al. (1989) classic leading-convective, trailing-stratiform MCS archetype. This illustration shows how flow from the rear of the system is accelerated via the pressure gradient force and transported downward, the strongest winds forming the rear-inflow jet (RIJ) (e.g., Smull and Houze 1987). The degree to which the combined momentum of the environmental and storm-induced wind fields is transported downward depends on a number of factors including the strength of the RIJ and the magnitude of negative buoyancy in the trailing stratiform region (e.g., Houze et al. 1989; Lafore and Moncrieff 1989), as well as downdrafts and/or negative buoyancy generated in the convective region (e.g., Zipser 1977; Klimowski 1994). The extent to which the RIJ descends relative to the surface has implications for MCS motion as well as the potential for damaging winds. Weisman (1992) details how RIJ descent may be determined by the resulting vorticity balance between the convective and stratiform MCS regions as a result of the relative strength of horizontal buoyancy gradients between the surface cold pool and midlevels, and more recent research by Trapp and Weisman (2003) and Atkins and St. Laurent (2009a) finds that a descending RIJ may cause severe surface winds when collocated with a mesovortex along the leading convective line. The MCS momentum field is ultimately the combined effect of the processes described above, in addition to contributions imparted by both the larger-scale flow (e.g., Smull and Houze 1987) as well as convective-scale transports of varying magnitude occurring throughout the storm (e.g., Yuter and Houze 1995b; Bryan et al. 2003). CMT is defined herein as the vertical transport of horizontal momentum that results from the presence of an MCS. That is, the term includes both mesoscale and

convective-scale adjustments, and in the broadest sense refers to all changes realized in the momentum field, including those due to both pressure gradient accelerations and transport.

The overarching goal of this investigation is to improve understanding of the processes that drive MCS motion and low-level momentum in MCSs, but the study will focus on the role of CMT. Enhanced insight in this area will help to improve severe weather forecasting and potentially increase warning times for phenomena such as straight-line wind damage – an issue of critical concern when strong rear inflow descends to the surface as described above (e.g., Johns and Hirt 1987; Weisman 1992; Wakimoto et al. 2006). Additional motivation for this work stems from the neglect of CMT in some convective parameterization (CP) schemes. One shortcoming of some CP schemes [e.g., operational implementations of the Betts-Miller-Janjić (Betts 1986; Janjić 1994), Kain-Fritsch (Kain and Fritsch 1993), and Grell (Grell 1993) schemes] is the omission or oversimplification of momentum adjustment¹ – it is hypothesized that this may sometimes inhibit accurate representation of MCS motion in operational model forecasts. This limitation has also been suggested by previous research demonstrating that NWP model forecasts of an observed MCS in which a CP scheme is employed exhibited a negative bias in forecasted MCS speed (Mahoney and Lackmann 2007). CP schemes are challenged to represent the effects of processes on both the meso- and convective scales that affect the accuracy of simulated MCS motion. For example, Correia et al. (2008) found a distorted RIJ (generally considered a mesoscale feature) resulting from the use of a CP scheme, and many past studies caution against the omission of critical convective-scale processes (e.g., convective downdrafts, turbulent mixing) in simulations using larger grid spacing and a CP scheme (e.g., Weisman et al. 1997; Bryan et al. 2003). Therefore, while there exist many challenges to successful numerical simulations of MCSs [e.g., correct representation of the vertical heating profile (Pandya and Durran

¹ The treatment of momentum adjustment varies widely in different CP schemes, from complete omission, to more sophisticated schemes based on perturbation pressure gradient relationships (e.g., Wu and Yanai 1994; Carr and Bretherton 2001; Han and Pan 2006; Moncrieff and Liu 2006; Hogan and Pauley 2007; Wu et al. 2007).

1996; Correia et al. 2008)], neglecting or crudely approximating CMT within an MCS is likely detrimental to MCS motion forecasts from both the mesoscale (e.g., RIJ-related effects) and convective-scale (e.g., downdraft resolution) perspectives. Thus, while CMT is defined herein to include both scales of motion, differentiating the two for CP scheme applications may be an avenue of future research. While increased computing power may eventually render CP schemes unnecessary for short- and medium-range operational forecasting, they will likely remain essential for both global and regional climate models and ensemble forecasts; therefore, improving such schemes will remain a valuable contribution, even after mesoscale operational models are run without them.

MCS motion is comprised of an advective component, \vec{C}_A , and a propagative component, \vec{C}_P , where the motion of the MCS (\vec{C}) is the sum of these two components, $\vec{C} = \vec{C}_A + \vec{C}_P$ (e.g., Fig 1.2; Newton and Newton 1959; Bluestein and Jain 1985; Corfidi et al. 1996; Fritsch and Forbes 2001). The advective component of motion is generally determined by the mean cloud-bearing wind (e.g., Newton and Newton 1959; Corfidi et al. 1996), whereas propagation may be continuous (e.g., driven by the continual spreading of the sub-cloud cold pool) or discrete (forming ahead of an existing gust front, e.g., Fovell et al. 2006). The processes that determine the motion of observed MCSs remain incompletely understood, and identifying the physical processes that dominate in a given background environment and ultimately determine MCS groundspeed is difficult (e.g., Houze 2004). The present study first asks: *In what ways does CMT affect MCS motion?* The findings described herein provide a unique contribution to the study of MCS motion by describing a process that (to the author's knowledge) has not been thoroughly examined as it specifically relates to MCS motion. This study further examines whether changes in MCS speed are primarily due to the advective component of system motion (i.e., system speed changes as a result of changes in the mean cloud-bearing wind), or to the propagative component (i.e., altering cold pool characteristics, thereby affecting new cell growth and thus system speed), and what internal or external storm processes or characteristics maximize or minimize the importance of CMT. This chapter concludes by

describing CMT and its treatment in previous studies; remaining chapters then quantify the process in a numerically-simulated MCS to examine its effect on system motion and surface wind speeds, and then test its sensitivity to a variety of storm-scale and environmental parameters.

1.2. Background

1.2.1 Previous related research

Past studies have examined CMT within MCSs, but most have focused on its effect on the large-scale momentum field of the surrounding environment, or its parameterization in large-scale numerical models (e.g., Houze 1973; Grubišić and Moncrieff 2000; Mechem et al. 2006). Studies by Houze et al. (2000) and Mechem et al. (2006) have advanced the idea that momentum transport within and beneath the stratiform region of tropical MCSs can significantly impact the lower-tropospheric wind field. One of the two main regimes studied by Mechem et al. (2006) examines the enhancement of surface westerly winds via the downward transport of upper-level westerly momentum. While their findings focus on the effect of this transport on the large-scale momentum field, it follows that such a feedback might also impact the translational speed of the MCS by changing the wind at lower levels or within the cold pool. One idea to be examined herein is the effect of this latter aspect, distinct from that of most previous studies: *What influence does the vertical transport of horizontal momentum (of both large-scale and perturbation winds) by an MCS have on the ground speed of the MCS itself?*

Many of the previous studies that have examined CMT in MCSs have employed momentum budgets (e.g., Sanders and Emanuel 1977; Lemone 1983; Gao et al. 1990; Gallus and Johnson 1992; Yang and Houze 1996; Trier et al. 1998; Mechem et al. 2006). Such studies all describe the challenges inherent to studying CMT within these systems: unlike many thermodynamic variables, momentum suffers the added complexity imposed by nonconservative effects due to pressure perturbation forces – thus, determining the role of CMT is decidedly more difficult compared to convective tendencies of other

conserved quantities. In addition to the effect of CMT on large-scale and tropical circulations, some papers investigating derechos and related MCS phenomena also highlight the potential importance of momentum transport as a key determinant of surface wind speed (a small number of studies also indirectly mention relevance to MCS motion) (e.g., Brandes 1977; Johns and Hirt 1987; Johns and Doswell 1992; Vescio and Johnson 1992; Weisman 1992, 1993; Corfidi et al. 1996; Geerts 2001; Corfidi 2003; van den Broeke et al. 2005). This topic is discussed further in section 1.2.3, as well as in Chapters 5 and 6.

1.2.2 MCS momentum transport

The two main branches of flow in an MCS that can be associated with strong vertical momentum transport are shown in Fig. 1.1. The momentum field of the MCS can be described by the anelastic equation of motion:

$$\frac{\partial \vec{U}}{\partial t} = -\frac{1}{\rho_0} \nabla p' + B \hat{k} - \vec{U} \cdot \nabla \vec{U} - 2\Omega \times \vec{U} \quad (1.1)$$

where \vec{U} represents the three-dimensional wind field, p' is the pressure perturbation from the hydrostatic base state, $B = -g \left(\frac{\rho'}{\rho_0} - q_h \right)$, q_h is the hydrometeor mixing ratio, friction is ignored, and the rest of the terms retain their usual meanings.

The generation and evolution of the RIJ is largely described by the perturbation pressure gradient and buoyancy forces in (1.1). The RIJ is accelerated by the perturbation pressure gradient force that results from the midlevel mesolow (itself a result of the vertical profile of latent heating), and the descent of the accelerated RIJ is largely attributable to negative buoyancy in the trailing stratiform region that arises due to melting, sublimation, evaporation, and water loading (e.g., Srivastava 1987; Braun and Houze 1997; Grim et al. 2009a). It has been shown that in some cases, the RIJ helps to maintain the surface cold pool via thermodynamic enhancement of environmental cooling (i.e., increasing negative buoyancy by introducing dry environmental air into which

falling hydrometeors may melt, evaporate, or sublimate), as well as by increasing cold pool wind speeds through dynamical processes such as downward momentum transport [accounted for in the advection term in (1.1)] (e.g., Smull and Houze 1987; Haertel and Johnson 2000; Houze et al. 2000; Mechem et al. 2006). Here, it is hypothesized that CMT may impact MCS motion in two possible ways (though others may exist as well):

1. The advective component of MCS motion may be enhanced via the forward penetration of elevated portions of the RIJ. This scenario describes high-momentum air from aloft being transported forward (and to a lesser extent downward, but not into the surface-based cold pool); and/or
2. System speed may increase as downward CMT increases the speed of the cold pool itself (by increasing the speed of the winds within it); the MCS thus moves more quickly as new convection forms on the faster-moving cold pool boundary.

These possibilities are addressed in Chapter 3.

1.2.3 Momentum transport and near-surface thunderstorm wind generation

1.2.3.1 Convectively driven windstorms

It is widely recognized that MCSs produce downdrafts that can result in surface wind damage as well as human casualties and injuries. Wakimoto (2001) provides a comprehensive summary of past research on convectively-driven wind storms, and points out that most past studies have focused primarily on the downburst-driven severe wind generation mechanism. A downburst is generally defined as an area of strong winds that are produced by a convective downdraft and occur over an area measuring ~1 km to 10 km in horizontal extent. Downbursts are sometimes divided into the sub-classifications *microburst* (surface outflow diameter < 4 km, with peak winds lasting 2 – 5 minutes) and *macroburst* (surface outflow diameter 4 km or larger, with peak winds lasting 5 – 20 minutes). The downburst-driven severe convective wind mechanism as described in early studies by Fujita (1985) (Fig. 1.3) has led to a larger body of research dedicated to

elucidating this phenomenon, and many such studies have focused on the roles of condensate loading and thermal buoyancy (e.g., Srivastava 1985, 1987; Knupp 1988; Proctor 1989). Wakimoto (2001) uses the inviscid vertical momentum equation to discuss the fundamental forcing mechanisms for the thunderstorm downdraft:

$$\frac{d\bar{w}}{dt} = -\frac{1}{r} \frac{\partial \bar{p}'}{\partial z} + g \left[\frac{\theta_v'}{\theta_{v_0}} - \frac{c_v}{c_p} \frac{p'}{p_0} - (r_c + r_r + r_i) \right], \quad (1.2)$$

where \bar{w} = mean vertical velocity, r_c = mixing ratio of cloud water, r_r = mixing ratio of rain water, r_i = mixing ratio of ice water, and primed quantities indicate departures from a basic stage (subscript 0) that varies only in height. To the extent that all damaging winds from thunderstorms and MCS are indeed driven by outflow that occurs at the base of a downdraft (e.g., Johns and Doswell 1992), (1.2) can be used to illustrate the potential for generating severe surface winds via buoyancy perturbations, pressure perturbations, and hydrometeor loading. Several studies have also discussed surface pressure patterns unique to MCSs that may also locally accelerate surface flow to severe magnitudes (e.g., Johnson and Hamilton 1988; Loehrer and Johnson 1995).

Derechos represent still another category of severe wind-producing storms, and are often associated with MCSs and more specifically, with bow echoes. Derechos are generally defined as any family of downburst clusters produced by an extratropical MCS (AMS glossary), although individual studies (e.g., Johns and Hirt 1987) have developed additional criteria to identify these events. Bow echo damage in general has been shown to be caused by mesoscale downdrafts that produce outflow winds exceeding 30 ms^{-1} . However, most observed damage swaths feature embedded pockets of more intense damage occurring on much smaller scales. Determining where and by what process such isolated areas of wind damage occur remains an outstanding question facing both researchers and forecasters.

1.2.3.2 CMT as a possible mechanism for surface wind gust generation in MCSs

One of the most common types of MCS organization is the “leading convective line-trailing stratiform” MCS (e.g., Newton 1950; Houze et al. 1990; Parker and Johnson 2000). This MCS prototype is characterized by a leading convective line followed by a region of stratiform precipitation. The trailing stratiform region (TSR) is typically 50 – 200 km wide and features two main flow regimes: front-to-rear flow that ascends from middle to upper levels, and rear-to-front flow that descends from middle to low levels (e.g., Fig. 1.1). Both airstreams are of dynamical and structural importance to the MCS itself; the ascending front-to-rear flow distributes hydrometeors into the stratiform region from the leading convective region, and the rear-to-front flow (or rear-inflow jet) is heavily influenced by the TSR itself and may directly impact the surface cold pool as described in the preceding section. The connection between the RIJ and surface cold pool is one way in which MCSs, and particularly MCSs with substantial trailing stratiform regions (and thus a larger trailing area of descent), may have a marked effect on both MCS motion and low-level wind speeds.

Past studies have shown that momentum transport within an MCS may have operational forecasting implications with respect to the prediction of surface wind gusts (e.g., Foster 1958; Johns and Doswell 1992; Weisman 1992; Geerts 2001; Kuchera and Parker 2006). While numerous past studies investigating the causes of severe surface winds have focused on the classic downburst model driven by strong, thermodynamically driven downdrafts that diverge strongly upon intercepting the surface (e.g., Fujita 1985; Wakimoto 2001), studies such as those by Foster (1958) and Geerts (2001) have also attempted to document the influence of CMT on surface wind gusts and also incorporate the process into forecast parameters and indices. However, such studies have highlighted the difficulty in successfully adding the effect to achieve improved forecasts, and hence the contribution CMT to surface wind gusts remains poorly understood.

As Geerts (2001) affirms, the literature on strong, convectively-generated surface winds rarely mentions the downward transport of horizontal momentum as a contributing process, despite a number of studies that have found it to be a key driving mechanism (e.g., Eilts and Doviak 1987; Weisman 1992; Orf and Anderson 1999). While some

studies of derechos have mentioned CMT, the summary of windstorm-producing mechanisms in Wakimoto (2001) (in addition to summaries provided in other studies) focuses mainly on thermodynamic and pressure perturbation influences on the downdraft itself. That is, vertical advection as expressed in the horizontal momentum equation (i.e., the x- and y-components of (1.1)) is omitted entirely from many of these discussions, and thus neglected as a potential contributor to horizontal wind gusts. It is conceivable that in many cases, strong surface winds may not necessitate an especially intense downdraft itself, provided that strong winds from aloft are brought far enough surface-ward by moderate (e.g., $< 5 \text{ ms}^{-1}$) or even relatively weak (e.g., $< 1 \text{ ms}^{-1}$) downward motions. Chapter 5 will investigate more closely how the CMT process may contribute to severe wind generation and Chapter 6 will discuss further potential significance of CMT from a forecasting perspective.

1.3 Summary

Momentum transport within MCSs has been studied for a number of purposes. Early works such as Newton (1950) and Lemone (1983) first hypothesized its significance to MCS dynamics, and more recent works (e.g., Mechem et al. 2006) have suggested a strong link between CMT and the large-scale flow. Its parameterization in larger-scale numerical models has been addressed by many authors [summarized by Carr and Bretherton (2001)], and a connection between CMT and low-level wind generation has been noted by both early and more recent studies alike (e.g., Foster 1958; Johns and Doswell 1992; Geerts 2001). Still other authors have considered its relationship with MCS motion (e.g., Orf and Anderson 1999; Corfidi 2003).

Despite these past investigations, understanding of the significance of CMT in MCSs remains incomplete. The analysis detailed in the following chapters will focus on two main questions:

1. What is the significance of CMT to MCS motion?
2. How does CMT affect the generation of strong surface winds?

Study methodology is detailed in Chapter 2, and Chapter 3 quantifies the CMT process in an idealized MCS. Chapter 4 discusses the results of four sensitivity experiments with respect to the dynamics of MCS motion, and Chapter 5 analyzes the generation of surface wind speed differences in the same four sensitivity tests. Finally, Chapter 6 discusses the overall findings and significance of CMT and suggests future work toward incorporating findings into MCS forecast applications.

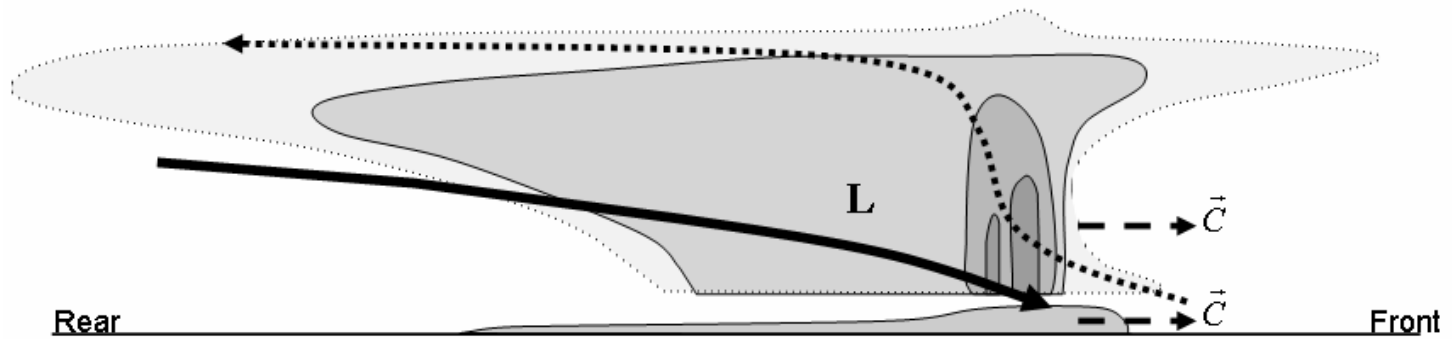


Figure 1.1: Schematic of hypothesized momentum transport mechanism in an idealized MCS. Based on Houze et al. 1989, where outermost dotted outline represents cloud outline, inner shaded solid contours represent radar reflectivity, and shaded area at surface represents the cold pool. Bold “L” denotes approximate area of midlevel mesolow; thick downward-sloping arrow shows rear-to-front flow, and dashed upward-sloping arrow shows front-to-rear flow branch. Dashed arrow denotes “c”, the accelerated speed at which the cold pool and MCS move.

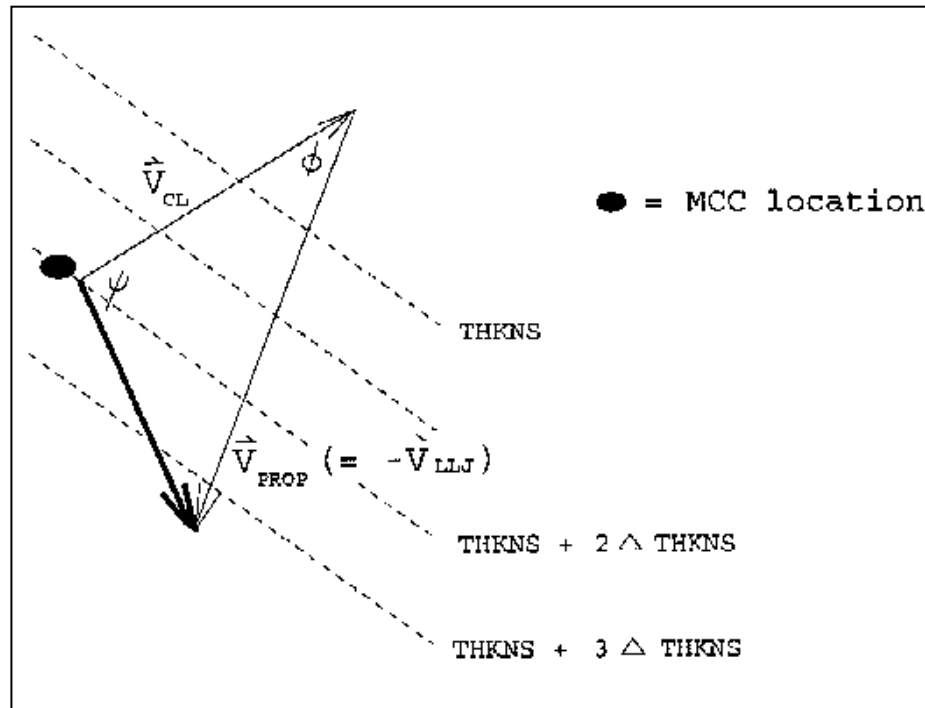


Figure 1.2: From Corfidi (1996): Conceptual model of MCS movement (V_{MBE}) as the vector sum of the mean flow in the cloud layer (V_{CL}) and the propagation component (V_{PROP}). Angles ϕ and ψ are used to calculate V_{MBE} given observed values of V_{CL} and V_{LLJ}

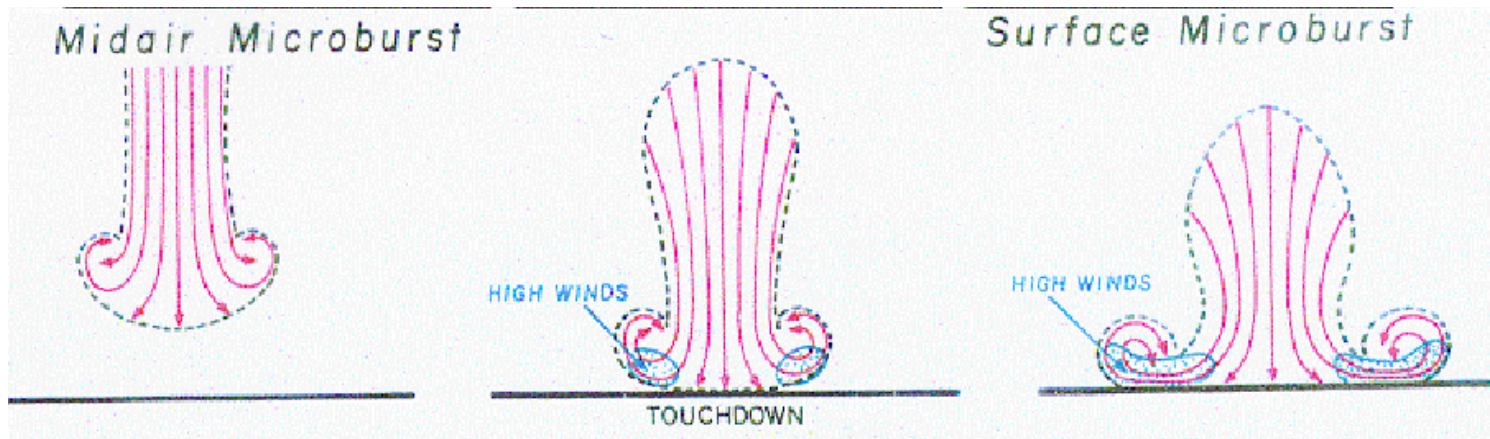


Figure 1.3: Conceptual model of a microburst hypothesized to explain ground-damage patterns, with three stages of development shown. From Wakimoto (2001), based on a figure from Fujita (1985).

Chapter 2

Methodology

2.1 Quasi-idealized modeling approach

2.1.1 Model set-up and initial conditions

In order to rigorously investigate convective momentum transport in an MCS, a high-resolution, four-dimensional, dynamically consistent MCS dataset is desired. As advocated by Keyser and Uccellini (1987), a reliable and realistic numerical simulation can provide such a dataset; a modeling framework also facilitates diagnostic analyses and allows for sensitivity tests. In order to examine an MCS that is simplified for clarity of analysis but that also develops in a three-dimensional, thermal-wind-balanced environment, the Weather Research and Forecasting (WRF; Skamarock et al. 2007) model is used in a way that employs a combination of real-case and idealized modeling techniques. This combination benefits from the lucidity of idealized simulations by using simplified initial and boundary conditions that remove small-scale features and perturbations found in observations, while also taking advantage of a real-case modeling framework able to employ a more complete suite of physics options. The simulations presented here are initiated in a baroclinic background environment (an element largely neglected by many purely-idealized modeling studies of the past). This approach allows a more realistic treatment of the larger-scale environment by including an upper-level jet stream that is in thermal wind balance, and by accounting for the influence of the Coriolis force on MCS evolution (important to MCS motion over extended time intervals); Skamarock et al. (1994), Jewett and Wilhelmson (2006), and Richardson et al. (2007) also discuss the advantages of such a framework.

Initial conditions for the simulations are generated using empirical relationships to produce a simple westerly jet stream in an environment with CAPE and a horizontal wind field in thermal wind balance. For the simulation presented in Chapter 3, and all other simulations discussed except for one in which mid-levels are dried (DRYM; detailed in

the next section), Fig. 2.1 shows the initial height and wind fields in the x-y plane as well as in a north-south vertical cross-section, in addition to the surface-based CAPE and CIN fields, and Fig. 2.2a shows the initial sounding. In order to produce a jet stream and achieve thermal wind balance, the entire initial sounding is first uniformly adjusted to be cooler (warmer) as latitude increases (decreases); in this way, the initial conditions more realistically represent the baroclinic background environment common to midlatitude MCSs (relative to more idealized studies in which a single uniform initial sounding is often used). One notable difference between an observed jet stream and the jet stream created here is the lack of a sloping tropopause (Fig. 2.1b); however, this omission allows for a more uniform equilibrium level at all locations.

The initial thermodynamic profile is an adaptation of that used in Weisman and Klemp (1982) such that characteristics of MCS environments noted in later studies (e.g., Bluestein and Jain 1985; Houze et al. 1990; Parker and Johnson 2004b) are also incorporated. These modifications include drying upper levels by ~10% of the values used by Weisman and Klemp (1982), and also adding a weak capping inversion in order to prevent ubiquitous convective initiation in the initially-unstable atmosphere – Fig. 2.2b-e reflects these changes by comparing the sounding used to initialize the model runs here to those found or used by other past midlatitude MCS studies. The initial geopotential height and wind fields are produced by first calculating the virtual temperature from the sounding temperature and moisture values. Next, the geopotential height is computed from virtual temperature, and the geostrophic wind field is finally derived from the geopotential height field.

Convection is triggered by the addition of a 2.5°C warm bubble (with unchanged mixing ratio) with horizontal dimensions ~100 km x 40 km located between the surface and 3 km (Fig. 2.3). Several experiments were conducted to examine sensitivity to the trigger but little impact was found; cold and warm anomalies of varying sizes, depths, and intensities all ultimately produce very similar MCSs.

The resulting input files are then used as initial conditions in the three-dimensional “real” WRF model to simulate an MCS that possesses many of the salient

features found in observed cases. An inner domain with 1-km horizontal grid spacing (676 km x 604 km; Fig. 2.1a) lies within an outer domain of 4-km grid spacing (1800 km x 1800 km). Neither domain utilizes a CP scheme, but both employ the Yonsei University (YSU) planetary boundary layer (PBL) scheme (Hong et al. 2006) to more completely represent the effects of surface friction and above-ground turbulence that are otherwise not resolved by 1-km grid spacing but that are important to accurately represent MCS motion. Bryan et al. (2003) note a number of shortcomings of using 1-km grid spacing to simulate deep convection. While this study would ideally use $O(100\text{m})$ grid spacing as advocated by Bryan et al. (2003), computational limitations preclude it. Thus, interpretation of results must include the possibility that turbulent processes such as entrainment and small-scale overturning, precipitation amount and distribution, and energy spectra may not be good benchmarks for observed MCSs. However, Bryan et al. (2003) concede that 1-km grid spacing is able to reproduce key squall line circulations, thus it is employed here and comparisons are only drawn between simulations that all use 1-km grid spacing, as opposed to comparison with observations. Model simulation times are hereafter denoted by “forecast time” FHH or FHH:mm, specifying the number of hours (HH) and minutes (mm) into the simulation. Further details of the WRF model setup for the simulation are presented in Table 2.1.

2.1.2 Neglect of the Coriolis force and the use of homogeneous initial conditions

A more traditional modeling approach, in which horizontally homogeneous initial conditions were employed and the Coriolis force was neglected, was also tested in order to explore the ramifications of this alternative to more idealized MCS modeling. Comparison of the two methods reveals findings that closely mirror those of past comparison studies such as Skamarock et al. (1994). That is, both approaches result in a quasi-linear MCS that moves in a generally eastward direction and share similar features and system-scale dynamics (e.g., the presence of a mid-level mesolow, sub-cloud cold pool, and descending RIJ) (Fig. 2.4). However, MCS motion is markedly different between the two frameworks; the full-Coriolis simulation moves toward the southeast,

likely the combined result of several relevant processes, including Coriolis torque on low-level winds in the cold pool as well as enhanced CAPE toward the south (e.g., Skamarock et al. 1994), in a manner that more closely resembles the motion of observed midlatitude MCS cases that motivate this work. In contrast, simulations using horizontally homogeneous initial conditions and neglecting the Coriolis force produce an MCS that moves due eastward and is much larger in lateral extent (e.g., Fig. 2.4a,b). Some of the dynamical differences between these approaches are further considered in Appendix A. However, because this study seeks to examine the motion of observed midlatitude MCSs and thereby eventually improve the prediction of MCS motion, the “quasi-idealized” approach with Coriolis effects is employed herein.

2.2 Momentum budget methodology

To isolate the effect of CMT on MCS motion, an Eulerian storm-relative momentum budget is computed for the MCS simulation analyzed in Chapter 3, based on the general methodologies of Trier et al. (1998) and Mechem et al. (2006). (Budgets are also performed for two other simulations in Chapter 4 and follow the same methodology as described here as well.) The momentum budget is also evaluated in order to (i) determine which terms in the momentum equation contribute most to the enhanced wind speeds in the leading portion of the cold pool, and (ii) obtain a momentum budget of an MCS against which to ultimately compare CMT in MCSs of varying background environments, or in simulations that utilize a CP scheme. To accomplish this, WRF model output is used to compute the terms of the horizontal momentum equation,

$$\frac{\partial \vec{V}}{\partial t} = -\vec{U} \cdot \nabla \vec{V} - f\hat{k} \times \vec{V} - \frac{1}{\rho} \nabla p + R \quad (2.1)^1$$

¹ From (2), it is apparent that rather than assessing the full momentum fields, this framework actually examines the velocity tendency (i.e., acceleration) per unit mass.

where \vec{V} is the horizontal wind vector and R denotes a residual, detailed below. In order to focus on the acceleration of the system and the associated roles of the various budget terms, \vec{V} (with grid-relative² x- and y- components u and v) is defined as the sum of MCS motion and storm-relative wind speeds; that is, $u = u_{SR} + c_x$ and $v = v_{SR} + c_y$, where c_x and c_y are the speeds at which the MCS moves in the east-west and north-south directions, respectively. After substituting these values and differentiating the basic state and perturbation variables using overbars and primes, the scalar components of (2) become:

$$\underbrace{\frac{\partial u}{\partial t} + c_x \frac{\partial u}{\partial x} + c_y \frac{\partial u}{\partial y}}_{TEN_x} = \underbrace{-(u - c_x) \frac{\partial u}{\partial x}}_{HAu_x} - \underbrace{(v - c_y) \frac{\partial u}{\partial y}}_{HAu_y} - \underbrace{w \frac{\partial u'}{\partial z}}_{VAu'} - \underbrace{w \frac{\partial \bar{u}}{\partial z}}_{VA\bar{u}} + \underbrace{fv}_{COR_x} - \underbrace{\frac{1}{\rho} \frac{\partial p}{\partial x}}_{PGA_x} + \underbrace{RES}_x, \quad (2.2)$$

$$\underbrace{\frac{\partial v}{\partial t} + c_x \frac{\partial v}{\partial x} + c_y \frac{\partial v}{\partial y}}_{TEN_y} = \underbrace{-(u - c_x) \frac{\partial v}{\partial x}}_{HAV_x} - \underbrace{(v - c_y) \frac{\partial v}{\partial y}}_{HAV_y} - \underbrace{w \frac{\partial v'}{\partial z}}_{VAv'} - \underbrace{fu}_{COR_y} - \underbrace{\frac{1}{\rho} \frac{\partial p}{\partial y}}_{PGA_y} + \underbrace{RES}_y \quad (2.3)$$

where \bar{u} is the grid-relative background (initial) wind field (i.e., u at F00), $u' = u - \bar{u}$ (with the same convention applied to v), and the other terms have their usual meanings. MCS translational speed (c_x , c_y) is calculated by averaging the distance covered per 1-hour period by the leading edge of the convection (as denoted by simulated composite radar reflectivity > 40 dBz); making the momentum budget storm-relative avoids the dominance of the horizontal advection terms and highlights those processes that contribute to changes in MCS motion rather than maintenance of constant MCS speed. Also, note that the vertical advection of the background u-wind field \bar{u} ($VA\bar{u}$) is

² Wind components u and v are grid-relative, but differences between grid- and north-relative winds within this particular domain are negligible.

distinguished from the vertical advection of the perturbation wind field (VAu' , VAv') so that the specific role of each process may be assessed and compared. The residual term, RES , accounts for the combination of “subgridscale effects,” as termed by Mechem et al. (2006); this term is small, each component of RES generally accounts for less than 10% of the total budget when averaged over relevant levels. RES includes the errors inherent in calculating the left-hand-side local tendency terms in (2.2) and (2.3), as well as our neglect of numerical diffusion and PBL and turbulent flux tendencies. Thus, it largely represents the retarding force of friction close to the earth’s surface and mixing in convective updrafts [as reflected by relatively large near-surface and updraft PBL parameterization momentum tendencies (*not shown*)]. The TEN terms are calculated by taking a centered-difference time derivative for u and v at each output time, with $\Delta t = 5$ minutes. The terms in (2.2) and (2.3) are computed for all of the 5-minute output intervals of the simulation, then averaged over 30-minute intervals centered about :00 and :30 of every hour; although the system moves throughout each 30-minute interval, the temporal averaging reduces noise, allowing assessment of the processes of interest.

Finally, to supplement the Eulerian momentum budget described above, a Lagrangian momentum budget is also presented in Chapter 3, using parcel trajectories. In doing so, only the forces and accelerations a parcel experiences as it descends from the RIJ-level and into the cold pool are calculated, as described by

$$\frac{d\vec{V}}{dt} = -\frac{1}{\rho}\nabla p - f\vec{k} \times \vec{V} + R, \quad (2.4)$$

where R is analogous to RES in (2.2) and (2.3). The Lagrangian perspective more clearly illustrates the integrated accelerations along parcel paths. The transport of momentum can then be understood in terms of the rearrangement of these parcels over time.

2.3 Sensitivity experiments: Model set-up

The WRF model methodology discussed in 2.1 is used to produce a series of simulations that test the sensitivity of the motion and surface winds of MCSs to changes in environmental mid-level moisture and the microphysical processes of evaporation

melting, and sublimation. A similar methodology is used by Yang and Houze (1995), in which microphysical processes and environmental humidity are varied in two-dimensional simulations with the goal of determining whether the RIJ is determined in larger part by environmental factors or by physical processes internal to storm. While differences in MCS speed were identified in their simulations, neither MCS speed nor surface wind speed magnitude were the focus of the study and neither was examined. Here, a similar matrix of model sensitivity simulations is incorporated, but using the three-dimensional quasi-idealized set-up described in 2.1. Our analysis instead focuses on the role of environmental humidity and microphysical processes in altering MCS motion and surface wind speeds, and the role of CMT (if any) in these processes; these results are discussed in Chapters 4 and 5.

The same initial conditions and model configuration as outlined in section 2.1 are used for these sensitivity simulations, except for the changes detailed below. The suite of simulations chosen for final analysis include a control (CTRL) simulation and four sensitivity simulations as described in Table 2.2.

2.3.1 Control (CTRL)

The control simulation (CTRL) discussed in Chapters 4 and 5 uses the same initial conditions as detailed above, and the same model set-up as described in Table 2.1. The only change made is the use of the WSM6 [WRF Single Moment 6-class scheme; Hong and Lim (2006)] microphysics scheme as opposed to the Purdue Lin scheme (Lin et al. 1983; Chen and Sun 2002)³. This change does not result in significant differences in MCS speed or structure; it is implemented to facilitate modification of the microphysical parameterization code in order to produce the sensitivity experiments discussed below.

2.3.2 Dry mid-levels (DRYM)

³ Thus, the simulation discussed in Chapter 3 is not referred to as CTRL; the latter uses the WSM6 microphysics parameterization and is the control simulation among the sensitivity simulations such that all five simulations in Table 2.2 use the WSM6 microphysics scheme.

A simulation is generated to test the effect of reducing mid-level relative humidity on CMT, MCS motion, and near-surface wind speeds; the specific goals and research questions behind this experiment are detailed in Chapter 4. The “dry mid-levels” simulation (DRYM) uses the same model details and parameterizations as the CTRL run, but the initial sounding is changed to include a reduction of moisture from the 750-hPa level to the 450-hPa level. The reduction in relative humidity follows the methodology of Yang and Houze (1995), in which the initial environmental moisture at mid-levels is reduced by approximately half at the driest part of the sounding, and is gradually blended back toward the initial moisture values at the top and bottom of the layer. The CTRL and DRYM initial soundings are compared in Fig. 2.5.

2.3.3 Reduced evaporation (REVP)

The reduced evaporation experiment (REVP) is identical to the CTRL run, except that latent cooling due to evaporation of liquid water (rainwater, cloud water, and melting graupel) is reduced to 25% of its calculated value at each microphysics scheme timestep. An attempt was made to remove evaporative cooling entirely, but this resulted in a loss of the MCS altogether within several hours of the simulation due to a complete absence of a surface cold pool with which to lift pre-storm parcels to their level of free convection.

2.3.4 No melting (NMLT)

The no-melting (NMLT) simulation is identical to the CTRL simulation except that the WSM6 microphysics scheme is modified to omit melting and thus air is not cooled when ice particles (snow, cloud ice, and graupel) (would otherwise) melt. The impact of melting on CMT, MCS motion, and low-level wind speeds is specifically analyzed from this experiment, as past studies have found the effect of melting in an MCS to be quite large with respect to both heating profiles and the intensity of vertical motion (e.g., Braun and Houze 1995; Yang and Houze 1995; Grim et al. 2009b). Yang and Houze (1995) compare a similar experiment with a simulation in which cooling due to melting is only neglected for precipitation in the trailing stratiform region of the MCS;

this idea was considered here as well, but the simulations in Yang and Houze (1995) were found to be very similar.

2.3.5 No sublimation (NSUB)

Studies (e.g., Yang and Houze 1995; Grim et al. 2009b) have found that sublimational cooling in the rear anvil of the trailing stratiform region may be key to the initiation of downward air motion above the 0°C level. The impact of this effect and its potential role in CMT and MCS motion is investigated by the no-sublimation simulation (NSUB), in which the sublimation process is neglected and sublimational cooling thus no longer occurs.

The results of the sensitivity experiments detailed above are analyzed in Chapters 4 and 5.

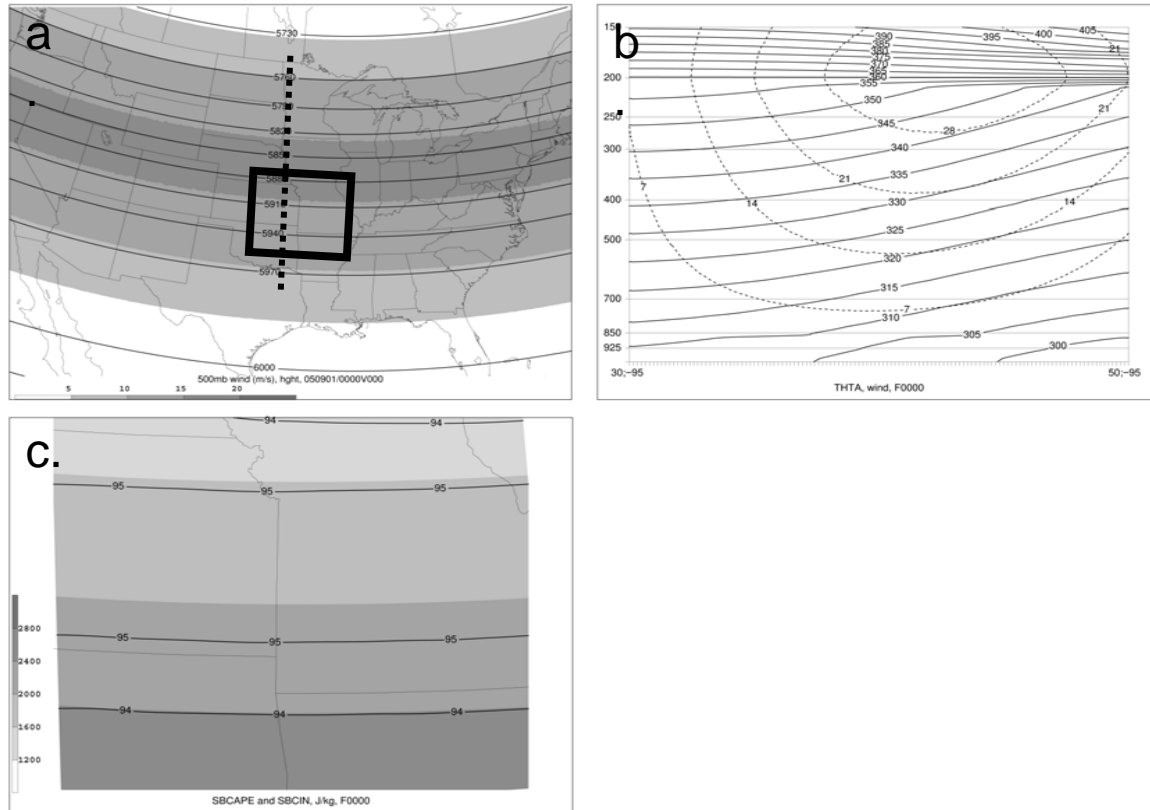


Figure 2.1: Initial background state (F00) for idealized MCS simulation. (a) 500-hPa geopotential height (m, contours), and wind (shaded as in color bar at left, m/s). Inner (1-km gridspacing) WRF domain outlined in thick black box, and cross-section in (b) shown by dashed line. (b) north (right) - south (left) cross-section as shown in (a), isentropes (K, solid contours, interval 5K starting at 300K) and isotachs (knots, dashed contours, interval 7m/s), (c) surface-based CAPE (shaded as in legend at left, J/kg) and surface-based convective inhibition (CIN, contours, interval 1 J/kg) over WRF model domain at initial time (F00).

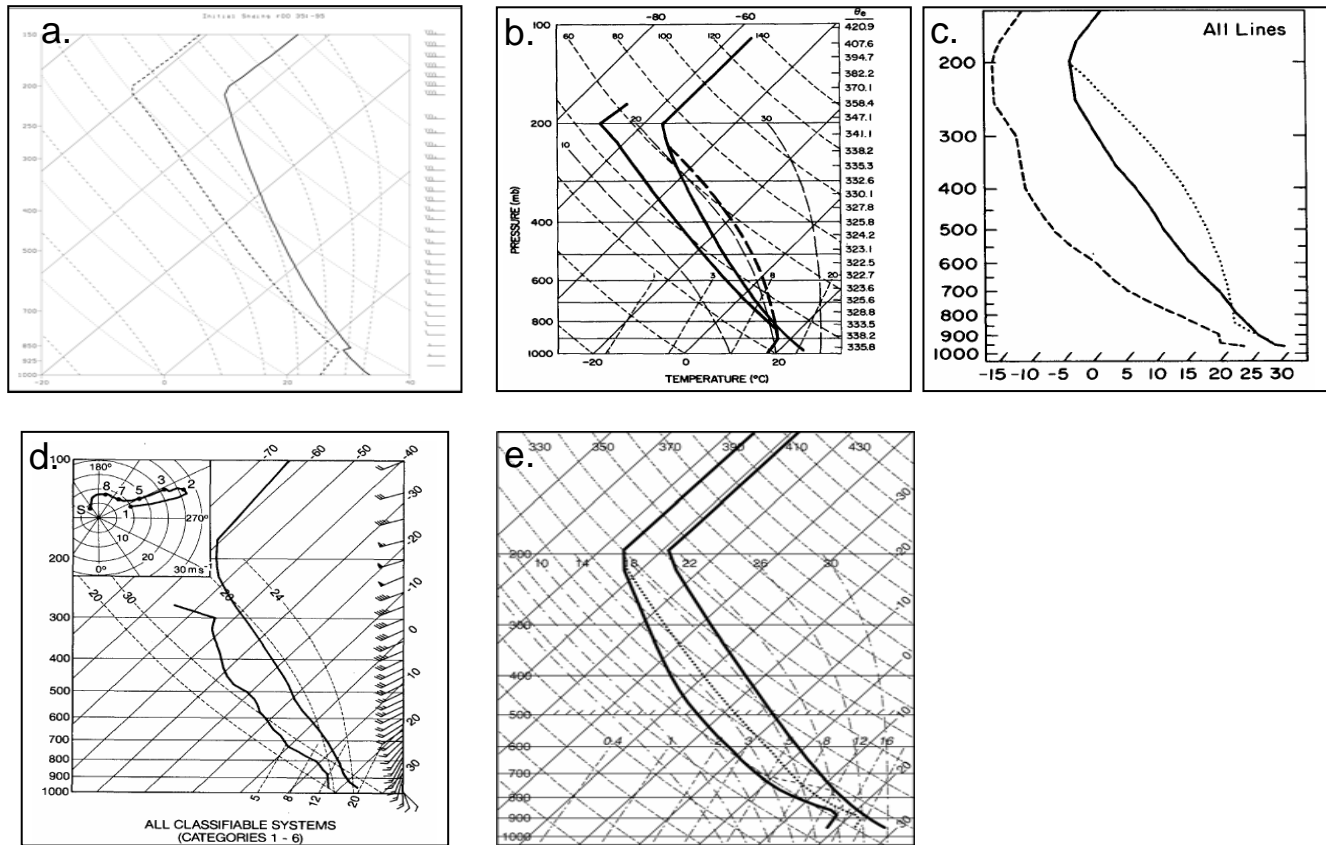


Figure 2.2 (a) Initial sounding shape used to initialize the quasi-idealized MCS simulation (at 35°lat; -95°lon). Temperature (°C, solid line), dewpoint (°C, dashed line), wind barbs in knots at right. Compared to other initial soundings used or found by past studies: (b) Weisman and Klemp (1982) initial sounding (c) Bluestein and Jain (1985) composite sounding; (d) Houze et al. (1990) mean sounding; and (e) Parker and Johnson (2000) initial sounding.

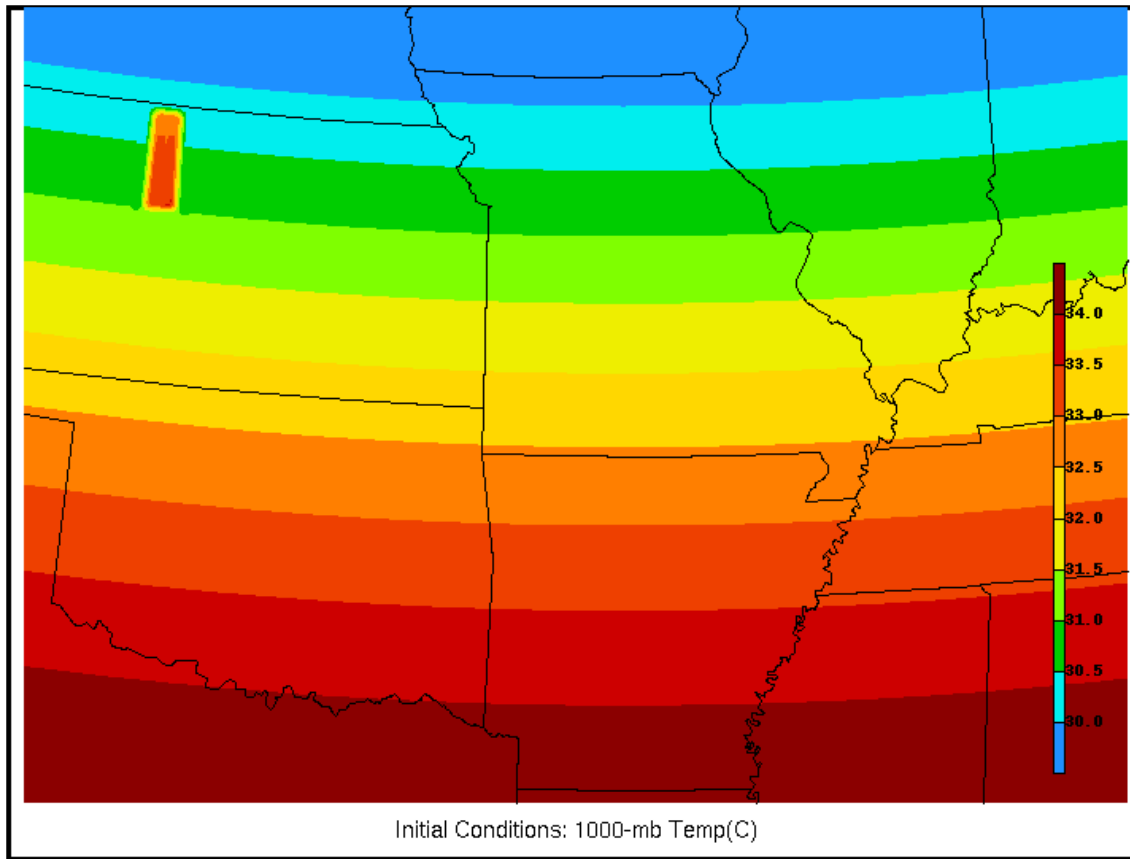


Figure 2.3: Initial (F00) 1000-hPa temperature ($^{\circ}\text{C}$, every 0.5°C as indicated at right) for quasi-idealized MCS simulation.

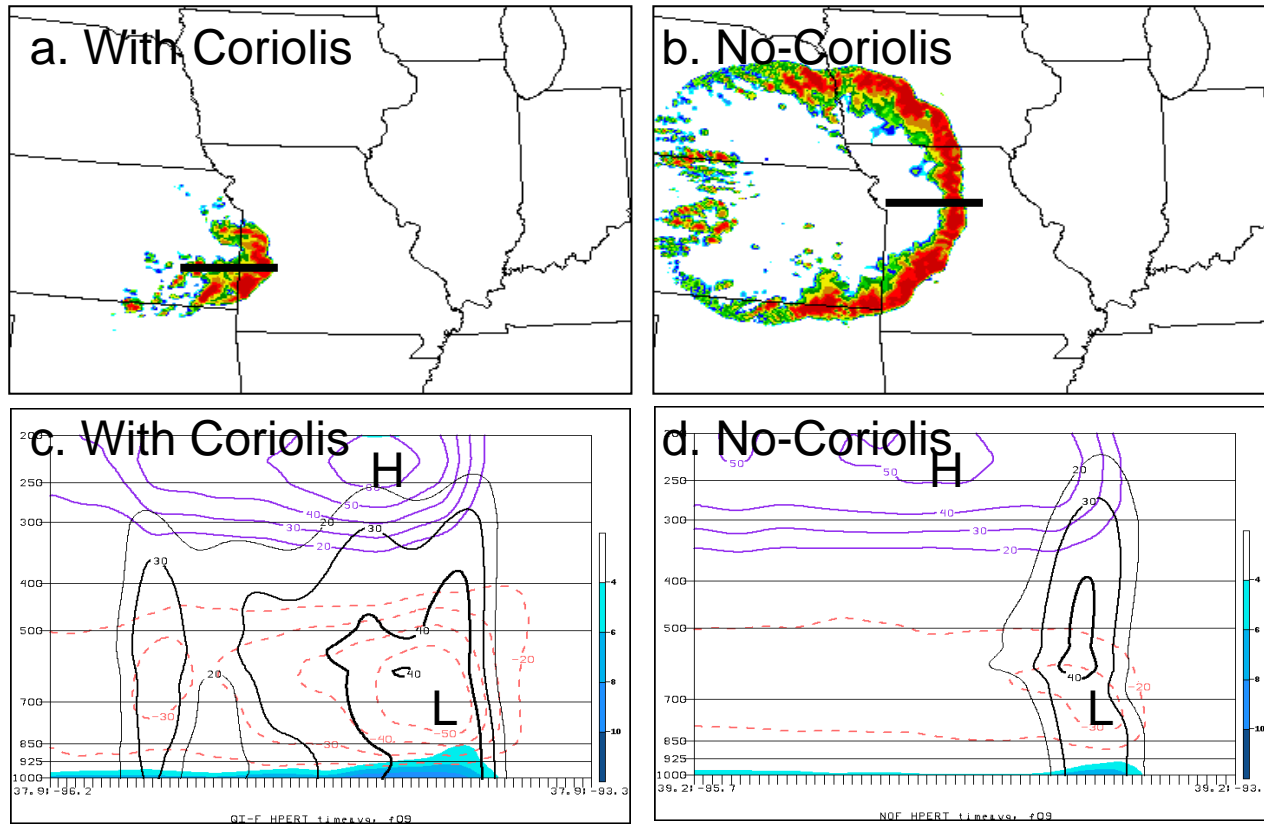


Figure 2.4: Simulated composite reflectivity (dBZ) at F09 in simulations (a) with Coriolis and horizontally heterogeneous initial conditions, and (b) without Coriolis and horizontally homogeneous initial conditions. Black lines denote cross-sections depicted in panels (c) and (d); (c) east-west vertical cross-section along line shown in Fig. 2.3a at F09, averaged in an along-line direction in 40-km segments. Cold pool (shaded as shown beginning at $T' = -2^{\circ}C$), negative (positive) geopotential height perturbation in solid (dashed) contours m^2s^{-2} ; and simulated reflectivity (dBZ, black contours as labeled, every 10dBZ beginning at 20 dBZ). (d) As in (c) except for No-Coriolis run taken along black line shown in Fig. 2.3b.

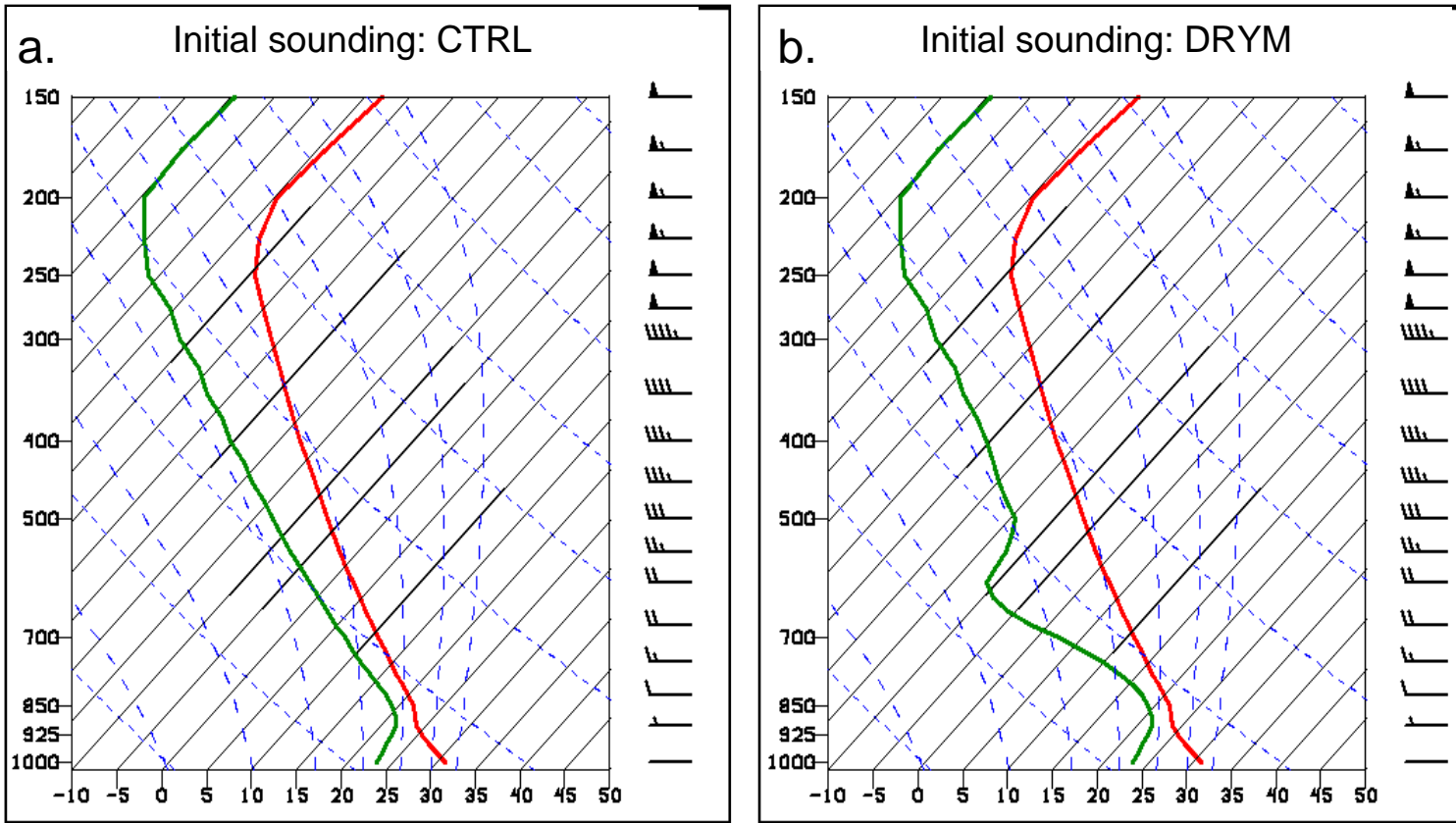


Figure 2.5: Comparison of initial sounding shape used to initialize the quasi-idealized MCS simulation (at 35°lat; -95°lon) for (a) CTRL simulation, and (b) DRYM (dry mid-levels) simulation. Temperature (°C, solid line), dewpoint (°C, dashed line), wind barbs in knots at right.

Table 2.1: WRF model set-up and parameterization

Model version	WRF (ARW) Version 2.2
Duration	00 UTC initialization; run out 12 hours; output every 5 minutes
Grid	1-km grid spacing (within a 4-km outer nest)
	676 x 604 gridpoint domain (outer domain 450x450)
	31 vertical levels
Physics	Explicit convection (no CP scheme)
	Purdue Lin microphysics
	YSU planetary boundary layer (PBL) scheme
	Second-order turbulence and mixing option; horizontal Smagorinsky first-order eddy coefficient option*
	No radiation or land-surface schemes employed; surface fluxes off
Initial conditions	Initial conditions projected on World Meteorological Organization (WMO) 218 grid, with 12-km grid spacing (terrain removed).

*Model sensitivity experiments showed that the organization and movement of the MCS displayed limited sensitivity to the turbulence/diffusion parameterizations chosen.

Table 2.2: Sensitivity simulation details

Simulation	
CTRL	As in Table 2.1, except WSM6 microphysics
DRYM	Mid-levels dried by ~25% following Yang and Houze (1995). Modified sounding shown in Fig. 1b.
REVP	Evaporation reduced by 75% in WSM6 microphysics scheme
NMLT	Melting removed in WSM6 microphysics scheme
NSUB	Sublimation removed in WSM6 microphysics scheme

Chapter 3

The role of momentum transport in the motion of a quasi-idealized mesoscale convective system

3.1 MCS simulation analysis

Following the methodology described in section 2.1, the WRF model is used to simulate an MCS that can serve as both a surrogate data source in the description and analysis of MCS dynamics and motion, and also as a data source with which to perform diagnostic studies (e.g., Keyser and Uccellini 1987). This simulation and the following analysis focus on the following questions:

- (i) In what ways does CMT affect MCS motion?
- (ii) Are changes in MCS speed due primarily due to the advective component of system motion (i.e., system speed changes as a result of changes in the mean cloud-bearing wind), or to the propagative component (i.e., altering cold pool characteristics, thereby affecting new cell growth and thus system speed)?
- (iii) What are the relative sizes and impacts of the advection of the ambient wind versus the storm-perturbation wind?
- (iv) Is the impact (and potential omission or inadequate representation) of CMT in NWP model forecasts and/or human forecasts of MCS motion a significant forecast concern?

3.1.1 MCS structure

The evolution of the MCS produced by the WRF model is illustrated by the simulated radar reflectivity at 3-h intervals (Fig. 3.1). The system organizes into a quasi-linear, bowing MCS that exhibits an intense leading convective line followed by a smaller region of lighter precipitation, generally reflecting the classic “leading

convective-trailing stratiform” MCS structure¹ (e.g., Newton 1950; Houze et al. 1990). Hourly precipitation rates range from $\sim 5\text{mmh}^{-1}$ in the lighter stratiform regions to greater than 60mmh^{-1} in the most intense convective maxima (Fig. 3.2). The cross-sections shown in Fig. 3.3 illustrate the development of the descending RIJ during the system’s developing (mature) stage in Fig. 3.3a (Fig. 3.3c). The descending RIJ originates around the 4 – 5-km level in the rear of the system and lowers into the cold pool as the trailing stratiform region develops; this evolution is illustrated by the sloping wind maximum and the ground-relative perturbation wind vectors. The front-to-rear flow branch as depicted by Fig. 1.1 is implied by an area of weak easterlies aloft, as winds in the storm-relative sense flow from east-to-west above 5 km (*not shown*). The perturbation pressure field (Figs. 3.3b, 3.3d) also illustrates dynamical features that compare favorably with past observational and modeling studies of 3D MCSs (e.g., Trier et al. 1998; Houze 2004), such as the deepening of the pressure minimum located just to the rear of the leading convective line and the increased pressure aloft (above 10 km); a surface-based mesohigh is also present along portions of the line but has a diluted signature in Fig. 3.3 due to the deep midlevel mesolow just above it. This pattern is consistent with the hydrostatic response to a convective heating maximum overlying a surface cold pool, and the associated acceleration of the rear-to-front and front-to-rear flow matches the findings of studies such as Lemone (1983), Zhang et al. (1989), and Yang and Houze (1996). Therefore, this simulated MCS appears to be a credible representation of the types of systems which motivate this work, and offers the opportunity to use the model output to more closely investigate the CMT process.

3.1.2 MCS motion

¹ Although the region of stratiform precipitation in this particular simulation is not extensive relative to many observed mid-latitude systems, its breadth is substantial considering the propensity of many numerical simulations of MCSs (particularly those employing bulk microphysics parameterizations) to under-represent stratiform precipitation (e.g., Lynn et al. 2005; Gallus and Pfeifer 2008; Morrison et al. 2009).

In order to understand the nature of the simulated MCS motion, the evolution of the MCS and its cold pool from the developing to mature stages is analyzed (Fig. 3.4). As the system matures and intensifies, the leading edge of the cold pool remains adjacent to the leading line of new convection, implying continuous cold pool forcing for new convection (Fig. 3.4). Strong low-level convergence is maximized at the leading edge of the cold pool, over which air is forced upward (e.g., Charba 1974; Rotunno et al. 1988). This upward motion and the maximum of low-level convergence are also evident in cross-sections across the system’s leading edge (e.g., Figs. 3.3a, 3.3c). Thus, the development of new cells along the outflow boundary illustrates that the MCS is “gust-front driven” in the manner described by Weisman and Klemp (1986).

Using the $T' = -2^\circ\text{C}$ isosurface to define the three-dimensional cold pool boundary, the average cold pool depth is ~ 1.5 km (ranging from 1 km along the northern and southern ends of the line to nearly 4 km at the MCS apex). The maximum temperature perturbation generally approaches -10°C at the surface and averages -6°C through its depth; such values are consistent with those found by previous observational and modeling studies (e.g., Engerer et al. 2008). The speed at which the cold pool moves can be calculated by its theoretical density current speed, c (e.g., Bluestein 1993, Eqn. 2.5.270, *not shown*). However, it is known that this expression often does not match the true surface speed of the cold pool and MCS, and that the theoretical speed based on density within the cold pool alone may over-estimate the actual cold pool speed by as much as 100% (e.g., Nicholls et al. 1988; Xue 2000; Bryan and Rotunno 2008). Despite the strong sensitivity of buoyancy-based cold pool calculations to relatively small thermal and pressure perturbations, it is desirable to establish an estimate of theoretical cold pool speed here. Thus, the modified expression suggested by studies such as Nicholls et al. (1988) and Trier et al. (2006) is adopted, in which the effects of hydrometeor loading and the mid- to upper-level buoyancy anomalies are included:

$$c = \left[-2g \int_0^H \left(\frac{\theta'}{\theta_0} \right)_{\text{coldpool}} + \int_H^{Z_T} \left(\frac{\theta'}{\theta_0} \right)_{\text{warmcloud}} - \int_0^{Z_T} q_h dz \right]^{1/2}, \quad (3.1)$$

where H is the depth of the cold pool (~ 2 km), Z_T is the height at which the pressure perturbation above the cloud goes to zero (~ 14 km), and θ' is the potential temperature perturbation as compared to the base-state θ_0 , as defined by along-line averaged vertical profiles in the leading 20 km of the cold pool following Trier et al. (2006). Calculations of the theoretical cold pool speed according to (6) are shown in Fig. 3.5. Differences between the theoretical and observed cold pool speeds, particularly during periods of MCS acceleration (discussed below), indicate that the winds in the cold pool are *not* simply a product of the static pressure field produced by the cold pool.

The advective component of MCS motion is often estimated by measuring the mean wind in the cloud-bearing layer (e.g., Corfidi et al. 1996). Along an approximately east-west moving portion of the MCS, the mean wind speed (u) in the 900 – 200-hPa layer (e.g., Fritsch and Forbes 2001) from F05 – F12 is ~ 14 ms^{-1} ; the dotted line in Fig. 3.5 shows the evolution of this field over time.

The translational speed of the system was calculated as detailed in section 2.2, and the solid line in Fig. 3.5 shows that the system speed accelerates from about 6 ms^{-1} to 22 ms^{-1} from the MCS's initial to mature stages. The dashed line in Fig. 3.5 illustrates the average value of the maximum windspeed found over the lowest 3 km of each grid column in the leading 40 km of the cold pool (a volume over which additional quantities are averaged in the following section). MCS speed and the average maximum wind speed in the leading portion of the cold pool are relatively closely matched, and the evolution of each field with time is also similar (the two quantities have a correlation coefficient of 0.9 and a root-mean-square error of 2 ms^{-1}); similarly high correspondence is found for the overall average windspeeds in the cold pool even when slightly different cold pool volume definitions are used. This relationship also implies that the *TEN* terms in (2.2) and (2.3) closely represent the tendency of MCS motion by describing changes in wind speed at the leading edge of the cold pool (Figs. 3.4, 3.5). Thus, *the MCS largely moves at the speed of the winds in the leading edge of its cold pool, which is likewise the speed at which the actual cold pool and gust front move* (e.g., Goff 1976; Lafore and Moncrieff 1989). Furthermore, comparing the calculated theoretical cold pool speeds to the actual

cold pool speeds reveals that the theoretical value not only underestimates (overestimates) the actual value at mature (initial) stages, but also fails to fully explain the period of maximum acceleration from F05 – F07; this suggests that the speed of the cold pool is not driven and/or maintained by density current mechanics alone.

3.2. CMT in the simulated MCS

3.2.1 System evolution and vertical momentum fluxes

The evolution of the wind field along cross-section C-C' (as shown in Fig. 3.1d) illustrates the development and descent of stronger winds (predominantly westerlies) with time, as weaker wind speeds (predominantly weaker westerlies/storm-relative easterlies) ascend in the front-to-rear flow (Fig. 3.6). Plotting vertical momentum fluxes helps illustrate the CMT process; a downward flux of westerly momentum is evident in the lower rear of the system below 3 km altitude, corresponding to the descending flow of the RIJ (Fig. 3.7). As the system matures, these flux magnitudes grow considerably toward the leading edge of the cold pool (*not shown*). Horizontal plots of $-\frac{\partial}{\partial z}uw$ (Figs. 3.7c, 3.7e) reveal maximized vertical momentum flux convergence in lower layers (~800 m), consistent with the descending flow of the RIJ and the westerly maximum produced near and below 1.5 km (Figs. 3.3a, 3.3c). This demonstrates the importance of CMT in these lower levels, where the downward transport of momentum maximizes. The behavior of the wind field shown in Fig. 3.6, as well as the plots of the vertical momentum flux in Fig. 3.7 depict the descent of the (generally westerly) wind speed maximum from mid-levels (4 – 8 km) in the developing stages of the MCS, to lower levels and approaching the surface as the system matures. Concurring with the findings of Houze et al. (2000) and Mechem et al. (2006), the combination of these sloping, downward motions from areas of stronger winds aloft and the mid-level accelerations provided by the perturbation pressure field (e.g., Fig. 3.3) indicates that the near-surface wind field of the mature MCS results in part from the downward transport of increased momentum aloft. The

contribution from CMT can also explain the discrepancy between the observed cold pool speed of the simulated system and the theoretical cold pool speed calculated above.

3.2.2 Momentum budget analyses

As detailed in section 2.2, two momentum budgets are computed using WRF model output, with the ultimate goals of (i) ascertaining which terms in the momentum equation contribute most to the enhanced wind speeds in the leading portion of the cold pool, and (ii) quantifying the role of CMT in the MCS momentum field and hence its forward motion.

Beginning with the Eulerian framework, a summary of each momentum budget term at 800 m is shown in Fig. 3.8; this level represents the middle – lower portion of the surface-based cold pool. The \vec{V} -tendency term (TEN) in Fig. 3.8a represents the sum of left-hand sides of (2.2) and (2.3) at F06, which is chosen as the main momentum budget analysis time as it marks the beginning of the period of maximum system acceleration (e.g., Fig. 3.5). The vectors show general storm-relative forward acceleration along the leading edge of the system, toward the east and southeast. Rearward-pointing vectors located toward the back of the system reflect the deceleration of the wind speeds behind the pressure maximum at the leading edge of the cold pool. At this level and time, the vertical advection term (Fig. 3.8b) largely determines the acceleration in the forward portion of the cold pool, as evidenced by the southeastward-directed vectors along the front of the MCS. The remaining terms (HA , COR , PGA , and RES terms in panels c – f, respectively) instead contribute rearward (or small forward) accelerations in these lower levels; thus they do not appear to be major contributors to the acceleration of the leading line of the MCS (at lower levels). Examination of the budget terms at higher altitudes (*not shown*) reveals an increase in the PGA and vertical advection terms, particularly in the stratiform region of the system; this pattern is illustrated by the cross-sections shown in Fig. 3.9.

Comparison of the leading budget terms (TEN_x , PGA_x , HAu_x , $VA\bar{u}$, and VAu') at the beginning of the period of maximum MCS acceleration (F06) illustrates the

contribution of each term to the low-level westerly wind maximum (Fig. 3.9). It is clear that in the RIJ region (as depicted by the shaded isotachs) both PGA_x and $VA\bar{u}$ (Figs. 3.9b, 3.9e) are large contributors to MCS zonal acceleration, with PGA_x accelerating the rear inflow, and $VA\bar{u}$ transporting a portion of the background westerlies downward. In the leading convective portion of the MCS, the VAu' term largely determines the positive u -momentum tendency (Fig. 3.9d), with a contribution in the leading edge of the cold pool from HA (Fig. 3.9c). While cross-sections represent a limited horizontal area, the data are averaged over 30-minute intervals, and the pattern seen in the four momentum budget terms shown is generally representative of the mean pattern along the line.

In order to compare and summarize the relative importance of each term in the u -momentum equation (2.2), the budget terms are averaged in two system-relative volumes (illustrated in both Fig. 3.10 and by the outlined boxes in Fig. 3.11); one at the leading edge of the cold pool ($VOL_{leading}$, Fig. 3.10a) and the other toward the middle-to-rear portion of the system ($VOL_{trailing}$, Fig. 3.10b). The volumes are laterally bounded to the north and south according to the portion of the system that moves most nearly zonally, and the east-to-west extent is limited to 0 – 40km (40 – 120km) behind the leading edge of the cold pool for $VOL_{leading}$ ($VOL_{trailing}$). In the storm-following volumes, budget terms are evaluated in the east-west direction only. While 3-D effects of a curved system such as this one are likely important near the ends of the line (e.g., Trier et al.1998), a centrally-located and eastward-moving portion of the line is selected such that the x -components of motion sufficiently represent the processes of interest. However, in a storm-relative sense (i.e., whether a process acts with or against the system's forward motion) along other portions of the line, the y -component contributions from (2.3) (and depicted in Fig. 3.8) are consistent with those examined here. The division of the system into these two volumes mimics many previous MCS momentum budgets which have divided the system into “leading (convective)” and “trailing (stratiform)” sections (e.g., Gallus and Johnson 1992; Yang and Houze 1996; Trier et al. 1998; Mechum et al. 2006). Defining the volumes to include lower-to-mid levels following the leading edge of the system (0 – 3 km and 0 – 6 km for $VOL_{leading}$ and $VOL_{trailing}$, respectively) serves to focus

on the low-level storm outflow contained within the cold pool and also on the rear-to-front flow branch, which contributes to changes in low-level westerly momentum² (e.g., Fig. 1.1).

Figure 3.10a reveals a consistent positive contribution from VAu' in $VOL_{leading}$, confirming that the vertical advection of perturbation rear-to-front flow is of first-order importance in strengthening westerly flow in the forward part of the storm. Further back from the leading line in $VOL_{trailing}$ (Fig. 3.10b), the vertical advection of the background wind ($VA\bar{u}$) and PGA_x contribute to the local acceleration of the RIJ, while the $H Au_x$ term decreases in time as the strongest westerlies progress toward the leading edge of the cold pool and the system accelerates.

The simulated MCS moves at a speed that very closely matches the average wind speed in the forward portion of the cold pool (i.e., $VOL_{leading}$), as shown in Fig. 3.5. Therefore, at the leading edge of the MCS, the Eulerian tendency term (TEN) represents the storm-relative acceleration of the momentum field and thus the change in system motion (Fig. 3.12); strong correlation ($r = 0.97$) between large TEN values and periods of MCS acceleration indicates that the remaining terms in (2.2) and (2.3) can provide insight into the contribution of each process to changes in MCS motion. Due to the gust-front driven nature of system motion, as well as the strong correlation between the winds in the forward portion of the cold pool and the speed at which the MCS moves, the momentum budget volume averages in $VOL_{leading}$ may be used to determine which terms contribute most to the enhanced wind speeds there (Fig. 3.13). Throughout the lifetime of the system, VAu' adds a large positive contribution to MCS forward motion in the leading volume (Fig. 3.13b). In $VOL_{leading}$, VAu' averages $\sim 13 \text{ m s}^{-1}\text{h}^{-1}$ throughout the simulation, clearly contributing to the acceleration of the system. The magnitude and evolution of VAu' relative to the u -momentum tendency at the leading edge of the cold pool (shown by

² Multiple volumes were examined in order to select the most appropriate areas over which to average the terms in (2.2) and (2.3), however, little sensitivity was found when increasing or decreasing volume depth or spatial extent within $\sim 1\text{km}$ or 40km , respectively. The volumes are defined to isolate the rear-to-front flow branch by excluding the front-to-rear flow branch as much as possible, though implications of the front-to-rear flow in the convective region may be addressed in future work.

the thick black TEN_x line in Fig. 3.10) thus illustrate that its contribution to MCS speed is non-negligible.

As described above, a volume encompassing the mid-to-rear portion of the storm ($VOL_{trailing}$) is also defined in order to diagnose the role of the budget terms in the generally westerly momentum field produced in the RIJ region. Similar to $VOL_{leading}$, the tendency values for $VOL_{trailing}$ (Fig. 3.10b) also correlate reasonably well with MCS motion, reinforcing the utility of examining the trailing stratiform region of the storm and its role in the MCS momentum field. Within the trailing volume, it is clear that VAu' is much smaller than in $VOL_{leading}$ (Fig. 3.13c,f); this is partially due to the volume generally trailing the local u' maximum (Fig. 3.11), but also reveals a shortcoming of the volume approach. That is, averaging over a jet feature such as u' masks the full contribution of this field, as cancellation near the field maximum causes its volume average to be close to zero. Therefore, while considerable information can be gleaned from the volume-averaged budget for most terms, the role of VAu' in $VOL_{trailing}$ is likely better assessed by alternative approaches such as displays of flux and flux convergence as in Fig. 3.7. However, the volume-averaging approach does clearly illustrate that in $VOL_{trailing}$ there is a relatively modest but significant contribution from both the PGA_x term and the $VA\bar{u}$ term; both supply a steady acceleration of $2 - 8 \text{ ms}^{-1}\text{h}^{-1}$ to the rear-to-front flow in the trailing stratiform portion of the system. From an Eulerian perspective, it is difficult to comment on how these terms contribute specifically to storm motion, given that the overall effect is likely integrated along the gradually-descending RIJ (and also that the contribution of both PGA_x and $VA\bar{u}$ may extend above 6 km in some areas).

By eliminating the advection terms and instead moving *with* the descending parcels, the Lagrangian budget is calculated to more fully understand (i) the local acceleration of the RIJ, (ii) the extent to which PGA impacts MCS motion, and (iii) the connection between the leading and trailing volumes used above, creating a seamless picture of airstream accelerations. The Lagrangian budget computes parcel acceleration

and the *PGA* and *COR* fields along parcel trajectories, according to (2.4). Figure 3.14a shows a composite of 50 trajectories that originate in the RIJ (~5km altitude at F06), revealing that the average parcel motion sampled is one of descent from mid-levels into the cold pool (to within approximately 100 m of the surface) by F11. Along this trajectory, there is a marked period of maximized acceleration, from F07:00 (25200s) to F08:25 (30300s), during which a strong pressure gradient acceleration exists in the direction of parcel motion (by accounting for the acceleration terms in the direction of parcel motion, the Coriolis term may be neglected, as it only acts perpendicular to parcel motion). Over this 85-min time interval, the pressure gradient acceleration accounts for an acceleration of $\sim 8.5 \text{ ms}^{-1}$ (its average value $\sim 6 \text{ ms}^{-1}\text{h}^{-1}$), and the composite trajectory's average wind speed indeed strengthens by $\sim 9.5 \text{ ms}^{-1}$ (Fig. 3.14b). Because the *PGA* term is the only means by which the MCS momentum field may accelerate or decelerate along a parcel trajectory (as friction and turbulence are neglected), the role of the mid-level mesolow and resulting pressure gradient acceleration in the CMT process is more clearly defined.

The Lagrangian budget further illuminates the critical role of downward CMT in bringing the accelerated RIJ flow surface-ward. The parcels experience more than half of their acceleration (nearly 7 ms^{-1}) prior to the steep descent toward the surface [beginning around F07:45 (27900s); Fig. 3.14a], illustrating that vertical advection (i.e., CMT) is a critical process by which cold pool wind speeds and thus MCS speed increase; this is corroborated by the dominance of V_{Au}' in Fig. 3.10. The combination of the storm-relative Eulerian and Lagrangian budgets illustrate the evolving roles of various forcing terms. Specifically, it is demonstrated that the *PGA* term plays an important role in accelerating the RIJ that is then transported downward via vertical advection; similar to the findings of Zhang et al. (2003). The average trajectory path also reveals a direct connection between the RIJ and the cold pool as suggested by many past studies (e.g., Zipser 1977; Smull and Houze 1987; Lafore and Moncrieff 1989), and that in many places near the leading portion of the system, the RIJ indeed descends to the surface (or closely above). As discussed by previous studies (e.g., Newton 1950; Johns and Doswell

1992; Weisman 1992; Geerts 2001) this detail holds important implications for wind speeds experienced at the earth's surface.

While it is difficult to precisely quantify the total impact of $VA\bar{u}$ to system motion (as it is an integrated effect along the RIJ), positive $VA\bar{u}$ tendencies in the trailing stratiform region suggest that this process does contribute non-negligibly to increasing momentum at the leading portion of the cold pool. Furthermore, evaluating the background wind speed differences of Lagrangian budget parcels reveals that $VA\bar{u}$ may be responsible for increasing the local wind speed in the cold pool by $5 - 10 \text{ ms}^{-1}$ during times of maximum parcel descent. The importance of the environmental background flow has been indicated by past studies as well; Evans and Doswell (2001) suggest that the strength of the background wind field may play an important role in both the motion of MCSs as well as the potential for severe surface wind damage. Furthermore, vertical motions and associated mass transports in the trailing stratiform region of MCSs are also shown to be important to both system dynamics and precipitation processes in studies such as Yuter and Houze (1995b), Mechem et al. (2006), and Grim et al. (2009a).

3.3 Synthesis of role of CMT in MCS motion

Figure 3.15 schematizes the processes described by the momentum budgets, synthesizing the main results gleaned from horizontal and vertical cross-sections, parcel trajectories, and storm-following volume-averages. The schematic illustrates the strength of VAu' in the fore of the system, while emphasizing the dominance of PGA and $VA\bar{u}$ in the rear of the system. While the magnitudes of latter two terms are less in $VOL_{trailing}$ than VAu' in $VOL_{leading}$, their contribution to the rear-to-front wind field in $VOL_{trailing}$ is critical, particularly the acceleration imparted by the PGA term, as noted by the Lagrangian momentum budget. The combined impact of these processes on system motion can be noted most clearly from F05 to F07, as the eastward-accelerating budget terms near the leading edge result in accelerated MCS motion (e.g., Figs. 3.5, 3.10). *The results from this analysis show that the vertical advection of accelerated perturbation winds (and to a lesser degree, the vertical advection of the ambient momentum)*

contributes non-negligibly to the strength of the winds in the cold pool and the forward speed of the system.

Finally, as previously discussed, this study not only seeks to quantify the contribution of CMT to MCS motion, but to also determine the specific physical process responsible for this acceleration. The results presented herein show that downward transport from aloft increases wind speeds within the cold pool and thereby accelerates the ground speed of both the cold pool and MCS itself. Thus, the change in MCS speed is due to changes in the propagative component of motion, \vec{C}_p (i.e., research question (ii) in 3.1). This is supported by (i) the favorable agreement and correlation found between the wind speeds in the cold pool and the speed at which the system moves (e.g., Fig. 3.5), (ii) the behavior of air parcels as they accelerate and then descend into the cold pool from aloft (e.g., Fig. 3.14), and (iii) the inability of the mean cloud-bearing wind to account for the MCS speed (Fig. 3.5). Therefore, the process is *not* a simple strengthening of the mean cloud-bearing-wind that results in increased advection, but rather an acceleration of the cold pool itself, and the subsequent acceleration of the system. Thus, *for MCSs that are cold-pool driven, the downward transport of high-momentum air from aloft increases the speed at which the entire system propagates* (assuming that the pre-MCS environment continues to support convective development).

3.4 Summary and forecast implications

This simulation and series of diagnostic assessments demonstrate that the motion of a numerically-simulated MCS is significantly impacted by the transport of horizontal momentum by vertical motions within the MCS. Momentum budgets of a numerically simulated mid-latitude MCS are computed and reveal that the vertical advection of the perturbation wind (VAu') contributes largely to the momentum field at the leading edge of the cold pool -- the region in which the resulting accelerated winds drive system motion. Additionally, the momentum budgets also show that the pressure gradient acceleration (PGA) and, to a lesser degree the vertical advection of the background environmental wind ($VA\bar{u}$), contribute to the acceleration of rear-to-front momentum in

the middle- to rearward portions of the storm, generating and reinforcing the perturbation flow transports into the cold pool and accelerating the MCS.

The simulation presented in the present chapter illustrates a significant contribution to MCS speed from CMT: system acceleration during times of large downward transport (as shown by both the Eulerian and Lagrangian budgets) suggests a contribution to system acceleration from CMT on the order of $5 - 10 \text{ ms}^{-1}$ over a period of 3 – 4 hours (Figs. 3.5, 3.10). While previous studies have examined CMT from alternative angles such as its role in generating severe surface winds or driving the large-scale momentum budget, the process is rarely considered in the literature as one that significantly influences the speed at which MCSs move (as opposed to buoyancy effects in the cold pool, gravity-wave motion, etc). This portion of the investigation demonstrates the specific role of CMT in accelerating MCS motion using trajectories, momentum fluxes, and both Eulerian and Lagrangian momentum budgets to elucidate this contribution both qualitatively and quantitatively.

The significance of the contribution of CMT to the total MCS momentum field also illustrates that the omission of this process in many operational NWP model CP schemes is questionable, and may conceivably contribute to a negative bias in numerical forecasts of MCS motion at grid lengths where CP schemes are needed (Mahoney and Lackmann 2007). When considering the potential impact of an acceleration on the order of $5 - 10 \text{ ms}^{-1}$ as noted above, over a 12- or 24-hour operational forecast utilizing a CP scheme and thus neglecting this process, such a difference is clearly important. It is also possible that current “manual” MCS motion forecast methods [e.g., Corfidi vectors (Corfidi et al. 1996)] may benefit from a more precise inclusion of the CMT processes described herein; this possibility is discussed further in Chapter 6. Finally, the impact of this process is of importance to severe weather forecasting: downward CMT in MCSs likely contributes to severe surface winds and downbursts (e.g., Johns and Hirt 1987; Vescio and Johnson 1992; Weisman 1992; Geerts 2001), and possibly non-supercellular tornadogenesis as well (e.g., Atkins et al. 2005). Several recent studies have discussed the combined role of mesovortices along the leading edge of the convective line and a

descending RIJ in causing strong surface winds (e.g., Trapp and Weisman 2003; Wakimoto et al. 2006; Atkins and St. Laurent 2009a). This process, its connection to CMT, and its specific potential implications to forecasting severe surface winds are discussed in Chapters 5 and 6.

Increased understanding of the CMT process appears to offer possible improvement to several aspects of severe weather analysis and forecasting, and there exist a number of different avenues for exploring this potential. One question prompted by the preceding discussion is the significance of the trailing stratiform region (TSR) and the processes inherent therein to determining the relative importance of CMT in a given MCS. While the analysis of the particular MCS discussed here suggests that the primary contribution of CMT to system motion is in $VOL_{leading}$ (the leading convective region), the literature suggests that the TSR has a significant impact on determining both RIJ properties as well as downward motion (and thus downward momentum transport) throughout the system (e.g., Weisman 1992; Yuter and Houze 1995b; Mechem et al. 2006; Grim et al. 2009a,b). Furthermore, variability of the TSR in observed MCSs (e.g., Smull and Houze 1987; Parker and Johnson 2000; Smith et al. 2009) suggests that differences in this region may significantly alter the relative significance of CMT across a spectrum of MCSs and MCS environments. Therefore, the following two chapters focus on several issues related to the TSR by exploring the impact of the background environment and relevant microphysical processes as each relates to vertical motion and CMT within MCSs.

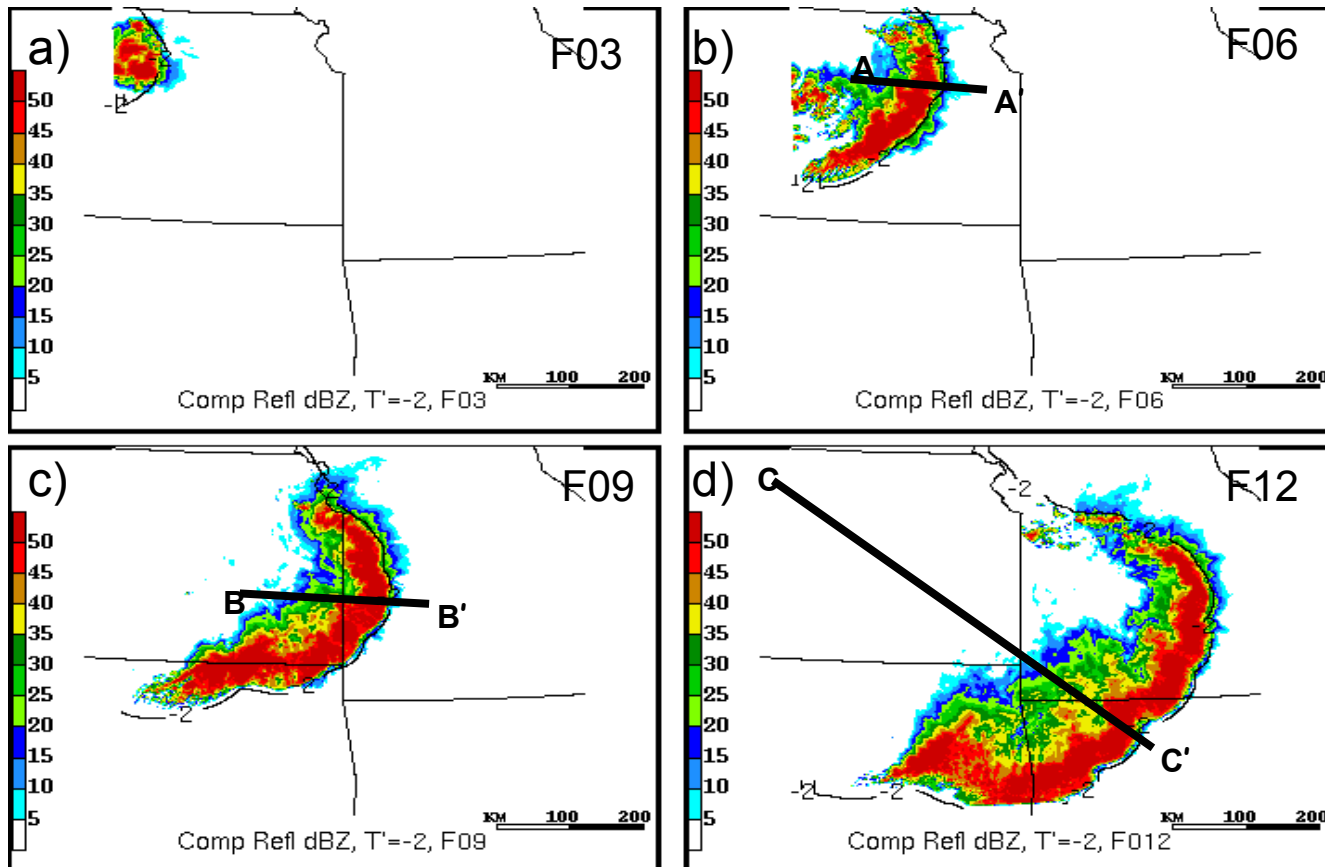


Figure 3.1: Simulated composite reflectivity (dBZ, shaded as indicated at right) and cold pool outline ($T' = -2^\circ\text{C}$ at 0 m (black, solid)), at (a) F03, (b) F06, (c) F09, and (d) F12. Lines A-A', B-B', and C-C' in (b) - (d) depict cross-sections shown in subsequent figures; distance (km) as denoted by scale legend.

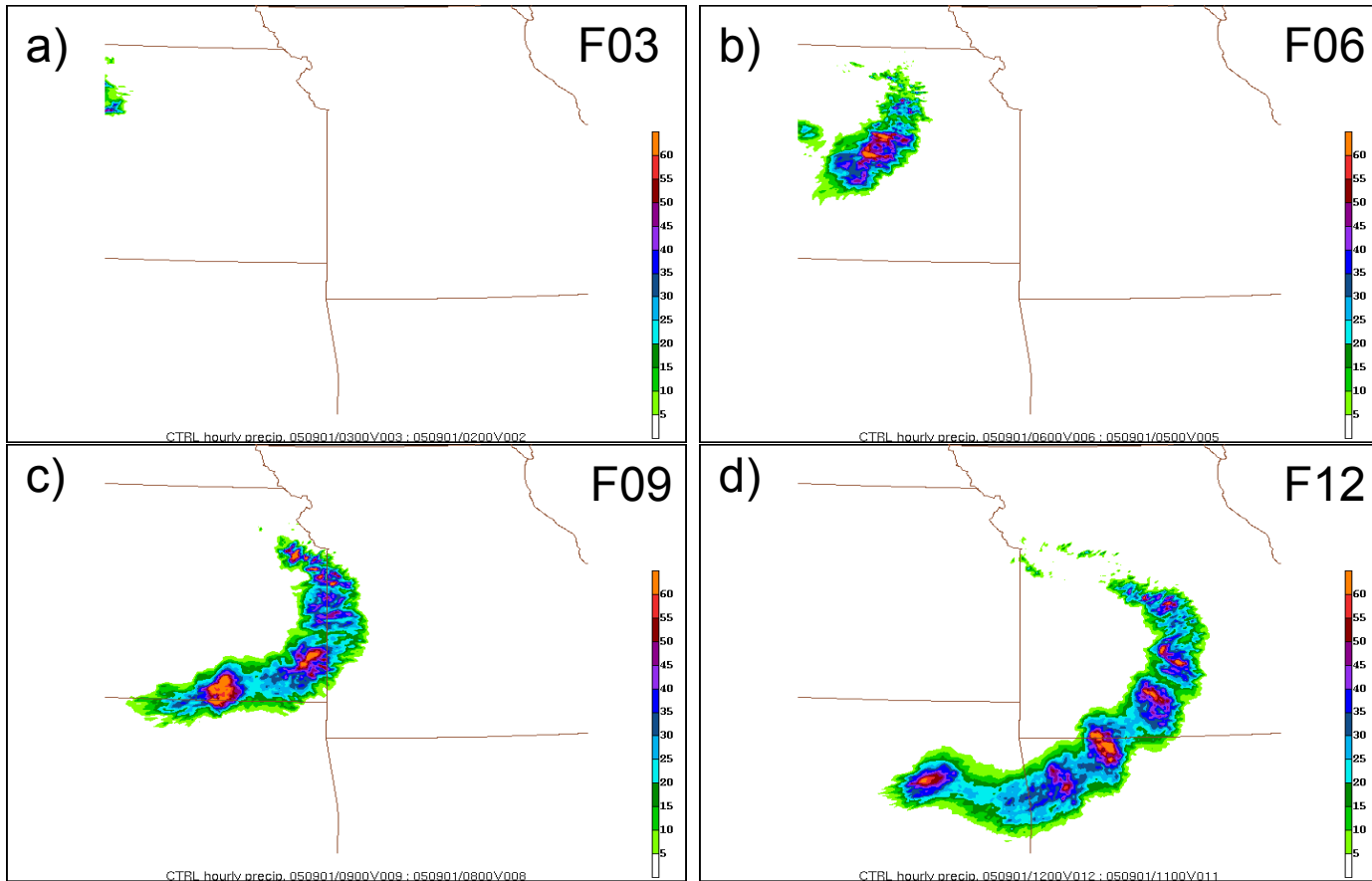


Figure 3.2: Hourly precipitation (mm, shaded as indicated at right) ending at (a) F03, (b) F06, (c) F09, and (d) F12.

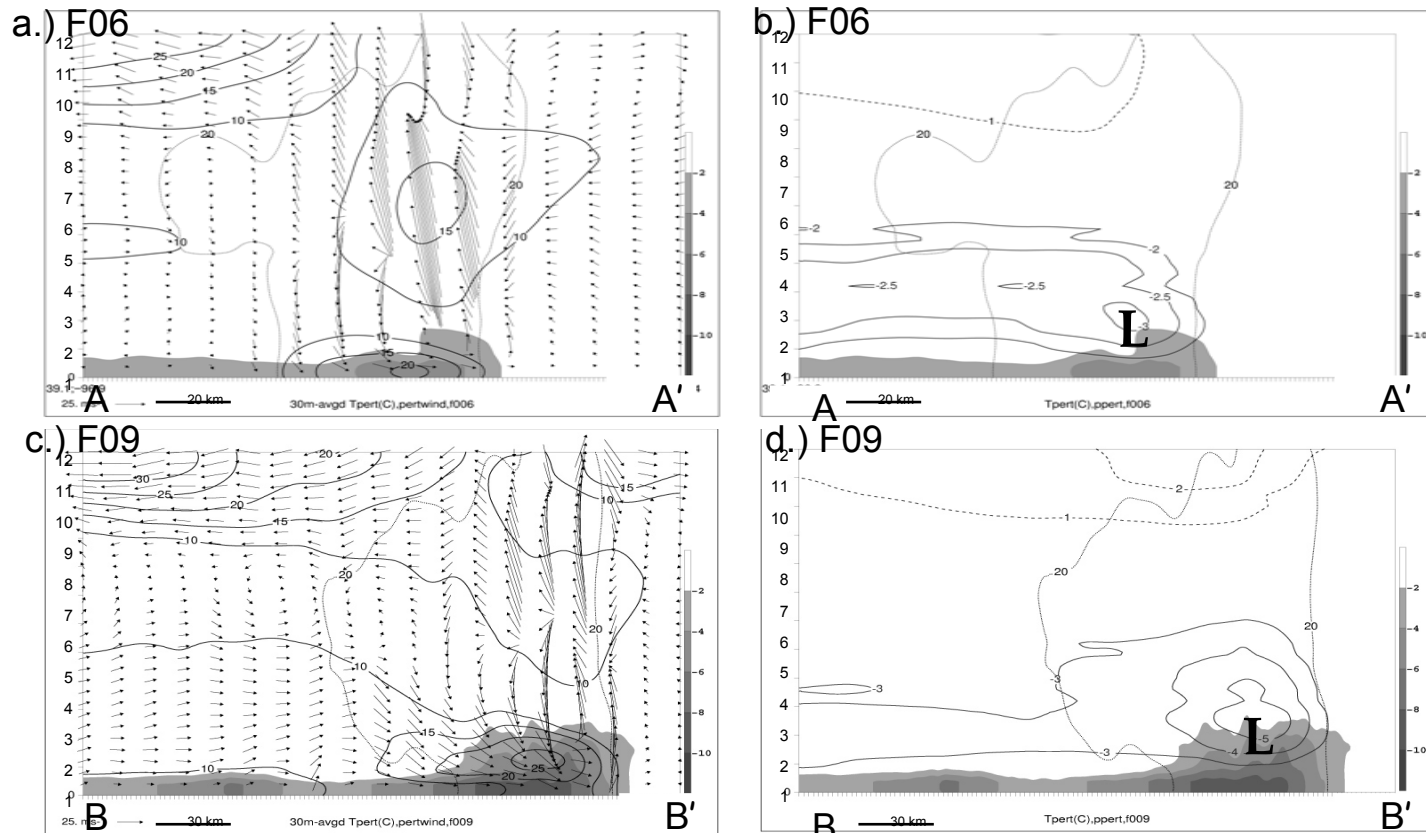


Figure 3.3: (a) East-west cross-section along line A-A' as in Fig. 3.1 at F06, averaged in an along-line direction in 40-km segments. Cold pool (shaded as shown beginning at $T' = -2^{\circ}\text{C}$), magnitude of total perturbation wind $((u^2 + v^2)^{1/2}, \text{ms}^{-1})$ and simulated reflectivity (dBZ, gray dotted contour, 20 dBZ). Black arrows show ground-relative perturbation flow in the x-z plane scaled as shown by reference vector in lower left corner; (b) as in (a), except solid (dashed) contours represent negative (positive) pressure perturbation in hPa; (c) as in (a) except along B-B' as in Fig. 3.1c at F09; (d) as in (b) except along B-B' as in Fig. 3.1c at F09.

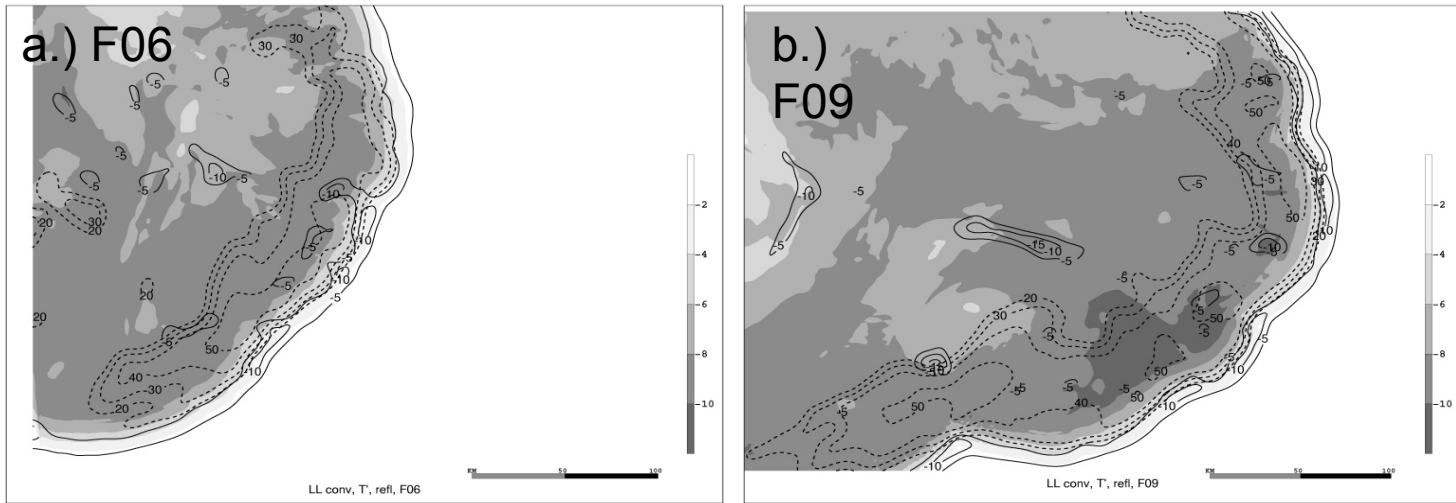


Figure 3.4: (a) Low-level (2-m) temperature perturbation from initial environment (K, shaded as in legend at right), divergence (black contours, $-5 \times 10^{-4} \text{ s}^{-1}$ interval, starting at $-5 \times 10^{-4} \text{ s}^{-1}$) at 10 m, and composite reflectivity (dashed, interval 10dBZ, starting at 20dBZ) at F06; (b) as in (a) but valid at F09.

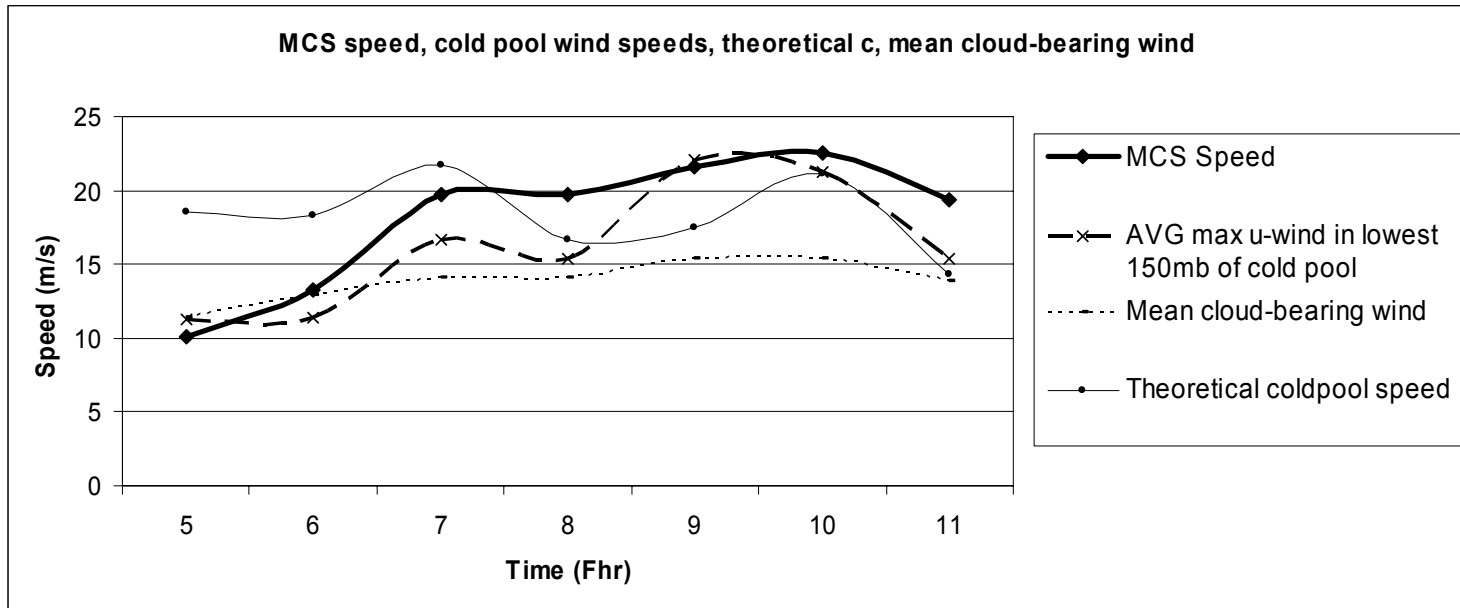


Figure 3.5: Speed of MCS (ms^{-1} , solid), average of gridpoint maximum wind speed in the lowest 3 km of the cold pool (ms^{-1} , large dashed), average mean cloud-bearing wind (from 900 – 200 hPa, ms^{-1} , small dashed), and theoretical cold pool speed c (ms^{-1} , thin solid).

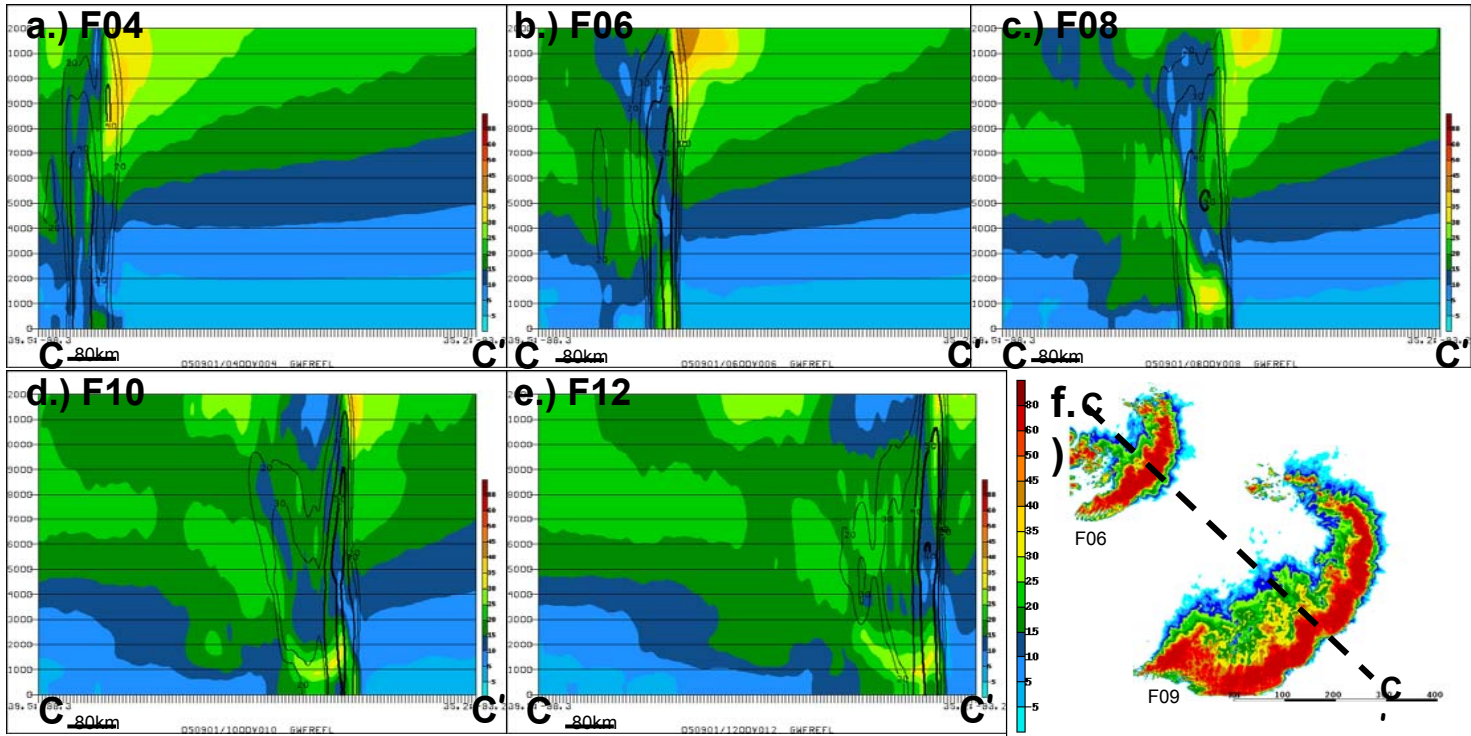


Figure 3.6: (a) Total wind speed (ms^{-1}) along line C-C' shown in Fig. 3.1d and panel f (shaded, according to legend at right) and simulated reflectivity (contours, interval 10dBZ, starting at 20dBZ) at F04; (b) as in (a) except for F06; (c) as in (a) except for F08; (d) as in (a) except for F10; (e) as in (a) except for F12; (f) cross-section C-C' (black dashed) and simulated composite reflectivity at times F06 and F09 as labeled and shaded as in Fig. 3.1

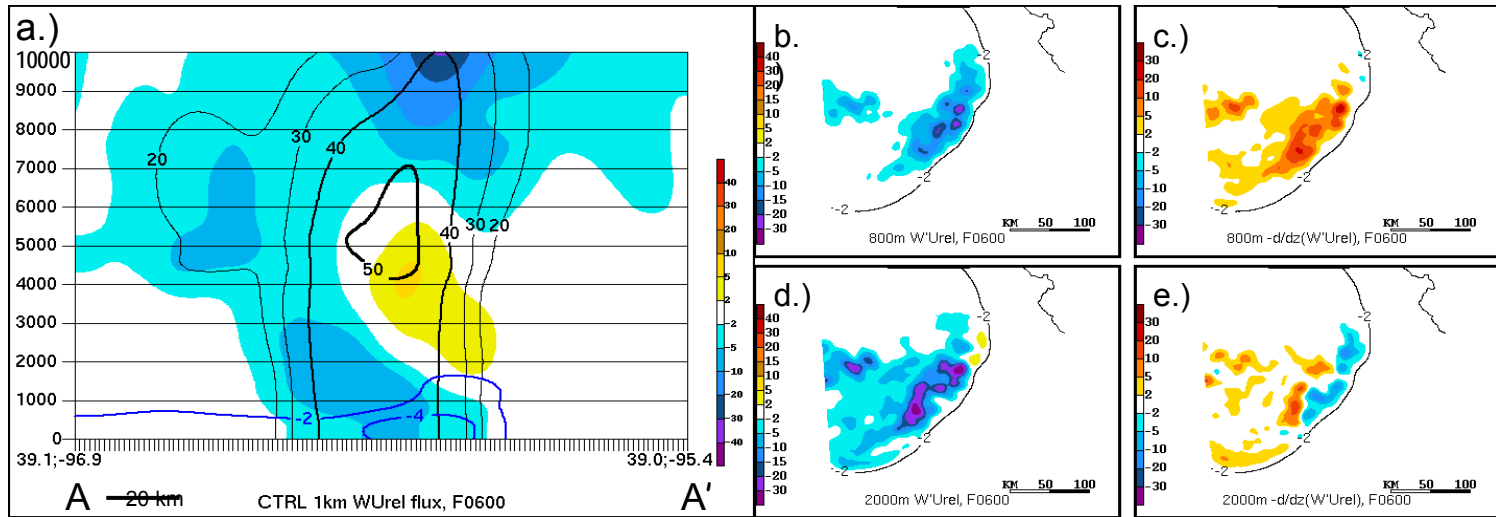


Figure 3.7: (a) East-west cross-section through leading edge of MCS along line A-A' at F06 (as shown in Fig. 3.1b) showing cold pool (T' , blue contours, -2°C intervals starting at -4°C), and downward momentum flux (shaded as in legend at right) and simulated radar reflectivity (black contours, 10dBZ intervals starting at 20dBZ); (b) downward momentum flux at 800 m at F09 (m^2s^{-2}), $T'=-2^\circ\text{C}$ at 0 m (black, solid), (c) as in (b) but for $-d/dz(uw)$, where positive values denote convergence (ms^{-2}), (d) as in (b) except at the 2000-m level, (e) as in (d) except at the 2000-m level.

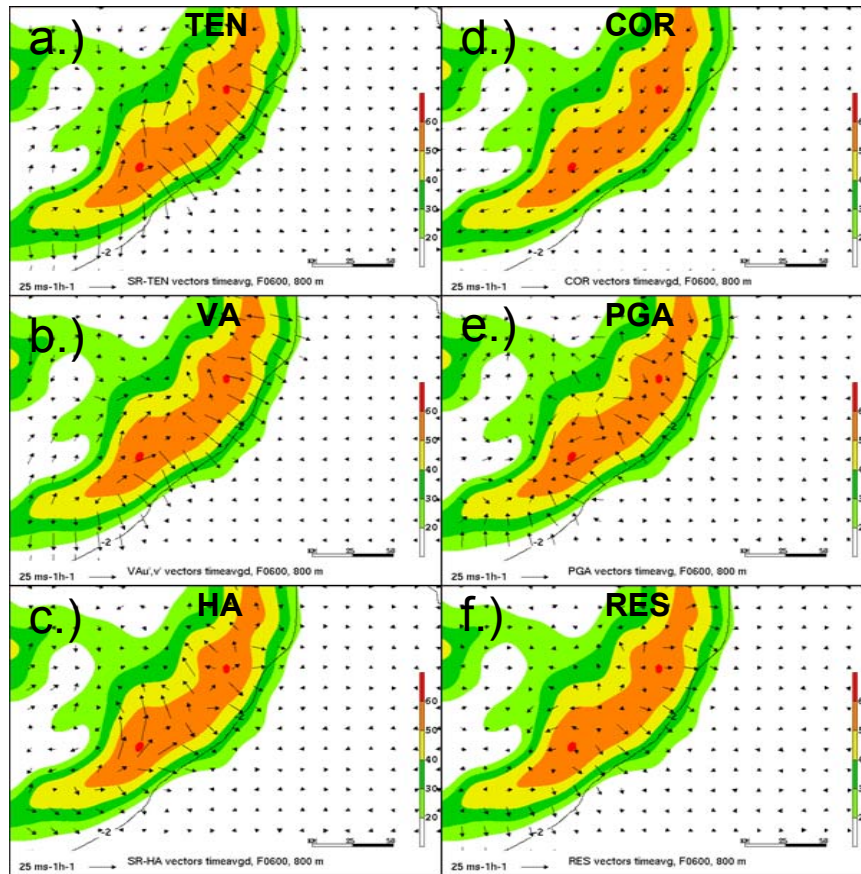


Figure 3.8: a) Simulated reflectivity (dBZ, shaded, as in legend at right), $T = -2^{\circ}\text{C}$ at 0 m (black, solid), and the vector sum of the u- and v-tendency (TEN) terms from Eqns. (2.2) and (2.3) (vectors, $\text{ms}^{-1}\text{h}^{-1}$, scaled as shown by reference vector in lower left corner) at 800 m at F06; b) as in a) except vectors show VA term, c) as in a) except vectors show HA, d) as in a) except vectors show COR term, e) as in a) except vectors show PGA term, f) as in a) except vectors show RES.

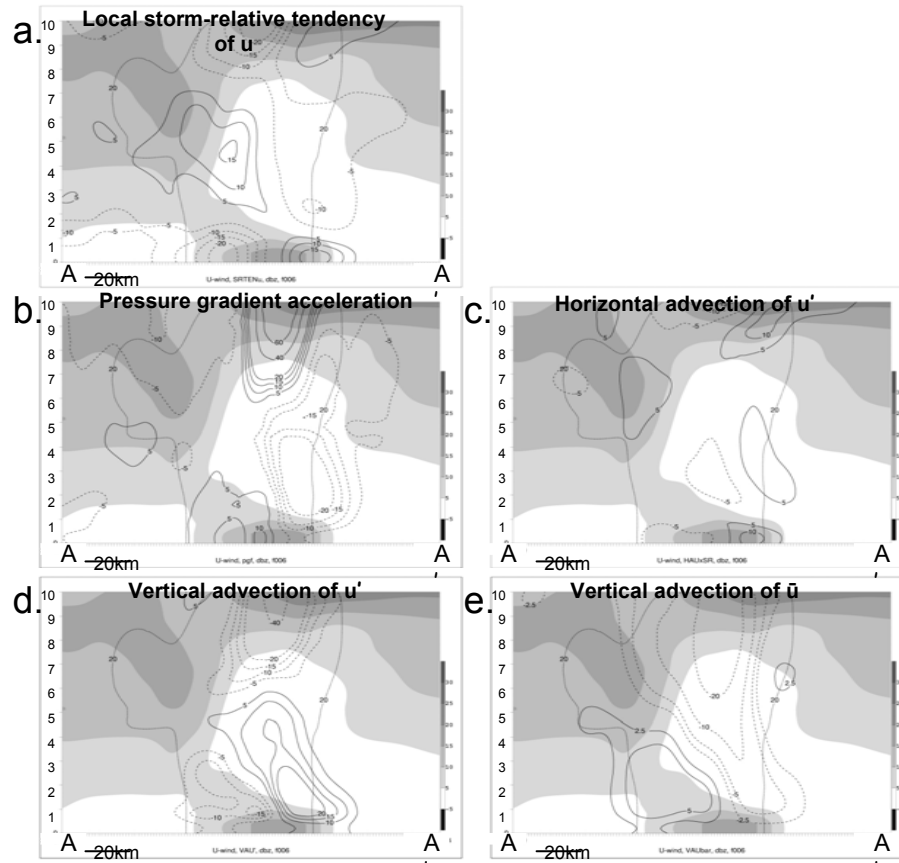


Figure 3.9: Cross-sections of momentum budget terms along line A-A' (shown in Fig. 3.1b) at F06: (a) u' (m/s, shaded as in legend at right) and TEN_x ($ms^{-1}h^{-1}$, positive (negative) values in solid (dashed) contours), and 30-dBZ contour (dotted) of simulated reflectivity; (b) as in (a) except PGA_x ; (c) as in (b) except HAu_x ; (d) as in (a) except VAu' ; (e) as in (a) except $VA\bar{u}$.

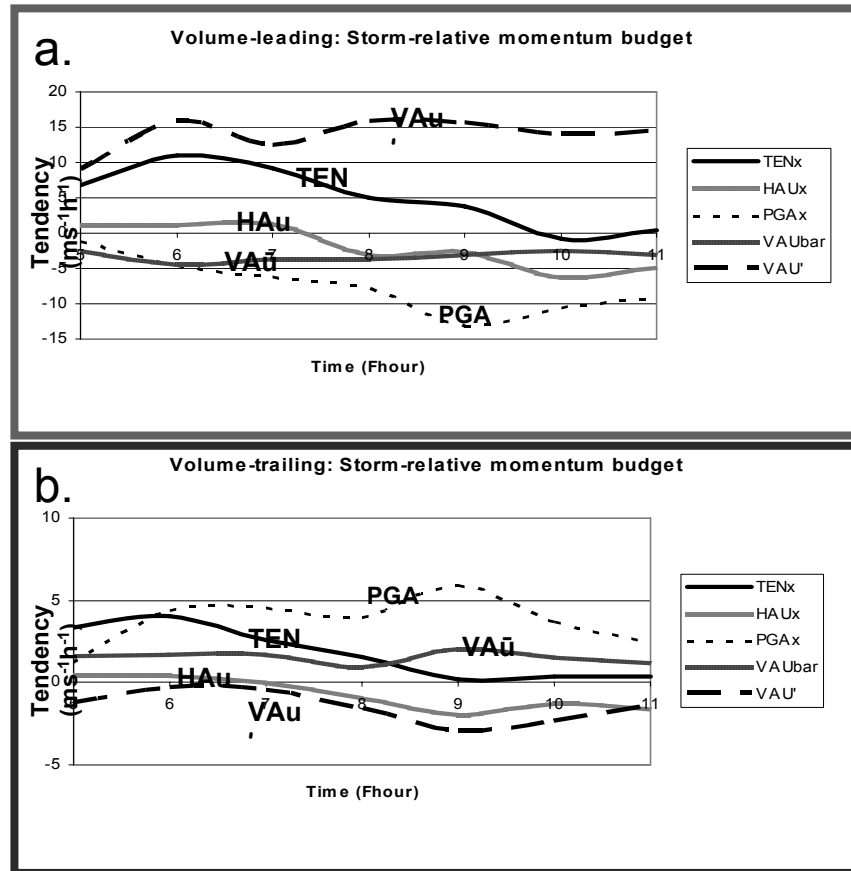
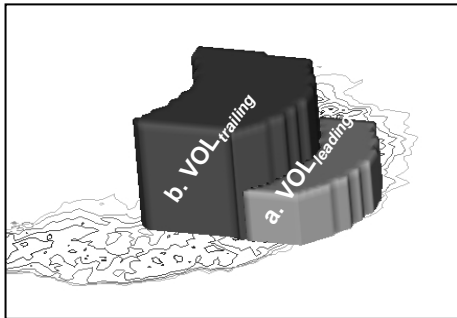


Figure 3.10: Volume-averaged momentum budget terms as labeled in key for times F05 – F11 for the (a) leading volume and (b) trailing volume (note different scales of y-axes).

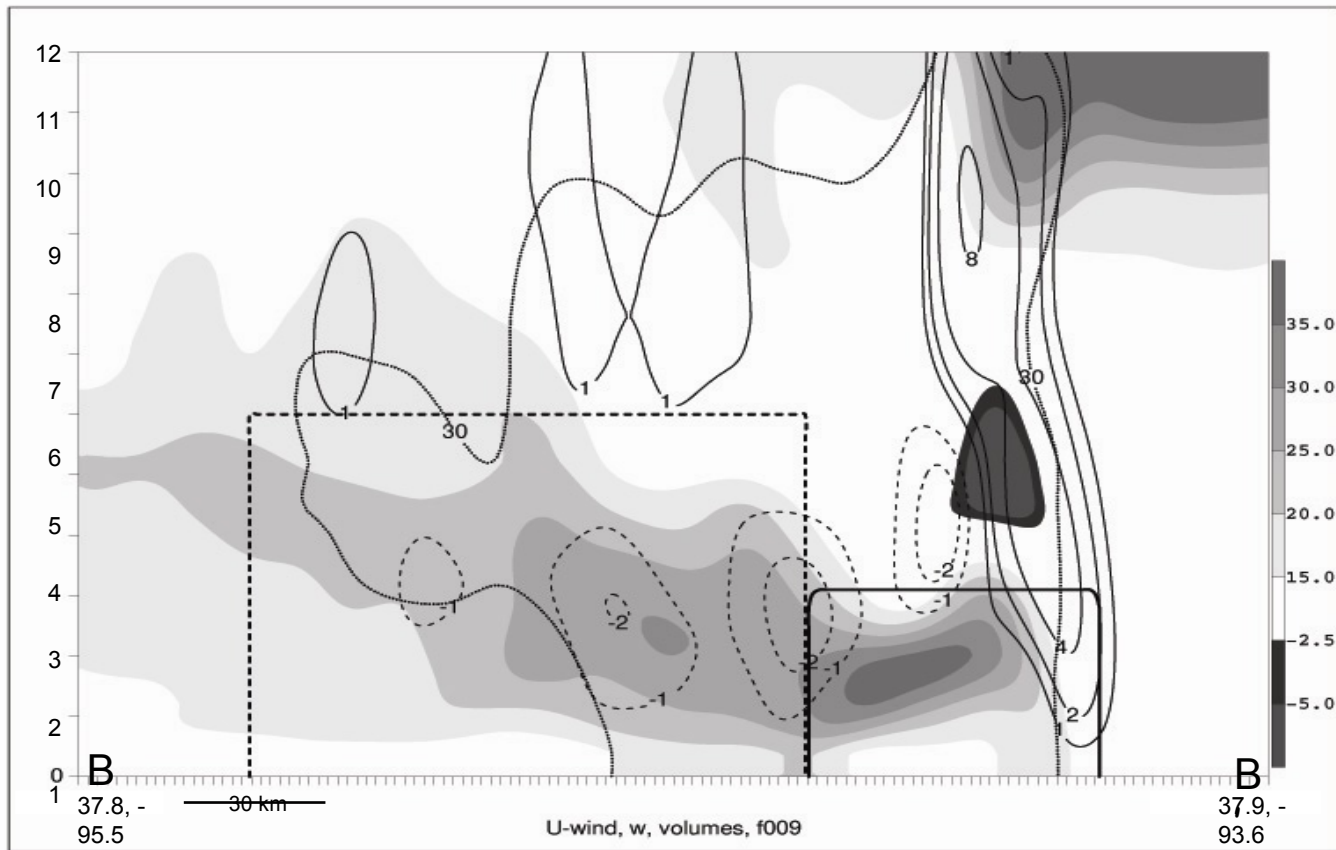


Figure 3.11: Cross-section of u (shaded, m/s as in legend at right), and w (m/s, positive(negative) black solid (dashed) contours) at F09 along B-B' as in Fig. 3.1c. Solid (dashed) box outlines volumes $VOL_{leading}$ ($VOL_{trailing}$), and simulated reflectivity contour of 30dBZ (dotted).

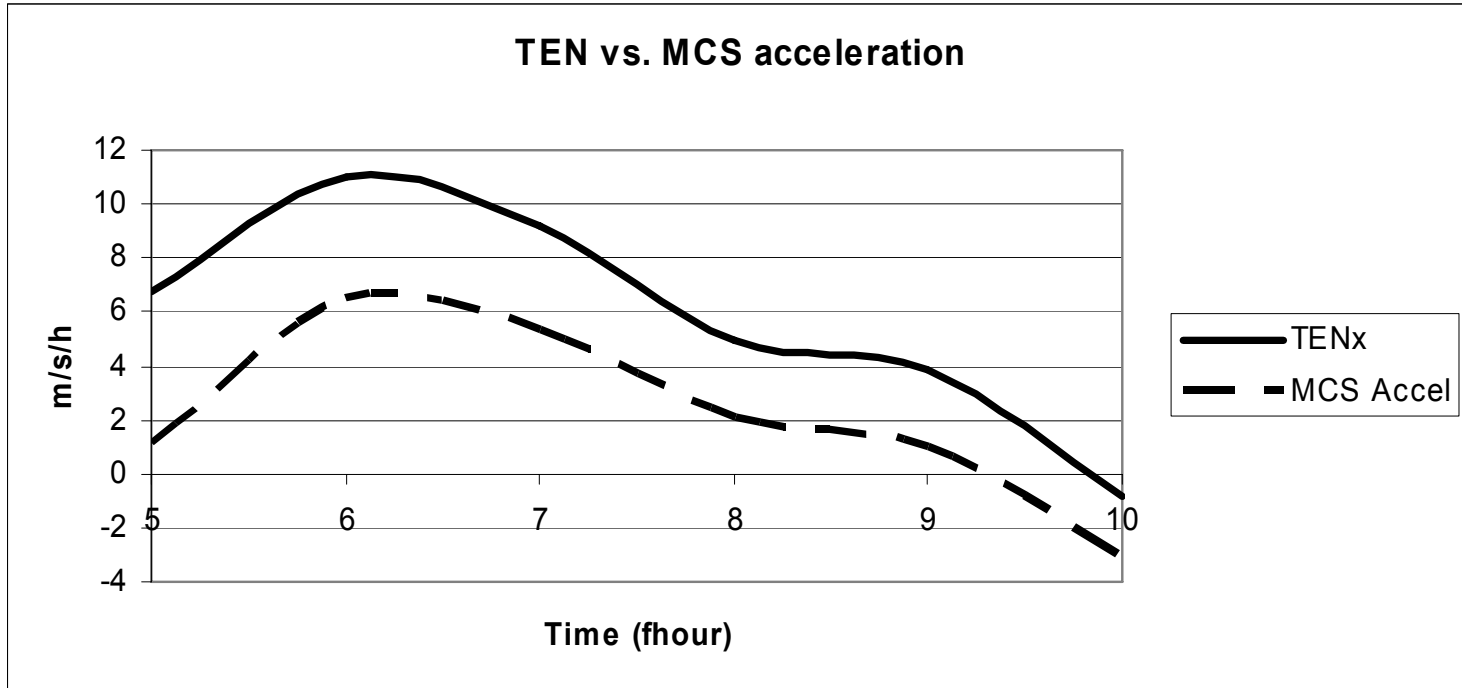


Figure 3.12: TEN_x in $VOL_{leading}$ (solid, $ms^{-1}h^{-1}$) and x-component of MCS acceleration (dashed, $ms^{-1}h^{-1}$) vs. time (x-axis, hours).

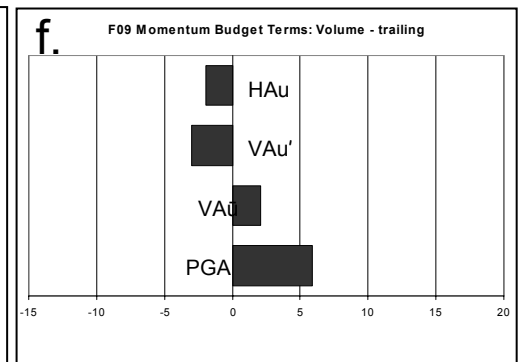
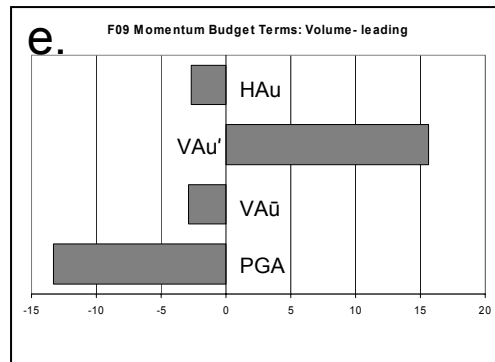
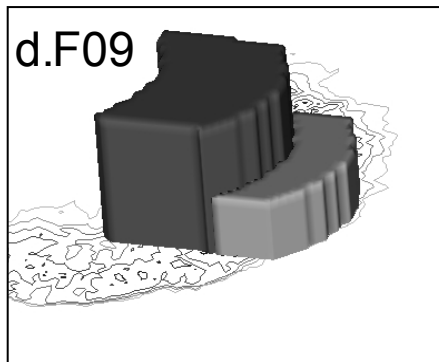
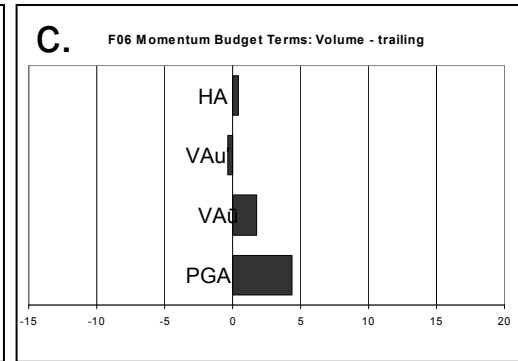
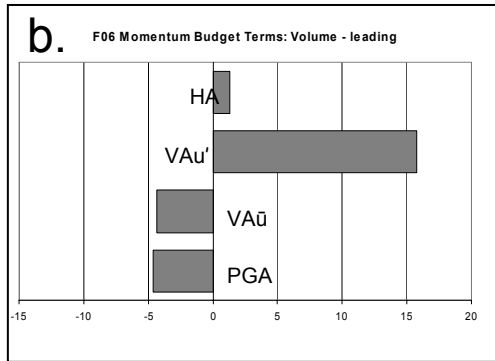
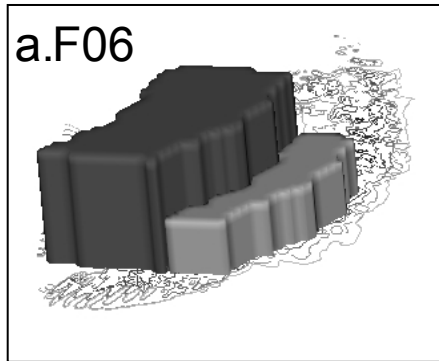


Figure 3.13: a) VOL_{leading} (light gray) and VOL_{trailing} (dark gray) at F06, b) momentum budget term averages as labeled over VOL_{leading} at F06 in $\text{ms}^{-1}\text{h}^{-1}$, c) as in b) but for VOL_{trailing} , d) as in a) but for F09, e) as in b) but for F09, f) as in c) but for F09.

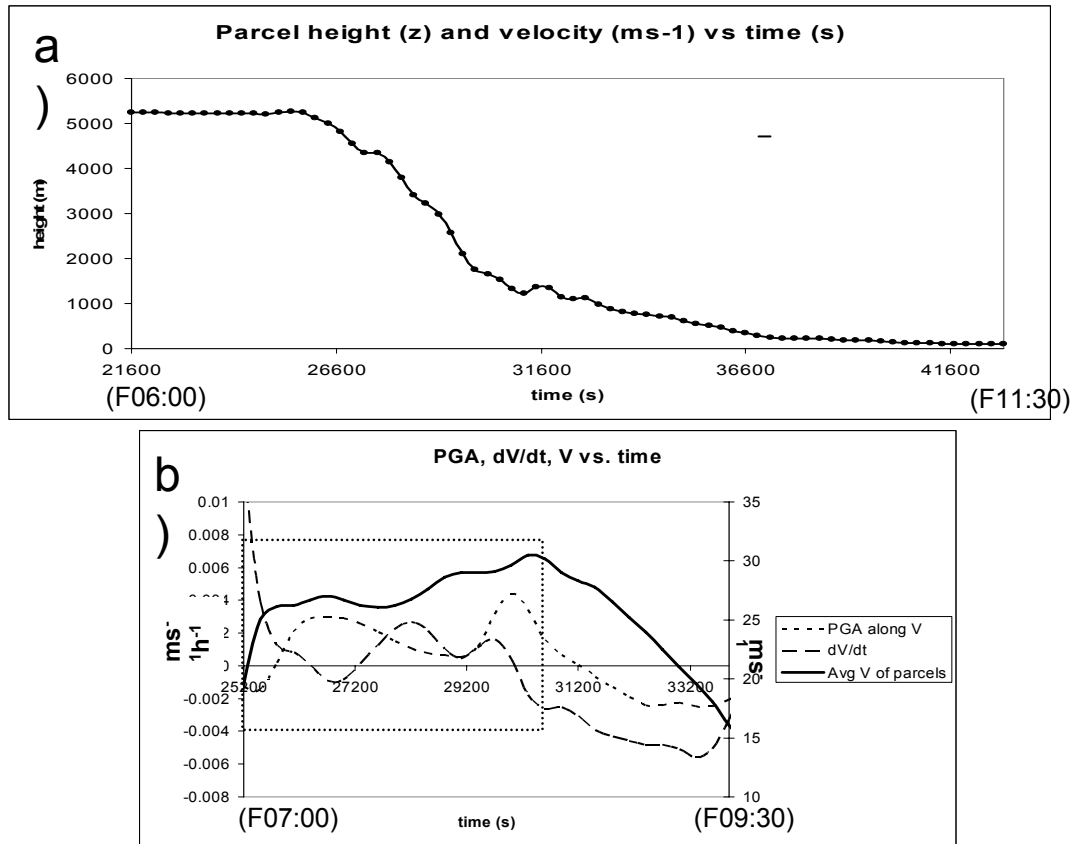


Figure 3.14: a) Height (y-axis, m) vs. time (x-axis, sec) of average trajectory of 50 parcels originating at RIJ-level at F06; b) PGA (short dashed, ms⁻², values on left y-axis), acceleration (d|V|/dt, long dashed, ms⁻², values on left y-axis), and wind speed (|V|, solid, ms⁻¹, values on y-axis at right) for time period t = 25200s (F07:00) to t=34200s (F09:30) only. Dotted box in panel b) denotes period of acceleration from t = 25200s to t = 30300s.

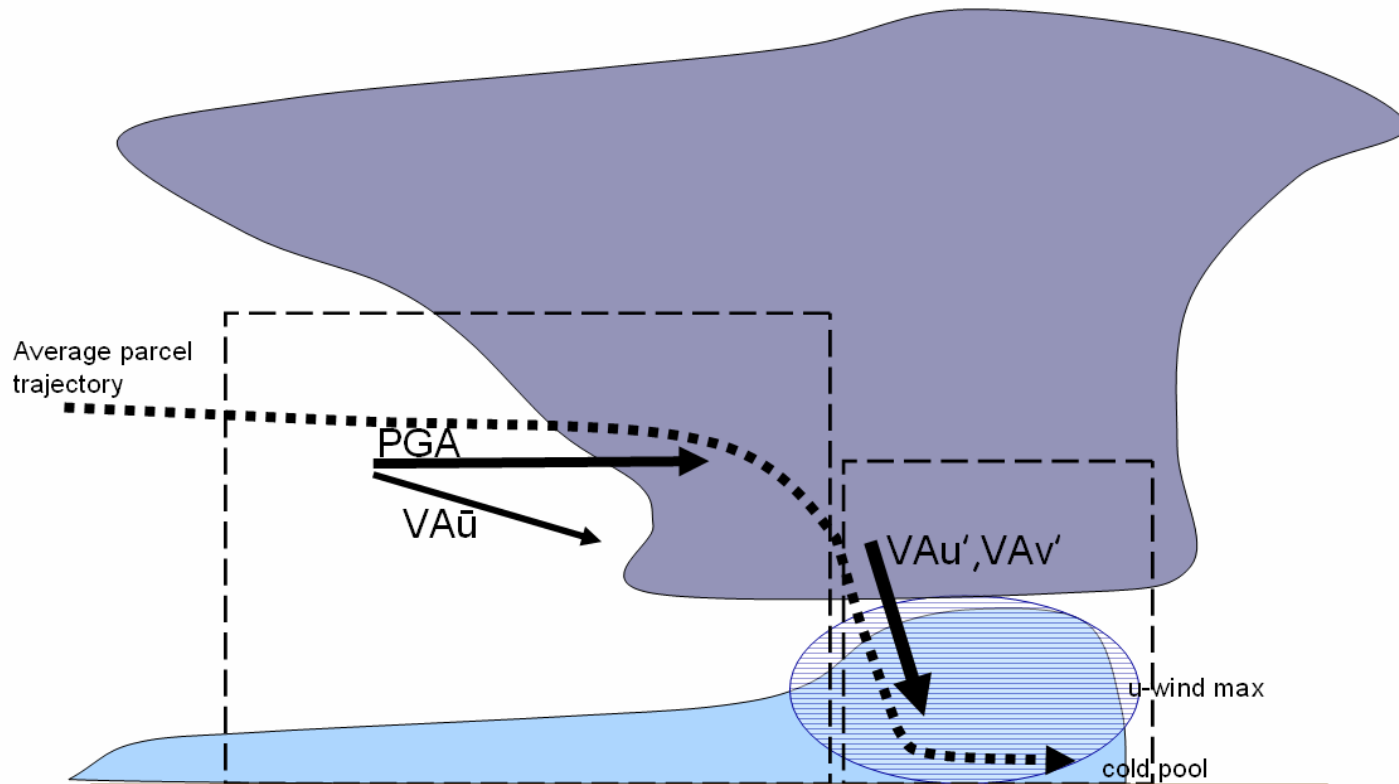


Figure 3.15: Schematic of relative contributions of momentum budget terms PGA , VA processes to CMT as indicated by black arrows (thickness of arrows an approximate indication of relative magnitude of terms, and dashed boxes show general locations of $VOL_{leading}$ and $VOL_{trailing}$).

Chapter 4

Sensitivity of CMT and MCS motion to changes in environmental humidity and model microphysics

4.1 Motivation

Chapter 3 establishes the significance of the contribution of CMT to MCS motion in one quasi-idealized numerical simulation in one specific environment. In order to connect these findings with the primary motivation of understanding how MCSs move, it is necessary to establish the sensitivity and relative importance of CMT in MCSs occurring in various types of environments and featuring different storm-scale characteristics. Thus, a suite of experiments is desirable to further refine understanding of CMT and MCS motion by exploring its sensitivity to physical processes that may be regulated in a numerical model (e.g., cooling due to evaporation, melting, or sublimation).

There exist multiple avenues that one could pursue with respect to the aforementioned exploration of “parameter space” of the significance of CMT in MCSs. One possibility is to vary the background kinematic environment by altering wind profiles and environmental shear. Another opportunity involves examining storm-scale characteristics such as storm-relative flow, representation of hydrometeors and microphysical processes, and system organization. The former approach is accompanied by few potential hurdles to consider.

First, a change of modeling framework from that used in Chapter 3 is necessary for optimal execution of kinematic sensitivity tests. That is, if a larger requirement of this line of research is to keep the initial model environment in thermal wind balance for reasons discussed in Chapter 2, then changes in the thermal gradient will be required for any change made to the wind field. It is clear that changing both fields at once complicates interpretation of results, and this challenge has been noted by previous studies such as Skamarock et al. (1994). Second, there is a certain degree of predictability in changing wind profiles for a case such as this. That is, increasing mean wind speeds

will clearly increase MCS motion via advection, and changes in shear as related to MCS intensity and motion have been explored quite thoroughly throughout the literature (e.g., Newton and Fankhauser 1964; Rotunno et al. 1988; Weisman 1992; 1993; Corfidi et al. 1996; Evans and Doswell 2001); therefore it is unclear that findings from these types of experiments would necessarily add significant value to the understanding of CMT and MCS motion.

Nevertheless, since the basic kinematic environment of an MCS literally defines the expression for CMT, several model simulations testing the sensitivity to environmental wind speed and shear have indeed been performed, and preliminary results are briefly summarized in Appendix B. But for the reasons provided above, as well as the large body of research that continues to reveal new gaps in our understanding of the feedback of MCS dynamics and microphysical processes (e.g., Fovell and Ogura 1988; Yuter and Houze 1995a; Wakimoto 2001; Grim et al. 2009a,b; Smith 2009) the sensitivity experiments analyzed here are designed to address questions (specified below) related to CMT and MCS motion with respect to changes in environmental moisture and storm-scale microphysics.

The experimental design of this series of sensitivity tests is similar to that of previous studies that examine sensitivity of various aspects of MCSs to microphysical processes, such as Fovell and Ogura (1988), Yang and Houze (1995), and Grim et al. (2009b). Yang and Houze (1995) in particular use a very similar methodology to what is used here in order to investigate the sensitivity of MCS rear inflow to ice microphysics and environmental humidity. While their experiments do not focus on changes in simulated MCS speed, differences in groundspeed between the runs are observed (Table 4.1). Using similar methodology, the experimental framework employed here aims to instead address the role of environmental humidity and microphysical processes in determining (i) MCS speed, (ii) CMT, and (iii) theoretical (buoyancy-based) cold pool speed. As the strength and organization of rear-inflow and the horizontal extent and model representation of the trailing stratiform region have significant potential impacts on all of the above areas, these fields will also be examined.

As detailed in Chapter 2, the simulations chosen for sensitivity analysis are:

1. Control (CTRL)
2. Dry mid-levels (DRYM)
3. Reduced evaporation (REVP)
4. No melting (NMLT)
5. No sublimation (NSUB)

Model set-up and initial conditions details for each experiment are given in Chapter 2, and experiment hypotheses and model output are discussed and analyzed below.

4.2 Background/Previous research

Previous studies have examined the impact of microphysical processes and environmental humidity in MCSs using a variety of experimental designs to learn more about the role of these processes in MCS organization and dynamics. Observations and both idealized and real-case model simulations have been used to examine the role of these processes in determining rear inflow strength and structure, vertical motion, the horizontal extent of the trailing stratiform region, and various pressure perturbation features (e.g., Zhang and Gao 1989; Braun and Houze 1995; Yang and Houze 1995; Yuter and Houze 1995a,b; Grim et al. 2009a,b; Morrison et al. 2009).

Rear-inflow strength has been one topic of considerable study over the past several decades. Per the importance of the RIJ in the CMT process (as shown in Chapter 3) and the considerable variability it has been found to show in the trailing stratiform region of individual MCSs (e.g., Smull and Houze 1987), it is useful to briefly summarize the current working conceptual model of rear inflow in the leading convective-trailing stratiform MCS framework. The formation of rear-inflow is generally acknowledged to begin with a mid-level area of low pressure that is established in response to latent heating due to convection within a developing MCS (e.g., Smull and Houze 1987). A pressure gradient acceleration then occurs toward the area of low pressure, increasing mid-level windspeeds in a rear-to-front storm-relative direction, with a variable degree of interaction with background environmental winds (Smull and Houze 1987) and the

possibility of further enhancing mid-level flow via a constructive feedback with bookend vortices (Weisman 1993). If a trailing stratiform region (TSR) forms and persists [a process that depends on both the environmental wind shear profile (e.g., Rotunno et al. 1988; Parker and Johnson 2004a), as well as a suite of microphysical processes (e.g., Yuter and Houze 1995a,b)], a secondary heating maximum will develop in response (though with an altered vertical heating profile) and another area of minimized pressure will form rearward of the first mid-level mesolow (e.g., Klimowski 1994; Yang and Houze 1995; Smith et al. 2009). This secondary area of rear-to-front-directed pressure gradient acceleration thus develops a secondary area of rear inflow. If the MCS persists in this form for a significant amount of time (on the order of 1h or more) then a coherent stream of rear inflow is likely develop along the line. However, rear inflow generally displays significant heterogeneity in both the horizontal and vertical, with stronger areas of rear inflow generally corresponding to stronger areas of convection (e.g., Fig. 4.1; Klimowski 1994; Yang and Houze 1995). Furthermore, interaction with large-scale winds may be variable in different environments, potentially enhancing and/or reducing rear inflow strength in various places along the line as well.

The descent of the RIJ is also not continuous along the line, with areas of descent maximized in areas of enhanced cooling from sublimation, melting, and evaporation (e.g., Smith et al. 2009; Grim et al 2009b), as well as in areas of enhanced dynamically-driven downdrafts such as those driven by convective downdrafts (e.g., Weisman 1992; Yuter and Houze 1995a; Wakimoto et al. 2006), precipitation loading (Srivastava 1985), a gravity-wave or bore response (Pandya and Durran 1996), or as determined by local vorticity balance (Weisman 1992; 1993). Dissipation of rear inflow begins as areas of active convection decrease, and its ultimate dissolution depends on how long latent heating maxima persist associated with areas of longer-lasting convective and/or stratiform precipitation (e.g., Klimowski 1994).

With the foregoing conceptual model of MCS rear inflow and RIJ descent in mind, it is not surprising that a large number of studies have examined the sensitivity of these processes to different model microphysics schemes and microphysical processes

(Fovell and Ogura 1988; Braun and Houze 1995; Yang and Houze 1995; Ferrier et al. 1995; Liu and Moncrieff 2007; Morrison et al. 2009). Toward connecting these better-known feedbacks with the conceptual model of CMT provided in Chapter 3, this particular set of sensitivity experiments thus focuses specifically on the effect these processes have on CMT and MCS motion.

4.3 Sensitivity tests

4.3.1 Control (CTRL)

The control simulation (CTRL) is identical to the simulation analyzed in Chapter 3 with the exception of the microphysical parameterization. CTRL uses the WSM6 scheme while the run used in Chapter 3 uses the Purdue Lin scheme. As stated in Chapter 2, this change was made to facilitate the microphysical scheme alterations required for the desired suite of sensitivity experiments. Differences in the two simulations (CTRL and that of Chapter 3) are subtle (cf. Figs. 4.2, 3.1), and will not be detailed here. The MCSs move in a similar speed and direction, and momentum budget terms between the simulations are also very closely-matched.

4.3.2 Dry mid-levels (DRYM)

4.3.2.1 DRYM hypotheses

In order to examine how CMT and MCS motion respond to a decrease in mid-level humidity, a simulation was produced using drier mid-level initial conditions as detailed in Chapter 2. Based on previous studies, multiple hypotheses exist regarding possible impacts on the simulated MCS. One proposition is that MCS speed will increase due to enhanced evaporative cooling into dry air. An increase in groundspeed is possible due to a) an increase of theoretical cold pool speed (c) by colder cold pool temperatures, b) increased CMT via enhanced mid-to-low-level downward motion associated with enhanced mid-level cooling, or c) a combination of the above.

A counter-hypothesis is that MCS speed may be unchanged or even decrease if drier mid-level air is entrained into the updraft and the system weakens overall. One way that this may occur is by drier air decreasing updraft buoyancy and thus decreasing updraft strength, leading to less condensate to evaporate and thus a cold pool intensity that is either unchanged or even weaker than the CTRL simulation¹. Another possibility is described by Yang and Houze (1995), in which the entrainment of drier air produces mid-level cooling that counteracts the vorticity tendency produced by the surface cold pool. This causes the system to tilt more upright, weakening the front-to-rear flow, and decreasing the size and intensity of the TSR. Less evaporation, melting, and sublimation in the TSR weaken negative buoyancy and thus horizontal buoyancy gradients there, thereby weakening rear inflow as well. Interestingly, the results of Yang and Houze (1995) show that despite a weaker overall system, a decrease in MCS speed is not observed.

4.3.2.2 DRYM results

The DRYM simulation results indeed reveal differences relative to CTRL with respect to both spatial and temporal development (Fig. 4.3). The DRYM simulation produces a smaller system with less trailing stratiform precipitation at most times, and the system as a whole moves in a more due-eastward direction. Calculating MCS motion as detailed in Chapter 2 (i.e., computing the hourly distance covered by the most bowing (eastward) part of the system) shows that while the simulation-average groundspeed over the DRYM simulation appears similar to CTRL, there are notable differences in periods of acceleration and deceleration (Fig. 4.4). Specifically, DRYM accelerates more at first (~F05 – F07), and moves faster than CTRL toward the end of the simulation (~F10 – F12) but the overall acceleration of CTRL is of larger magnitude (i.e., an increase of 15 ms^{-1} over 4 hours versus a $\sim 9 \text{ ms}^{-1}$ increase over 5 hours).

¹ Bryan et al. (2003) demonstrates that 1-km grid spacing may be too coarse to adequately represent updraft entrainment processes, thus it is possible that this effect may be understated in the simulations discussed herein.

Vertical cross-sections taken along the leading edge of the bow echo (and averaged every 40 km in an along-line direction to improve representativity in run comparisons) show several dynamical differences between the simulations. Fig. 4.5 reveals a slightly deeper but less intense surface cold pool (in terms of temperature perturbation) and a slightly weaker mid-level mesolow in DRYM. The downward component of motion in the main region of RIJ descent is slightly greater in DRYM (Fig. 4.6), which is consistent with decreased buoyancy there as well (Fig. 4.7). A contoured frequency by altitude diagram [CFAD; Yuter and Houze 1995b] may also be used to identify differences in the TSR of CTRL and DRYM. Examination of the stratiform area² beyond the convective line at F09 (when each system was in its mature stage) shows an increase in downward motion (Fig. 4.8), enhanced cooling by the microphysical parameterization scheme (Fig. 4.9), and slightly stronger mid-level rear-inflow (Fig. 4.10). Momentum flux plots show enhanced flux values (and flux convergence) in DRYM at mid- to low-levels (Fig. 4.11), consistent with increases in the magnitude of low-level downward motion (Fig. 4.12). The relationship between the above noted physical field differences and MCS speed will be analyzed within the context of CMT and MCS motion using a momentum budget in section 4.4.3.

4.3.3 Reduced evaporation (REVP)

4.3.3.1 REVP hypotheses

As many studies have illustrated the fundamental role that evaporative cooling plays in forming and strengthening downdrafts in convective systems (e.g., Paluch 1979; Knupp 1987; Fovell and Ogura 1988; Kingsmill and Wakimoto 1991), it is hypothesized that decreased evaporation will lead to slower MCS groundspeed. The purpose in performing this test is rather to diagnose what specific process is responsible for any decrease in MCS speed to the extent that process separation is possible. Specifically, is a

² Stratiform gridcells were separated from convective gridcells according to the following definitions: (i) convective gridcell: $w \geq 2$ m/s at 2km AGL OR composite reflectivity > 30 dBZ, using a 5-km radius around each “convective” point. Stratiform gridcell: all those cells that are not convective but still have composite reflectivity > 15 dBZ.

slower groundspeed the result of buoyancy-based cold pool arguments only (i.e. decreased evaporative cooling preventing the cold pool from adequately forming), or a more dynamically-based argument of decreased CMT in response to less intense downward motion in the TSR?

4.3.3.2 REVP results

When evaporation is reduced by 75% in the microphysics parameterization scheme (REVP), the resulting MCS is smaller, takes more time to become an organized entity, and moves more slowly relative to CTRL (Fig. 4.13)³. Along-line-averaged cross-sections at F09 show a weak (and at times barely-existent) surface cold pool and a mid-level mesolow less than half the magnitude as seen in CTRL (Fig. 4.14). While rear-inflow does descend in the ~1-km – 5-km layer, the enhanced flow does not reach the surface, and low-level winds are very weak (Fig. 4.15). Buoyancy is only slightly negative beneath the system (Fig. 4.16), and downward motion is modulated in the weaker REVP system (Fig. 4.17). The cooling tendencies produced in the microphysics scheme are (by design) severely reduced in REVP (Fig. 4.18), and horizontal wind speeds (especially those at low levels, ~1 km AGL) are much weaker than those observed in the CTRL simulation (Fig. 4.19).

4.3.4 No melting (NMLT)

4.3.4.1 NMLT hypotheses

Cooling due to the melting of snow, ice, and graupel has been shown to have significant effects on MCSs. Yang and Houze (1995) find that latent cooling by melting accounts for at least 25% of RIJ intensity, and observational studies have found that melting in both the convective and stratiform regions can induce significant downdrafts

³ Simulations were also performed in which evaporation was reduced by 25% and 50%. The 75% reduction produced the most pronounced results and the degree of change made is more congruous with the complete removal of melting and sublimation in NMLT and NSUB respectively. However, while not as marked as the decreases seen when reducing evaporation by 75%, the other simulations showed qualitative similarities in terms of slower MCS speed and weaker cold pool as well.

and mesoscale circulations (e.g., Szeto et al. 1988; Braun and Houze 1995). Similar to the REVP simulation, decreased MCS groundspeed in the absence of melting is conceivable due to both (i) the omission of melting-induced cooling that may increase surface cold pool intensity (though likely having less of an impact than evaporation as most cooling due to melting occurs aloft near the 0°C level), and/or (ii) decreased CMT if both the RIJ and the intensity of downward motion is reduced. Therefore, removing melting is hypothesized to slow MCS motion, if only to a small degree (relative to decreasing evaporation).

4.3.4.2 NMLT results

The no-melting (NMLT) simulation bears considerable resemblance to the CTRL simulation, but shows slight decreases in both system size and groundspeed (cf. Fig. 4.20, Fig. 4.2). Both the pressure perturbation features and the surface-based cold pool are generally slightly weaker relative to CTRL (Fig. 4.21). The magnitude of the RIJ at mid-levels is very similar between NMLT and CTRL, but differences are seen in low-level winds, with CTRL revealing low-level wind speeds that are $\sim 5 \text{ ms}^{-1}$ stronger than the NMLT simulation (Fig. 4.22). Differences in buoyancy are evident in the TSR, where the NMLT simulation maintains higher positive buoyancy values at and below the melting level, illustrating the effect of the absence of melting-induced cooling (Fig. 4.23). Along-line averaged cross-sections taken through the central bowing portion of the system show that NMLT maintains areas of large downward motion, mostly concentrated toward the fore of the leading convective region (Fig. 4.24); these maxima generally correspond to areas with a high concentration of unmelted graupel throughout the vertical column (Fig. 4.25). CTRL appears to generally maintain more uniform downward motion throughout the TSR.

CFADs evaluated in the main area of the TSR and RIJ show weaker strong downward motion at and around the melting level ($\sim 5 \text{ km AGL}$) (Fig. 4.26). The maximum of cooling seen at 4 – 5km AGL in the CTRL simulation is absent in NMLT, and the cooling maximum found $\sim 2 \text{ km}$ is consistent with the downward motion fields at

these levels (Fig. 4.27). The magnitude of the total low-level wind field is also slightly larger in CTRL (Fig. 4.28); this general pattern is also apparent in plots of momentum flux (Fig. 4.29). Momentum flux and transport will be discussed further in section 4.4.

4.3.5 No sublimation (NSUB)

4.3.5.1 NSUB hypotheses

Sublimation is known to affect rear-inflow strength as well as the location and intensity of downward motion in some convective systems (e.g., Klimowski 1994; Yang and Houze 1995; Grim et al. 2009b). While key to the initiation of downward motion above the 0°C level, it is generally acknowledged to be the least important latent cooling process in determining rear-inflow strength (e.g., Yang and Houze 1995). However, recent studies such as Smith et al. (2009) and Grim et al. (2009b) have suggested that sublimation below the rear anvil in the TSR may initiate or significantly enhance downward motion in the rear of the system, thereby potentially beginning the downward transport of horizontal momentum at both higher altitudes and over a greater distance from the leading edge of the system. The hypothesis for the simulation is thus that if there is a change in MCS groundspeed, it would be slower owing to decreased CMT resulting from a slightly weaker RIJ and a smaller and shallower area of descent in the TSR.

4.3.5.2 NSUB results

The omission of the sublimation process (NSUB) yields relatively few dynamical differences relative to CTRL. Simulated composite reflectivity fields reveal subtle differences in areas of light precipitation on the outer edges of the system and a slight enhancement of the spatial extent of the TSR (Fig. 4.30). Along-line averaged vertical cross-sections through the center of the system at F09 show a slightly more intense mid-level mesolow, and similar surface cold pool intensity relative to CTRL (Fig. 4.31). The descent of the RIJ is also similar between the simulations, although small differences can be noted toward the rear of the TSR, where slight downward motion is apparent in CTRL

but not in NSUB (Fig. 4.32). Buoyancy differences are evident throughout the TSR and especially toward the back edge of the system, as the enhanced buoyancy in NSUB reflects the lack of sublimational cooling there (Fig. 4.33). As in NMLT, downward vertical motion is more uniform throughout the TSR in CTRL relative to NSUB, with enhanced areas of descent found in NSUB toward the fore of the system (Fig. 4.34). These slightly more intense downdrafts appear to be associated with enhanced maxima of graupel aloft resulting from the prescribed lack of sublimation of all ice species (Fig. 4.35).

CFADs over the TSR and RIJ maxima show a decrease in downward motion in NSUB overall, with an accentuated decrease evident below the melting level (Fig. 4.36). Other changes in NSUB include markedly decreased cooling aloft (Fig. 4.37), and similar horizontal wind speeds (Fig. 4.38). Momentum flux values are also slightly decreased toward the rear of the TSR, where most of the descent decreases would be expected due to the removal of sublimative cooling (Fig. 4.39).

4.4 MCS speed comparisons

4.4.1 Groundspeed comparisons

The groundspeed of each simulated MCS is shown in Fig. 4.40. While the CTRL simulation reaches the highest speed of any of the runs at F09 and shows a larger total acceleration, it is not consistently faster across the entire simulation period. DRYM undergoes a total acceleration of 8 ms^{-1} from F05 – F11, compared to the acceleration of 15 ms^{-1} seen in CTRL from F05 – F09. REVP is consistently the slowest system, only accelerating from 12 ms^{-1} to 17 ms^{-1} by the end of the run. NMLT and NSUB maintain ground speeds within $1 - 2 \text{ ms}^{-1}$ of one another, and NMLT tends to lag CTRL by $1 - 3 \text{ ms}^{-1}$ on average, particularly before F10. The overall sign of these speed differences (i.e., an increase or decrease) are as expected, and as are generally stated in the hypotheses.

That more systematic and marked speed differences are not found between the simulations is somewhat surprising within the context of other studies such as Fovell and Ogura (1988), Braun and Houze (1995), Yang and Houze (1995), and Brizuela and

Nicolini (2008). However, as most past studies have employed idealized models or focused exclusively on the role of various microphysical process with respect to a certain feature (e.g., rear inflow, TSR extent, heating profiles, etc) it is possible that MCS motion and/or CMT simply does not vary as strongly as perhaps expected to these changes in this particular environment or simulation setup. One can envisage certain environments however, where each of these processes would potentially have a more pronounced effect (e.g., drier RIJ levels, enhanced environmental low-level jet, higher CAPE, etc.); these possibilities are discussed further in Chapter 6 and Appendix B. The implications of the quasi-idealized model framework as well as a cursory look at the impact of changing background kinematic conditions as opposed to microphysical processes are the topics of Appendix A and B.

While consistent trends in groundspeed differences are not as apparent as initially hypothesized between all of the runs, the differences that are apparent remain worthwhile to explore within the framework of CMT and cold pool properties.

4.4.2 Theoretical cold pool speed comparison

In Chapter 3, the theoretical cold pool speed is calculated to account for both the buoyancy perturbation in the cold pool itself, in addition to the effects of hydrometeor loading and the mid- to upper-level buoyancy anomalies introduced by heating aloft. This expression is distinguished here as c_{full} :

$$c_{full} = \left[-2g \int_0^H \left(\frac{\theta'}{\theta_0} \right)_{coldpool} + \int_H^{Z_T} \left(\frac{\theta'}{\theta_0} \right)_{warmcloud} - \int_0^{Z_T} q_h dz \right]^{1/2} \quad (4.1)$$

The theoretical cold pool speeds for each sensitivity experiment are calculated according to (4.1) in the same way described in Chapter 3, and the results are shown in Fig. 4.41b. The calculated theoretical cold pool speeds for CTRL and DRYM are relatively similar to

one another, and relative agreement between the theoretical speed and the observed⁴ speed increases after ~F08, although as in Chapter 3, the observed speed remains generally underestimated by c_{full} . That c_{full} for DRYM is greater than c_{full} for CTRL is largely attributable to the lessened intensity of DRYM and thus weaker warm anomaly aloft. c_{full} calculated for REVP is too slow at early stages (0 ms⁻¹ from F05 – F08 due to the lack of surface cold pool) and too fast at later times. c_{full} values for NMLT and NSUB are too high during the developing stage of each system; this is attributable to increased hydrometeor loading aloft resulting from unmelted and unsublimated frozen hydrometeors (e.g., Figs. 4.25, 4.35). After ~F08, c_{full} values come into better agreement with (but still underestimate) observed system motion.

Though (4.1) is generally considered to be an improvement over more basic formulations of theoretical cold pool speed employing only cold pool buoyancy perturbations, its completeness does introduce some complication when trying to isolate changes due only to changes in the cold pool itself. Therefore, the simplified expression used by most early studies of cold pool propagation is also examined here:

$$c_{buoy_only} = \left[-2g \int_0^H \left(\frac{\theta'}{\theta_0} \right)_{coldpool} \right]^{1/2} \quad (4.2)$$

While this equation has been shown by many studies to be incomplete and prone to overestimating cold pool speed by more than 25% (e.g., Nicholls et al. 1988; Bryan and Rotunno 2008), here it is used to determine periods of cold pool buoyancy-induced acceleration and deceleration, somewhat regardless of the specific numerical value. c_{buoy_only} tends to overestimate observed MCS motion by ~5 ms⁻¹ for all of the simulations (c.f. Figs. 4.41a,c), but illustrates where changes in cold pool depth or intensity alone may explain changes in observed MCS motion. Despite the consistent overestimate of MCS speed by c_{buoy_only} , there are marked periods of correlation between c_{buoy_only} and

⁴ While the MCSs analyzed herein are clearly never actually observed in nature, the use of the term “observed speed” refers to the MCS groundspeed as calculated and discussed in section 4.4.1.

observed MCS motion, particularly after ~F09 for each simulation. This suggests that as the MCS matures and the surface cold pool becomes fully established, the theoretical calculations appear to better explain MCS motion relative to earlier stages of development. However, some intervals disagree significantly in value and correlate poorly as well. Two instances of such disparity are evident in the DRYM simulation, during the F05 – F07 and F10 – F11 periods. During the F05 – F07 interval, both formulations of c indicated a marked *deceleration* of the theoretical cold pool speed from F05 – F06 (c_{full} decreases by 3 ms^{-1} and c_{buoy_only} decreases by 2 ms^{-1} over this interval), while the observed MCS speed actually *accelerates* by 1 ms^{-1} . Likewise, from F10 – F11 c_{full} decreases by 4 ms^{-1} and c_{buoy_only} decreases by 1 ms^{-1} while the MCS accelerates slightly. While relatively subtle, the disparities in both value and sign of acceleration suggest that compensating processes exist to account for the disagreement between theoretical values of c and the observed system speeds. Thus, as in Chapter 3, the possibility that CMT may be one such process is systematically addressed by focusing on the DRYM simulation and computing and comparing momentum budgets for both the CTRL and DRYM simulations.

4.4.3 CTRL vs. DRYM momentum budget comparison

Following the methodology detailed in Chapter 2, momentum budgets are calculated for the CTRL and DRYM simulations. As in Chapter 3, the x-components of the main budget terms are averaged within two volumes that move generally eastward. The volumes, $VOL_{leading}$ and $VOL_{trailing}$, are defined as before for CTRL, and altered for DRYM to account for the smaller horizontal extent of the convective and stratiform regions. To be consistent with the processes examined in each respective part of the storm in CTRL, the east-west width of each volume is halved in DRYM; an example of where the volumes are defined relative to other fields in one vertical cross-section are shown in Fig. 4.42.

Examination of the evolution of the main budget terms from F05 – F07 in each simulations' respective volumes shows that CTRL varies little from the budget analyzed

for the simulation in Chapter 3; overall, $V Au'$ and PGA still dominate forcing in $VOL_{leading}$ and $VOL_{trailing}$, respectively (Fig. 4.43a,b). While DRYM is initially a slightly weaker and smaller system and thus immediately shows some overall decreases in budget term magnitude owing to that, several dynamical differences are still evident in the comparison of its budget terms.

In DRYM, $V A\bar{u}$ in $VOL_{leading}$ is initially slightly positive, indicating a possible eastward contribution from the downward transport of ambient wind in the leading portion of the line (Fig. 4.43c). More notably, $V Au'$ is initially quite small ($0 - 5 \text{ ms}^{-1}\text{h}^{-1}$), but increases quickly from F06 – F11, becoming even larger than the term in the generally more intense CTRL simulation. Relative to the other terms, $V Au'$ is proportionally of larger magnitude in the DRYM simulation. $VOL_{trailing}$ shows a steady increase in the contribution from PGA as the midlevel mesolow deepens with time (Fig. 4.43d). $V A\bar{u}$ is generally larger than observed in the trailing volume in CTRL; this is consistent with the enhanced downward motion found throughout the TSR in DRYM (e.g., Figs. 4.11, 4.12). Vertical cross-sections taken at F09 compare the CMT terms ($V Au'$ and $V A\bar{u}$) in CTRL and DRYM; while there is considerable temporal and spatial variation in the simulated systems (and thus the rationale for the above volume-averaging approach), it is helpful to compare the general organization and distribution of $V Au'$ and $V A\bar{u}$ between the simulations (Fig. 4.44). While the area of large positive $V Au'$ ahead of the line indicates the upward transport of smaller windspeeds, both $V Au'$ and $V A\bar{u}$ exceed $10 \text{ ms}^{-1}\text{h}^{-1}$ at the leading edge of the cold pool and in the main region of RIJ descent.

Focusing on F05 and F09 (periods of both CTRL and DRYM acceleration) further highlights the differences revealed by the momentum budgets. At F05, $VOL_{leading}$ in CTRL shows eastward acceleration by PGA , $V Au'$, and $V A\bar{u}$ while DRYM shows smaller magnitudes in each term in the leading volume, but also larger contributions from $V A\bar{u}$ and PGA in $VOL_{trailing}$ (Fig. 4.45). While the differences are likely somewhat affected by the horizontal boundary definitions of the volumes, it is possible that the combined enhanced CMT terms across both volumes partially explain the faster ground speed of DRYM relative to CTRL during this period. By F09, the magnitude of $V Au'$ in $VOL_{leading}$

is similar between the runs, and PGA also remains positive in DRYM, likely due to the weakened midlevel mesohigh and related enhanced surface mesohigh found in DRYM (Figs. 4.46, 4.5). This is also evidenced in $VOL_{trailing}$, as $VA\bar{u}$ remains stronger in DRYM due to enhanced downward motion there, but PGA remains stronger in the CTRL due to the deeper mid-level mesolow (Figs. 4.46, 4.5).

Comparing the evolution of both vertical advection terms with MCS speed (c.f., Fig. 4.43c,d, Fig. 4.4) suggests that CMT *may* be a process that helps to explain the inability for theoretical cold pool speed calculations to adequately estimate MCS motion. The first period of acceleration in DRYM from F05 – F07 occurs during periods of positive contribution from both $V Au'$ in $VOL_{leading}$ and $VA\bar{u}$ in both $VOL_{leading}$ and $VOL_{trailing}$. The second period of main DRYM acceleration occurs from F08 – F10; while CMT terms are also increasing during this period, the cold pool is also intensifying, thus determining the exact process to explain system acceleration is complex. The results of the budget indicate that while CMT in DRYM is proportionally larger compared to other DRYM terms relative to the ratio of terms in the CTRL budget, there is no obvious feedback to changes in MCS groundspeed. This analysis is further complicated by the altered storm dynamics; the smaller size and weakened heating in DRYM make direct comparison challenging.

To eliminate sensitivity of the above results to the horizontal definition of $VOL_{leading}$ and $VOL_{trailing}$, CFADs are also utilized to illustrate (i) budget averages over a larger area, (ii) both positive and negative values without risk of cancellation from averaging, and (iii) variation of budget terms with altitude. At F06, CFADs evaluated over the TSR show similar (or slightly increased) values of the CMT fields in DRYM at low levels (below 3 km) (Fig. 4.47). The DRYM CMT fields become still greater than CTRL fields at F09, which is generally consistent with the budget results shown above (Fig. 4.48).

While differences are found in the relative magnitudes of CMT between the simulations, it remains difficult to attribute changes in motion to these fields due to other dynamical differences as noted above. While the motion of the simulations analyzed here

may not reveal straightforward relationships with CMT, differences with respect to sensible weather and potential forecasting implications of these results will be further detailed in Chapters 5 and 6.

4.5 Synthesis and summary of results

Four model experiments are performed to test the sensitivity of CMT and MCS motion to a drier midlevel environment (DRYM), reduced evaporation (REVP), and the removal of melting and sublimation (NMLT and NSUB, respectively). Overall, the results are in general agreement with initial hypotheses, which were:

- (i) Drier air at mid-levels will increase evaporative cooling and downward motion, increasing MCS motion by enhancing CMT and/or increased cold pool intensity (assuming that the storm remains of comparable intensity to the CTRL run).
- (ii) The reduction or removal of cooling microphysical processes will lessen both downward motion and cooling throughout the system, thereby decreasing both CMT and theoretical cold pool speed and retard system motion.

With respect to (i), results reveal that the simulated MCS produced in DRYM is different enough in intensity and direction of motion that a completely direct parameter-by-parameter comparison is difficult. As has been found by previous studies, the drier air at mid-levels does decrease MCS intensity somewhat, and a smaller and more eastward-propagating system results. While CTRL produces an MCS that accelerates more over a shorter period and its speed eventually maximizes at a greater value than in DRYM, the average speed of the DRYM system is slightly faster [$\sim 18\text{ms}^{-1}$ (CTRL) vs. $\sim 19\text{ms}^{-1}$ (DRYM)]. An additional goal was to isolate the main cause for any changes in MCS speed; despite the changes in storm structure, enough similarity remains between the two simulations to explore the differences in MCS motion, c , and CMT. These comparisons show that CMT is indeed enhanced at times in DRYM, resulting mostly from enhanced downward motion (as the RIJ, mid-to-low-level horizontal winds, and cold pool intensity remain of similar, or even weaker, magnitude in DRYM). Theoretical cold pool

calculations account for the observed system speed reasonably well at later times in the simulation, but fail to do so at earlier stages. The initial period of MCS acceleration in DRYM is actually marked by a slight decrease in surface cold pool intensity and theoretical cold pool speed, and CMT during this period is shown to be a probable contributor to system motion during a period evidently not completely determined by cold pool dynamics.

The second hypothesis (ii) is also generally supported by simulation results. REVP showed the most marked decrease in MCS motion (average groundspeed 14 ms^{-1}), followed by NMLT (average groundspeed 17 ms^{-1}) and NSUB (average groundspeed 18 ms^{-1}). The changes in REVP are likely attributable to both c and CMT decreases; the near lack of a surface cold pool clearly impedes MCS development and motion, and the weakened downward motion throughout the system impedes both downdrafts themselves, as well as any horizontal momentum they would be transporting surface-ward. NMLT shows a slowing of MCS groundspeed by $\sim 1 - 2 \text{ ms}^{-1}$ overall; this is quite consistent with the degree of change found in Yang and Houze (1995) (Table 4.1). As the cold pool intensity and theoretical cold pool speeds are generally equal to or even slightly greater than those found in CTRL, it is likely that this difference in motion is likely explained by decreased downward motion and decreased CMT, particularly in the TSR. Finally, NSUB shows very little decrease in observed overall speed from CTRL, and few dynamical or structural differences overall. While the horizontal extent of the TSR is slightly greater relative to CTRL, it appears that the effects of NSUB are most pronounced in leading anvil (e.g., Fig. 4.35), and not as dynamically significant in rear of system where downward transports are most influential within the CMT framework.

Collectively, the results of the sensitivity experiments suggest that while CMT does vary and impact MCS motion in response to the alteration of microphysical processes, the overall magnitude of changes to MCS speed found here (generally just $1 - 2 \text{ ms}^{-1}$) does not indicate obvious forecast implications. Furthermore, while the DRYM simulation does address a realistic environmental condition that would be of concern in the real atmosphere, the removal or reduction of evaporation, melting, and sublimation is

ultimately unrealistic (despite the utility of such measures within a sensitivity study framework). The results from such changes illustrate that if the complete removal of melting and sublimation does not strongly change MCS motion, it is unlikely that environmental changes affecting these processes in a more subtle manner would be a primary dictator of MCS motion in reality. However, more significant changes in CMT and MCS motion in DRYM and REVP do suggest that the evaporation process may have a significant impact in this framework, and also suggests that future research be directed in this area, perhaps running a more extensive suite of simulations in variable mid-level humidity to see where in that spectrum CMT and/or changes in MCS motion maximize.

Stein and Alpert (1993) outline a method for computing the interactions among various factors influencing atmospheric circulations. The method describes how to use numerical model output to optimally obtain the pure contribution of both an individual factor, as well as the contributions due to interactions between two or more factors. Specifically, their method states that for n factors, 2^n simulations are required for the separation of the contributions and their possible interactions. By only changing one factor at a time (i.e., mid-level relative humidity, evaporation, melting, or sublimation), the experiments discussed herein do not address the suite of possibilities that may result from interaction between the individual processes. That is, a “complete” set of 2^n experiments according to Stein and Alpert (1993) is not carried out here; in order to do so, several additional experiments are necessary. With respect to the microphysical cooling experiments discussed here, $n = 3$, where the three factors are the cooling due to (i) evaporation, (ii) melting, and (iii) sublimation. Therefore, 2^n experiments would be required to completely illustrate the contribution of the factors themselves as well as their synergistic interactions: beyond the four simulations shown here [(1) CTRL, (2) REVP, (3) NMLT, (4) NSUB], those would be (5) NMLT+REVP, (6) NMLT+NSUB; (7) NSUB+REVP; and (8) NMLT+NSUB+REVP [where “NMLT+REVP” indicates that

melting would be removed *and* evaporation would be reduced in the same simulation, with the same convention for (6), (7), and (8)]⁵.

Results of the single removal experiments (REVP, NMLT, NSUB) are limited in that they only address the impact each process has in isolation, and neglect the potential impact derived from the synergy between physical processes. The non-linearity inherent to the latter is shown to be largely non-negligible in studies such as Uccellini et al. (1987). The simulations discussed herein suggest that the remaining combination experiments [i.e. (5) – (8) above] would produce larger MCS speed differences than experienced when a single process is removed, but also that the magnitude of such differences is linearly additive at a *minimum*. It is instead more likely that non-linear interactions between the processes (e.g., not melting *or* sublimating ice) would have a greater decrease in MCS speed than the decrease that would be inferred by linearly adding the MCS speed effects attributable to each independent processes (e.g., $\sim 1 + \sim .5 = 1.5\text{ms}^{-1}$ for NMLT + NSUB). This can be conceptualized by considering the suite of microphysical interactions that have been found by many studies to contribute to both RIJ formation, formation of the TSR, and RIJ descent (e.g., Smull and Houze 1987; Fovell and Ogura 1988; Weisman 1992; Klimowski 1994; Yang and Houze 1995; Yuter and Houze 1995b; Smith et al. 2009), and that are summarized in the first section of this chapter. For one specific example, consider the feedback that exists between the formation of the RIJ and the microphysical processes themselves. That is, the strength and placement of the RIJ is driven by latent heating and cooling processes due to precipitation – in the case of NSUB+NMLT+REVP, the strength and position of the RIJ itself will be altered by decreasing or eliminating the secondary area of rear-inflow and descent thereof observed by Klimowski (1994) and others (e.g., Fig. 4.1), and both the spatial orientation and intensity of the surface cold pool will likely be reduced beyond what is already found in any of the individual process simulations. This would conceivably lead to a much weaker

⁵ As DRYM tests the role of decreased midlevel relative humidity, $n = 1$, and thus the two simulations CTRL and DRYM are technically sufficient by the 2^n rule. However, additional simulations across a broader spectrum of humidity values maybe offer enhanced insight as well. The same can also be stated for the reduction of evaporation, as the degree of reduction can be varied as well.

system from (1) a weaker RIJ, (2) decreased TSR descent, (3) slower cold pool groundspeed and (4) weakened cold pool induced forcing for ascent as well – this is just one conceivable set of highly nonlinear feedbacks that are possible. While carrying out the remaining four simulations is limited by computational constraints, completing such a set of future experiments might be useful both in the idealized or quasi-idealized framework as shown here, as well as using composites of observed MCS cases in varying environments. Finally, experiments that examine the response of MCS motion to changes in the “opposite direction” of those made here may also provide valuable context for the sensitivities noted here. Several additional runs have been performed and two – one in which evaporation is *increased* and one in which mid-level relative humidity is *increased* -- are briefly summarized in Appendix C.

It is also evident from this investigation that it is difficult, if not impossible, to truly separate the contribution of “cold pool dynamics” (i.e., density current propagation) from “CMT-forced” MCS motion. The two fields are fundamentally linked by the both the rear-to-front and front-to-rear main storm-scale flow branches, and the connection between the RIJ and surface cold pool is just one way that the combination of the two contributes to MCS motion. Therefore, toward answering the main research question posed for these experiments, it appears that MCS motion is indeed impacted by microphysical and environmental humidity changes via the CMT process, but that these processes remain very much connected to cold pool dynamics. In terms of the relative contributions of each process in time, the results here do suggest that CMT may be a more important process in determining MCS groundspeed as a system develops, but that once the MCS is mature, CMT likely plays a secondary role to density current dynamics.

However, the current results still highlight several potential avenues for future work regarding MCS motion and CMT. First, the sensitivity results discussed herein are largely dependent upon model representation of the TSR, as the processes central to this region are known to have a considerable impact on both downward motion throughout an MCS, as well as the strength and location of a the RIJ. However, many studies note the under-representation of the TSR in numerically-simulated MCSs, and even with the

inclusion of sophisticated ice microphysics parameterizations, models remain challenged to successfully represent both the transition zone and TSR in MCSs (e.g., Gallus and Pfeiffer 2009; Morrison et al. 2009). Therefore, using only models to assess the influence of CMT may be misleading, particularly in light of more recent studies that illustrate the formation of significant downward motion that is initiated at the far rear of the TSR (e.g., Smith et al. 2009; Grim et al. 2009b). The use of high-resolution observational data in combination with numerical simulations of observed cases would thus be useful to examine these processes in systems that may not be well-resolved using current numerical models.

Weisman (1992) addresses the processes that determine the descent of the RIJ, concluding that the combined roles of CAPE and shear balance, vorticity generation via horizontal buoyancy gradients, environmental humidity, and the complexity of the role of ice microphysics are difficult to address in observed MCSs. In fact, he notes that the “results [of his idealized simulations] emphasize how complex these feedbacks may be.” As RIJ descent is central to the conceptual model of CMT presented here, continued work in this area is essential as well. This problem is also one at the forefront of convective surface wind forecasting, discussed in the following chapter.

Finally, as mentioned in the first section of this chapter, MCS groundspeed may show considerably more sensitivity to alteration of background kinematics (i.e., changing background wind speeds and shear profiles) relative to that illustrated by these particular experiments. However, it can be argued that considerable research has already been done in the area of vertical shear and MCS dynamics (e.g., Newton and Fankhauser 1964, Rotunno et al. 1988; Weisman 1992; Corfidi et al. 1996; Orf and Anderson 1999; Coniglio et al. 2006), and that greater uncertainty exists in our understanding of microphysical feedbacks and sensitivities (e.g., Gallus and Pfeifer 2008; Morrison et al. 2009; Jankov et al. 2009). It is most likely that conclusions reached at the intersection of results of the nature summarized here and those found by previous studies focused on kinematics will offer the most value toward answering remaining fundamental yet unresolved questions regarding the processes that ultimately determines MCS motion.

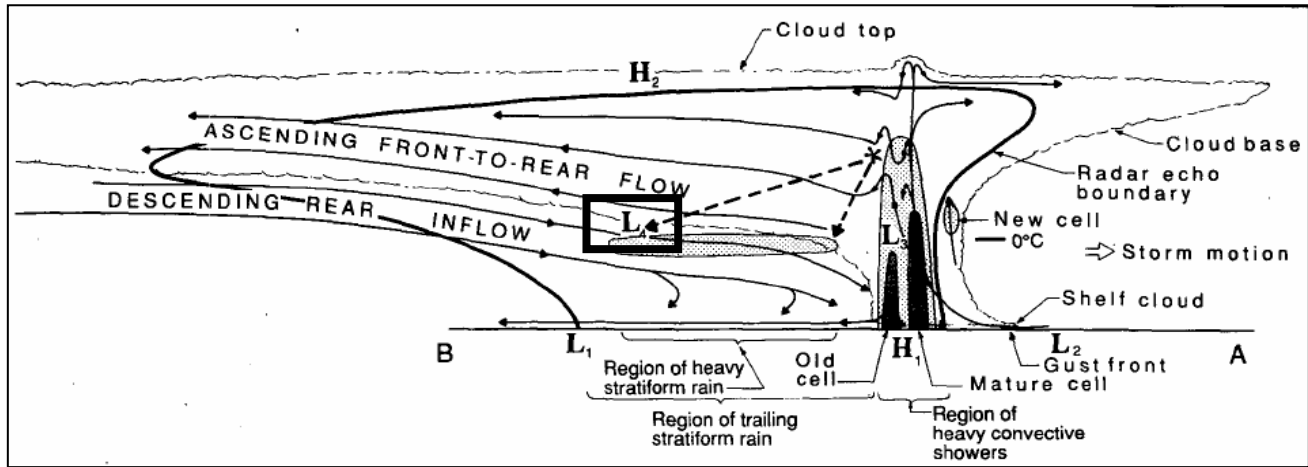


Figure 4.1: Conceptual model of a squall line with trailing stratiform region, from Houze et al. (1989). “L” (“H”) denotes areas of low (high) pressure; arrows shows major flow branches and circulations. Box indicates “secondary” low pressure area described in text.

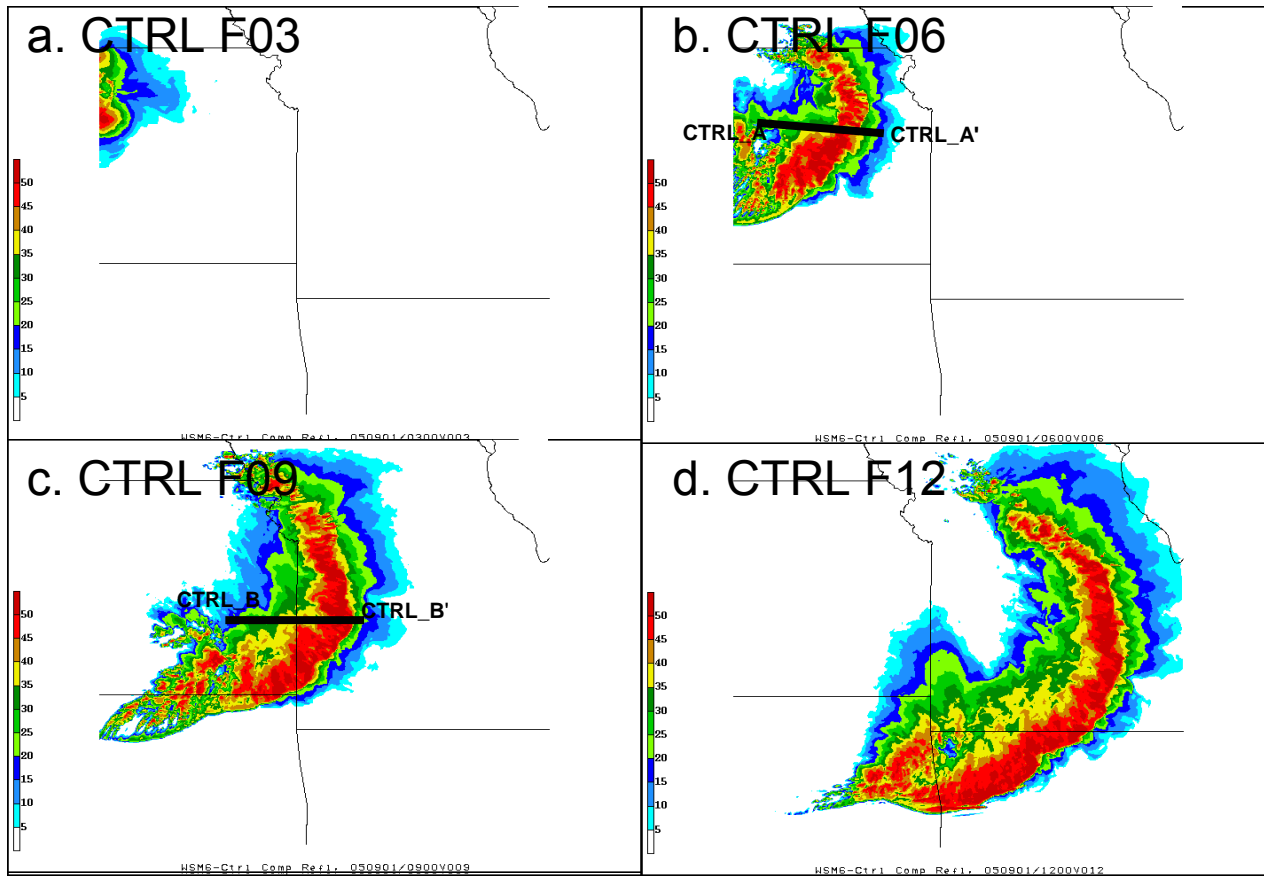


Figure 4.2: Simulated composite reflectivity (dBZ, shaded as indicated at right) and cold pool outline ($T' = -2^{\circ}\text{C}$ at 0 m (black, solid)), for CTRL run at (a) F03, (b) F06, (c) F09, and (d) F12. Lines CTRL_A-CTRL_A' and CTRL_B-CTRL_B' in (b) and (c) depict cross-sections shown in subsequent figures.

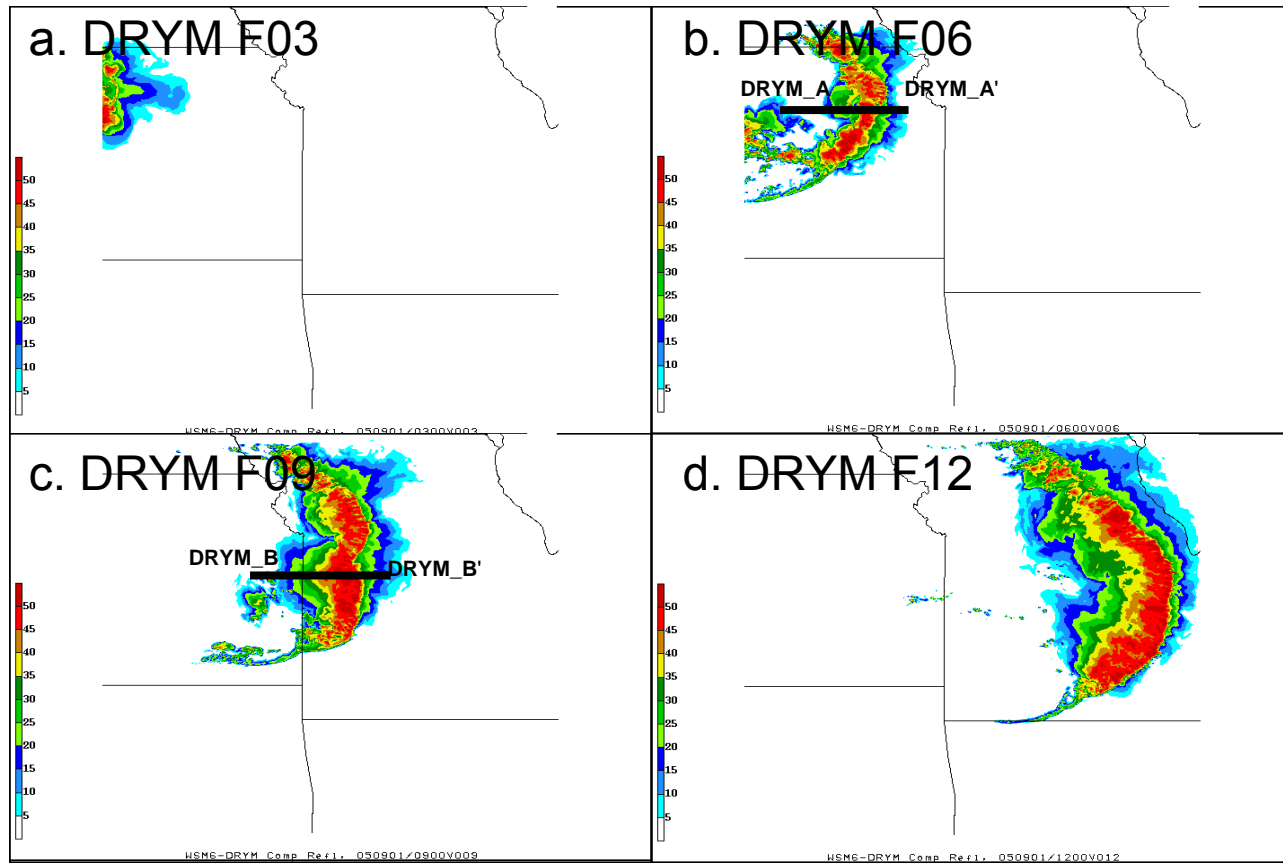


Figure 4.3: Simulated composite reflectivity (dBZ, shaded as indicated at right) and cold pool outline ($T' = -2^{\circ}\text{C}$ at 0 m (black, solid)), for DRYM run at (a) F03, (b) F06, (c) F09, and (d) F12. Lines DRYM_A-DRYM_A' and DRYM_B-DRYM_B' in (b) and (c) depict cross-sections shown in subsequent figures.

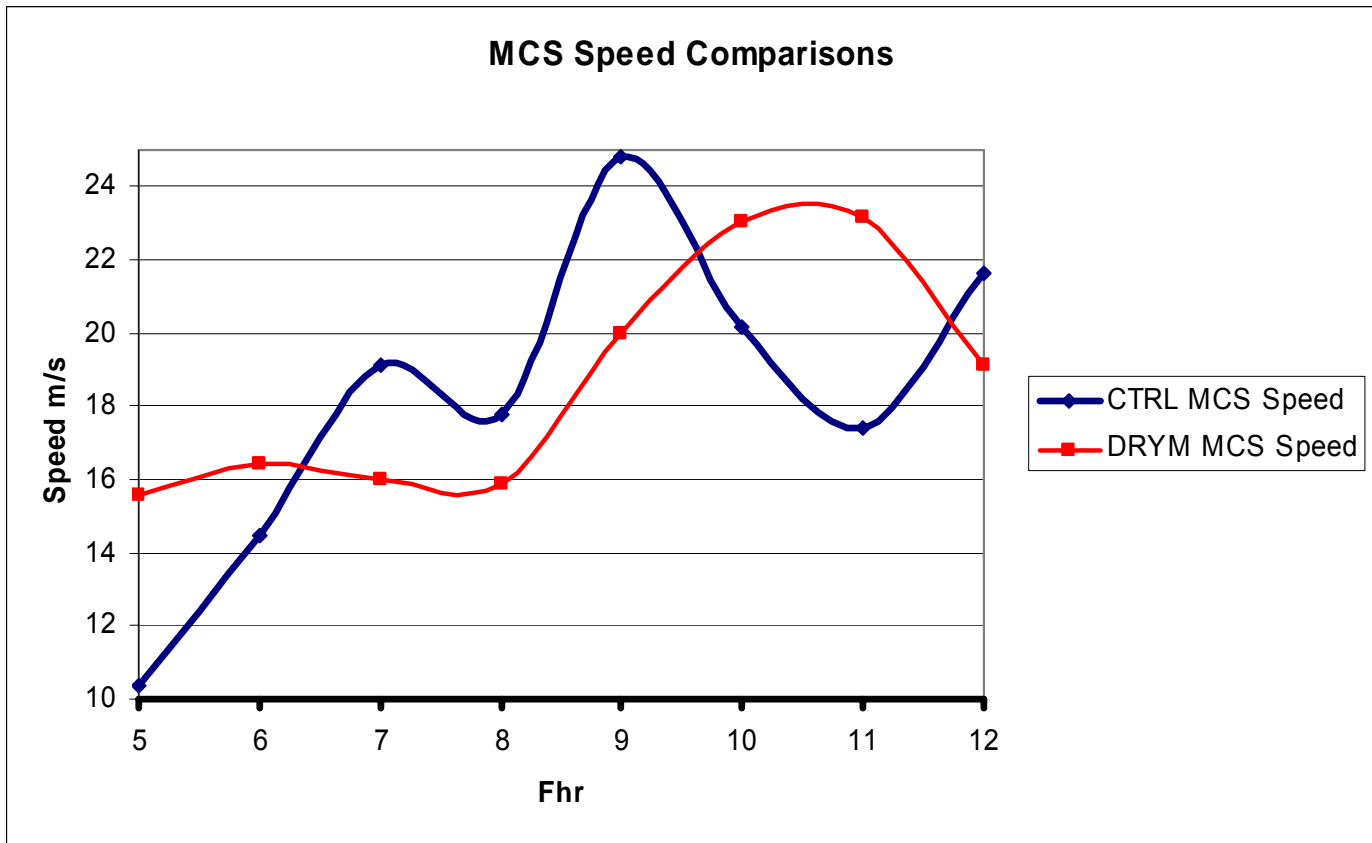


Figure 4.4: Groundspeed of MCS (ms^{-1}) for CTRL simulation (blue) and DRYM simulation (red).

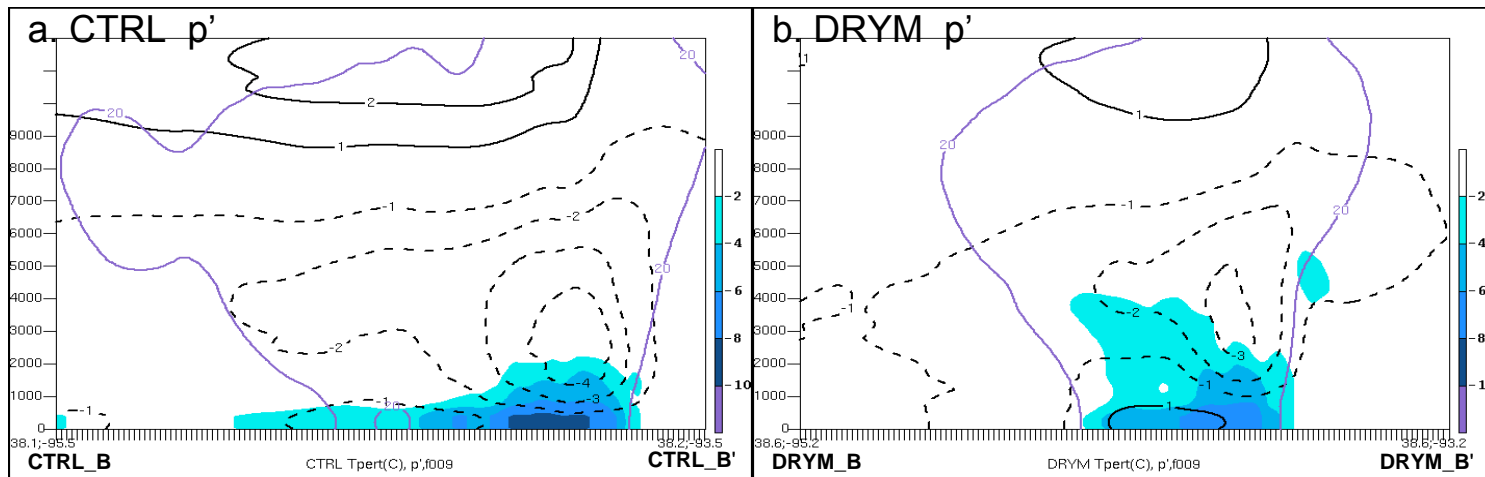


Figure 4.5: (a) East-west along-line averaged (in 40-km segments) cross-section along line CTRL_B-CTRL_B' as in Fig. 4.2c at F09. Cold pool (shaded as shown beginning at $T' = -2^{\circ}\text{C}$), solid (dashed) contours represent negative (positive) pressure perturbation in hPa magnitude of total perturbation wind $((u'^2 + v'^2)^{1/2}, \text{ms}^{-1})$, and simulated reflectivity (dBZ, purple contour, 20 dBZ); (b) as in (a) except for DRYM simulation taken along DRYM_B-DRYM_B' as in Fig. 4.3c. Distance of cross-sections 175-km.

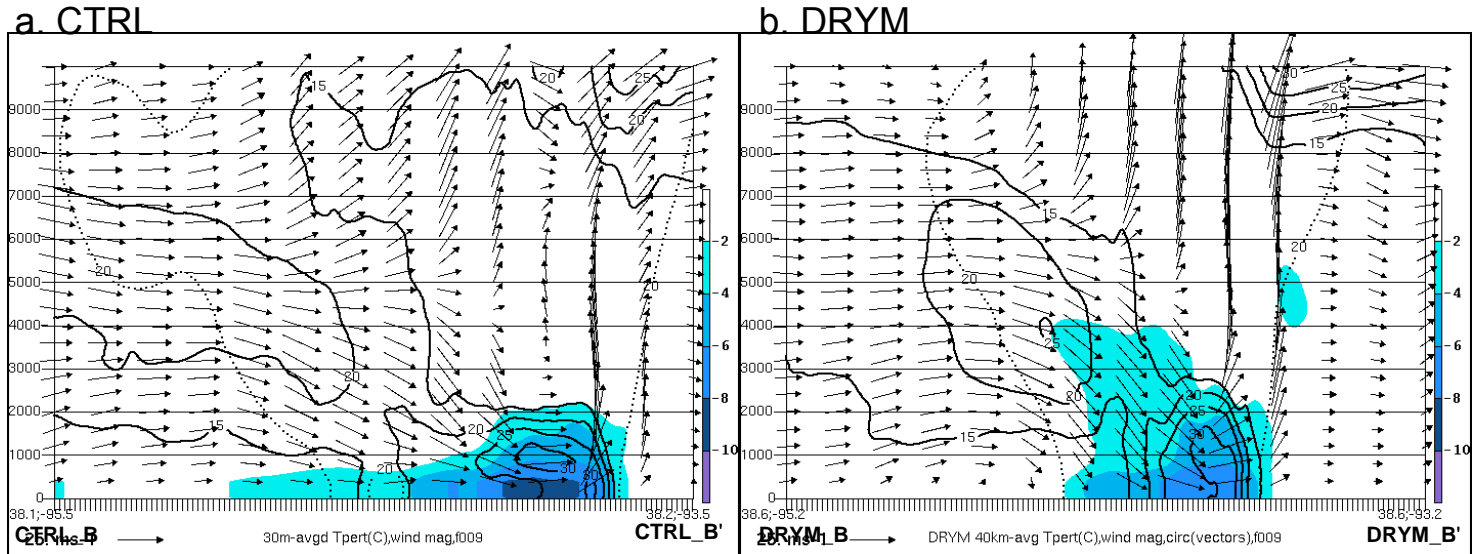


Figure 4.6: East-west cross-section along-line averaged (in 40-km segments) along line CTRL_B-CTRL_B' as in Fig. 4.2c at F09. (a) Cold pool (shaded as shown beginning at $T' = -2^{\circ}\text{C}$), magnitude of total perturbation wind ($(u'^2 + v'^2)^{1/2}$, ms^{-1}) and simulated reflectivity (dBZ, dotted contour, 20 dBZ). Black arrows show ground-relative perturbation flow in the x-z plane scaled as shown by reference vector in lower left corner; (b) as in (a) except for DRYM simulation taken along DRYM_B-DRYM_B' as in Fig. 4.3c.

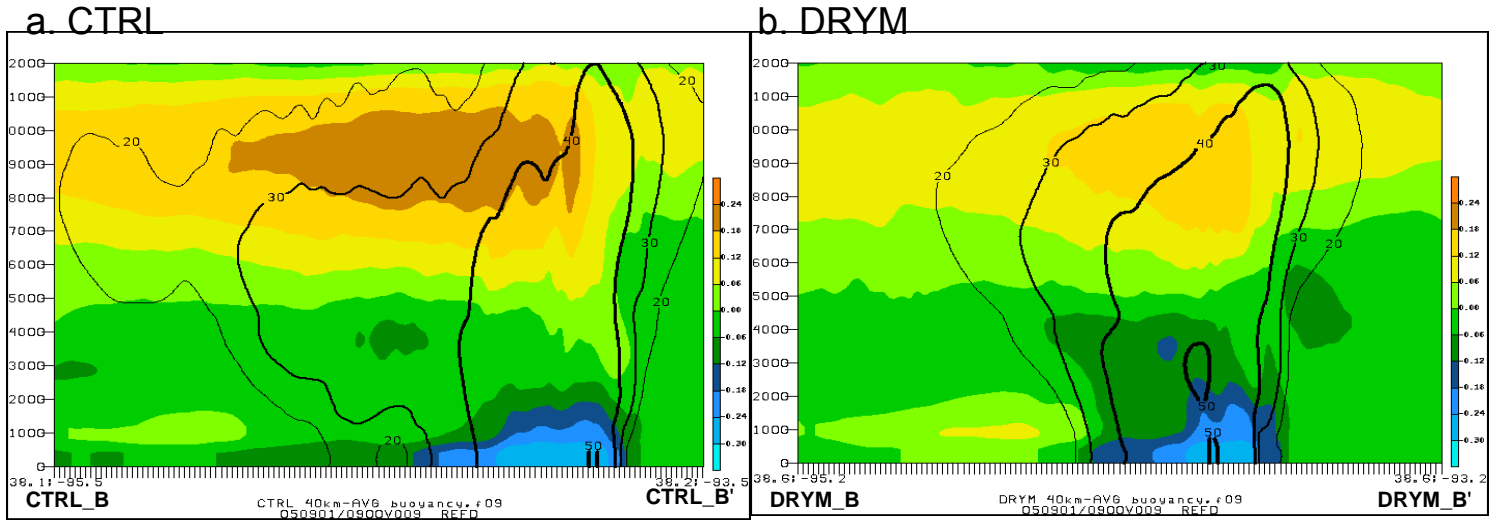


Figure 4.7: Cross-sections as in Fig. 4.6 except showing (a) buoyancy (ms^{-2} , shaded as shown) and simulated reflectivity (dBZ, black contours, every 10 dBZ starting at 20 dBZ); (b) as in (a) except for DRYM simulation. Values shaded in light green and cooler colors $< 0 \text{ ms}^{-2}$. Buoyancy calculated according to: $B = \theta_v' / \bar{\theta}_v - q_h$

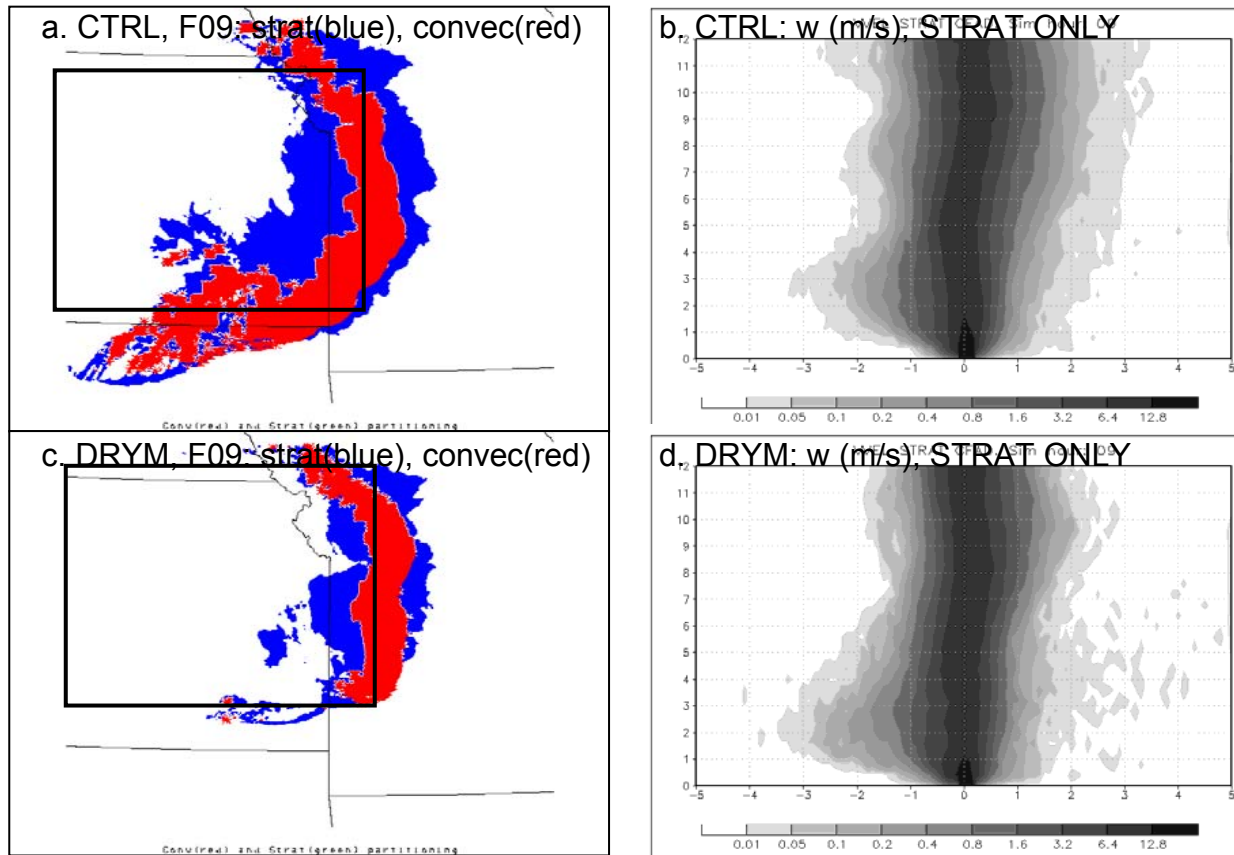


Figure 4.8: a) CTRL at F09: convective gridpoints (blue) and stratiform gridpoints (red) according to criteria described in text. Box denotes boundaries of areas in which stratiform gridcells are averaged within in images at right. (b); b) CFAD of CTRL vertical velocity w , at F09 for boxed blue stratiform area in (a). Bin size is 0.1 ms^{-1} and plot is contoured as indicated by shading and key at bottom; c) as in a) except for DRYM simulation; d) as in d) except for DRYM simulation.

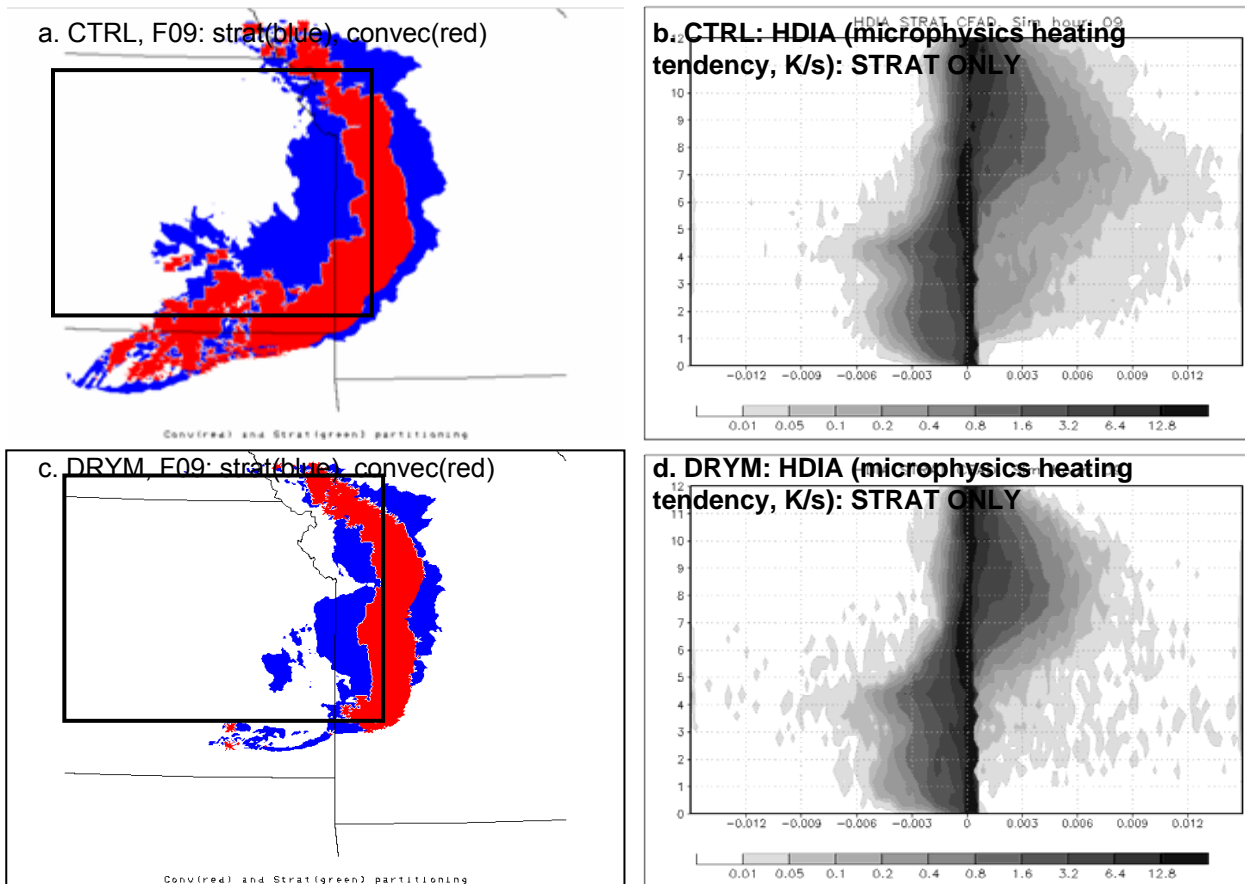
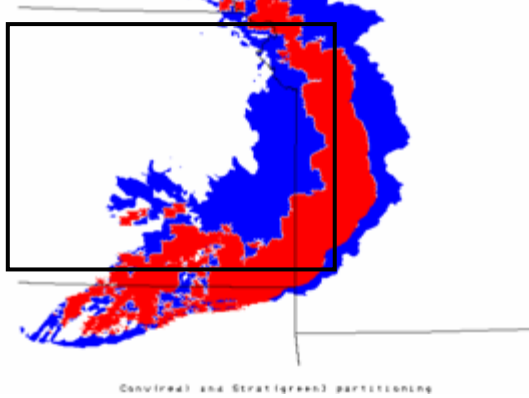
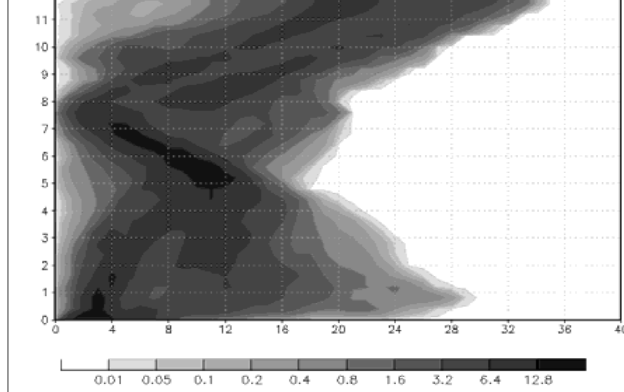


Figure 4.9: As in Fig. 4.8 except b) and d) display microphysical scheme heating tendency (K s^{-1}) with bin size $.00025 \text{ K s}^{-1}$.

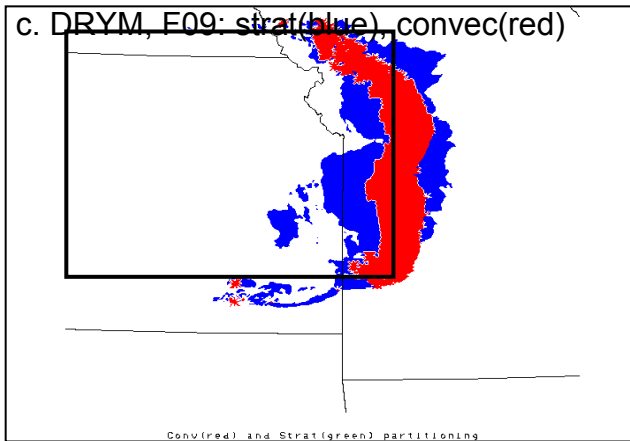
a. CTRL, F09: strat(blue), convec(red)



b. CTRL: $|u'+v'|$ (STRAT ONLY)



c. DRYM, F09: strat(blue), convec(red)



d. DRYM: $|u'+v'|$ (STRAT ONLY)

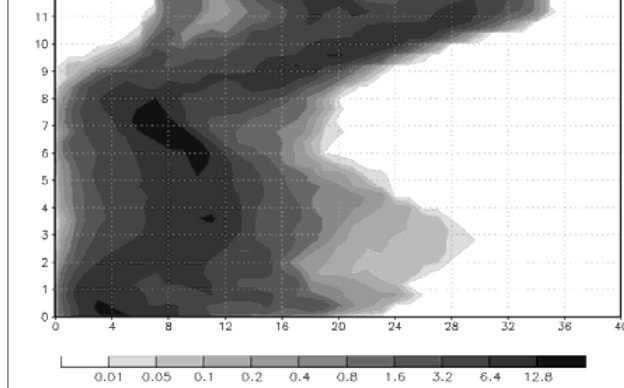
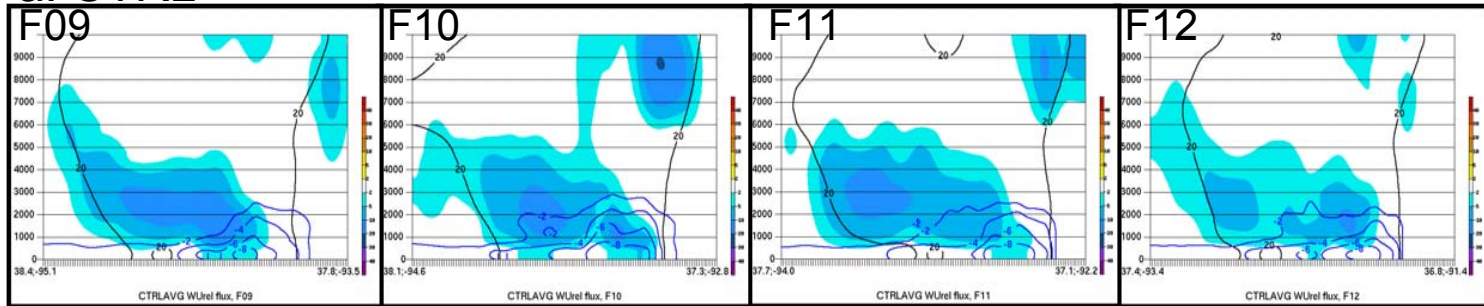


Figure 4.10: As in Fig. 4.8 except b) and d) display the magnitude of the perturbation wind speed $((u'^2 + v'^2)^{1/2}$, ms^{-1}), bin size 1 ms^{-1} .

a. CTRL



b. DRYM

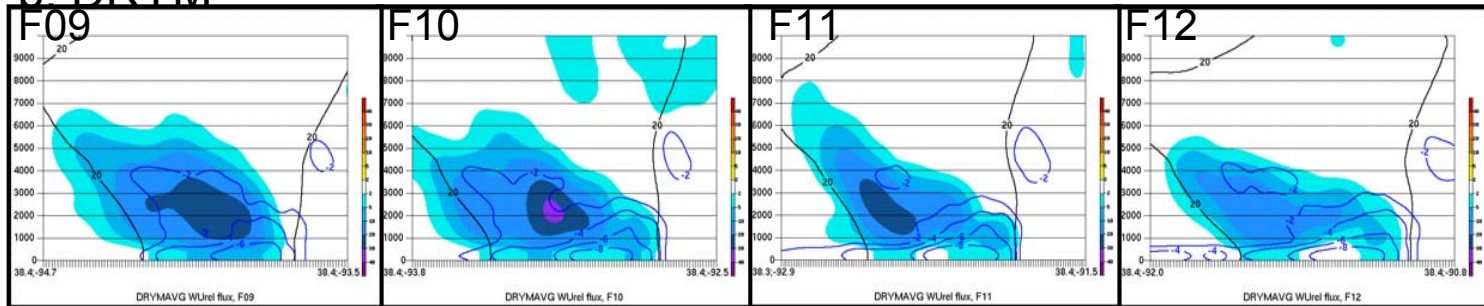
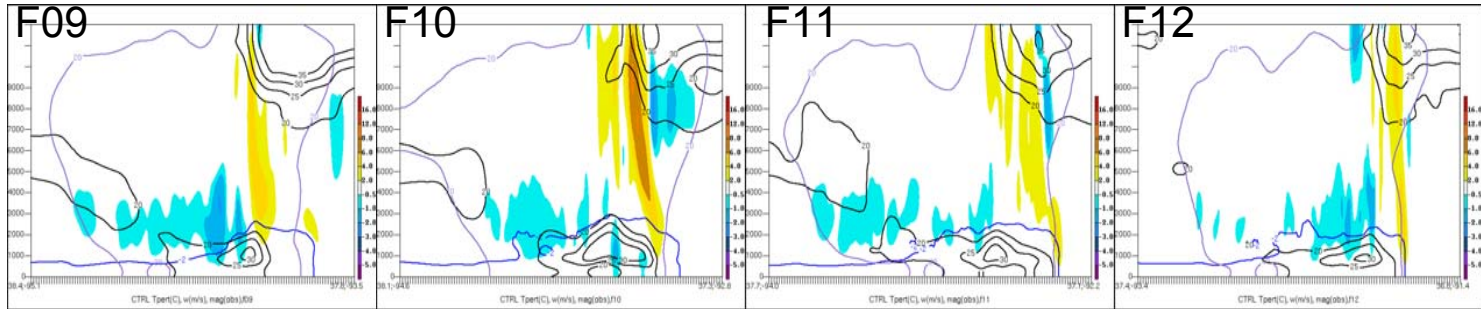


Figure 4.11: Row a) CTRL along-line averaged (in 40-km segments) vertical cross-sections through leading edge at most bowing segment showing cold pool (T' , blue contours, -2°C intervals starting at -4°C), and downward momentum flux (m^2s^{-2} , shaded as in legend at right) and simulated radar reflectivity (black contours, 10dBZ intervals starting at 20dBZ) from F09 – F12 as labeled; row b) as in a) except for DRYM.

a. CTRL



b. DRYM

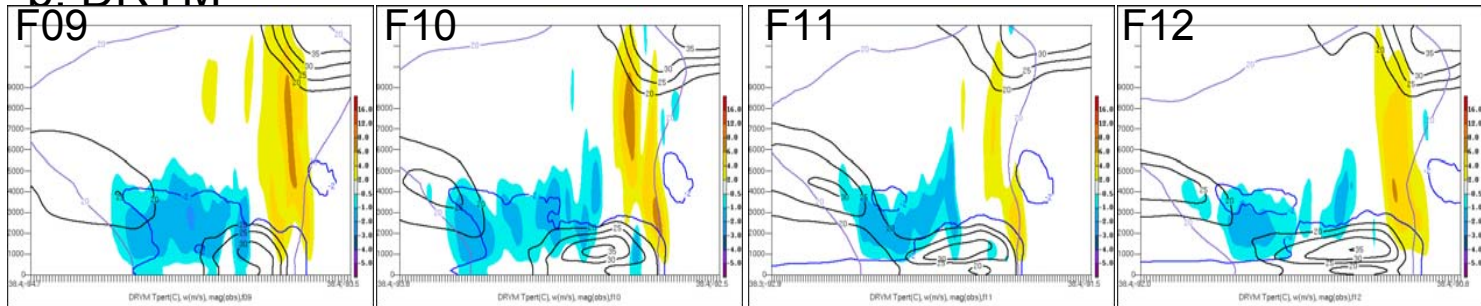


Figure 4.12: As in Fig. 4.11 except vertical velocity, w (ms^{-1} , shaded as indicated at right), magnitude of total wind speed $((u^2 + v^2)^{1/2}$, ms^{-1} black contours every 5ms^{-1} starting at 20ms^{-1}), and simulated reflectivity (dBZ, purple contour, 20 dBZ).

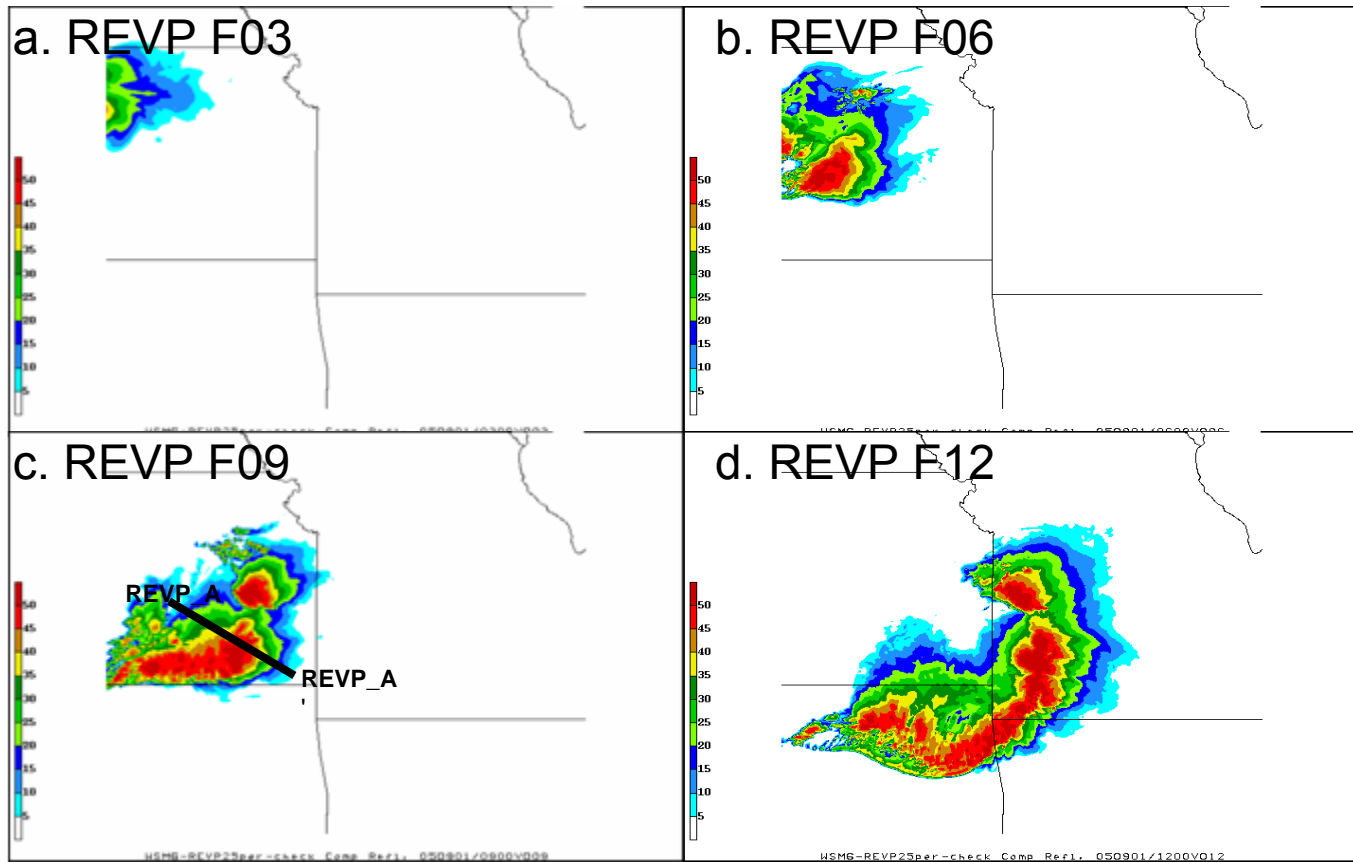


Figure 4.13: Simulated composite reflectivity (dBZ, shaded as indicated at right) and cold pool outline ($T'=-2^{\circ}\text{C}$ at 0 m (black, solid)), for REVP run at (a) F03, (b) F06, (c) F09, and (d) F12. Line REVP_A-REVP_A' in (c) depicts cross-section shown in subsequent figures.

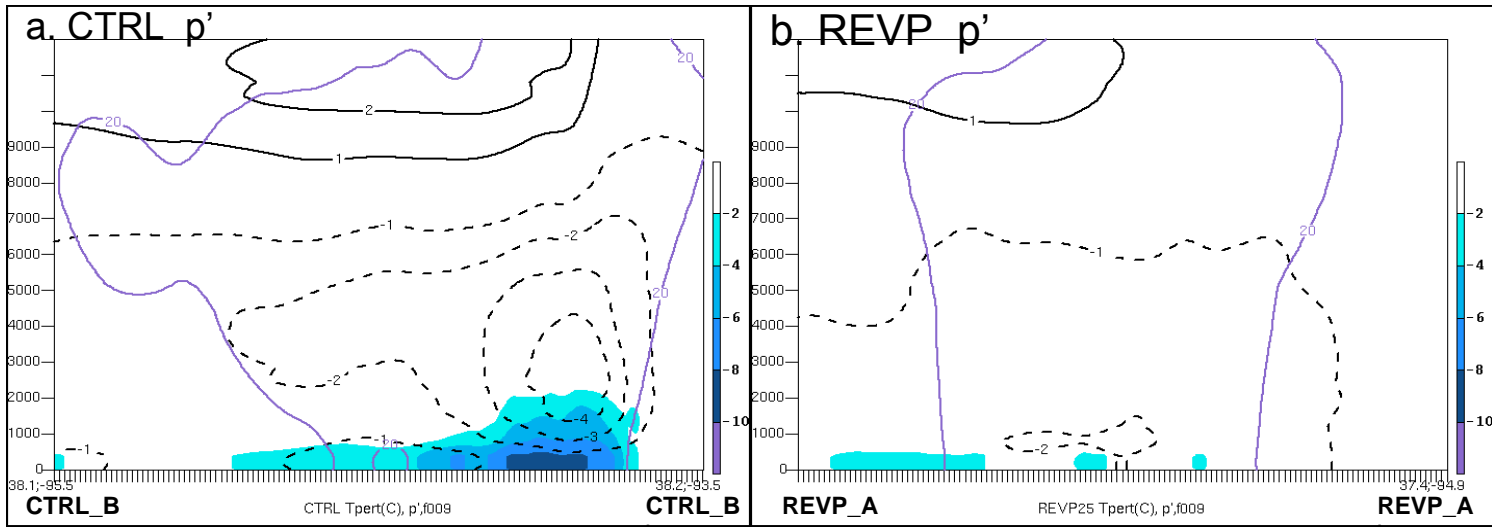


Figure 4.14: As in Fig. 4.5 except comparing CTRL and REVP simulations.

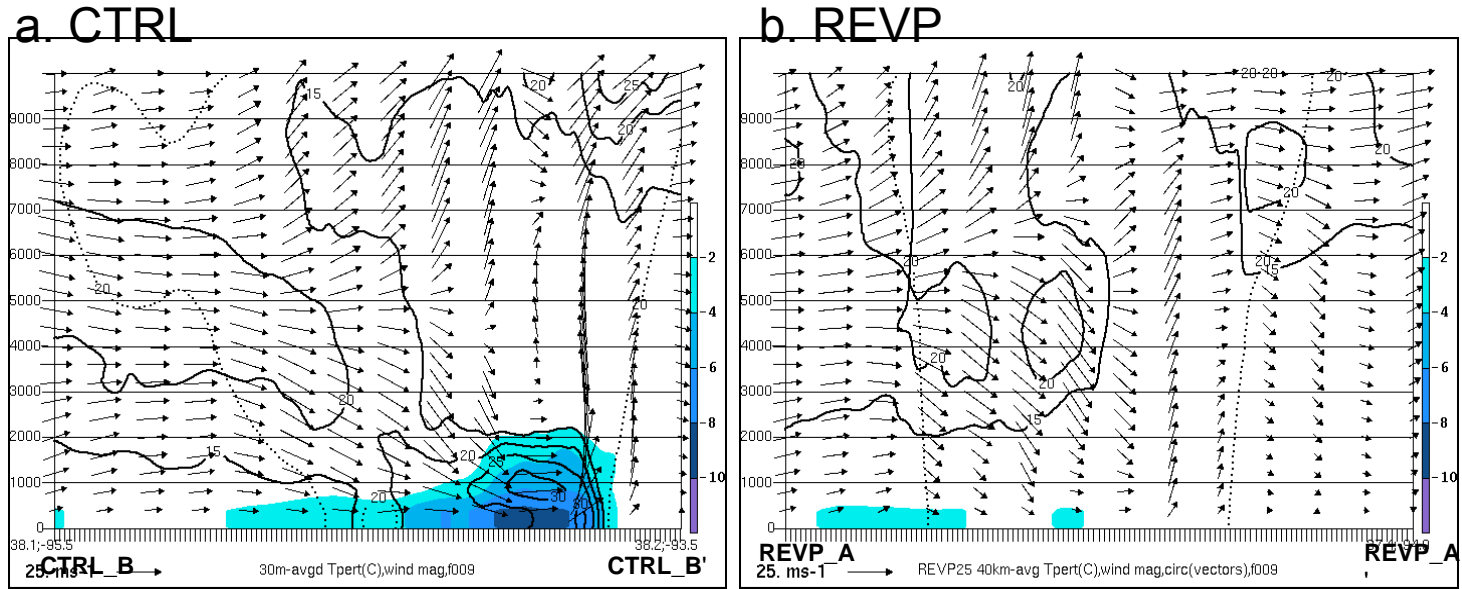


Figure 4.15: As in Fig. 4.6 except comparing CTRL and REVP simulations.

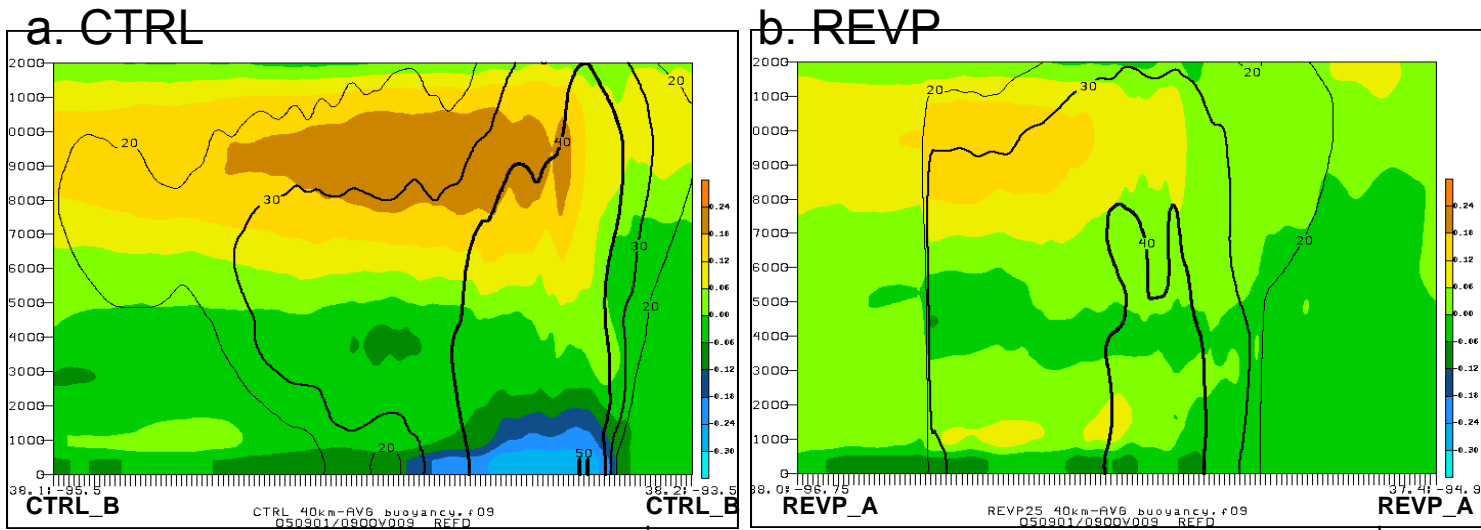


Figure 4.16: As in Fig. 4.7 except comparing CTRL and REVP simulations. (Back edge of system abrupt due to orientation of cross-section REVP_A – REVP_A' through along-line averaged data.)

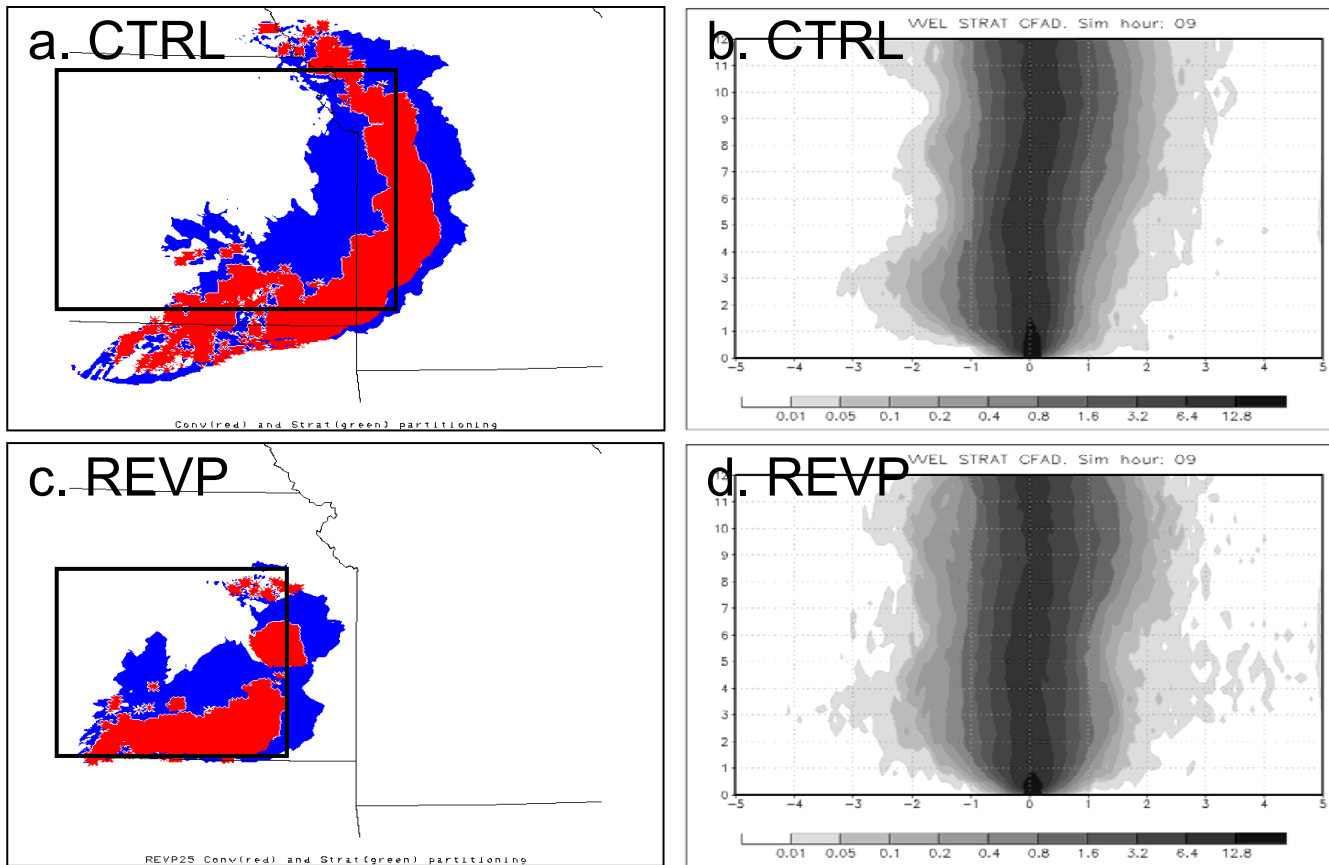


Figure 4.17: As in Fig. 4.8 except comparing CTRL and REVP simulations.

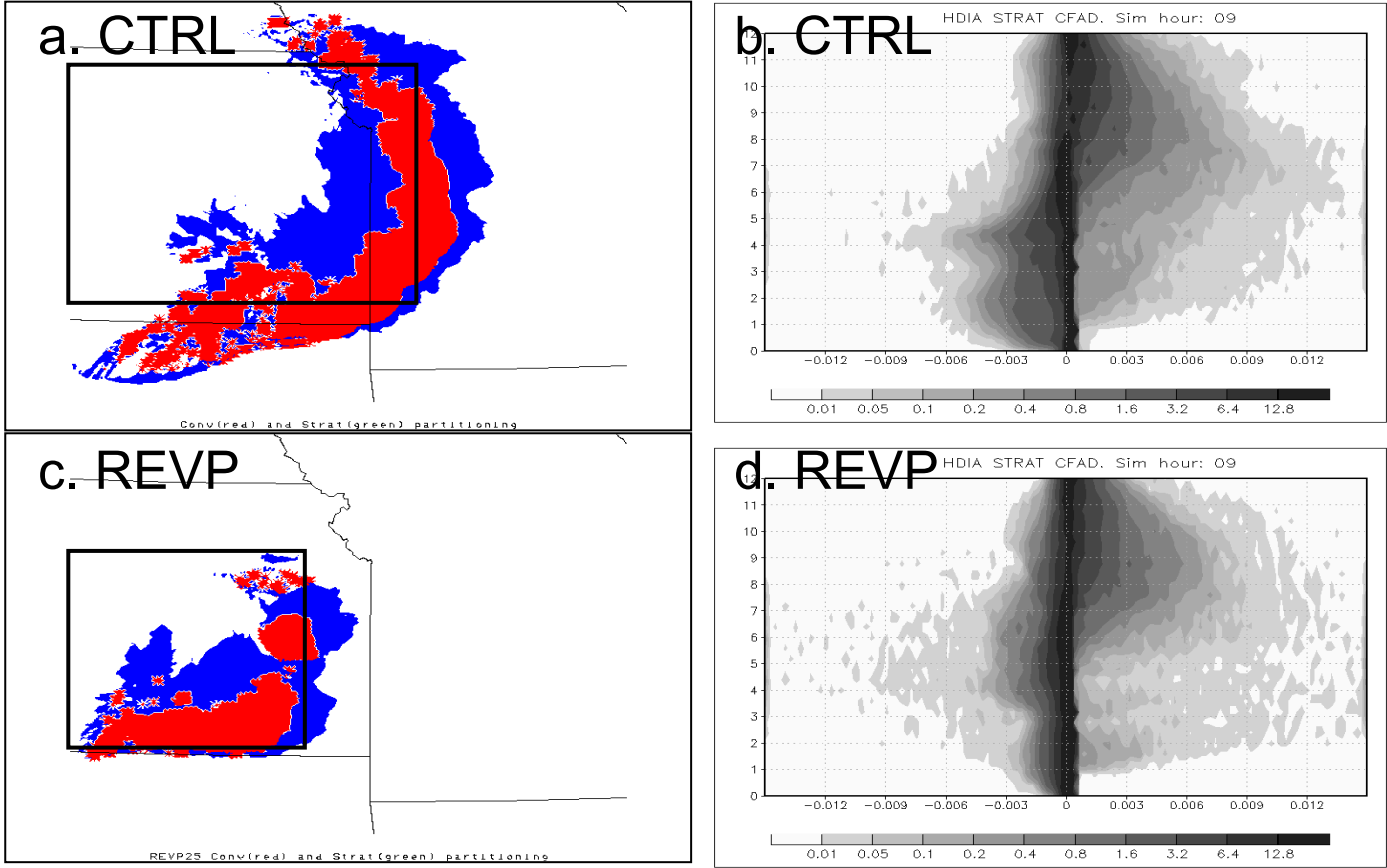


Figure 4.18: As in Fig. 4.9 except comparing CTRL and REVP simulations.

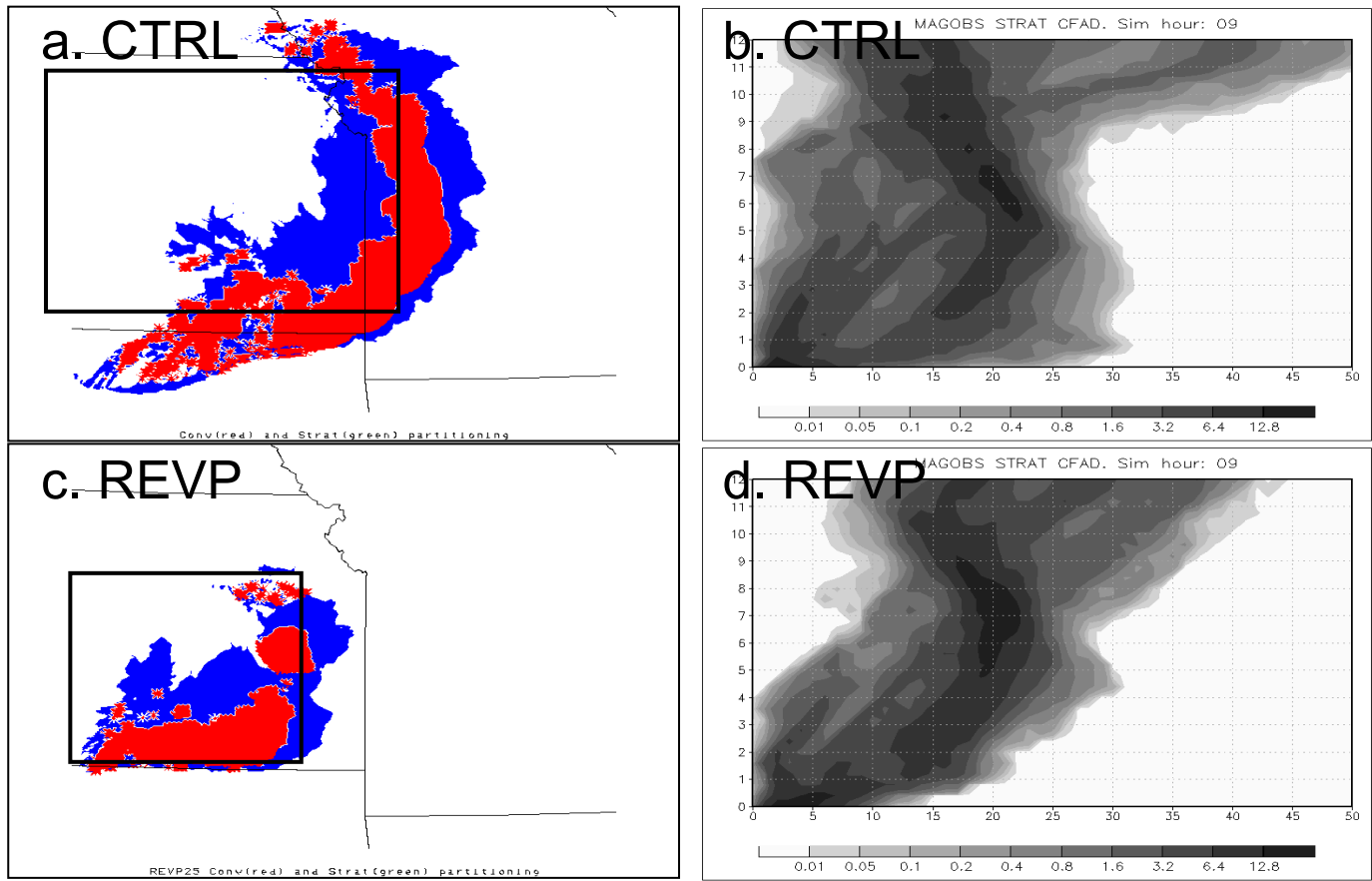


Figure 4.19: As in Fig. 4.10 except magnitude of full wind field, comparing CTRL and REVP simulations.

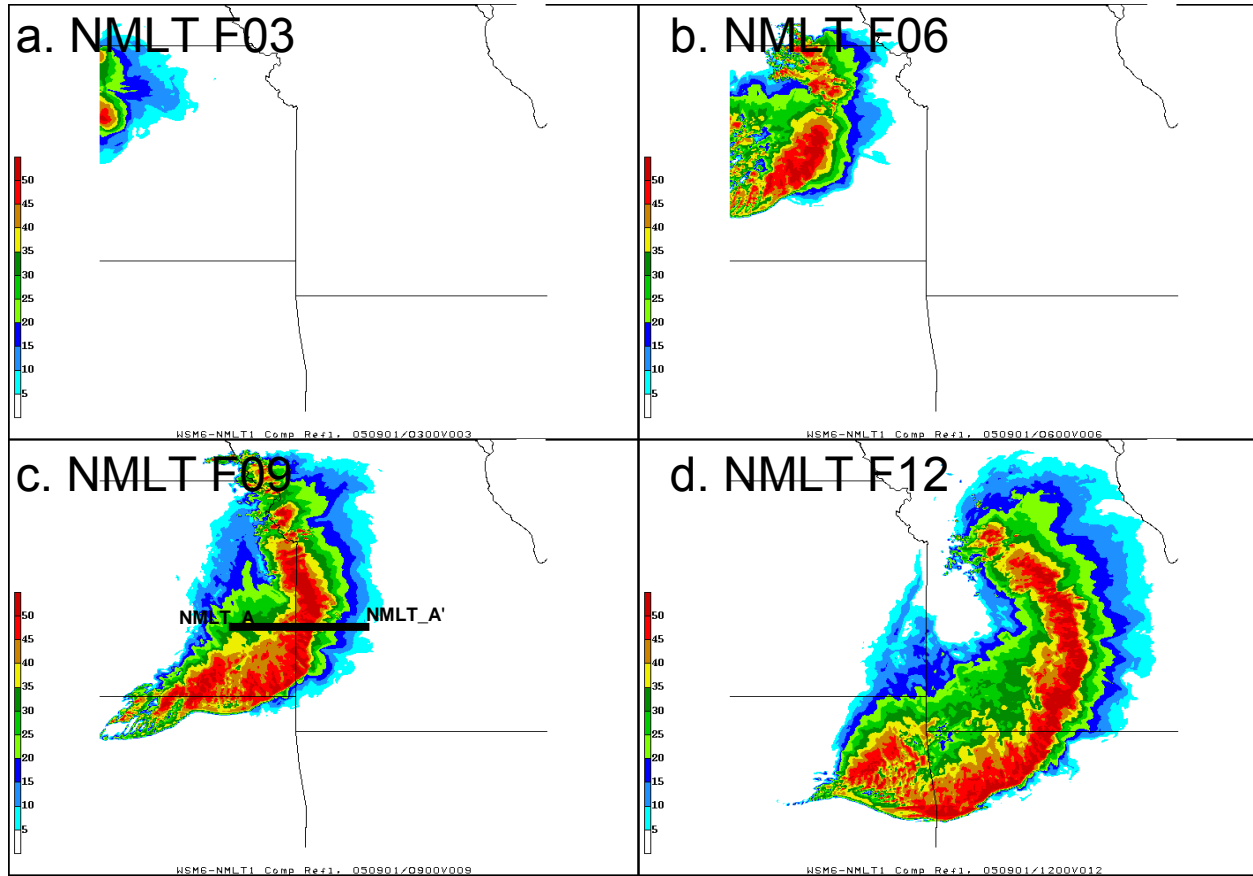


Figure 4.20: Simulated composite reflectivity (dBZ, shaded as indicated at right) and cold pool outline ($T' = -2^\circ\text{C}$ at 0 m (black, solid)), for NMLT run at (a) F03, (b) F06, (c) F09, and (d) F12. Line NMLT_A-NMLT_A' in (c) depicts cross-section shown in subsequent figures.

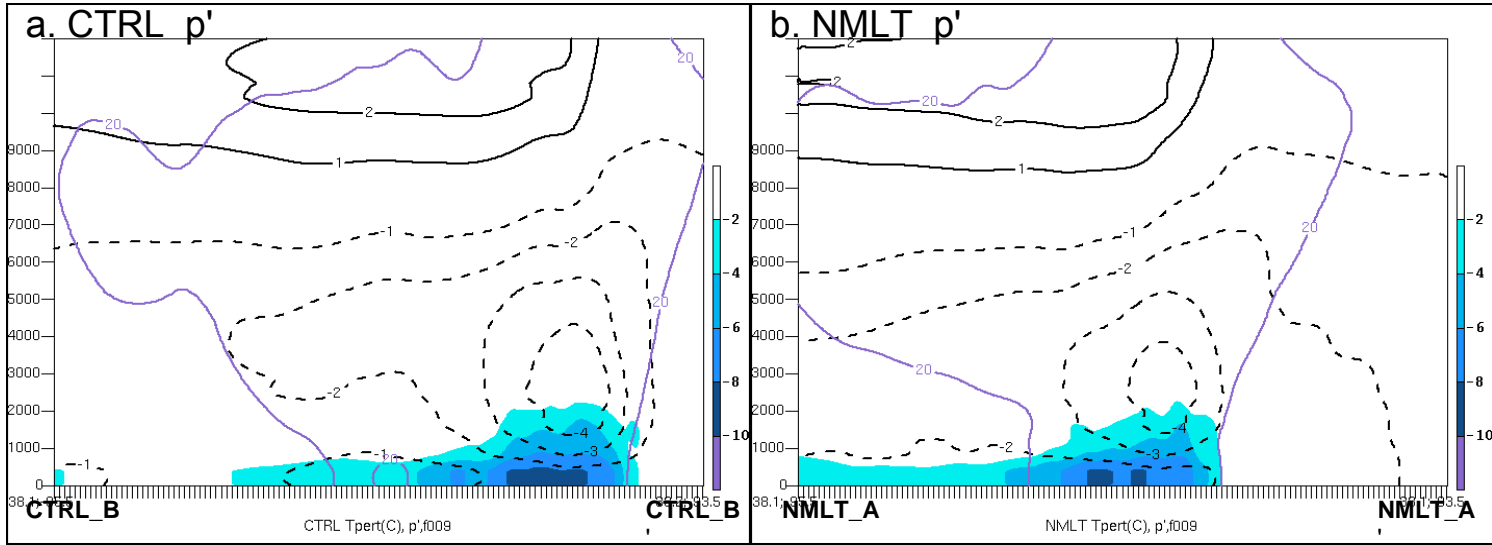


Figure 4.21: As in Fig. 4.5 except comparing CTRL and NMLT simulations.

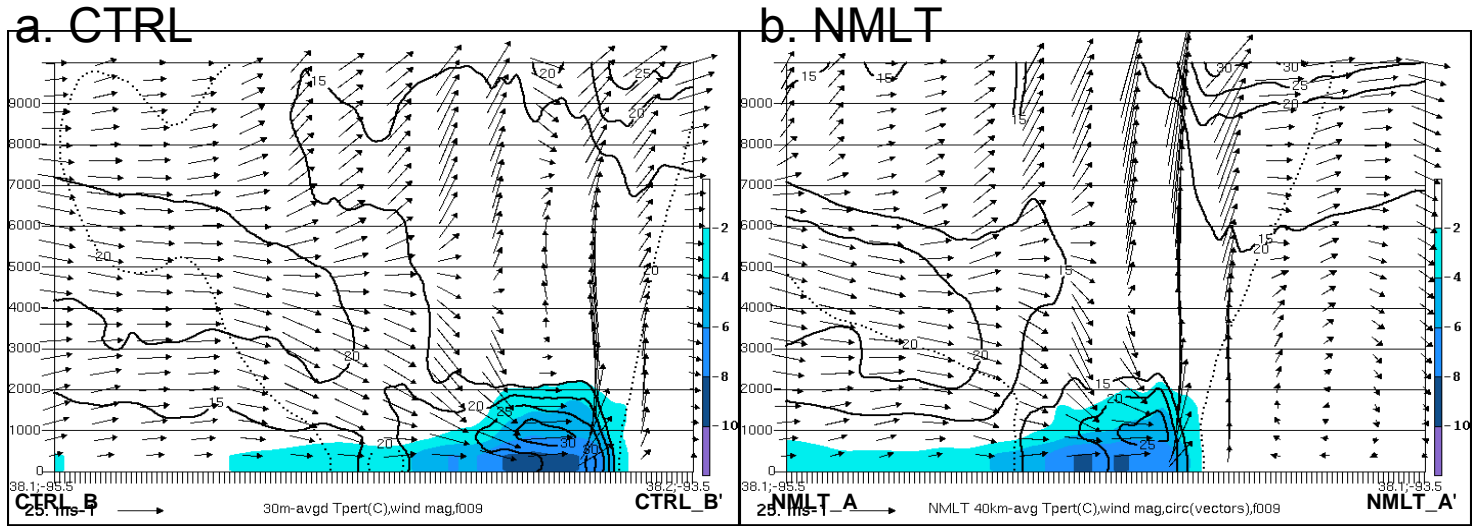


Figure 4.22: As in Fig. 4.6 except comparing CTRL and NMLT simulations.

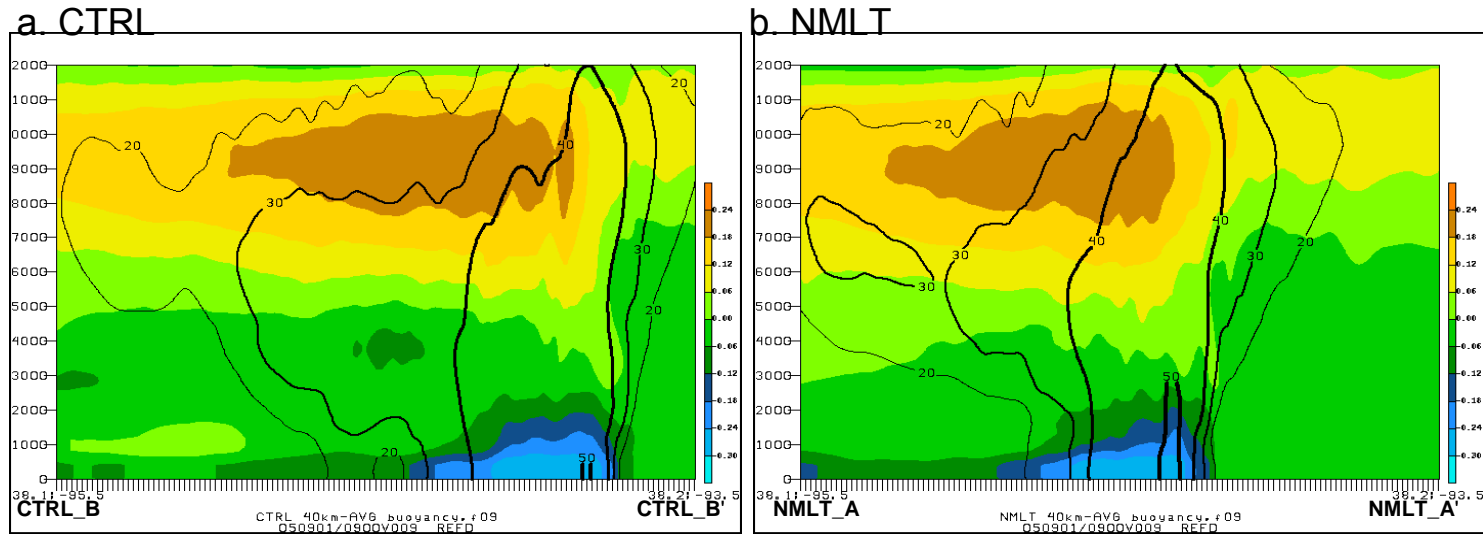
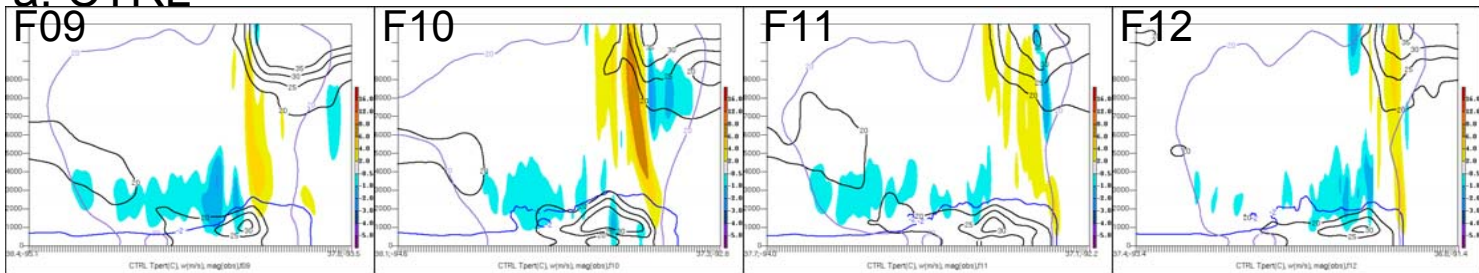


Figure 4.23: As in Fig. 4.7 except comparing CTRL and NMLT simulations.

a. CTRL



b. NMLT

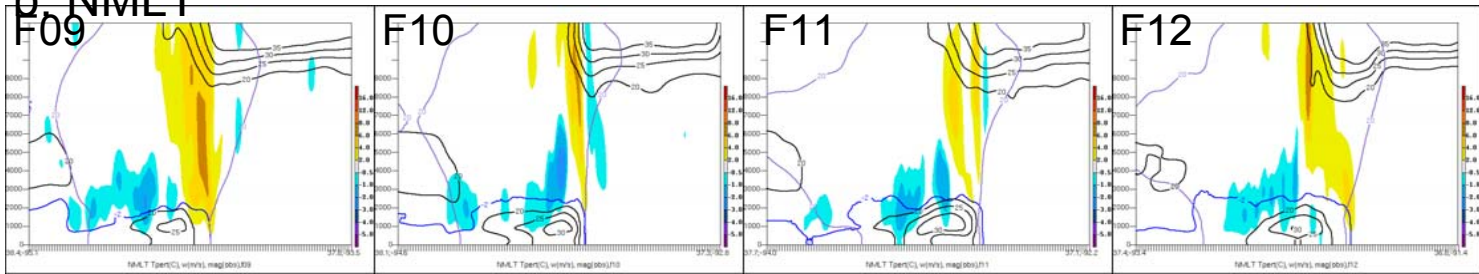
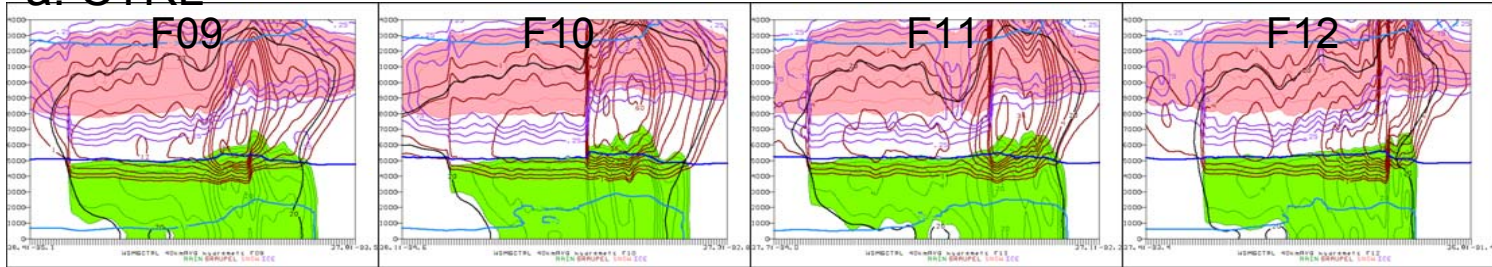


Figure 4.24: As in Fig. 4.12 except comparing CTRL and NMLT simulations.

a. CTRL



b. NMLT

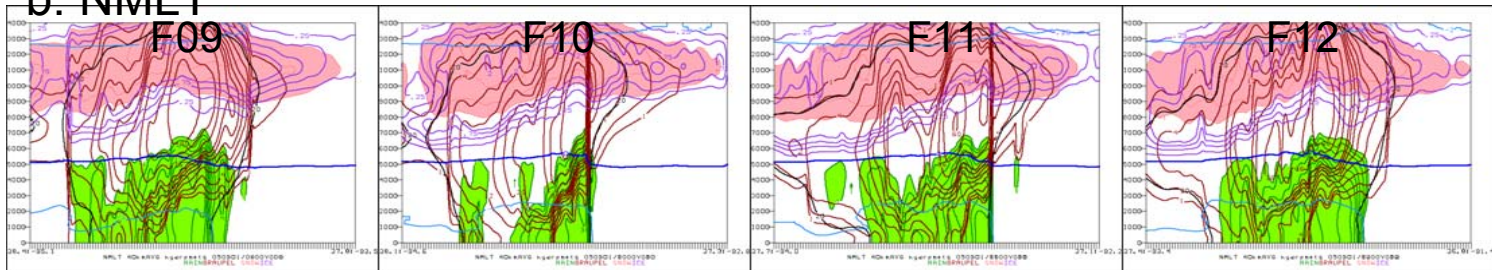


Figure 4.25: Vertical cross-sections as in Fig. 4.24, showing cold pool ($T' = -2^{\circ}\text{C}$, blue contours), hydrometeor mixing ratios (contours as labeled $\times 10^{-4}$, gkg^{-1}) for graupel (burgundy contours), cloud ice (purple), rain (green contours and fill), and snow (pink contours and fill) in CTRL (row A) and NMLT (row B) simulations.

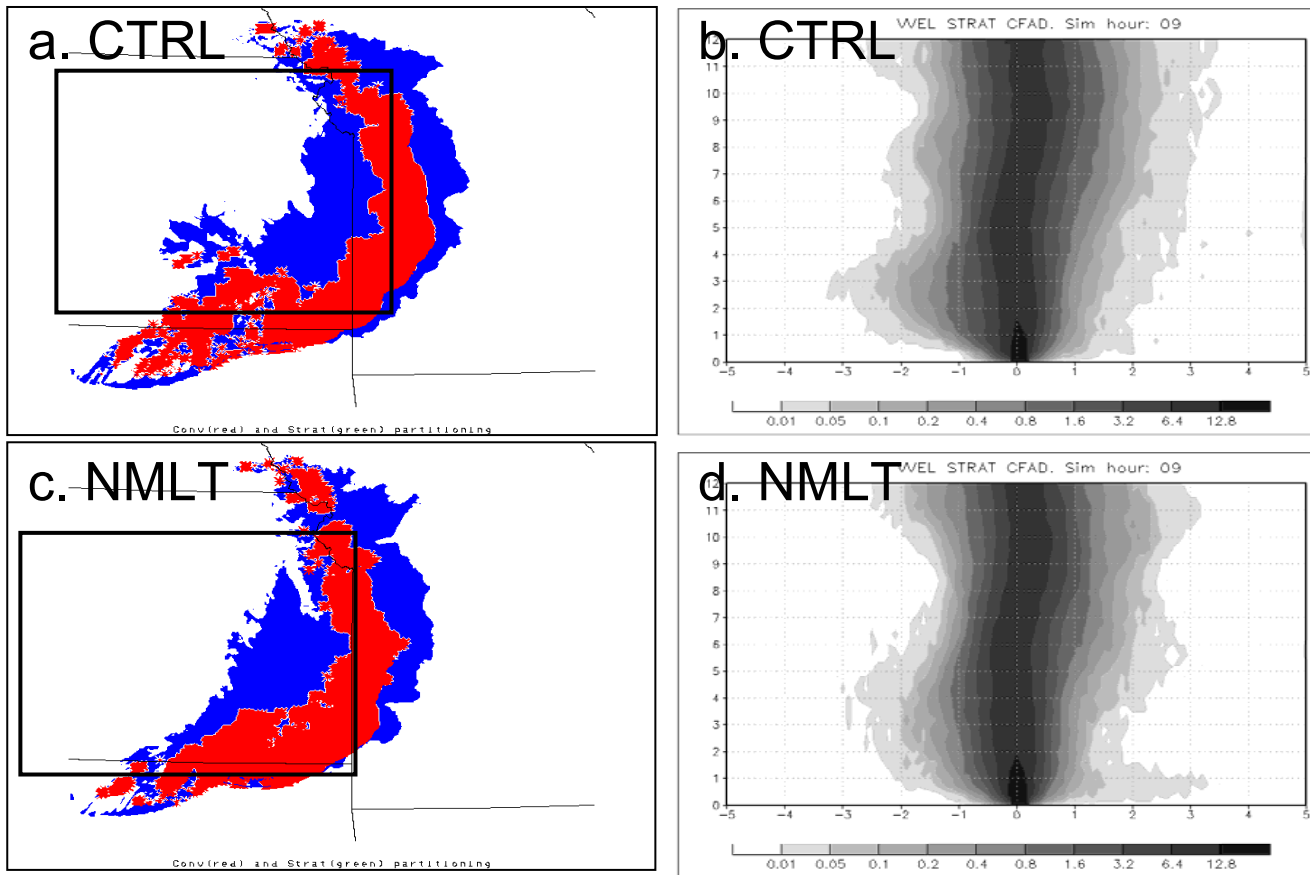


Figure 4.26: As in Fig. 4.8 except comparing CTRL and NMLT simulations.

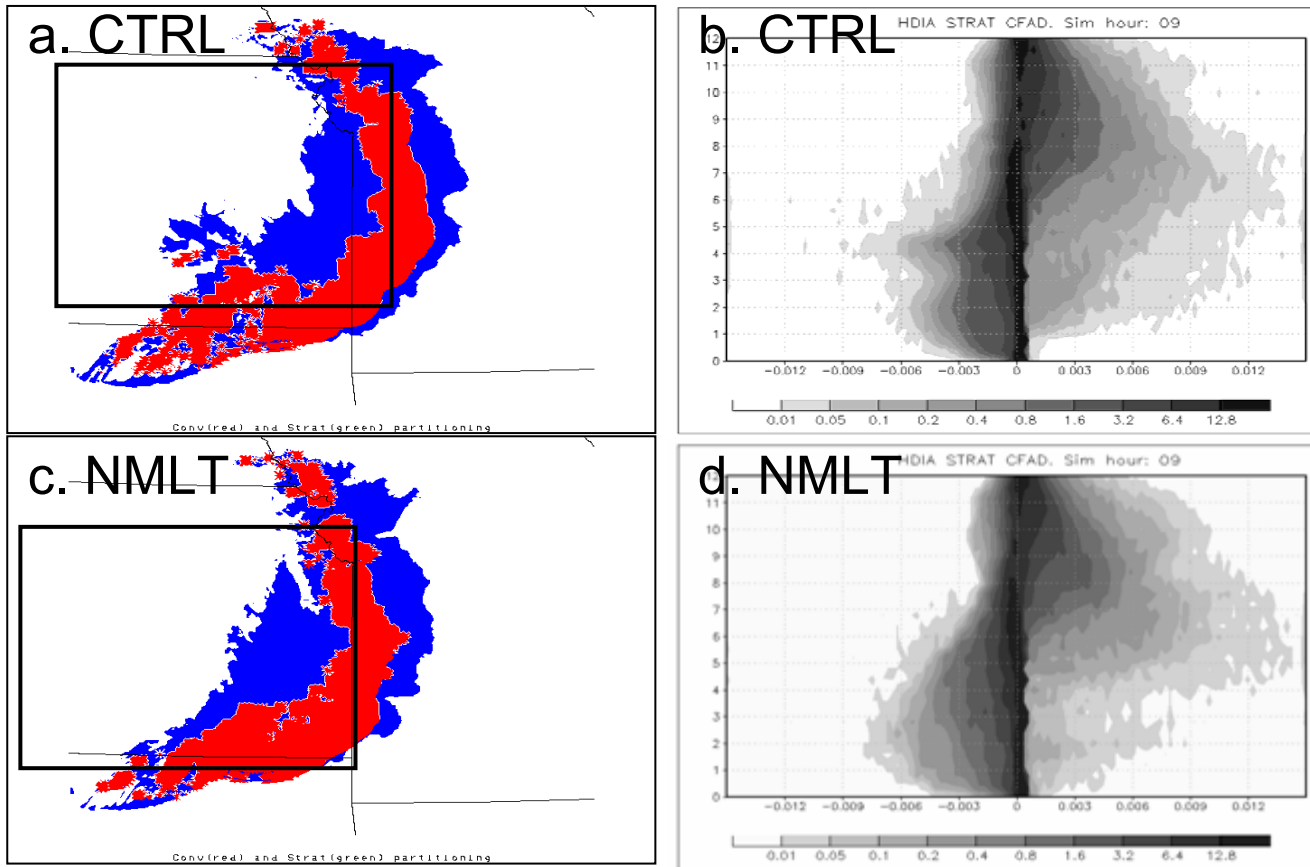


Figure 4.27: As in Fig. 4.9 except comparing CTRL and NMLT simulations.

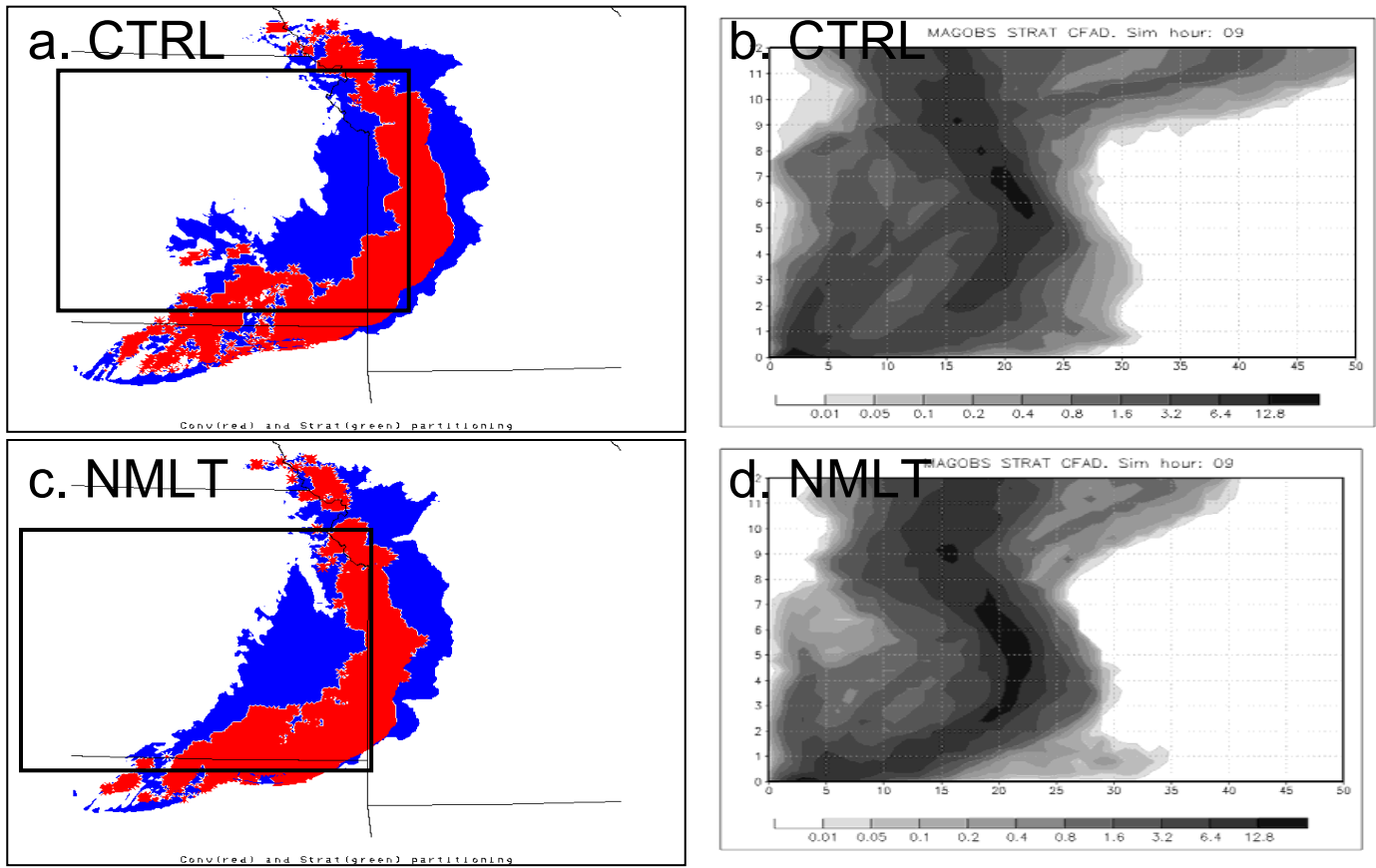
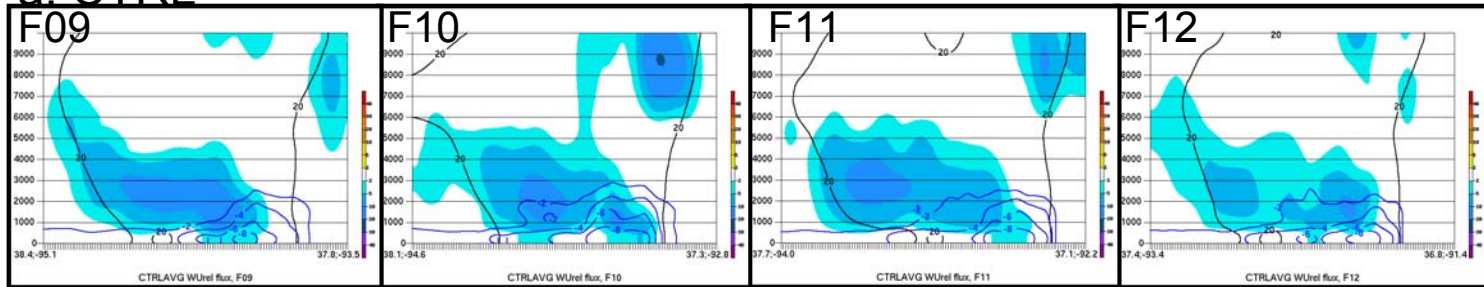


Figure 4.28: As in Fig. 4.19 except comparing CTRL and NMLT simulations.

a. CTRL



b. NMLT

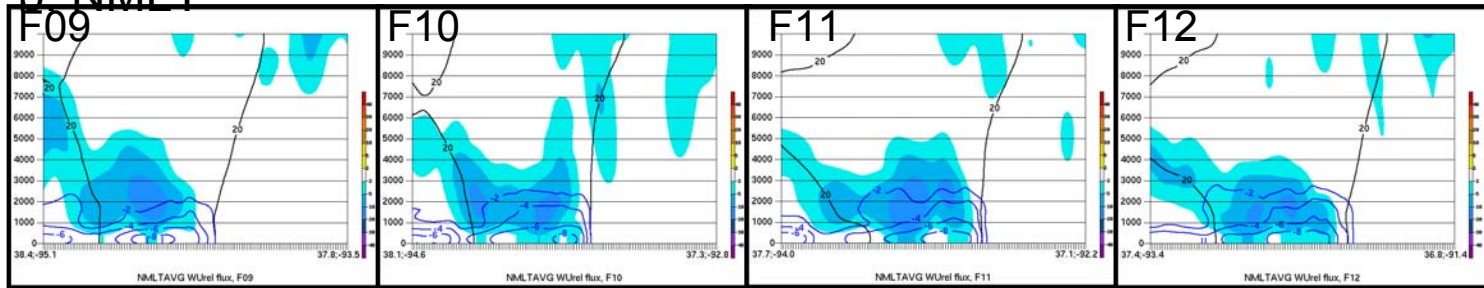


Figure 4.29: As in Fig. 4.11 except comparing CTRL and NMLT simulations.

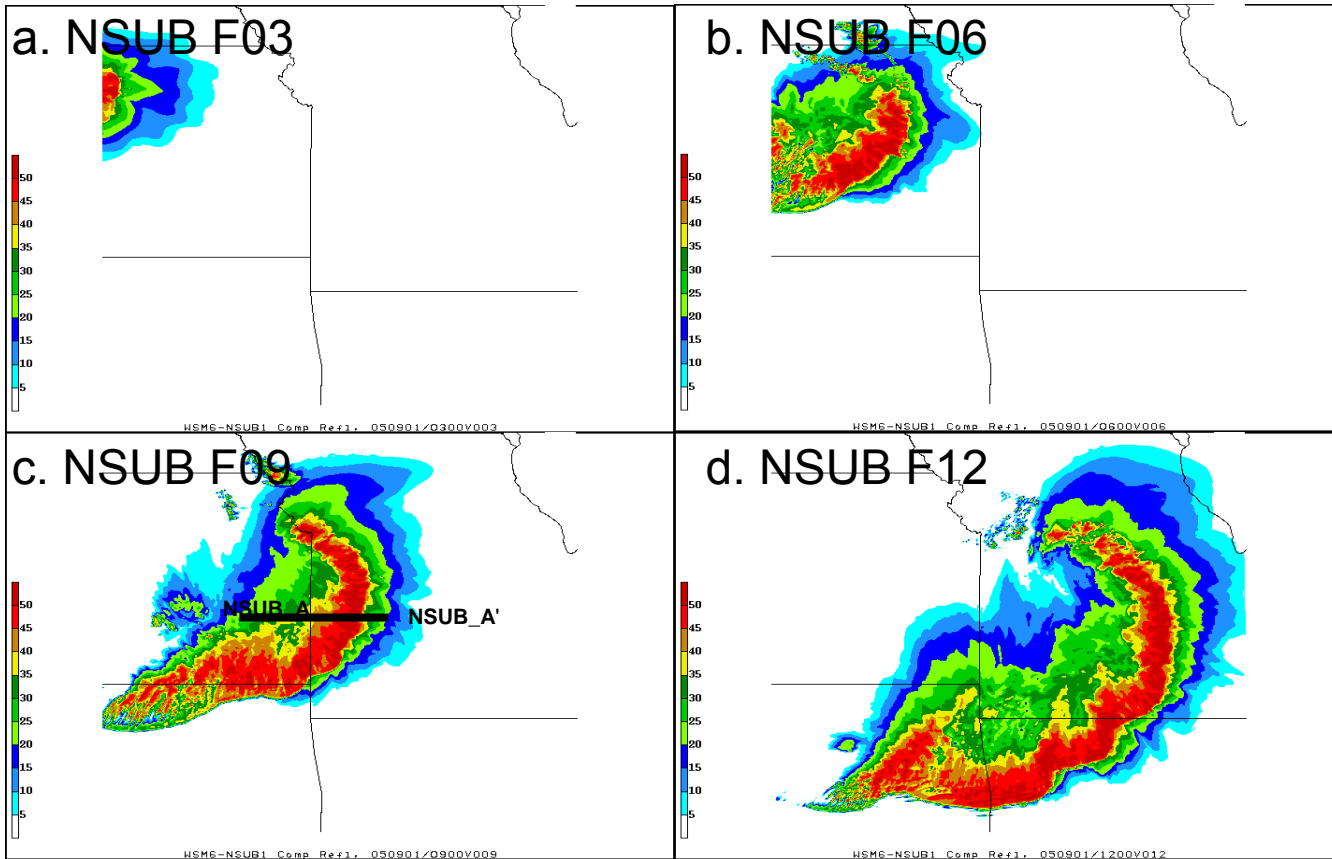


Figure 4.30: Simulated composite reflectivity (dBZ, shaded as indicated at right) and cold pool outline ($T' = -2^{\circ}\text{C}$ at 0 m (black, solid)), for NSUB run at (a) F03, (b) F06, (c) F09, and (d) F12. Line NSUB_A-NSUB_A' in (c) depicts cross-section shown in subsequent figures.

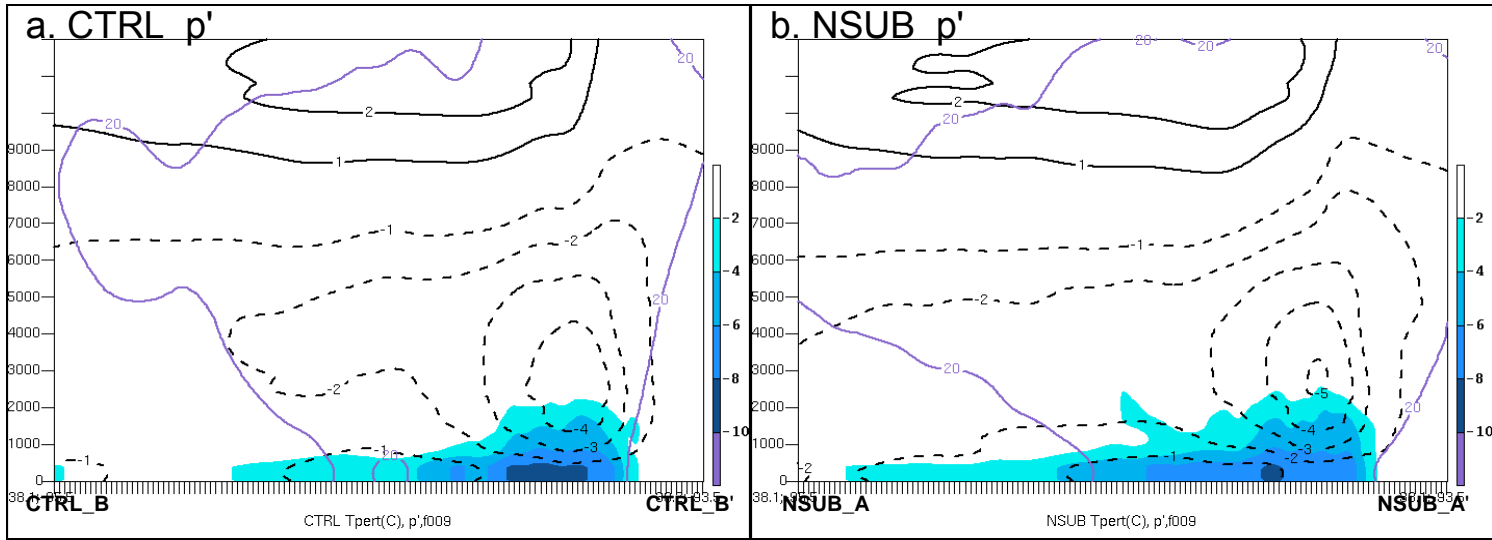


Figure 4.31: As in Fig. 4.5 except comparing CTRL and NSUB simulations.

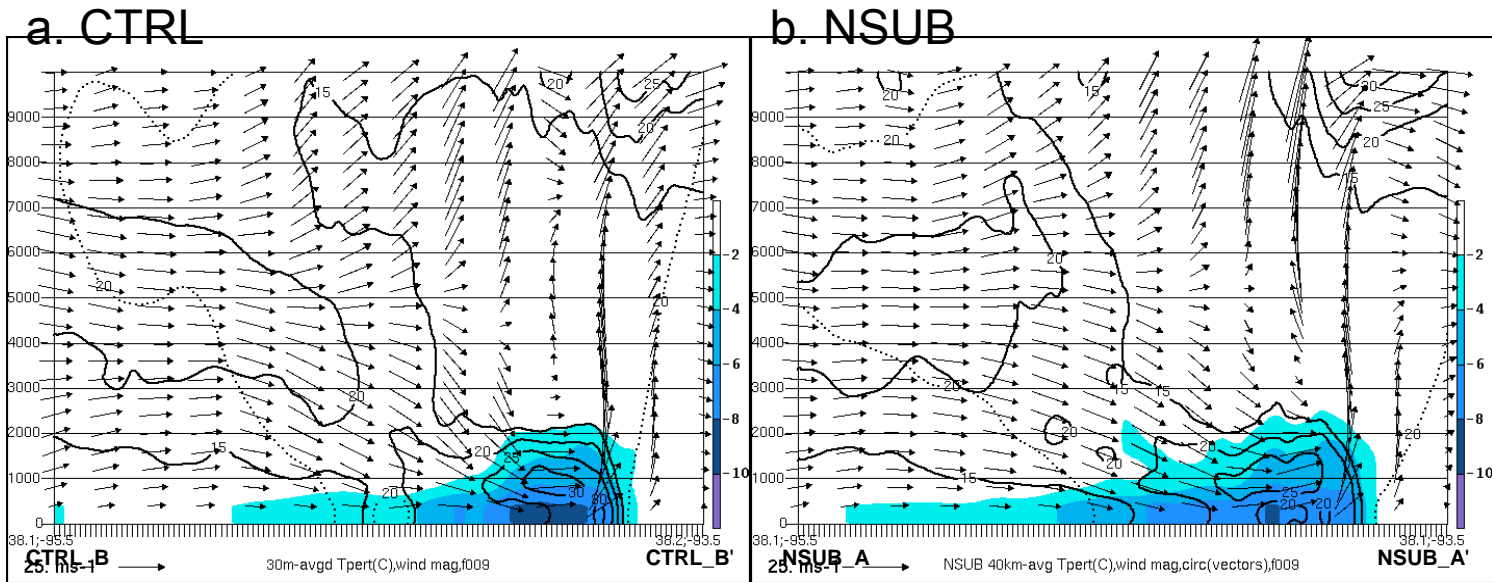


Figure 4.32: As in Fig. 4.6 except comparing CTRL and NSUB simulations.

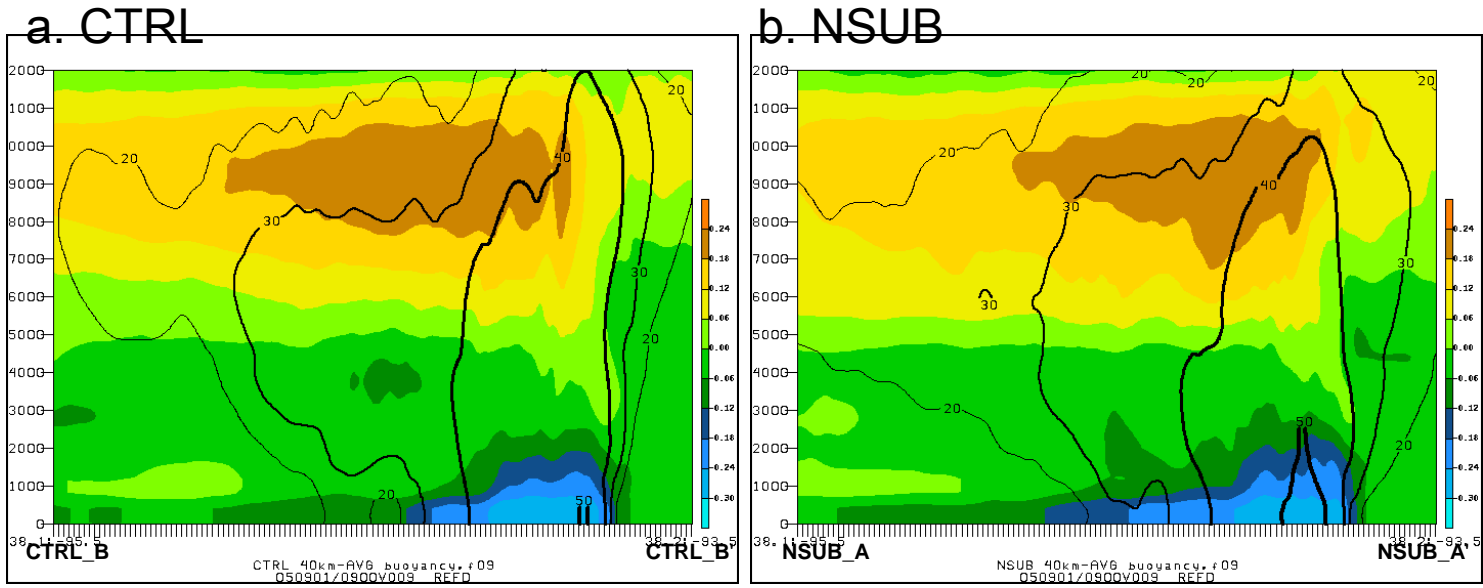


Figure 4.33: As in Fig. 4.7 except comparing CTRL and NSUB simulations.

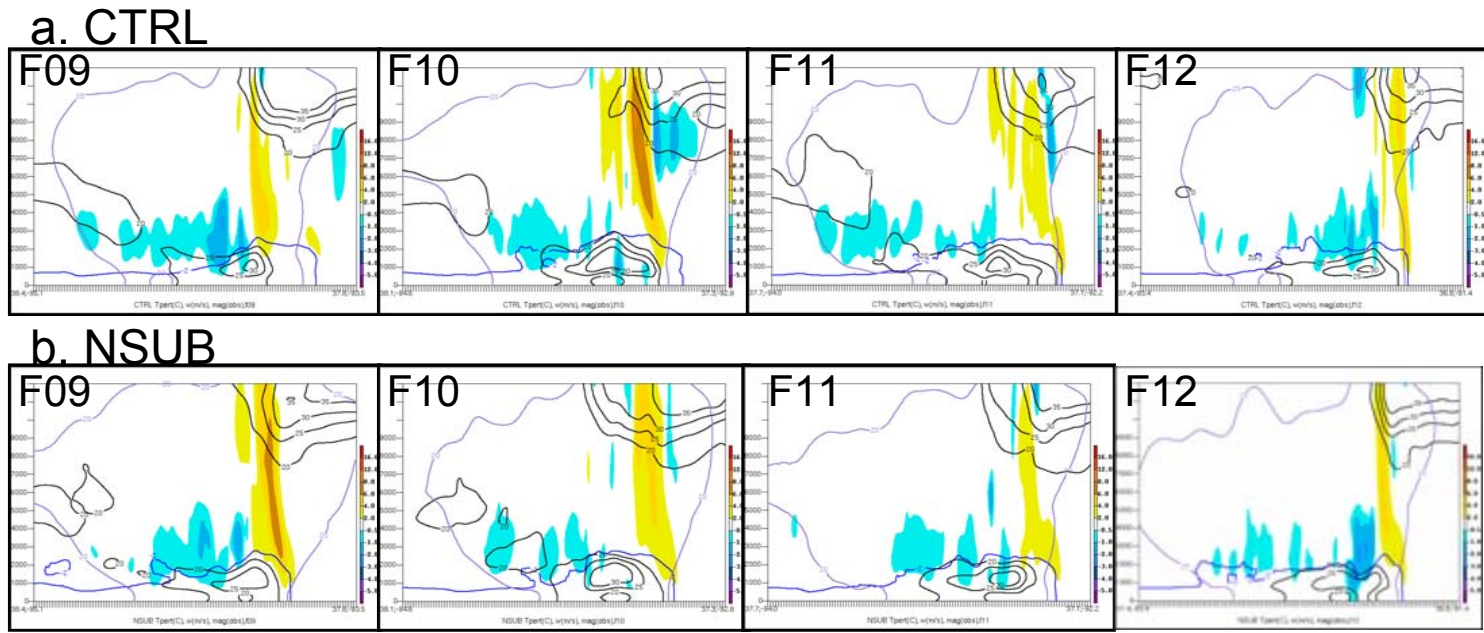
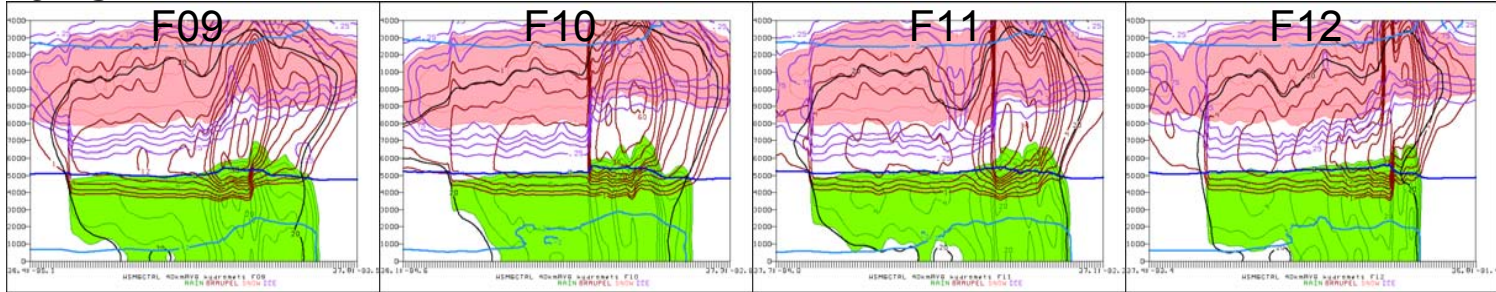


Figure 4.34: As in Fig. 4.12 except comparing CTRL and NSUB simulations.

a. CTRL



b. NSUB

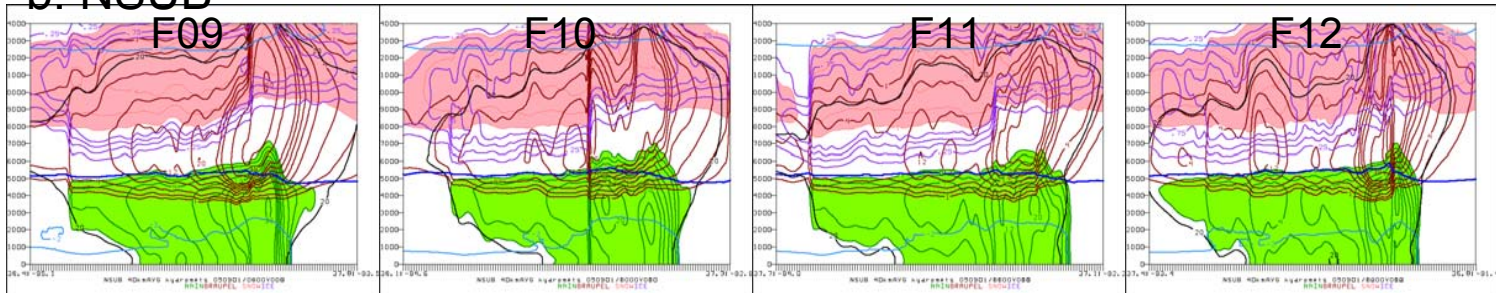


Figure 4.35: Vertical cross-sections as in Fig. 4.34, showing cold pool ($T' = -2^{\circ}\text{C}$, blue contour), hydrometeor mixing ratios (contours as labeled $\times 10^{-4}$, gkg^{-1}) for graupel (burgundy), cloud ice (purple), rain (green contours and fill), and snow (pink contours and fill) in CTRL (row A) and NSUB (row B) simulations.

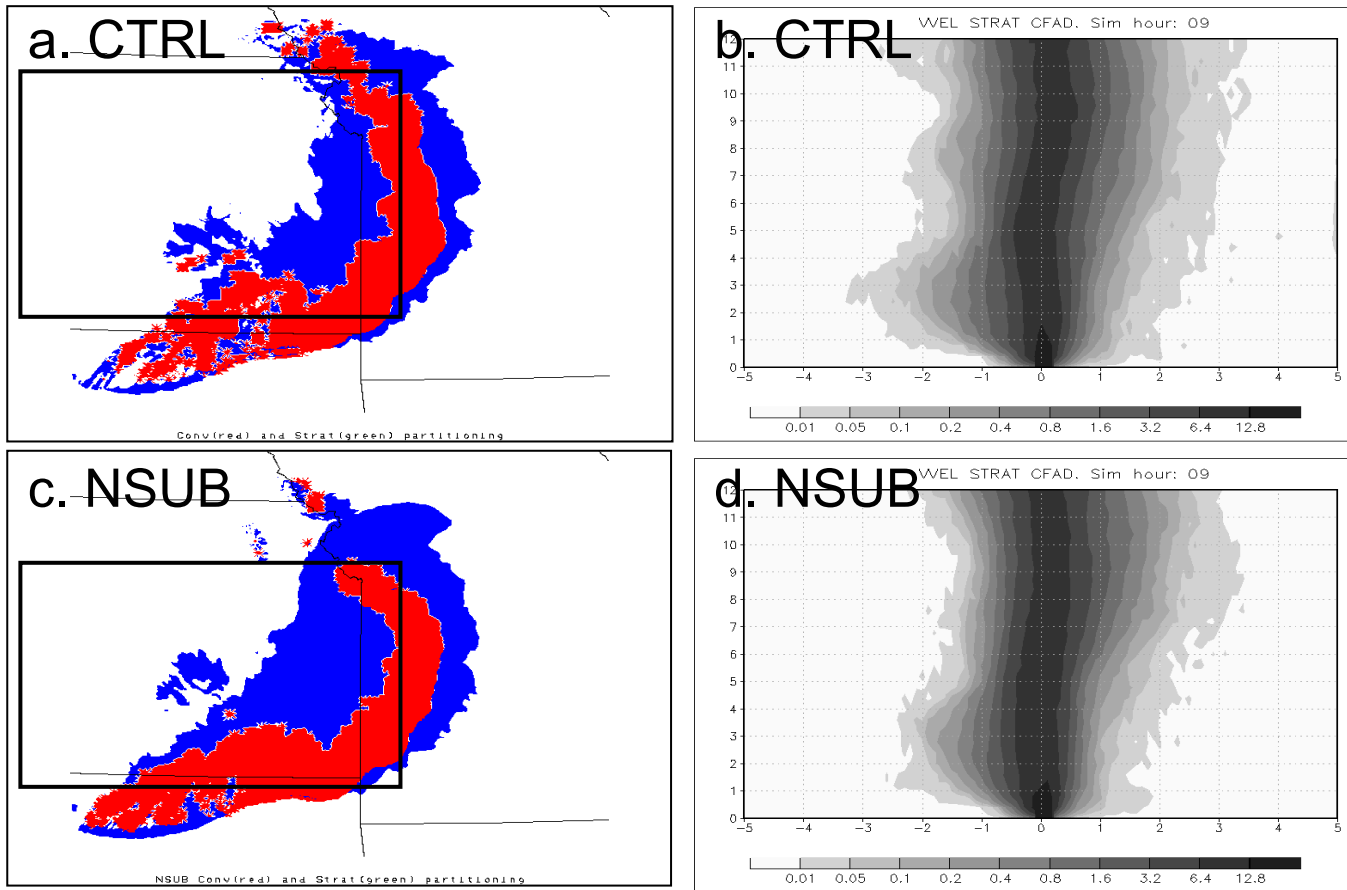


Figure 4.36: As in Fig. 4.8 except comparing CTRL and NSUB simulations.

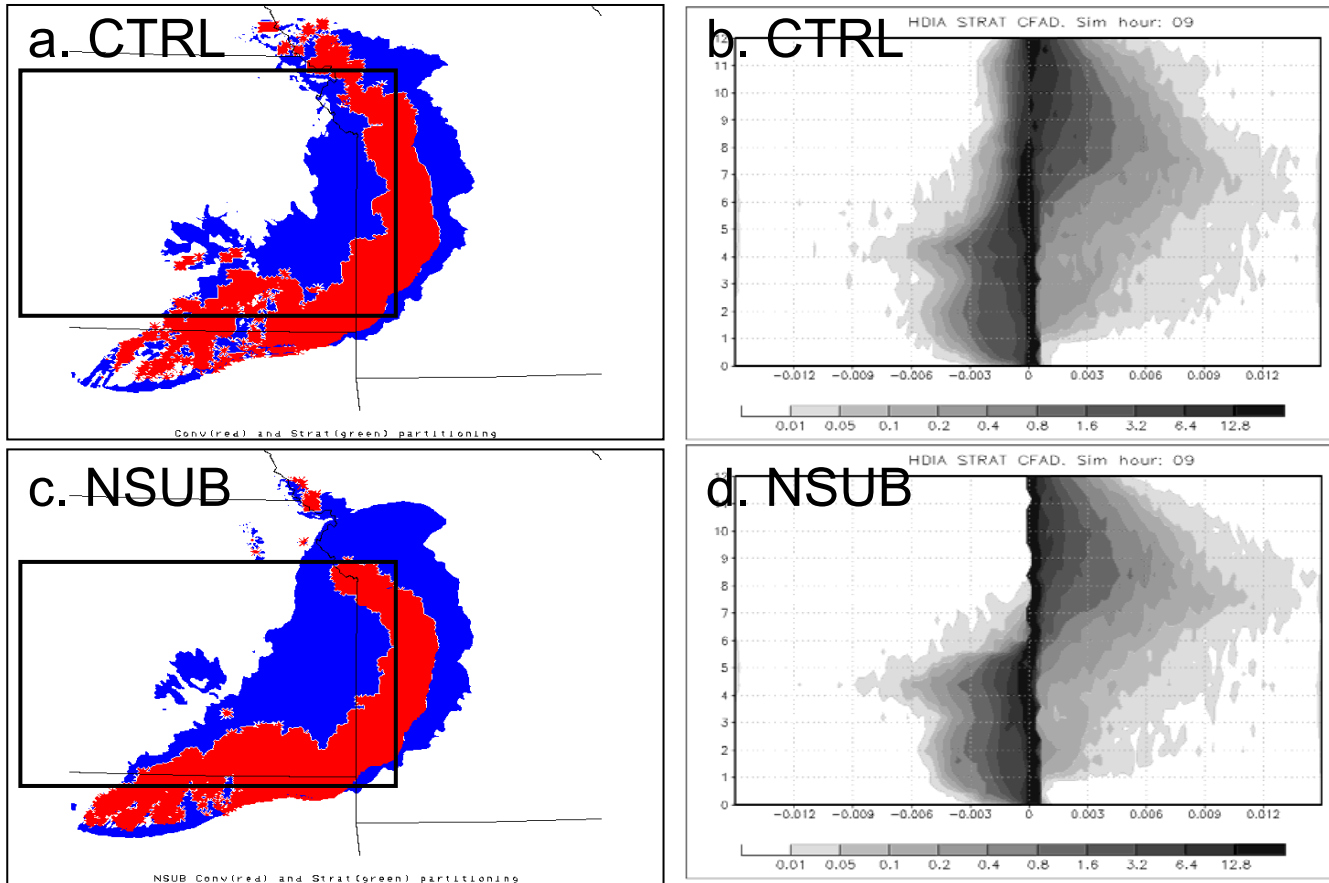


Figure 4.37: As in Fig. 4.9 except comparing CTRL and NSUB simulations.

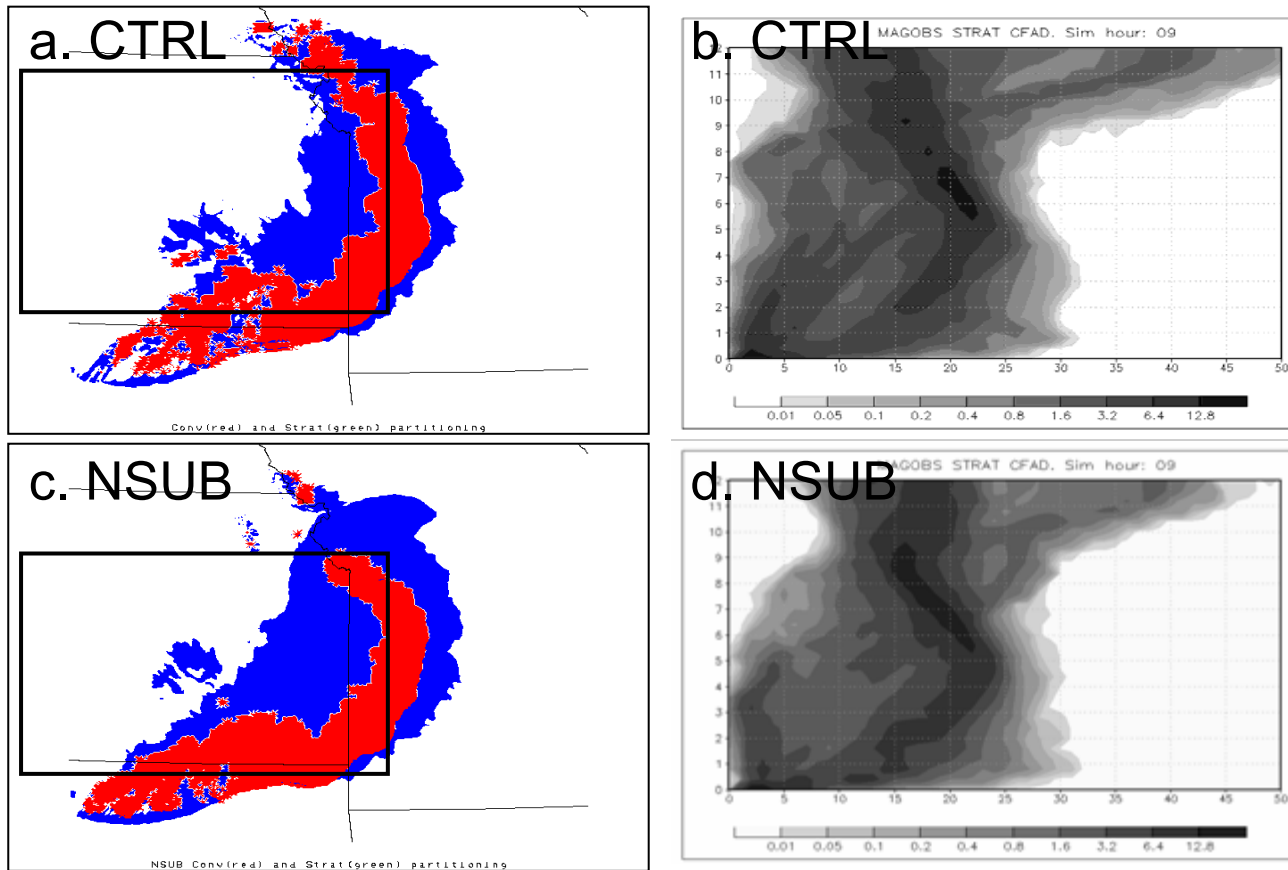
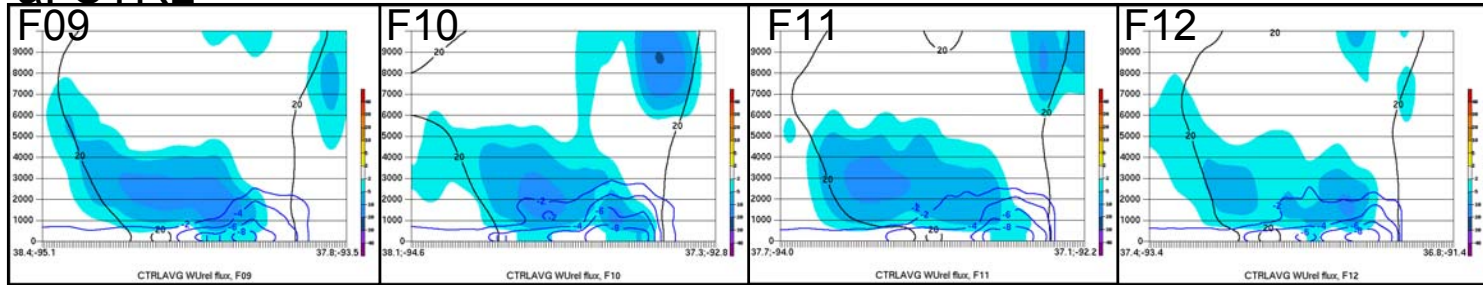


Figure 4.38: As in Fig. 4.19 except comparing CTRL and NSUB simulations.

a. CTRL



b. NSUB

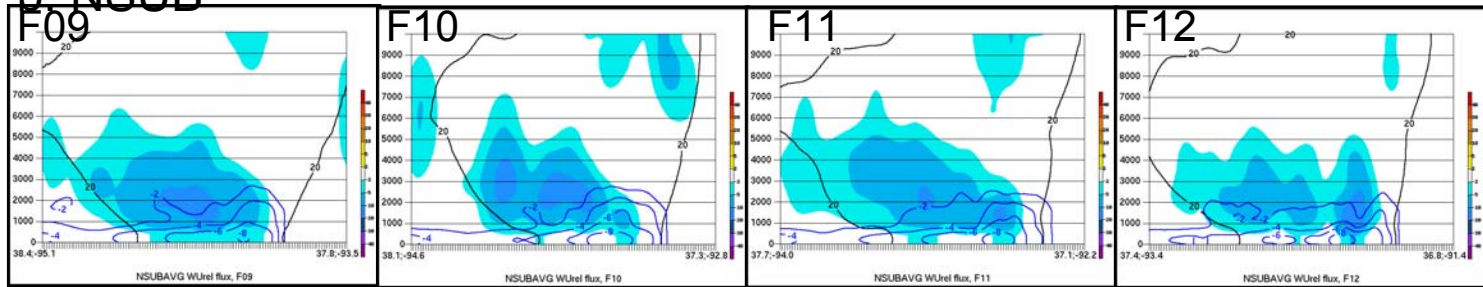


Figure 4.39: As in Fig. 4.11 except comparing CTRL and NSUB simulations.

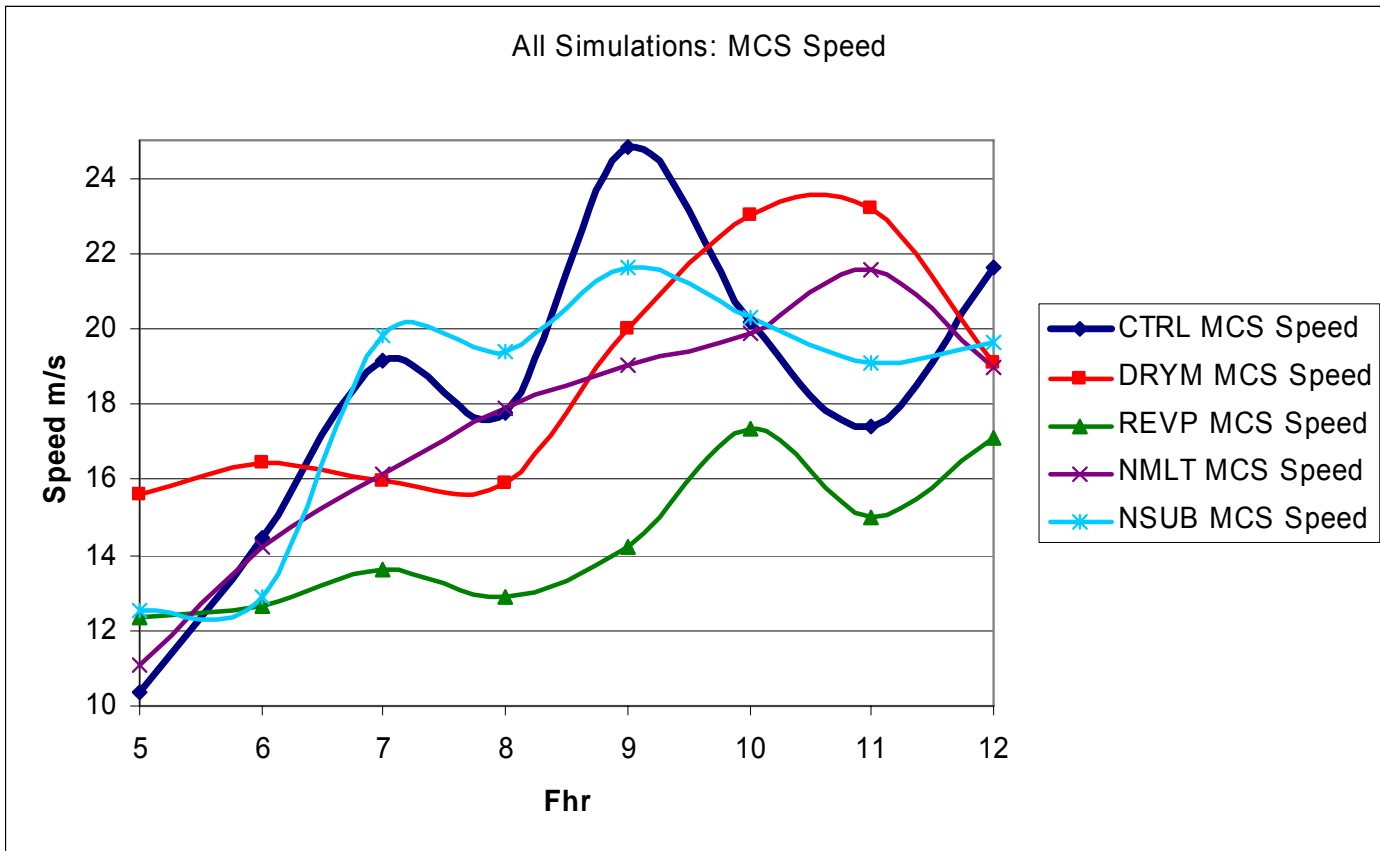


Figure 4.40: Comparison of MCS groundspeeds (ms^{-1}) for CTRL (dark blue), DRYM (red), REVP (green), NMLT (purple), NSUB (light blue).

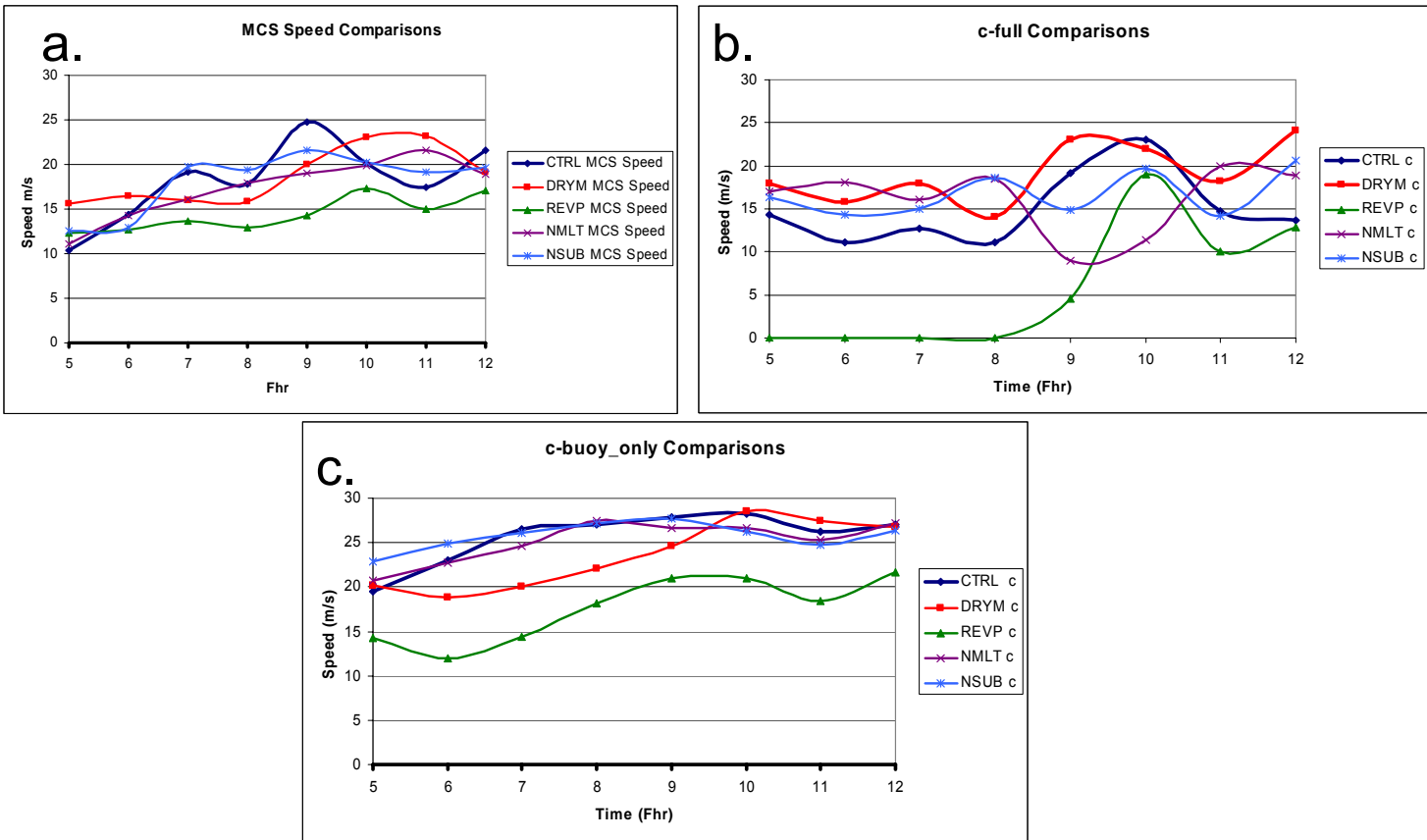


Figure 4.41: a) Comparison of MCS groundspeeds (ms^{-1}); b) theoretical cold pool speed (ms^{-1}) as calculated according to c_{full} in Eqn (4.1); c) theoretical cold pool speed (ms^{-1}) as calculated according to c_{buoy_only} in Eqn (4.2) for CTRL (dark blue), DRYM (red), REVP (green), NMLT (purple), NSUB (light blue).

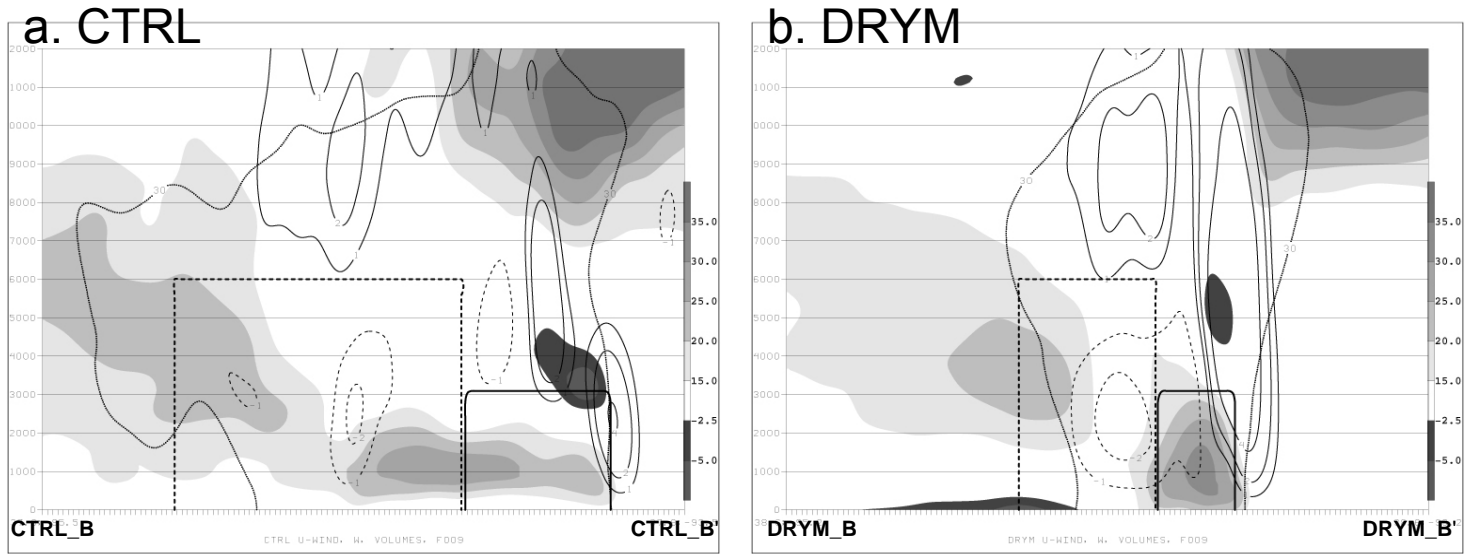


Figure 4.42: a) Cross-section of u (shaded, ms^{-1} as in legend at right), and w (ms^{-1} , positive(negative) black solid (dashed) contours) at F09 along CTRL_B-CTRL_B' as in Fig. 4.2c. Solid (dashed) box outlines volumes VOL_{leading} (VOL_{trailing}), and simulated reflectivity contour of 30dBZ (dotted); b) as in a) except for DRYM.

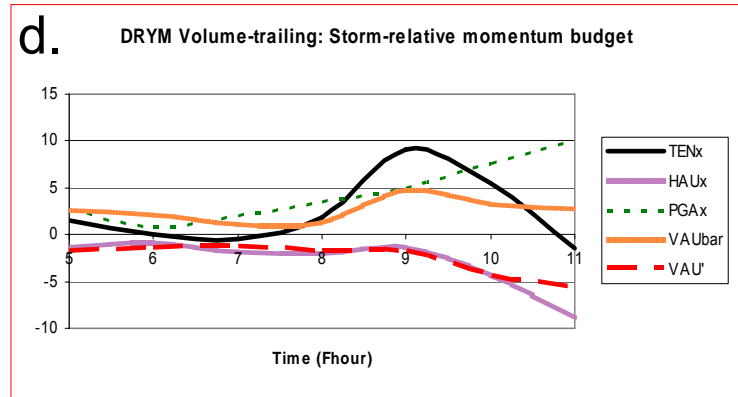
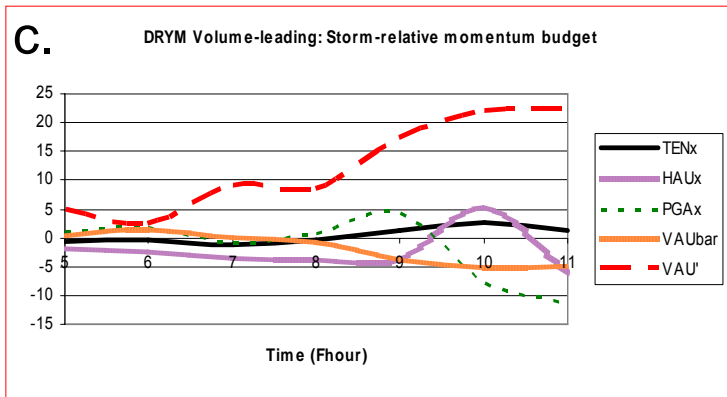
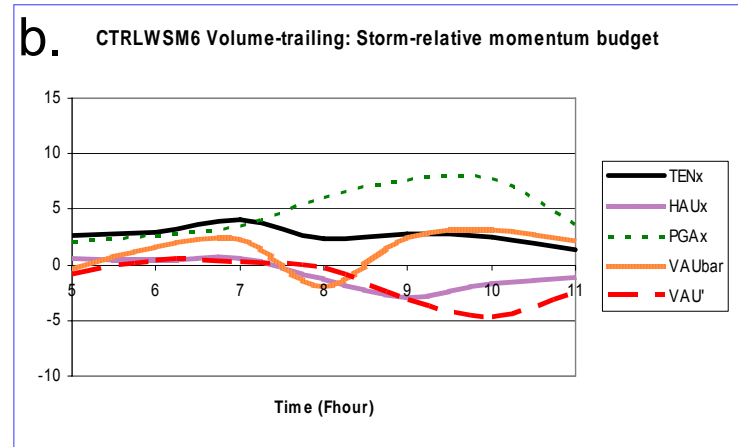
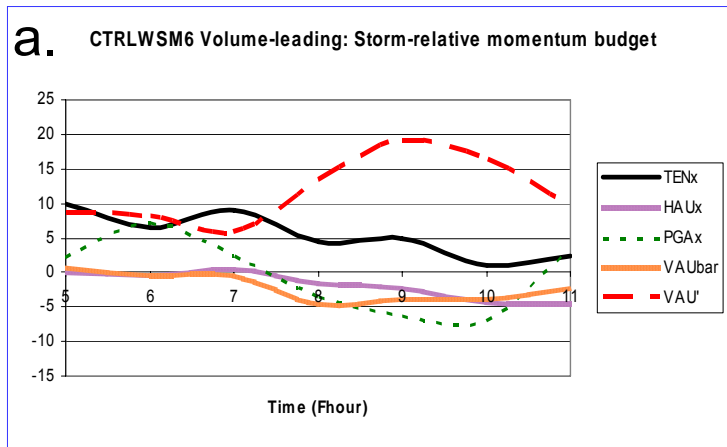


Figure 4.43: a) Volume-averaged momentum budget terms ($\text{ms}^{-1}\text{h}^{-1}$) for CTRL as labeled in key for times F05 – F11 for $\text{VOL}_{\text{leading}}$; b) as in a) but for $\text{VOL}_{\text{trailing}}$; c) as in a) except for DRYM; d) as in b) except for DRYM (note different y-axis scales between $\text{VOL}_{\text{leading}}$ and $\text{VOL}_{\text{trailing}}$).

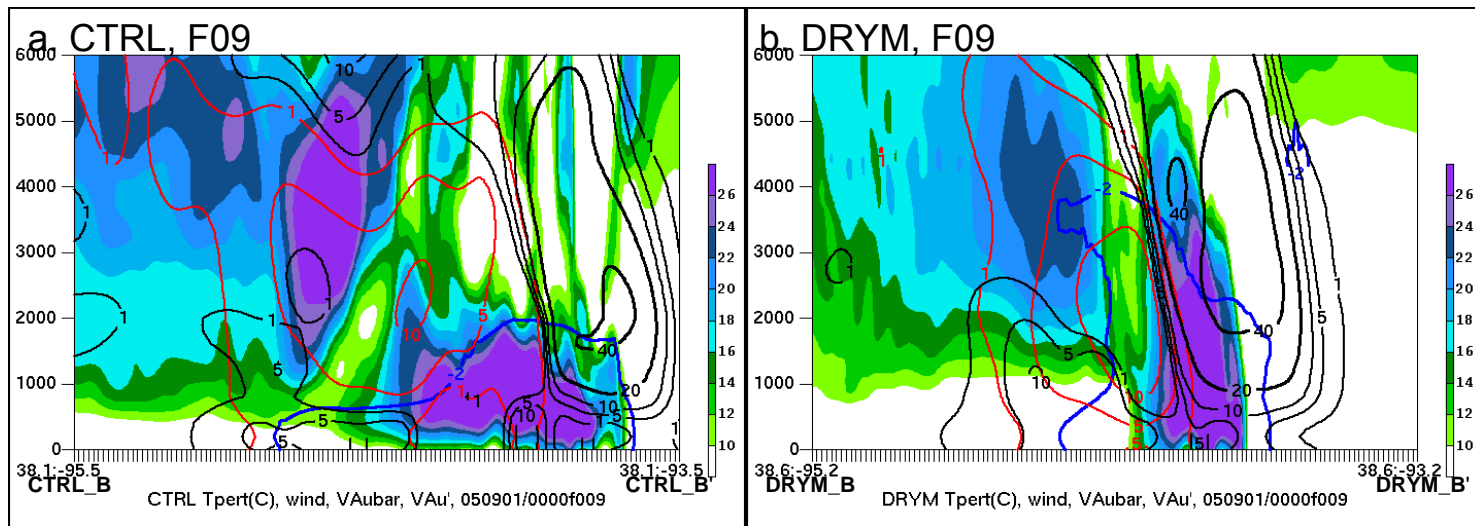


Figure 4.44: (a) East-west cross-section along line CTRL_B-CTRL_B' as in Fig. 4.2c at F09. Cold pool (blue contour, $T' = -2^{\circ}\text{C}$), total wind magnitude (ms^{-1} , shaded as indicated), VAu' (30-min averaged quantity, $\text{ms}^{-1}\text{h}^{-1}$, black contours starting $1 \text{ ms}^{-1}\text{h}^{-1}$), $VA\bar{u}$ (30-min averaged quantity, $\text{ms}^{-1}\text{h}^{-1}$, red contours starting at $1 \text{ ms}^{-1}\text{h}^{-1}$); (b) as in (a) except for DRYM simulation taken along DRYM_B-DRYM_B' as in Fig. 4.3c. Distance of cross-sections 175 km.

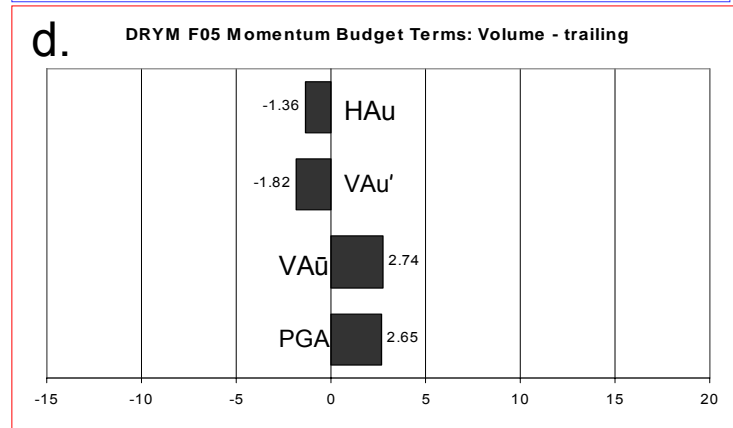
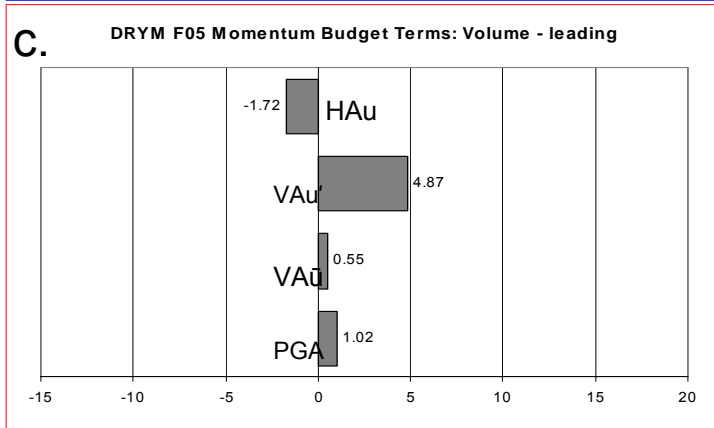
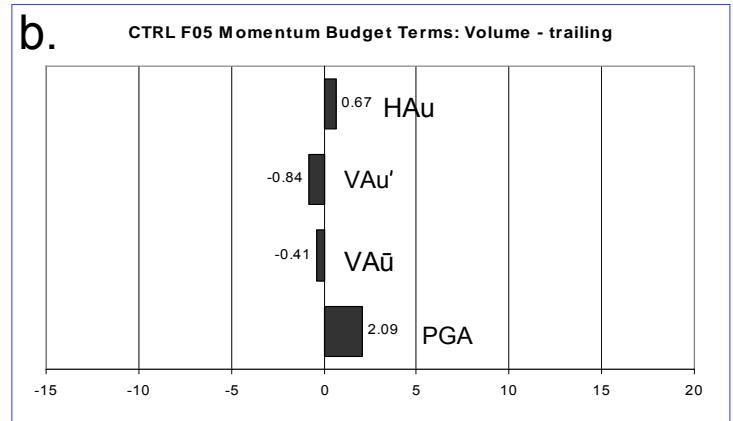
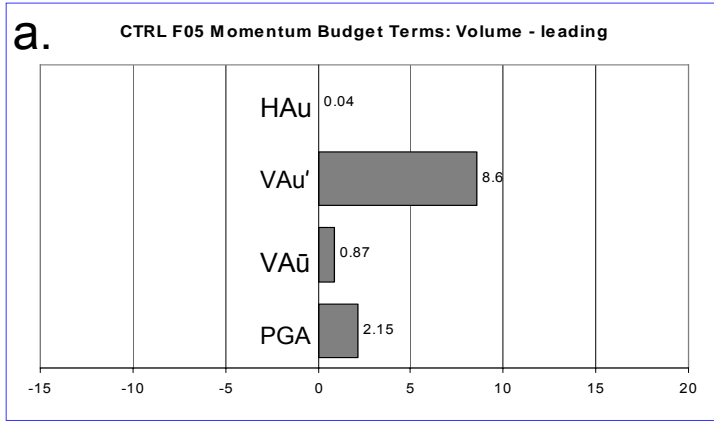


Figure 4.45: a) Momentum budget term averages ($\text{ms}^{-1}\text{h}^{-1}$) as labeled over for CTRL $\text{VOL}_{\text{leading}}$ at F05, b) as in a) but for $\text{VOL}_{\text{trailing}}$, c) as in a) but for DRYM, d) as in b) but for DRYM.

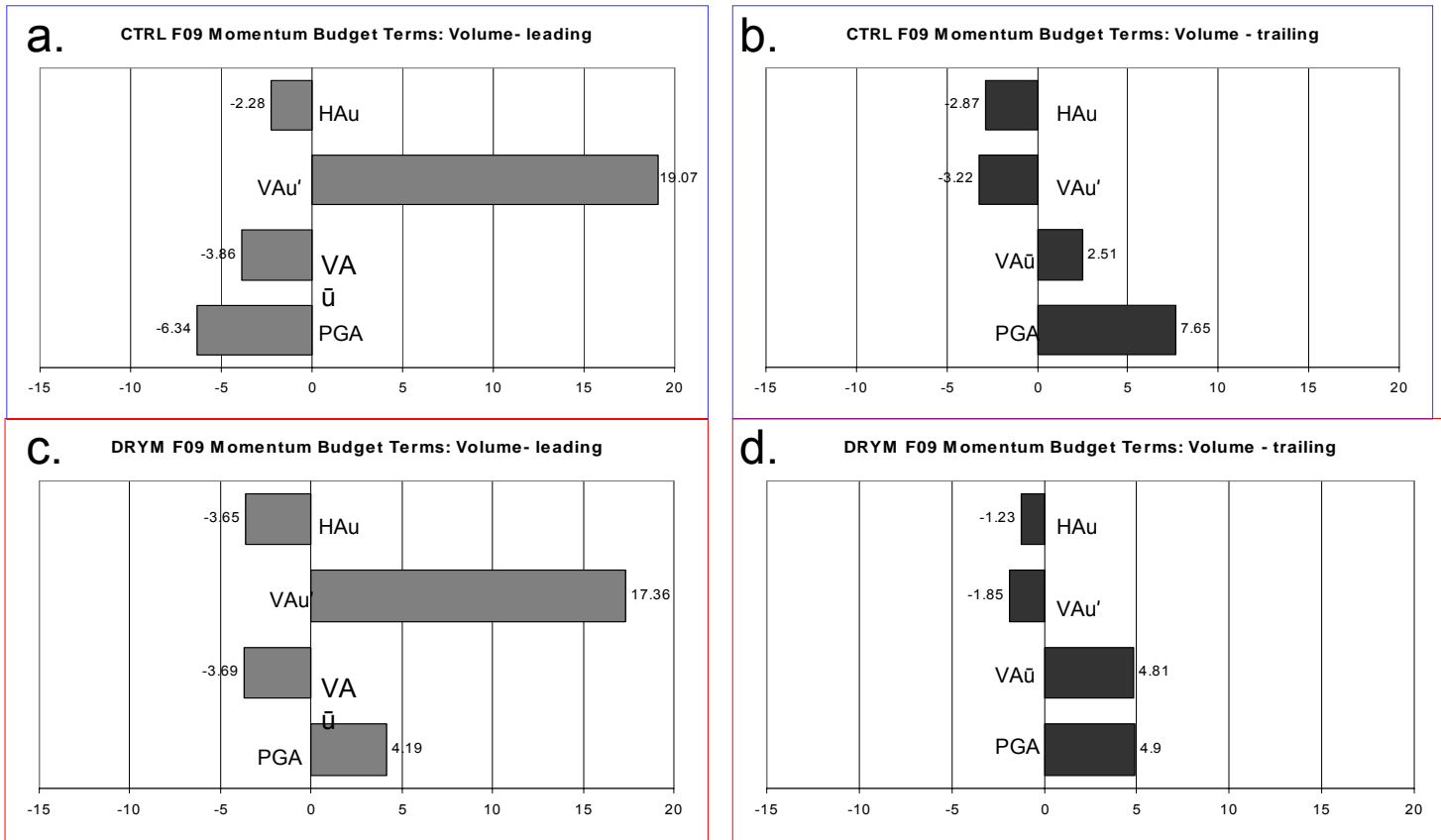


Figure 4.46: a) Momentum budget term averages ($\text{ms}^{-1}\text{h}^{-1}$) as labeled over for CTRL $\text{VOL}_{\text{leading}}$ at F09, b) as in a) but for $\text{VOL}_{\text{trailing}}$, c) as in a) but for DRYM, d) as in b) but for DRYM.

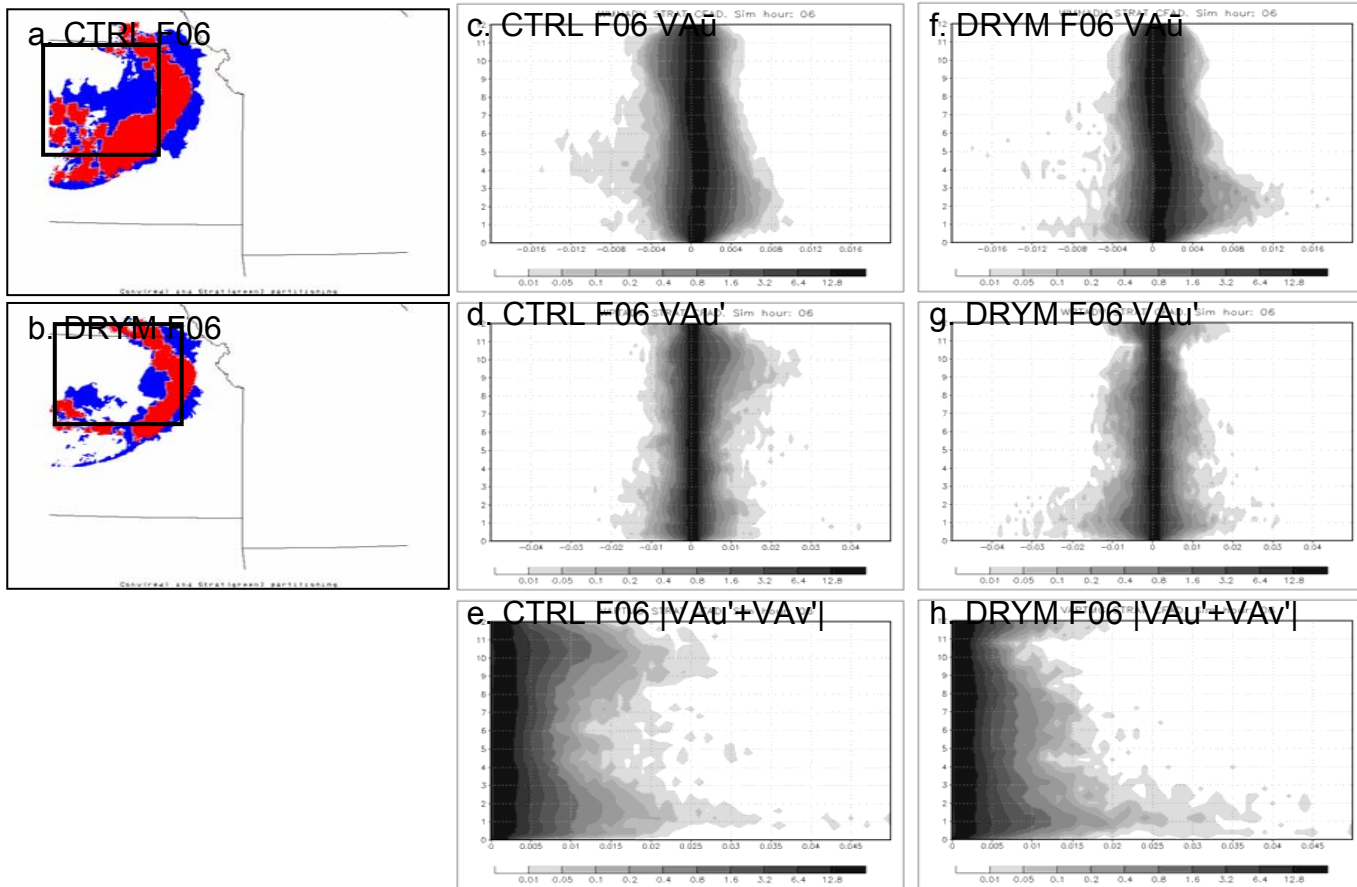


Figure 4.47: a) As in Fig. 4.8a except for F06; b) as in Fig. 4.8c except for F06; c) CFAD of VAu (bin size .0005 ms⁻¹s⁻¹); d) as in c) except for VAu', e) as in c) except for |VAu'+VAv'|; f) as in c) except for DRYM; g) as in d) except for DRYM; h) as in e) except for DRYM.

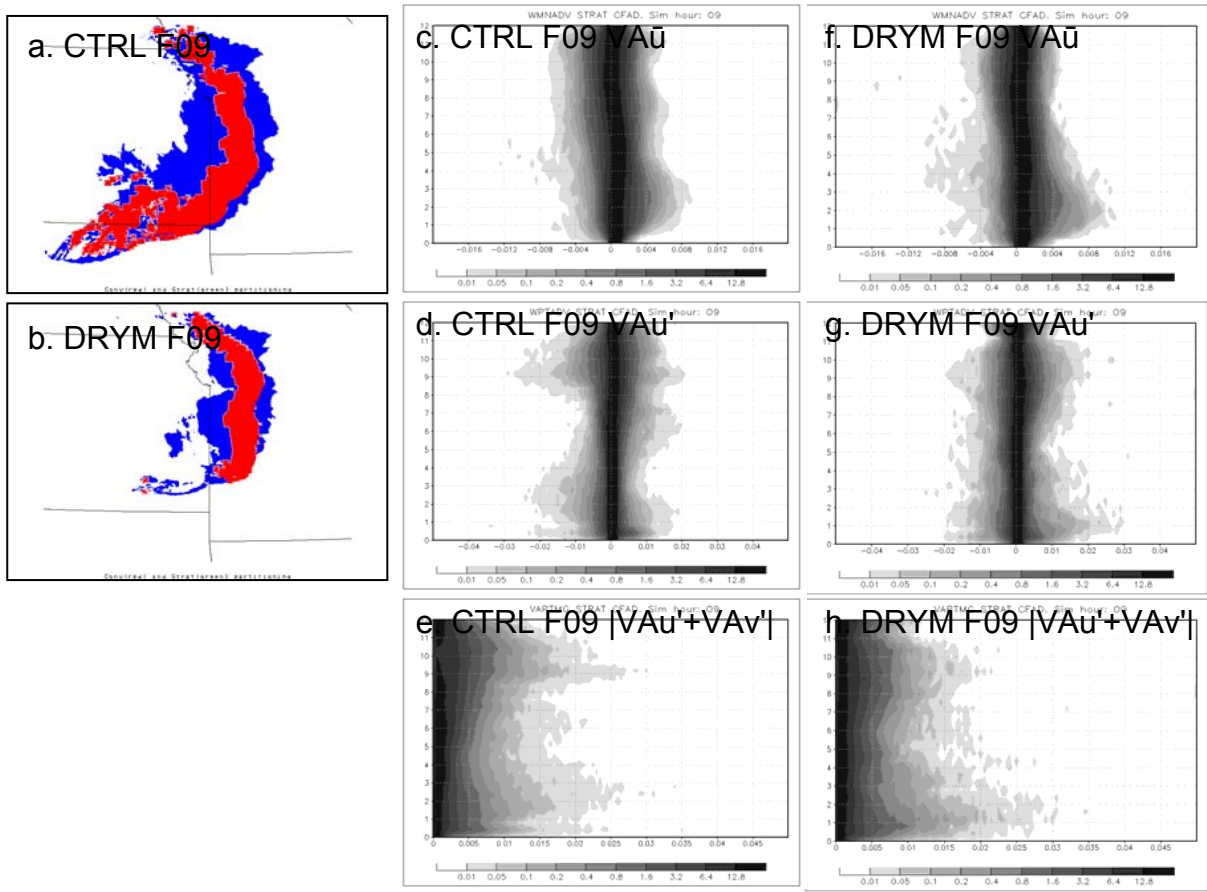


Figure 4.48: As in Fig. 4.47 except for F09.

Table 4.1: Table 2 from Yang and Houze (1995), summarizing storm speed, storm orientation, and rear-to-front flow structure for each sensitivity experiment.

TABLE 2. Summary of mature-stage RTF flow structure of experimental simulations.

Run	Storm speed	Storm orientation	RTF flow structure
CNTL	12.2 m s ⁻¹	upshear tilt	two maximum in the storm (8 m s ⁻¹)*
HAIL	11 m s ⁻¹	upshear tilt	one maximum in convective region
NICE	8 m s ⁻¹	upshear tilt	one maximum in convective region
NEVP	5 m s ⁻¹	upright to downshear tilt	a highly elevated RTF flow
NMLT	12 m s ⁻¹	less upshear tilt	two maximum in the storm (6 m s ⁻¹)
NSUB	10.8 m s ⁻¹	less upshear tilt	two maximum in the storm (7 m s ⁻¹)
DRYM	12.2 m s ⁻¹	more upright	two maximum in the storm (3 m s ⁻¹)

* Number in the parentheses is the maximum of RTF flow at the back edge of the stratiform precipitation during the mature stage ($t = 10\text{--}11$ h).

Chapter 5

CMT and strong surface winds produced by MCS outflow

The key challenge in many past studies of convectively-driven windstorms has been documenting the mechanism(s) that produce intense thunderstorm outflow at the earth's surface. Wakimoto (2001) provides a comprehensive summary of this body of literature, noting in conclusion that several aspects of convectively-driven downdrafts remain incompletely understood and require future study. Included in this list of topics necessitating significant further investigation are (i) determining the cause of small-scale damage swaths (such as those associated with mesovortices), (ii) understanding processes that inhibit or augment RIJ descent to the surface, and (iii) elucidating the role of microphysical processes in the genesis of convective downdrafts. This chapter examines the above topics within the context of CMT and surface wind generation.

The hypotheses outlined in Chapter 4 focus on the potential impacts of each model sensitivity experiment to CMT and MCS motion. As introduced in Chapter 1, CMT has been linked with the generation of damaging surface winds by past studies, but understanding of both the process itself, as well as its variability in different storm environments, remains incomplete (e.g., Johns and Doswell 1992; Geerts 2001; Wakimoto 2001). Thus, with respect to the same set of sensitivity test simulations from Chapter 4, hypotheses are also drawn regarding the possible changes to the generation of extreme surface winds by each simulated MCS, and are summarized as follows:

- (i) DRYM is expected to produce stronger low-level and surface-based winds due to enhanced downdrafts associated with increased negative buoyancy. Yang and Houze (1995) found that a similar experiment produced a more cellular MCS structure; thus, enhanced gusts from locally stronger convective downdrafts may be possible as well. A counter-hypothesis is that decreased surface wind speeds may be evident in some areas due to possible overall weakening of the MCS (i.e., weaker updrafts, weaker vertical heating profile, weaker convective downdrafts, etc.). A final

possibility incorporating both of the above hypotheses is that surface wind speeds may be further enhanced if a less intense surface cold pool (resulting from a potentially weaker MCS) causes the RIJ to descend over a larger surface area (e.g., Weisman 1992).

- (ii) REVP is hypothesized to have decreased occurrences of strong surface winds and overall reduced low-level wind speeds as a result of weakened evaporative cooling and thus less cooling-induced descent. Such weakening should impede both the downdraft itself from penetrating to the surface and also reduce CMT.
- (iii) NMLT is also expected to produce reduced coverage of strong and severe surface winds through decreased descent. Yang and Houze (1995) found that downward motion in the TSR decreases by 22% in the absence of melting, so the effect may be marked if downward motion in the TSR is responsible for a significant portion of surface wind speed maxima.
- (iv) NSUB is not expected to show a considerable change in surface wind speeds relative to CTRL due to its maximized importance aloft in the anvil regions. However, if omitting sublimation significantly affects RIJ descent (as some recent studies suggest), then it is possible that strong winds that result from the RIJ intersecting the surface may be reduced.

5.1 Sensitivity of severe surface wind production to environmental humidity and microphysical cooling processes

5.1.1 Severe surface wind definition/terminology

The National Weather Service (NWS) defines severe convective winds to be those measured at 10-m above ground level (AGL) in excess of 50 kt (25.7 ms^{-1}). Such observations are made according to the definition of “wind gust” found in the AMS *Glossary of Meteorology* (Glickman 2000), that is: “a sudden, brief increase in speed of the wind. According to U.S. weather observing practice, gusts are reported when the peak

wind speed reaches at least 16 knots and the variation in wind speed between the peaks and lulls is at least 9 knots. The duration of a gust is usually less than 20 seconds.” By contrast, “sustained winds” are defined as the “wind speed determined by averaging observed values over a two-minute period.”

The model time-step used in each simulation discussed here is 12 seconds, and model output is only produced every 5 min. Thus, the wind speeds reported herein generally fall between the above definitions of a “wind gust” and “sustained wind.” Furthermore, a large number of surface winds that meet the “severe” criteria likely occur between output times and are therefore omitted in the estimates discussed here. A number of additional issues complicate comparison of model 10-m winds to observations (such as questions of representativeness error due to spatial and temporal resolution). Thus, instantaneous model wind speed values are not ideal to use within the context of the strict “gust” definition above (e.g., Brasseur 2001). Therefore, the discussion of “severe surface winds” herein is not necessarily intended to represent the observations of severe surface wind had these systems occurred in nature. Instead, grid cell values of 10-m wind speed are quantified for relative comparisons between model simulations only, and it is understood that the representation of true severe surface wind occurrences is in this way likely an underestimate relative to what an MCS of similar intensity would produce in nature. At the same time, Bryan et al. (2003) illustrated the tendency for 1-km gridspacing to maximize low-level winds, we have also neglected surface friction, and there are many errors inherent in severe weather reports (e.g., Trapp et al. 2006); thus it is emphasized that the model severe surface winds are far from perfect in their approximation of severe wind reports in an observed MCS. Despite these approximations and the fact that other surface wind magnitude thresholds are also used in both figures and text analyses here, and the use of “severe” terminology is still reserved for the 50kt (25.7ms^{-1}) NWS criterion noted.

5.1.2 Comparison of occurrence of severe surface wind speeds in sensitivity simulations

The five simulations analyzed in Chapter 4 are also examined here with respect to changes in surface wind speed production. An estimate of severe surface wind speed occurrence is obtained by counting the total number of grid points with 10-m wind speed values $> 25.7\text{ms}^{-1}$ (Fig. 5.1a,b) and normalizing this number by storm area (i.e., the number of grid points in which simulated composite reflectivity exceeds 30dBZ) (Fig. 5.1c,d). Comparing the total number of reports per storm area for all five simulations shows that the DRYM simulation generates more than four times the number of severe surface winds produced by CTRL, REVP, and NSUB (Fig. 5.1d). The NMLT simulation actually produces slightly higher numbers of severe surface winds than CTRL, but as later analysis will show, this is due to isolated downbursts early in the simulation (\sim F05; Fig. 5.1a,c) that appear to result from unrealistically-large hydrometeor concentrations (and thus precipitation-loading) due to large, unmelted ice particles. REVP fails to produce any severe surface winds after \sim F05.

The following sections examine the variation of strong and severe surface winds in the sensitivity simulations. Considerable differences are noted between the CTRL and DRYM simulations in particular, with respect to spatial distribution, intensity, and generation mechanisms of severe surface winds (Fig. 5.2). Comparisons of these simulations are emphasized below, with a focus on severe winds associated with gust front mesovortices in section 5.2 and severe winds in the TSR in section 5.3.

5. 2 Association of CMT, mesovortices, and surface wind gust generation

5.2.1 Superpositioning of the RIJ and mesovortices

Mesovortices found along the leading edge of a bow echo gust front have been found by several recent studies to play an important role in the production of straight-line wind damage. Mesovortices are generally defined as meso- γ -scale (e.g., 2 – 40 km) circulations formed at low levels (usually $<1\text{km}$ AGL) on the bow echo gust front (e.g., Weisman and Trapp 2003). Several theories exist to explain mesovortex generation; Atkins and St. Laurent (2009b) document two different generation mechanisms capable of existing within the same system, and still other generating processes have been

suggested by studies such as Lee and Wilhelmson (1997), Weisman and Trapp (2003), Wakimoto et al. (2006), Wheatley and Trapp (2008), and others. The two generation mechanisms found in the most recent work by Atkins and St. Laurent (2009b) are shown in Fig. 5.3. Both mechanisms depend on some source of downward motion to tilt horizontal vorticity (formed by baroclinicity in the leading edge of the cold pool) upward into the vertical¹. However, the source of the downward motion varies between the mechanisms, as does the structure of mesovortices that are formed.

While the generation of the mesovortices themselves is not the focus of this work, it has been suggested that the enhanced surface winds that are often associated with mesovortices may be related to CMT. Wakimoto et al. (2006) and Atkins and St. Laurent (2009a) both describe a mechanism by which the collocation of a descending RIJ (and the CMT inherent therein) and the circulation associated with a gust front mesovortex may produce concentrated areas of intense winds where the wind fields associated with each feature are constructively superpositioned (Fig. 5.4).

The CTRL simulation discussed in Chapter 4 reveals several areas in which mesovortices and strong surface winds are collocated. Figure 5.2a shows areas of severe surface winds with respect to the leading edge of the cold pool in CTRL. Many of the areas of strong surface winds are located within and along the inflection points of the outflow that often indicate the presence of a gust front mesovortex. Examination of surface wind speed and low-level vorticity along the leading edge of the MCS confirm that the two fields are spatially correlated with one another at multiple locations along the line (Fig. 5.5a). Closer examination of four mesovortices present during the CTRL simulation MCS's mature phase (MV1 – MV4 as indicated in Fig. 5.5a) provides evidence for processes that bear strong resemblance to the general mechanism shown in Fig. 5.4. This is illustrated to varying degrees in each mesovortex by the areas of strong surface wind frequently found at the intersection of descending rear inflow (implied by

¹ Note that previous studies such as Wakimoto et al. (2006) have attributed mesovortex formation to *downward* tilting of this horizontal vorticity found in the cold pool vortex lines; while the solution of this discrepancy remains incompletely understood and is beyond the scope of this work, the reader is directed to Atkins and St. Laurent (2009b) section 5 for a discussion of this inconsistency.

areas of low-level descent and surface wind vectors pointing in a rear-to-front direction in Fig. 5.6) and the region to the south of the cyclonic mesovortex (in which flow associated with the mesovortex would generally be in the same direction as MCS motion and the descending rear inflow). While the spatial coverage of RIJ descent produces strong wind speed along extensive portions of the system, the strongest winds commonly occur in association with gust front mesovortices. In the vicinity of MV 1 – 4 specifically, the most intense windspeed maximum occurs where the cyclonic circulation associated with each mesovortex would presumably be superimposed on strong background flow provided by convective downdrafts and/or the descent of the RIJ.

Vertical cross-sections of MV1 – MV4 illustrate that there is variability in the degree and manner of RIJ descent in each mesovortex area (Fig. 5.7). MV1 is associated with a relatively weak RIJ that remains mostly elevated; the mesovortex itself is of comparable strength with MV2 – MV4, but the winds realized at the surface are weaker ($\sim 18\text{ms}^{-1}$ in MV1 vs. $\sim 30\text{ms}^{-1}$ in MV2 – MV4). MV2 shows strong mid-level winds that descend gradually toward the leading edge of the gust front, and in MV3 and MV4 the RIJ descends far behind the gust front (150 – 200 km), with strong, barely-elevated flow persisting less than $\sim 250\text{m}$ above the surface behind the leading edge of the gust front over this distance. For MV2 – MV4, closer inspection of the leading edge of the gust front shows that for each surface wind maxima, rear inflow had descended a considerable distance prior to penetrating the actual surface at the mesovortex location (Fig. 5.8).

Some studies have debated the role of mechanically-forced downdrafts versus precipitation-driven downdrafts in mesovortex formation (e.g., Trapp and Weisman 2003; Wakimoto et al. 2006). While the relevant analysis times here begin after the mesovortex has already formed, it appears that both types of downward motion ultimately contribute to downward motion linked to surface wind maxima. Hydrometeor fields for MV1 – MV4 show variable distributions of hydrometeor maxima, some of which appear to be associated with downdrafts below through precipitation-loading and drag (Fig. 5.9, features PD1 and PD2). Buoyancy minima are collocated with several areas of strong downward motion as well (particularly in the TSR), revealing the effect of microphysical

cooling aloft contributing to downward motion through precipitation processes. However, other areas of strong descent (particularly closer to the leading edge of the convective line) are not clearly associated with precipitation maxima and may thus be mechanically-forced as discussed by Wakimoto et al. (2006). The above mechanisms for downdraft generation thus suggest that in areas of mesovortex-enhanced surface winds (i) the accelerated flow of the RIJ itself (and the CMT inherent in its descent) serves as the main source of momentum that is ultimately responsible for the generation of strong or severe surface winds, and (ii) that the relative roles of convective downdrafts versus a descending RIJ in the production of strong low-level winds vary among individual surface wind maxima.

5.2.2 CMT and severe surface wind generation within mesovortices

A link between CMT and the generation of strong low-level winds in the vicinity of gust front mesovortices has been suggested by both observational and modeling studies such as Wakimoto et al. (2006) and Atkins and St. Laurent (2009a). The components of the total low-level CMT field [i.e., $VA\bar{u}$ and $|VAu' + VA v'|$ (hereafter $VA V'$)] as calculated by the momentum budgets presented in Chapter 4 illustrate areas in which the RIJ lowers behind the convective line and impinges on the surface, as shown by the maxima of $VA V'$ at 400m AGL in Fig. 5.10. Vertical cross-sections through each mesovortex show variable contributions from CMT associated with each mesovortex feature (Fig. 5.11). In the absence of strong RIJ descent, MV1 shows little to no CMT behind the gust front, and thus any enhancement in surface wind flow (weaker in MV1 relative to MV2 – MV4) appears to be due in most part to the mesovortex itself. Relatively weak low-level $VA V'$ is present below the TSR and in the convective downdraft region in MV2 [note that the large area of positive $VA V'$ preceding the line in all cross-sections corresponds to the upward transport of lower (or storm-relative easterly) windspeeds]. MV3 and MV4 both show marked CMT contributions from $VA V'$ in the TSR, corroborating the above analysis of the importance of the momentum derived from the RIJ descent. Increases in $VA V'$ toward the leading edge of the gust front

demonstrate that the rapid descent of perturbation winds to the surface (likely from convective downdrafts) ultimately connects the descended RIJ flow with the surface in MV3 and MV4, whereas MV2 exhibits severe winds that descend more gradually in the TSR, reaching the surface ahead of the main convective downdraft region. Finally, $V\bar{A}\bar{u}$ also imparts some contribution to the strengthening rear-to-front flow in the TSR; while it is smaller in magnitude, its distribution is more uniform (Fig. 5.11). The relative importance of the transport of ambient winds vs. storm-induced perturbation winds (i.e., $V\bar{A}\bar{u}$ vs $V\bar{A}\bar{V}$) and the area over which transport maxima occur may also play a role in the type of surface wind damage resulting from RIJ descent, even in the absence of a mesovortex. That is, studies have noted the variability of surface wind damage in terms of less intense, more diffuse surface damage as compared to more intense and localized damage swaths (e.g., Wakimoto et al. 2006). Such occurrences in the absence of a gust front mesovortex are discussed in the following section.

While CMT associated with the convective downdrafts appears to explain the final thrust of descent that ultimately produces intense wind at the surface (e.g., Fig. 5.11), earlier transports clearly play an important role in the initial lowering of the RIJ; this is essentially the process described in Chapter 3. The simulation analyzed in Chapter 3 illustrates that the downward transport of a pressure-gradient-accelerated RIJ provides the means by which accelerated mid-level air reaches the surface. This is well-illustrated by the trajectory analysis of RIJ parcels in that simulation; Figure 5.12 reproduces part of Fig. 3.14 to show the increased speed of the actual parcels as they descend through this rear-to-front flow (an increase from $\sim 15\text{ms}^{-1}$ – $\sim 30\text{ms}^{-1}$ over ~ 1.5 hours), linking accelerations in the trailing portion of the system to those experienced at the surface along the leading edge of the gust front. This process, when added to the circulation induced by the low-level mesovortices, is very similar to the general severe wind generation process described by Wakimoto et al. (2006), but details of the specific processes and transports that ultimately generate the severe surface winds remain elusive.

One existing conceptual model of the role of the RIJ in mesovortex-enhanced severe wind generation describes an elevated midlevel RIJ that remains at mid-levels and

descends just behind the leading edge of the gust front; the RIJ is thought to be of secondary importance in wind generation relative to mesovortex circulation (e.g., Wakimoto et al. 2006; Wheatley et al. 2006; Atkins and St. Laurent 2009a). However, the above findings illustrate that the RIJ may descend incrementally, first to low levels (at or below just ~1 km AGL) and then descend to the surface in the presence of additional downward motion (such as the convective downdrafts found just behind the leading edge of the gust front².) Furthermore, mesovortices that occur in the absence of particularly strong wind speeds (e.g. MV1 and several other mesovortices in Fig. 5.5a) suggest that the mesovortex circulation in isolation (of a descended RIJ) may not be sufficient (or necessarily dominant) to significantly accelerate surface wind speeds in some cases (e.g., Atkins and St. Laurent 2009a; Fig. 5.4). While such modifications to the above conceptual model may lack obvious implications for predicting the presence or absence of severe surface winds at the gust front leading edge (as their occurrence seems likely in the event of favorable super-positioning regardless of which feature is “dominant”), it is conceivable that forecast implications may still exist and warrant further study. For example, if the RIJ descends at a greater relative distance beyond the leading edge of the system, strong surface winds become more likely over a greater surface area; it is also likely that the timing and placement of severe surface winds relative to the gust front leading edge would be impacted. A similar scenario and possible revised conceptual model focusing on RIJ descent specifically is described in the following section.

The CMT process helps to explain the generation of strong straight-line surface winds associated with gust front mesovortices and RIJs. A key question posed by several recent mesovortex studies is the relationship between mesovortices and bow echo tornadoes (e.g., Atkins et al. 2005; Wakimoto et al. 2006) – increased understanding of the distinction of straight-line wind processes and tornadogenesis in bow echoes may also benefit from improved understanding of convective-scale momentum transports at the bow echo apex. Furthermore, Atkins and St. Laurent (2009a) note that application of the

² It is also conceivable that the planetary boundary layer (PBL) scheme contributes to the CMT process by mechanically mixing RIJ winds downward; this is corroborated by enhanced PBL scheme momentum tendency values in areas in which the RIJ connects with cold pool winds (*not shown*).

RIJ-mesovortex severe wind mechanism has not been evaluated across “serial” bow echoes (Johns and Hirt 1987). The simulation shown here bears considerable resemblance to observed serial bow echoes (in that multiple bow echoes are embedded in a large parent squall line) and thus suggests that similar processes are indeed at work. However, a more rigorous investigation employing data from observed cases is necessary in order to better understand the potential differences. Finally, while it is beyond the scope of this particular study to completely isolate the severe surface wind generation mechanism across a number of mesovortex sizes and strengths, future work may benefit from use of momentum and vorticity budgets of the severe wind-mesovortex features themselves (particularly in a Lagrangian framework), as well as comparisons of the variation of mesovortex frequency, size, and strength in the various sensitivity simulations (as sensitivity is indeed suggested by the results shown here). In summary, if the prediction of concentrated areas of severe surface winds associated with bow echoes and mesovortices is to be attempted or improved, a momentum transport framework (e.g. Lagrangian analysis of descending parcels, etc.) and/or further investigation of the specific role of CMT is likely to greatly enhance understanding of the processes at work.

5.3 CMT and severe surface winds in the TSR

Descending rear-inflow jets have been observed to produce damaging surface winds, particularly at the apex of an MCS bow echo (e.g., Fujita 1978; Wheatley et al. 2006). Observations show that damage can occur along a storm’s leading edge both in isolated, small-scale swaths as discussed above, and also in larger, more diffuse areas (e.g., Forbes and Wakimoto 1983; Johns and Hirt 1987; Wakimoto et al. 2006). Wheatley et al. (2006) and Kuchera and Parker (2006) discuss how these two factions of severe thunderstorm wind mechanisms have typically been treated as separate problems in the literature, with most studies separating intense thunderstorm downdrafts due to precipitation or dynamic pressure forces (e.g., Fujita and Wakimoto 1981) from winds produced by more persistent, larger-scale features such as descending RIJs associated with bow echoes and MCSs (e.g., Weisman 1992; 1993). In either case, the location of

interest for severe wind generation is typically at or near the leading edge of the gust front or bow echo apex. Rutledge et al. (1988) and Weisman (1992) discuss RIJs that descend to the surface 20 – 30 km rearward of the leading edge of the cold pool, and Johnson and Hamilton (1988) discuss strong winds produced in the TSR by wake lows. The former cases are analyzed as non-severe, decaying systems, while the latter involves strong front-to-rear directed winds by local pressure gradient accelerations. While likely less common, it is conceivable that severe wind speeds may also be generated by RIJ processes in areas that extend well rearward of the leading edge of the gust front.

Most severe wind forecasting and nowcasting applications focus on predicting the processes that lead to intense, localized downdrafts formed along the leading edge of the gust front. These winds are often the product of the general “downburst” process – defined by Fujita (1978) as “a strong downdraft inducing an outward burst of damaging winds on or near the ground.” Many subsequent studies have further detailed this process by which convective downdrafts intersect the surface and diverge quickly outward, often producing an asymmetrical pattern of severe winds due to both shear- and pressure-gradient-induced accelerations (e.g., Fujita and Wakimoto 1981; Eilts and Doviak 1987; Vescio and Johnson 1992; Orf and Anderson 1999, Wakimoto 2001). Although the downdrafts themselves can have several possible causes, they are generally described as either precipitation-driven (e.g., hydrometeor-loading, cooling due to evaporation, melting, or sublimation) or mechanically-driven. Wakimoto (2001) provides a comprehensive summary of past studies of downburst initiation and dynamics.

While much research has been devoted to downbursts and related phenomenon (e.g., microbursts, macrobursts), understanding and predicting the descent of the RIJ and the potential for realizing severe surface winds in areas other than the bow echo apex has received much less attention. The following sections address the role that CMT may play in producing strong surface winds closer to the TSR and away from the gust front leading edge.

5.3.1 CTRL

Severe surface winds in the CTRL simulation are most common along the leading edge of the gust front and particularly near gust front mesovortices³, as described above (Fig. 5.2). However, several occurrences of severe or nearly-severe surface winds are generated in “atypical” locations that trail the gust front by more than 50km (e.g., Fig. 5.13). A vertical cross-section taken through the leading edge of the gust front at F06 illustrates that the area of strong surface winds found over 50km to the rear of the gust front appears to be generated by a different process (i.e., intensity and spatial concentration of downdraft) than those closer to the leading edge (Fig. 5.14); a series of vertical cross-sections demonstrates the persistence of these varied downdraft types (Fig. 5.15). Descent behind the leading edge of the gust front is characterized by low-level (0 – 3 km AGL) concentrated, intense downdrafts (points A and B in Fig. 5.14), trailed by a more diffuse area of weaker and slightly more elevated (1 – 5 km AGL) downdrafts, with magnitudes generally $\sim 0.5 \text{ ms}^{-1} - 2 \text{ ms}^{-1}$. For this particular area of the storm at this particular time, the surface winds that exceed the severe threshold are actually those associated with the weaker descent toward the TSR rather than stronger downdrafts at the leading edge of the cold pool. The series of vertical cross-sections (in addition to the previously discussed trajectory analysis of the descending RIJ) suggests that for severe surface wind generation here, strong downdrafts may not be necessary in order to produce strong surface winds, as the winds are more of a product of the accelerated horizontal momentum of the RIJ descending to the surface. While the winds at the leading edge of the gust front are accompanied by concentrated, intense downdrafts close to the leading edge (fitting Fujita’s downburst definition), strong surface winds located rearward appear to result mostly from the descent of the RIJ from the vertical advection of the accelerated horizontal momentum in the RIJ (Fig. 5.14). However, it should be noted that “convective” downdrafts in the TSR may account for some of this transport as well, although the spatial and temporal resolution of the dataset precludes clear identification of the origin (i.e. convective or stratiform) of the descent.

³ The results presented here suggest that mesovortices are most common in the CTRL simulation and less so in DRYM. It is beyond the scope of this work to investigate sensitivity of mesovortex formation to the model modifications made here, but work in this area is ongoing.

The role of momentum transport in the production of RIJ-driven severe surface winds is well-illustrated by $V\bar{A}\bar{u}$ and VAV' as before. Each field is plotted for the series of cross-sections as in Fig. 5.15, and also in more detail at F06 (Fig. 5.16, Fig. 5.17 respectively). The transport of the storm-induced rear-inflow is illustrated by the maximum of VAV' that persists just above the area of strong-severe surface winds trailing the cold pool's leading edge. The magnitude of this feature is quite large, generally exceeding $20 - 40 \text{ ms}^{-1}\text{h}^{-1}$ at $1 - 2 \text{ km AGL}$. While $V\bar{A}\bar{u}$ is generally $2 - 4$ times weaker than VAV' , the process does maximize ($\sim 10 - 15 \text{ ms}^{-1}\text{h}^{-1}$) just above the area of severe surface winds as well, showing that the downward transport of the ambient flow also contributes to the severe wind generation at the ground. The contribution of the background environmental wind to severe surface winds has been discussed by previous studies such as those by Foster (1958), Johns and Doswell (1992), Evans and Doswell (2001), Geerts (2001), and Kuchera and Parker (2006); this topic is further elaborated in Chapter 6.

5.3.2 DRYM

The DRYM simulation not only produces severe surface winds at more gridpoints relative to the CTRL simulation, but the spatial distribution relative to the leading edge of the gust front also differs. Similar to the process described above, the DRYM simulation produces severe winds across broad areas that trail the system's leading edge relative to CTRL (Fig. 5.2). These areas also tend to display more persistence in time as well, existing as continuous entities as opposed to isolated, short-lived microbursts (Fig. 5.18). While an overall enhancement in downward motion is expected due to increased evaporative cooling in the TSR, what specific process explains these areas of strong surface winds in the leading portion of the TSR?

A series of cross-sections is taken for DRYM at F07 as was done above for CTRL, focusing on an area in which strong surface wind speeds are produced both at the gust front as well as in a separate larger area behind it (Fig. 5.19). Examining the CMT fields ($V\bar{A}\bar{u}$ and VAV') demonstrates that the transport of horizontal momentum [both the

ambient momentum (\bar{u}) and perturbation momentum $u' + v'$ (V')] is stronger by up to 100% in many places in this particular feature in DRYM relative to that discussed above for CTRL (c.f. Fig. 5.20, Fig. 5.16). The enhanced contributions of each process to the strong surface winds that trail the gust front are especially evident at F0730 (Fig. 5.21). Examination of the intensity and patterns of descent also shows the enhanced regions of descent in the vicinity of the surface wind maxima relative to the CTRL simulation (cf. Figs. 5.15, 5.22).

For a more systematic assessment of the differences noted in the specific features above, a series of CFADs are again provided in Figs. 5.24 – 5.28. As expected, enhanced microphysical cooling is evident in DRYM, and the magnitude of downward motion is larger, particularly at low levels (Figs. 5.24, 5.25, respectively). The increase in downward motion thus suggests systematic increases in CMT over this region as well, assuming the horizontal momentum fields remain comparable. Fig. 5.26 shows subtle enhancement of the low-level wind magnitude ($\sim 0 - 2$ km AGL) in DRYM relative to CTRL, but RIJ-level winds in CTRL are generally stronger at this time ($\sim 3 - 6$ km AGL). This is consistent with the results discussed above, given the enhanced RIJ descent in the DRYM simulation.

The CMT terms as calculated by the momentum budgets (i.e., $VA\bar{u}$ and VAV') are both larger in DRYM relative to CTRL over this same region (positive values shown in Figs. 5.27 and 5.28, respectively). In light of these apparent dynamical differences, it is tempting to directly attribute increased surface wind speeds in the TSR to increased CMT. However, while it is conceivable that increased CMT via evaporative cooling-enhanced downward motion increases TSR severe wind speeds, the relationship may not be easily generalized to severe wind occurrences overall in other types of environments. First, one must examine the stability of the surface cold pool. The DRYM simulation generally shows a smaller surface temperature perturbation and spatial extent of the surface cold pool; studies such as Weisman (1992) have shown that the weaker the surface cold pool, the greater the potential for RIJ descent rearward of the convective region. Thus, comparisons of T' (Fig. 4.6), buoyancy (Fig. 4.7), c -calculations (Fig.

4.41c), and CMT fields (Fig. 5.20) shown herein and in Chapter 4, support the notion that the weaker cold pool in DRYM likely enhances the propensity for DRYM to produce more than four times the occurrence of severe surface winds relative CTRL.

Second, RIJ descent in the TSR and convective downdrafts in the leading convective region often produce two different types of severe wind. The former is often considered to be less intense and potentially longer-lasting, and the latter more localized, short-lived, and intense (e.g., Geerts 2001; Wakimoto 2001; Kuchera and Parker 2006). In the present set of comparisons, the DRYM simulation shows enhanced downdraft intensity in the TSR, and thus enhanced low-level momentum due to RIJ descent. In this particular simulation, downdraft intensity in the convective region of DRYM remains strong despite slightly weakened updrafts; thus winds at the leading edge of the gust front are similar between CTRL and DRYM. If the DRYM MCS was much weaker than that of CTRL (e.g., due to enhanced entrainment), it is conceivable that downdraft intensity near the leading edge of the gust front would decrease and fewer severe winds might be realized there. Here, the combination of enhanced TSR descent, increased low-level flow from CMT, and a slightly weaker and horizontally smaller surface cold pool appears to account for the significantly larger numbers of severe surface winds in the DRYM simulation, particularly those occurring in or toward the TSR. That RIJ descent accounts for these instances of severe surface winds appears to suggest a deviation from the current conceptual model of RIJ-driven surface winds in which descended rear inflow causes more diffuse and less intense surface wind swaths.

Studies such as Johns and Doswell (1992), Weisman (1992), Yang and Houze (1995), Evans and Doswell (2001), and Geerts (2001) have commented on the complexity of observed RIJ dynamics and related impacts on convective wind gust generation. Beyond this simple CTRL vs. DRYM comparison, other issues remain to be explored. For example, drying mid-levels in MCS simulations can have consequences of which analysis is beyond the scope of this investigation. For example (and as mentioned in the initial hypotheses), updraft buoyancy can be reduced due to dry air entrainment (despite the possibility that this process may be under-represented by a simulation using

1-km grid spacing), thus decreasing vertical motion and potential hydrometeor concentration as well. Such feedbacks may in turn affect updraft tilt and cold pool intensity, and thus obscure an already complex signal. While the feedbacks may not be perfectly understood, it is possible that further investigation of observed and simulated MCSs in a greater variety of environments may clarify the specific signals of greatest potential utility to forecasters.

5.3.3 REVP, NMLT, and NSUB

A comparison of severe surface winds and gust front locations for the REVP, NMLT, and NSUB simulations is provided in Fig. 5.29. As discussed in section 5.1.2, the NMLT simulation actually produces slightly higher occurrences of severe surface winds relative to CTRL. As shown in Fig. 5.29, such occurrences are quite isolated and mostly located away from the leading edge of the gust front. Figure 5.30 shows the main area of severe surface winds in NMLT to be associated with an intense hail shaft that extends all the way to the surface, likely present and of large intensity due in large part to the removal of the melting process. While lower-altitude downdrafts initiated by precipitation loading have been shown to lead to severe-wind producing downbursts (e.g., Kingsmill and Wakimoto 2001), the NMLT simulation demonstrates this process to occur over larger areas than any of the other simulations.

As the main surface wind speed differences seen in NMLT and NSUB appear to be a product of unrealistically large hydrometeor concentrations resulting from the experimental design of the microphysics sensitivity tests, these simulations will not be further analyzed here. However, that REVP produces virtually no severe surface wind occurrences is consistent with the enhanced surface wind speeds realized in DRYM (where evaporative cooling increases, e.g., Figs. 4.9; 4.18). A large number of previous studies as well as most current surface wind gust forecast indices systematically assess the potential for evaporative cooling to produce or strengthen downdrafts that may penetrate the surface and lead to wind damage (e.g., Wakimoto 2001; Kuchera and Parker 2006; Cohen et al. 2007). While the results of these simple sensitivity experiments

certainly corroborate that basic principle, the analysis of DRYM and CTRL in the preceding sections suggest that the sensitivity to evaporative potential may be strongly linked to kinematic considerations (e.g., increased CMT in the descending RIJ) as well as thermodynamic arguments (e.g., downburst production by cooling due to microphysical processes). Possible forecast implications of this idea are discussed in Chapter 6.

5.4 Summary

Wakimoto (2001) emphasizes that forecasting thunderstorm outflow windspeeds remains a critical but unresolved problem. While the contribution of CMT obviously does not explain or solve such a complex issue, the concept and process in general may offer an advantageous framework in which to better understand surface wind generation and ultimately contribute to improved wind gust forecasts and warnings.

In section 5.2, CMT is examined with respect to a proposed mechanism for severe surface wind production in the vicinity of mesovortices. Several of the leading theories for mesovortex generation are directly linked to the descent of the RIJ and/or convective downdrafts; a specific connection with CMT is suggested when severe surface are produced via a superpositioning of a descending RIJ and the low-level circulation associated with a gust front mesovortex (Wakimoto et al. 2006; Atkins and St. Laurent 2009a). Such a process is apparent in the CTRL simulation presented here, and illustrates the essential contribution of descended RIJ winds to producing severe surface windspeeds in most gust front mesovortices.

In section 5.3, the potential for a descending RIJ to generate strong surface winds at locations away from the leading edge of the gust front is discussed. While this process may occur in a variety of storm environments, it is shown that the additional downward motion imparted by decreasing the relative humidity of the mid-levels increases mid-to-low-level CMT fields and contributes to increased occurrences of strong surface winds.

The work of Weisman (1992) comprehensively investigates the processes that impact the degree to which a RIJ remains elevated or descends. The results of his study illustrate that understanding the introduction of mid-level dry air in this process in quite

complicated. Studies such as Fovell and Ogura (1988) and Yang and Houze (1995) have investigated the effect of dry air on downdraft strength, rear-inflow generation, and cold pool intensity in MCSs, which still others have commented on the possibility that momentum from rear inflow may increase lift along the leading edge of the cold pool (e.g., Smull and Houze 1987; Lafore and Moncrieff 1989). Further complexity exists when considering the ability of descending air to penetrate a surface cold pool; understanding of the potential for severe winds in a stable surface environment remains an area of ongoing research. Findings and discussions by Weisman (1992), Bryan and Weisman (2006), Kuchera and Parker (2006), Parker (2008), and James and Markowski (2009) have shown that the relationship between surface cold pool stability and severe surface winds remains somewhat ambiguous.

The idea that a descending RIJ can cause strong surface winds is not unique or novel, but most studies limit the discussion of the potential for RIJ-driven surface winds at the gust front leading edge or the apex of a bow echo. The distinction of these two areas of strong surface winds and the different generation mechanisms responsible may be relevant to forecasting or nowcasting the potential for and the intensity of severe surface wind gusts; ideas for future investigation of this area are outlined in Chapter 6. The results presented here add to a growing body of knowledge that improves our understanding of the specific processes that produce damaging surface winds, and may hold promise in updating both the conceptual framework of this topic as well as forecast strategies to better predict such occurrences.

The issue of surface wind speed generation in MCSs (Chapter 5) and system motion (Chapter 4) are certainly not separate; studies such as Johns and Hirt (1987), Orf and Anderson (1999), Evans and Doswell (2001), and Kuchera and Parker (2006) discuss aspects of the connection between the flow in which an MCS is embedded, the speed at which it moves, and the potential for damaging surface winds. The analyses in Chapters 3, 4, and 5 performed within the framework of CMT are indeed consistent with this hypothesized connection.

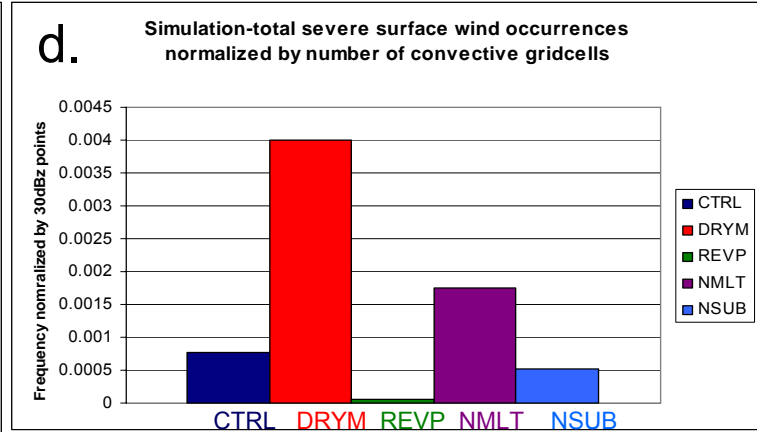
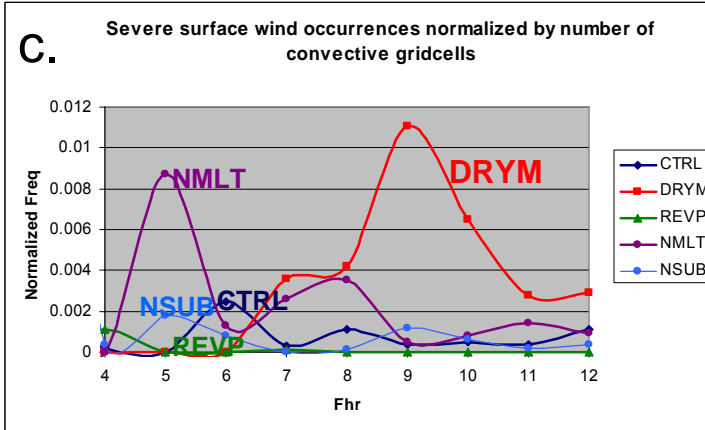
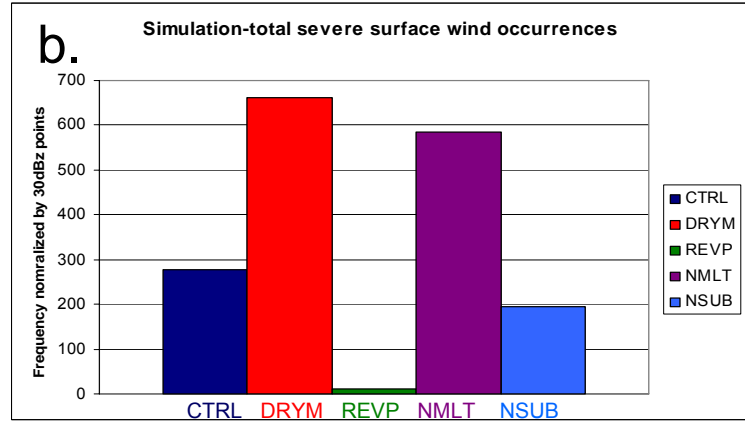
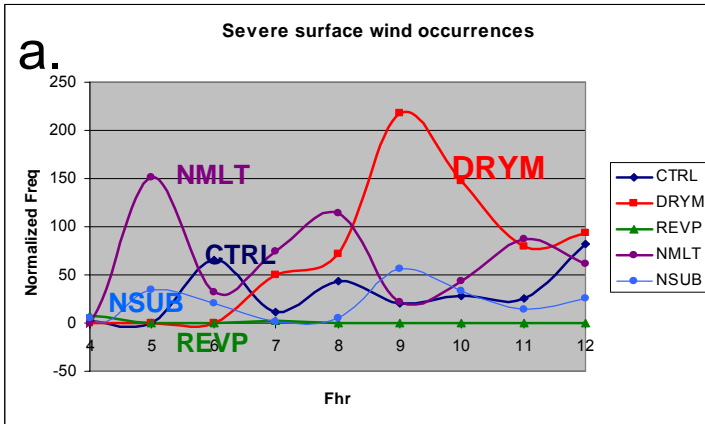


Figure 5.1: a) Total number of gridpoints with 10-m wind magnitude $> 25.7\text{ms}^{-1}$ vs. time (hours) on x-axis; b) total number of gridpoints with 10-m wind magnitude $> 25.7\text{ms}^{-1}$ for entire simulation; c) as in a) except normalized by storm area (number of gridcells with simulated composite reflectivity $> 30\text{dBZ}$); d) as in b) except for normalized values in c).

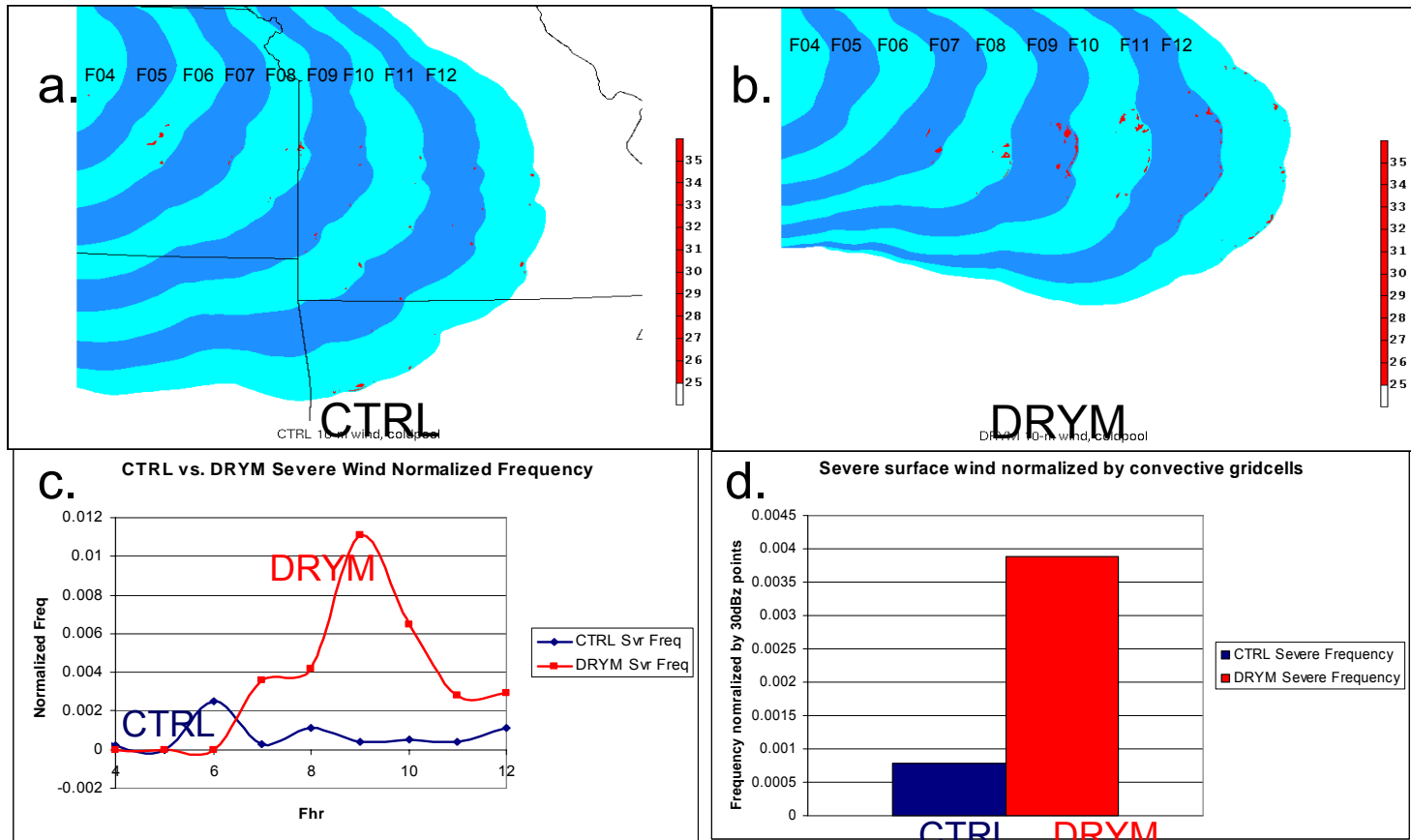


Figure 5.2: a) CTRL cold pool ($T' = -2^{\circ}\text{C}$, light and dark blue for times as labeled, areas of gridcell 10-m wind magnitude $> 25.7\text{ms}^{-1}$ (red, shaded); b) as in a) except for DRYM; c) as in Fig. 5.1c except comparing CTRL and DRYM only; d) as in Fig. 5.1d except comparing CTRL and DRYM only.

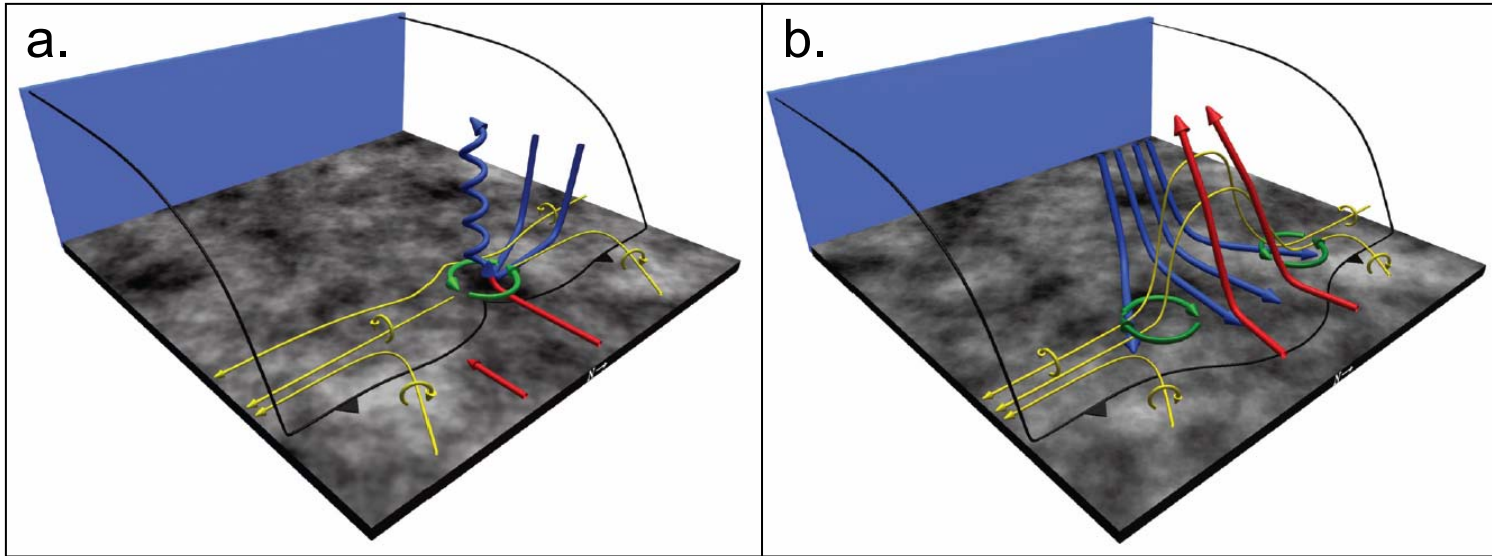


Figure 5.3: Mesovortex generation mechanisms from Atkins and St. Laurent (2009b). a) Cyclonic-only genesis; b) cyclonic-anticyclonic mesovortex couplet genesis. See Atkins and St. Laurent (2009b) for further detail.

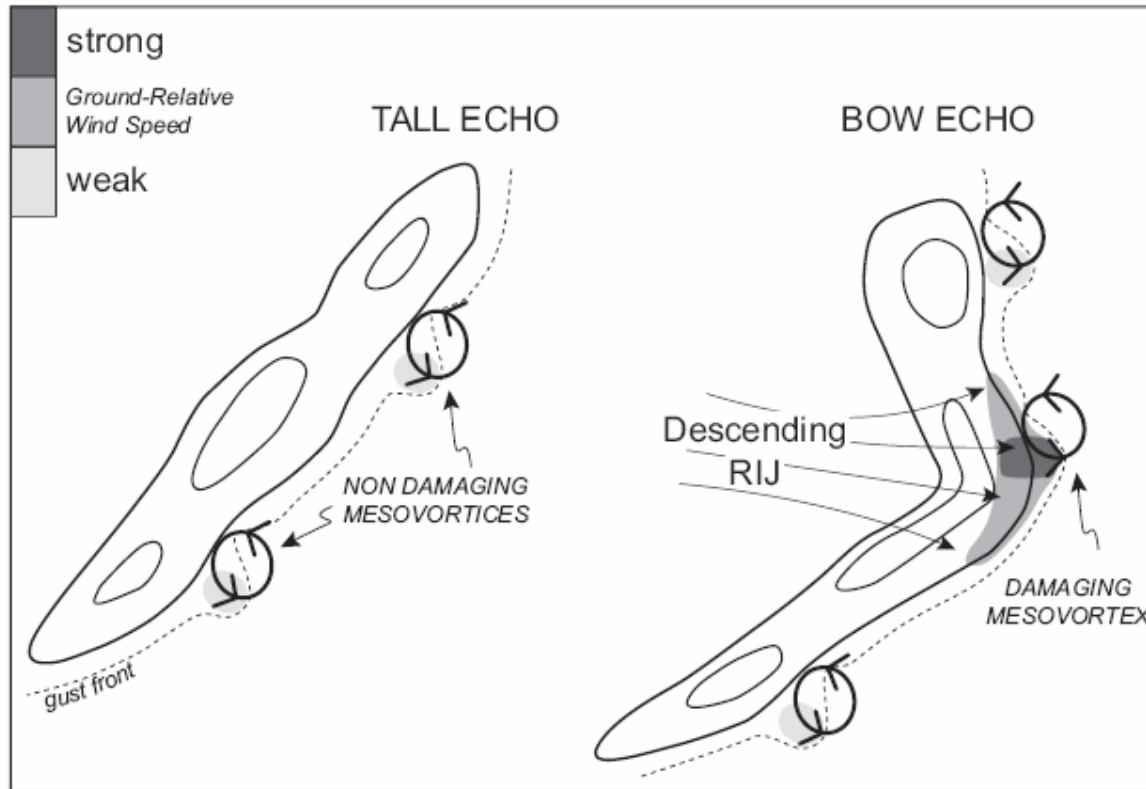


Figure 5.4: Damaging wind generation mechanism (right) from descending rear-inflow jet (RIJ) and gust front mesovortex superposition versus non-damaging mesovortices (left) from Atkins and St. Laurent (2009a).

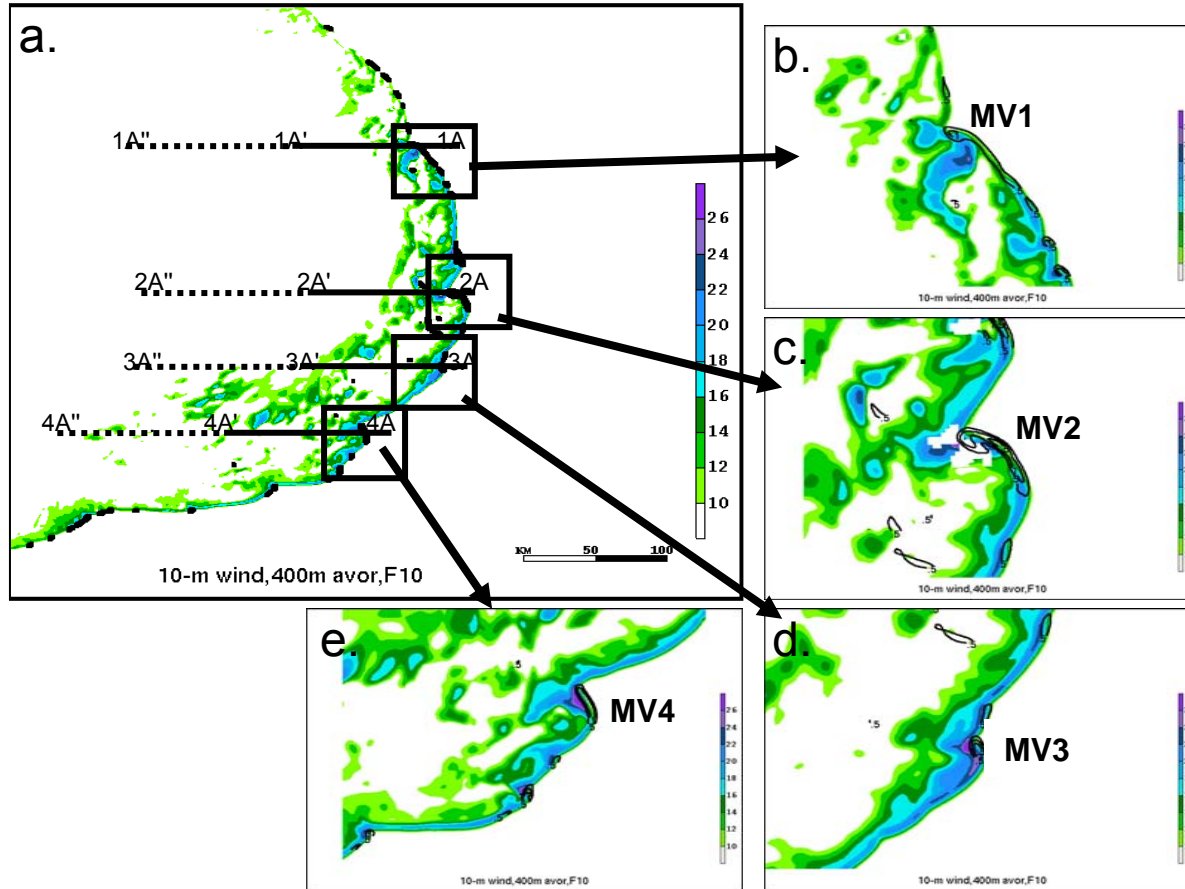


Figure 5.5: CTRL simulation at F10, a) 10-m winds (ms^{-1} , shaded as indicated at right), and 400-m absolute vorticity (black contours, every $0.5 \times 10^{-2} \text{ s}^{-1}$), black lines and labels denote cross-sections used in subsequent figures. b) – e) As in a) but zoomed-in panels in areas indicated by corresponding black boxes in a). Numbers identify individual mesovortices discussed in text.

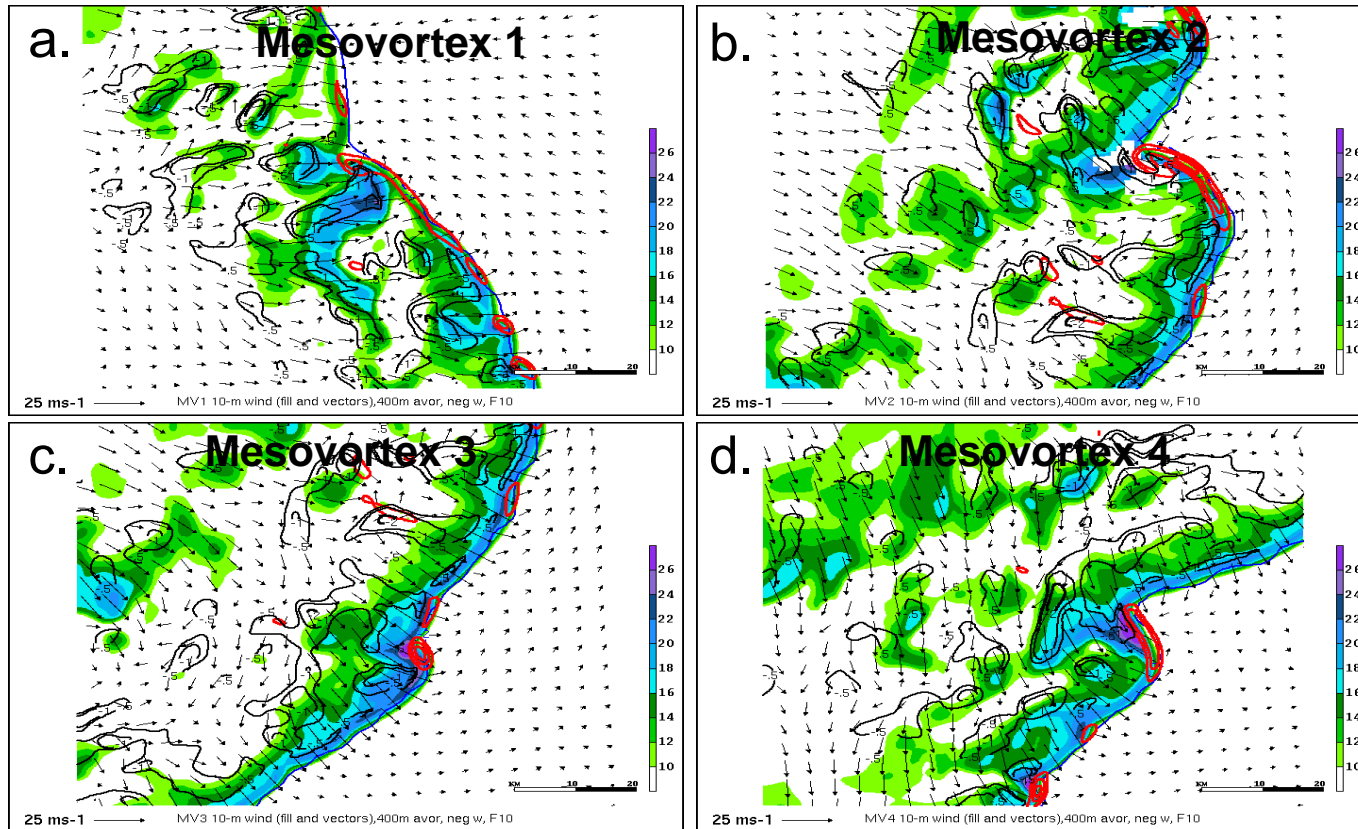


Figure 5.6: 10-m winds (vectors and fill), 400-m vort (red), 400-m w<0 (black): CTRL simulation 10-m winds (ms⁻¹, shaded as indicated at right and shown by vectors; reference vector in lower-left), 400-m absolute vorticity (red contours, every $0.5 \times 10^{-2} \text{ s}^{-1}$), 400-m w<0 (ms⁻¹, black contours, at -0.5, -1, and -2 ms⁻¹) at F10 for a) MV1 a) MV2, c) MV3, and d) MV4.

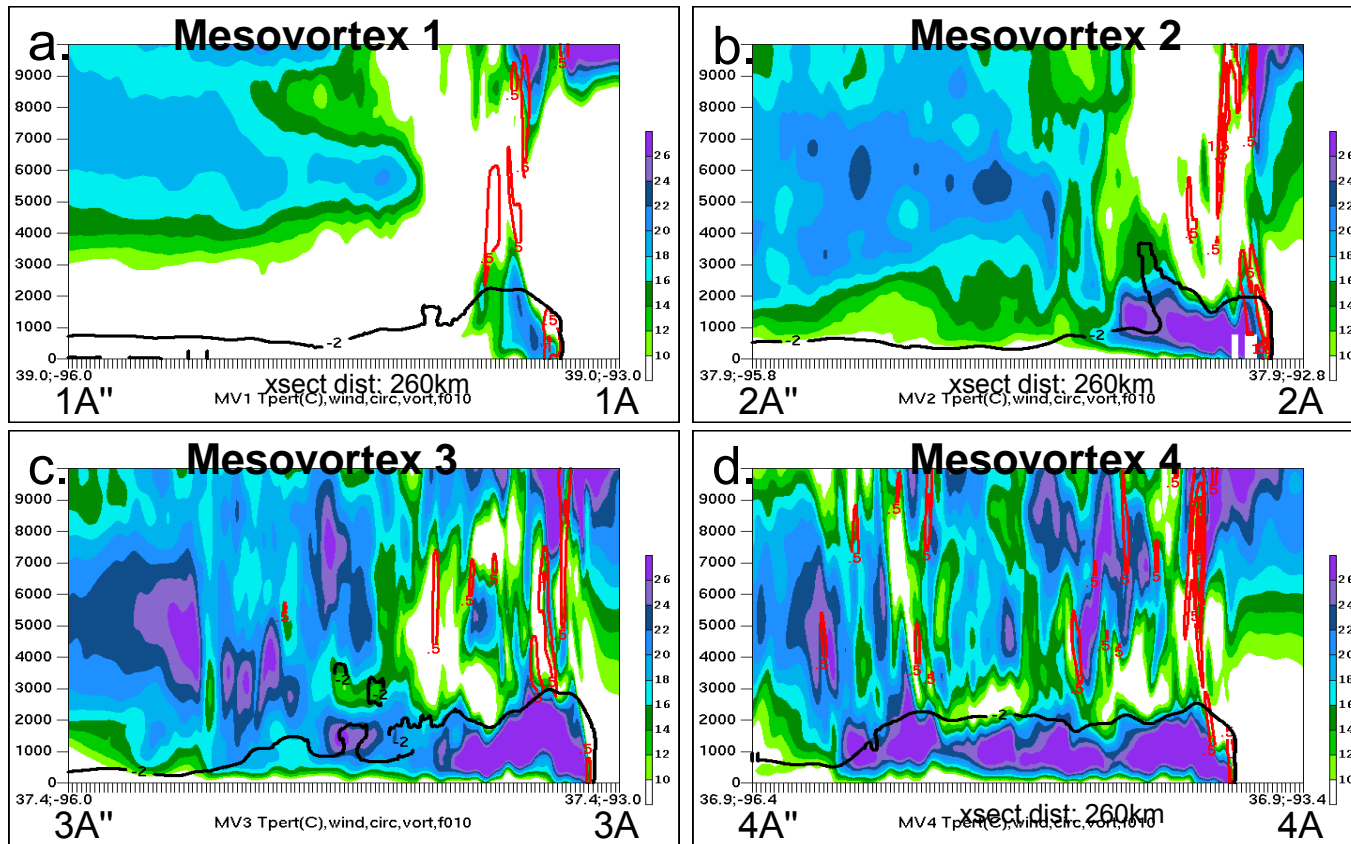


Figure 5.7: East-west vertical cross sections of CTRL at F10 for areas indicated in Fig. 5.5. Total wind magnitude (ms⁻¹, shaded as indicated), cold pool (T' = -2°C, black contour), and absolute vorticity (red contours, every 0.5x10⁻² s⁻¹) for CTRL at F10 for a) MV1 a) MV2, c) MV3, and d) MV4.

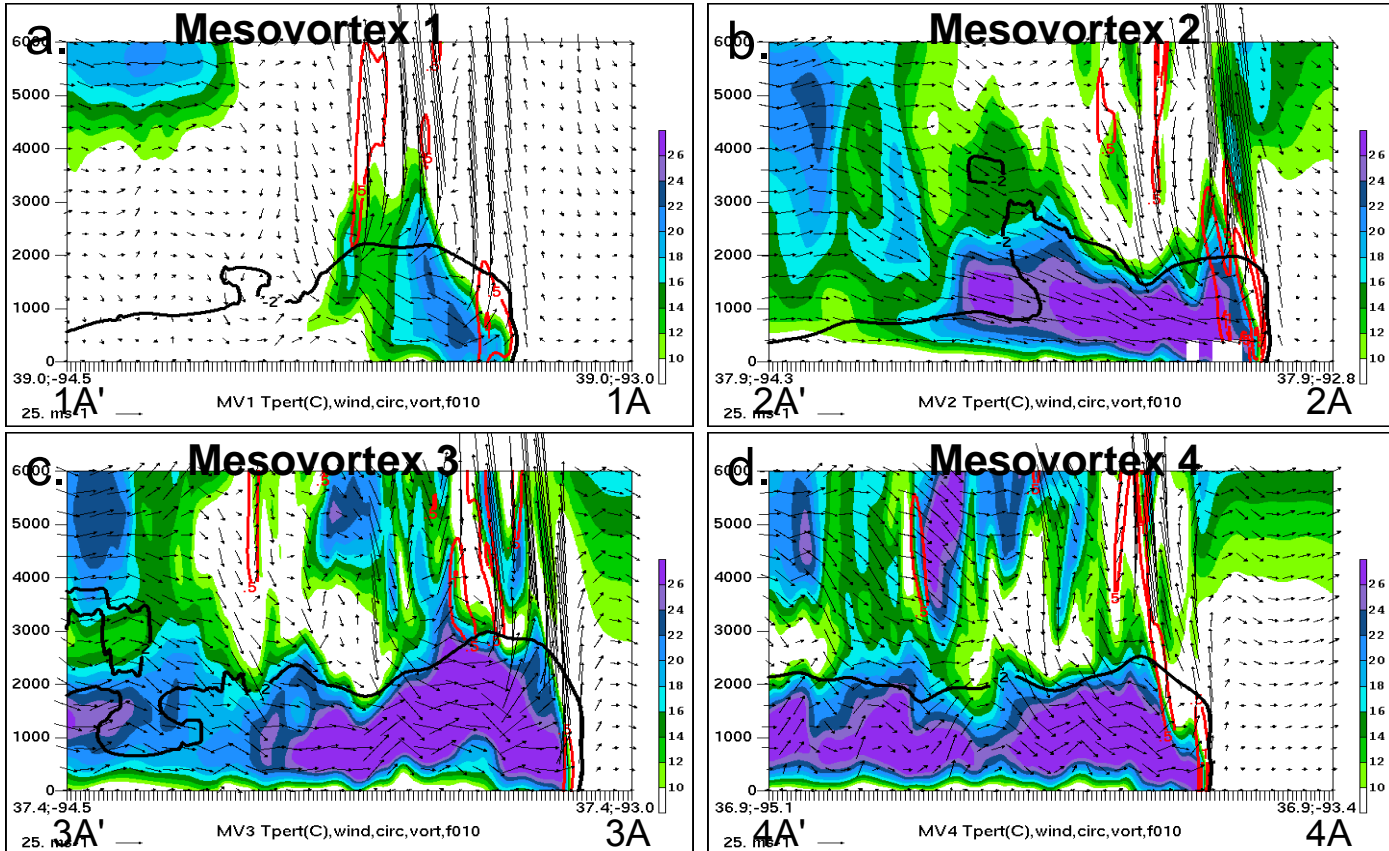


Figure 5.8: As in Fig. 5.7 except for along shortened cross-sections as labeled and shown in Fig. 5.5. Vectors show total wind magnitude (ms^{-1}) according to reference vector in lower left.

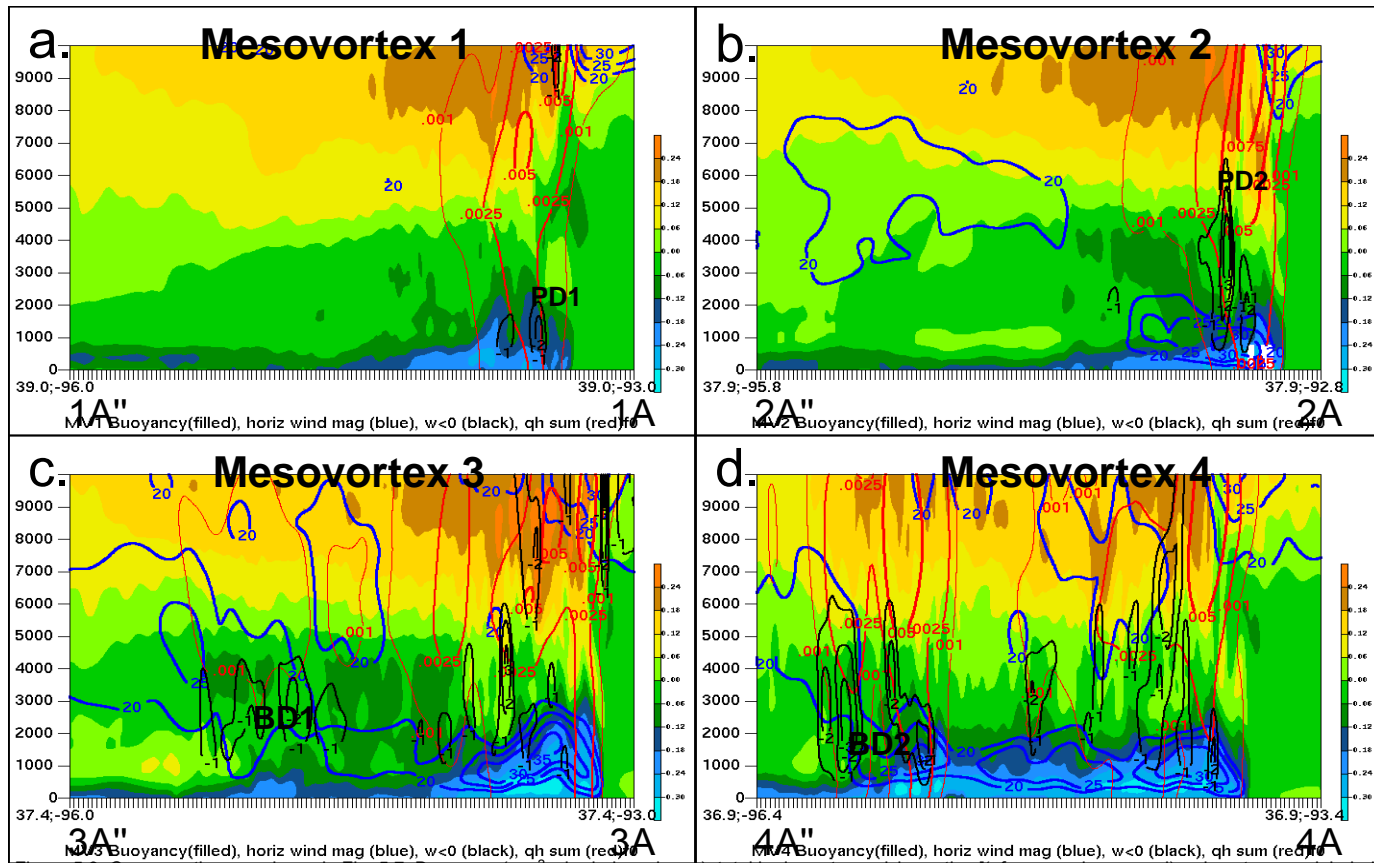


Figure 5.9: Cross-sections as shown in Fig. 5.7. Buoyancy (ms^{-2} , shaded as shown), total hydrometeor mixing ratios [(of snow, rain, graupel) red contours as labeled $\times 10^{-4}$, gkg^{-1}], isotachs of total wind (interval 5ms^{-1} starting at 20ms^{-1} , blue contours), and $w < 0$ (interval 1ms^{-1} , black contours, starting at -1ms^{-1}). PD1 and PD2 denote collocation of hydrometeor maxima and downdrafts; BD1 and BD2 denote regions of buoyancy minima and downdrafts in the TSR.

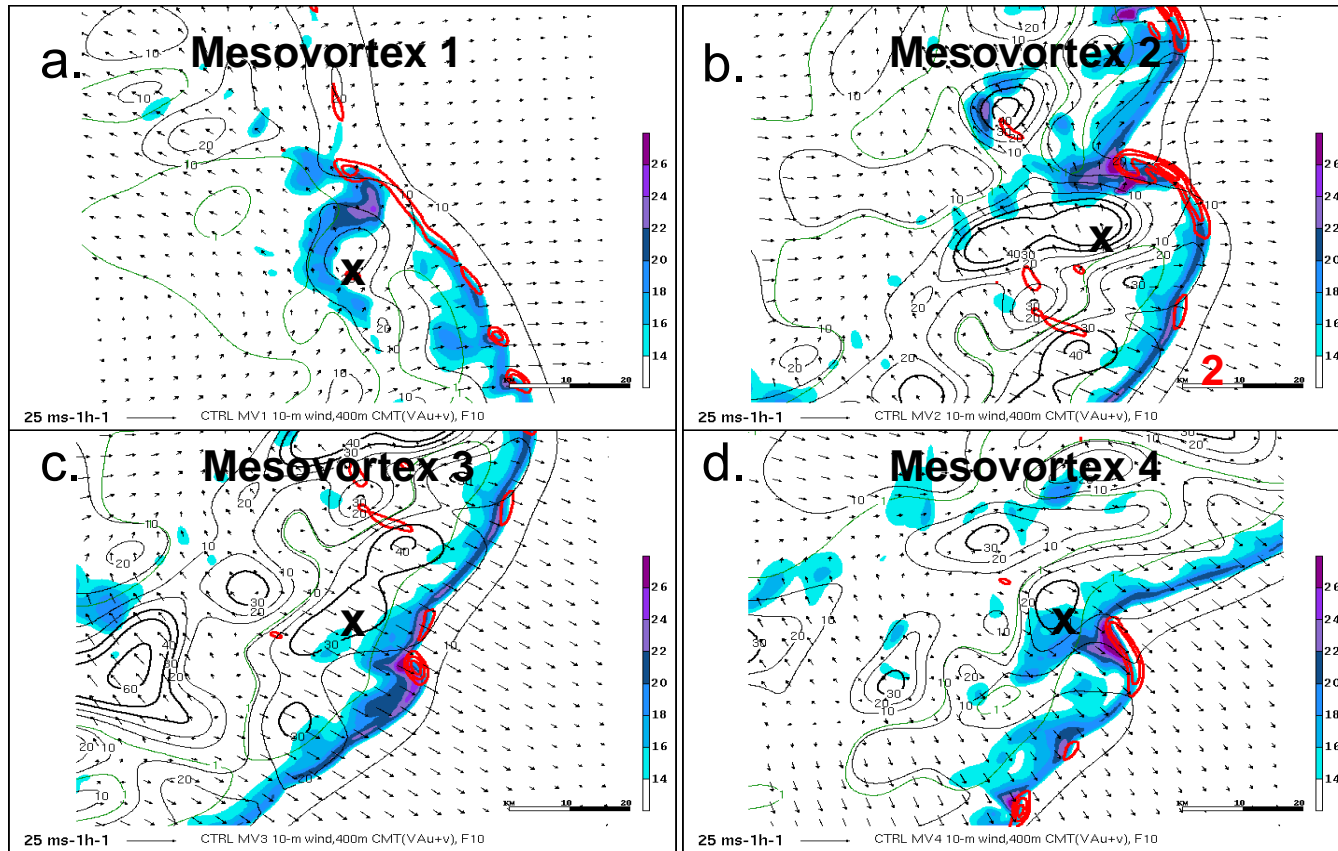


Figure 5.10: Magnitude of 10-m wind field (ms^{-1} , shaded), absolute vorticity (at 400 m, every $0.5 \cdot 10^{-2} \text{ s}^{-1}$, thick red contours), VAV' (i.e., $\text{VAu}' + \text{VAu}'$) (at 400 m, magnitude in black contours every $5 \text{ ms}^{-1} \text{ h}^{-1}$ beginning at 10, vectors according to reference vector), and VAu (at 400 m, every $1 \text{ ms}^{-1} \text{ h}^{-1}$ beginning at 1, thin green dashed contours) at F10 for CTRL simulation for a) MV1 a) MV2, c) MV3, and d) MV4. X's marks maxima of VAV' as discussed in text.

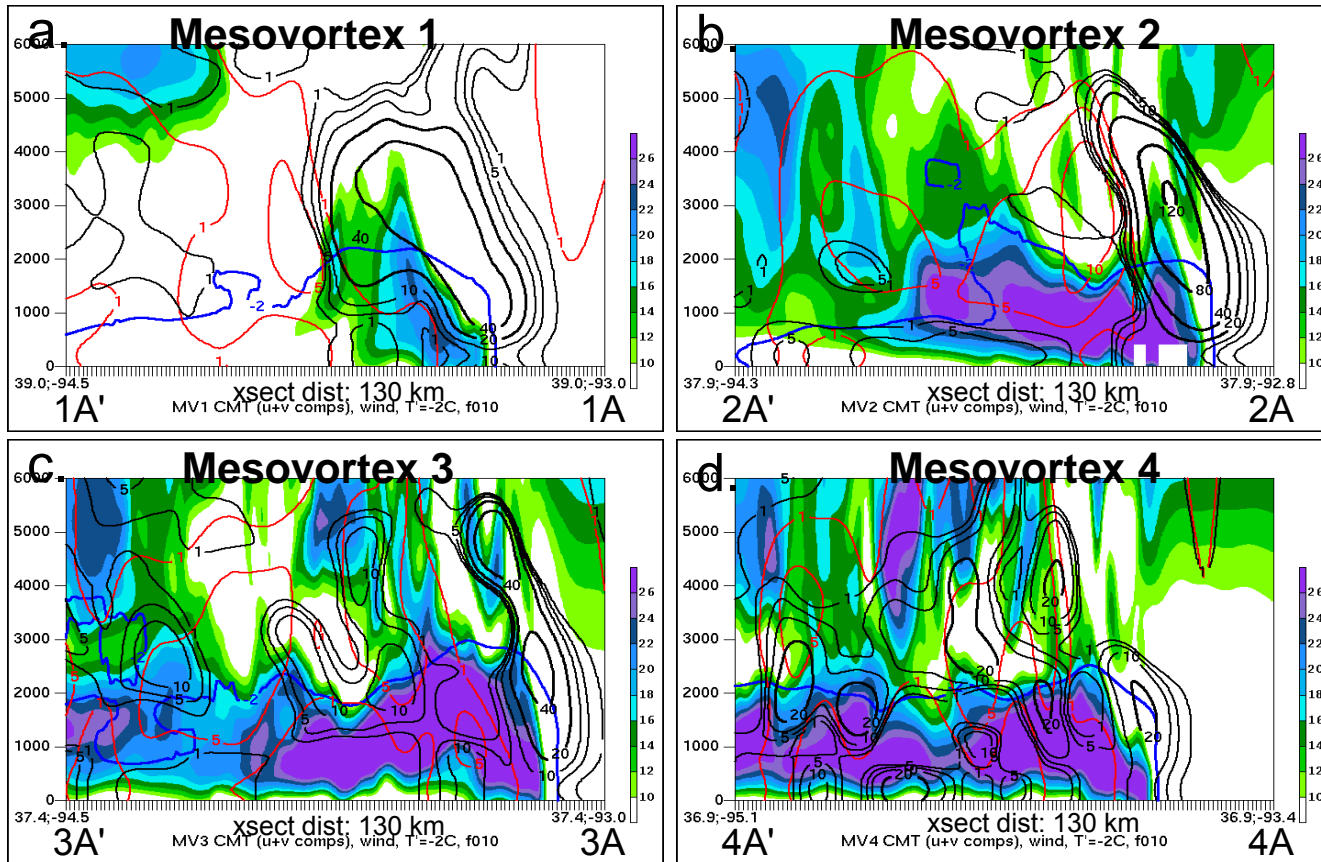


Figure 5.11: East-west cross-sections along lines indicated in Fig. 5.5a at F10. Cold pool (blue contour, $T' = -2^{\circ}\text{C}$), total wind magnitude (ms^{-1} , shaded as indicated), VAu' ($\text{ms}^{-1}\text{h}^{-1}$, black contours starting $1 \text{ ms}^{-1}\text{h}^{-1}$), $VA\bar{u}$ ($\text{ms}^{-1}\text{h}^{-1}$, red contours starting at $1 \text{ ms}^{-1}\text{h}^{-1}$) for a) MV1 a) MV2, c) MV3, and d) MV4.

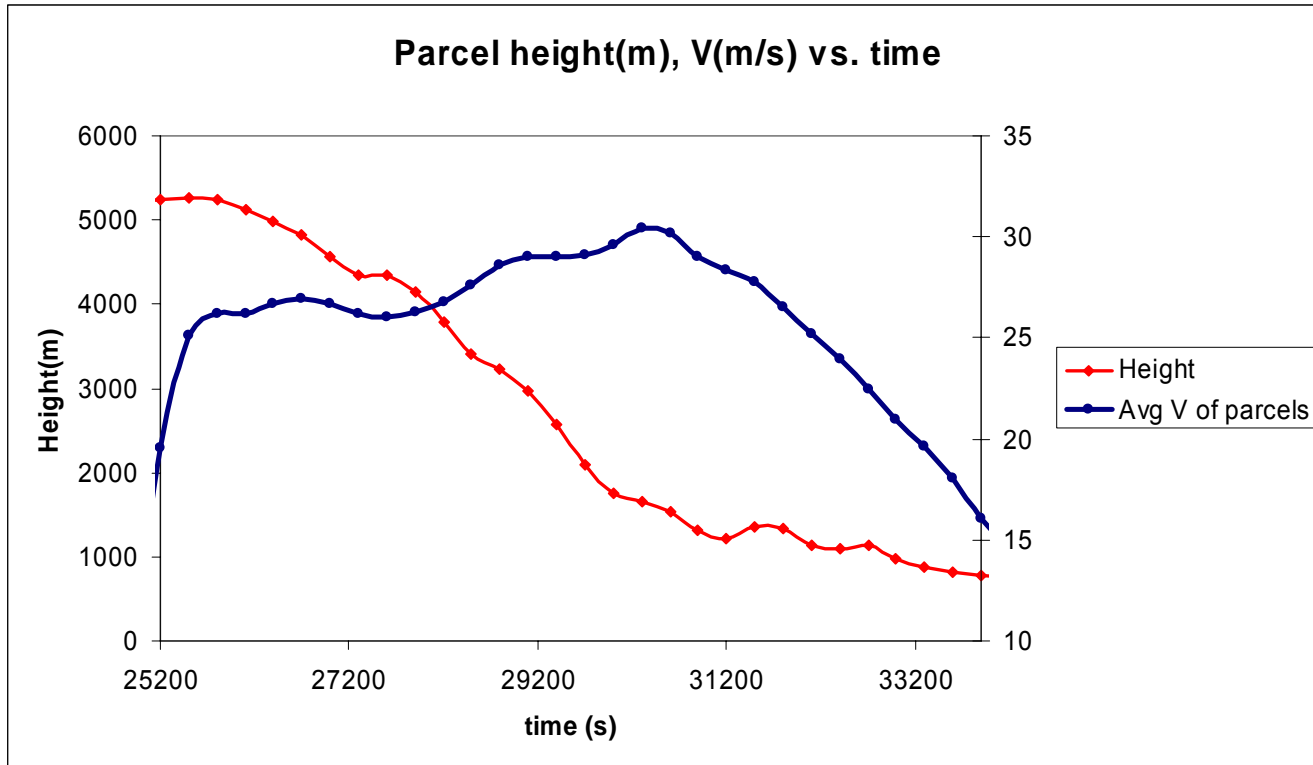


Figure 5.12: From simulation analyzed in Chapter 3 (as in Fig. 3.14): Composite parcel height (red line, m, values on y-axis at left) and wind speed ($|V|$, solid, ms^{-1} , values on y-axis at right) vs. time (x-axis, sec) of average trajectory of 50 parcels originating at RIJ-level for time period $t = 25200\text{s}$ (F07:00) to $t=34200\text{s}$ (F09:30).

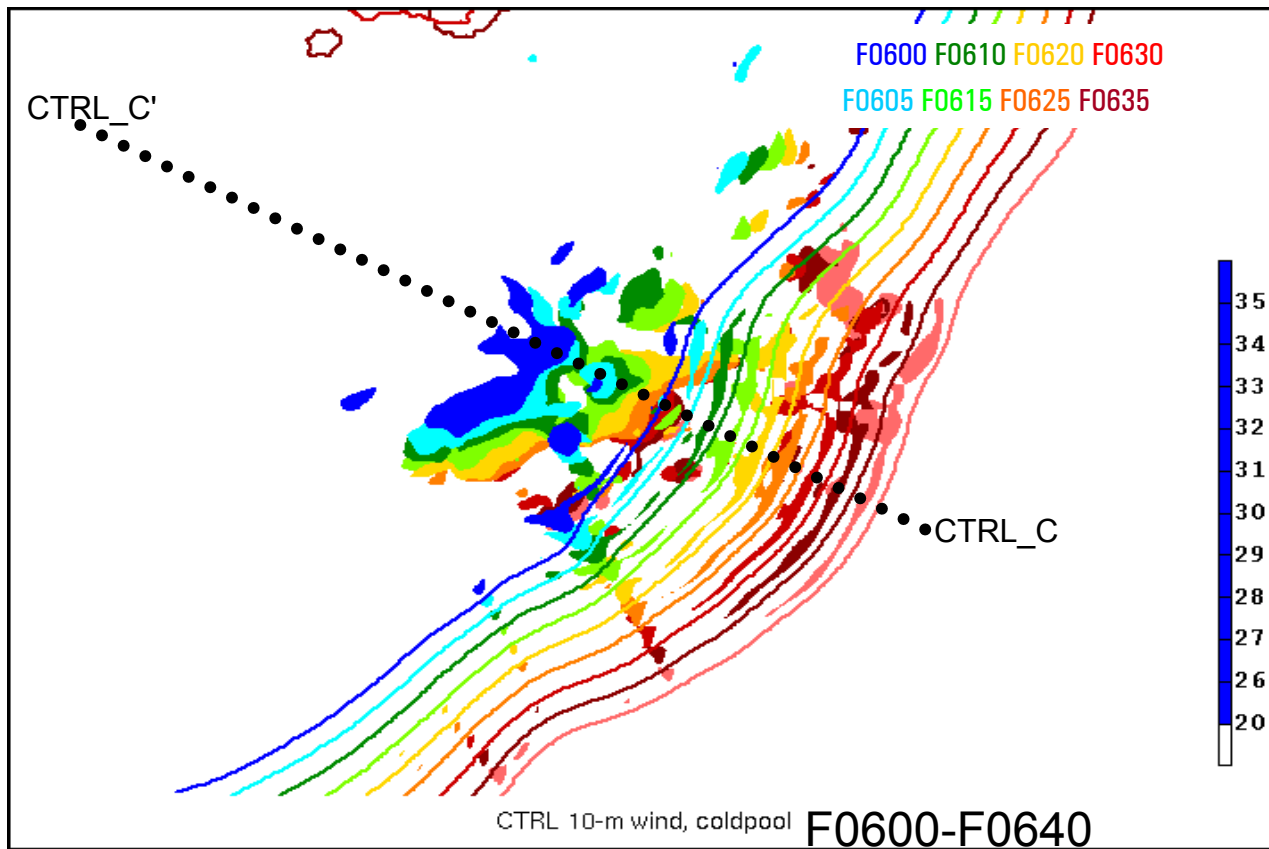


Figure 5.13: CTRL cold pool boundary ($T' = -2^{\circ}\text{C}$, contours), areas of gridcell 10-m wind magnitude $> 25.7\text{ms}^{-1}$ (shaded) for times F0600 – F0640 where colors denote different times as labeled in upper right.

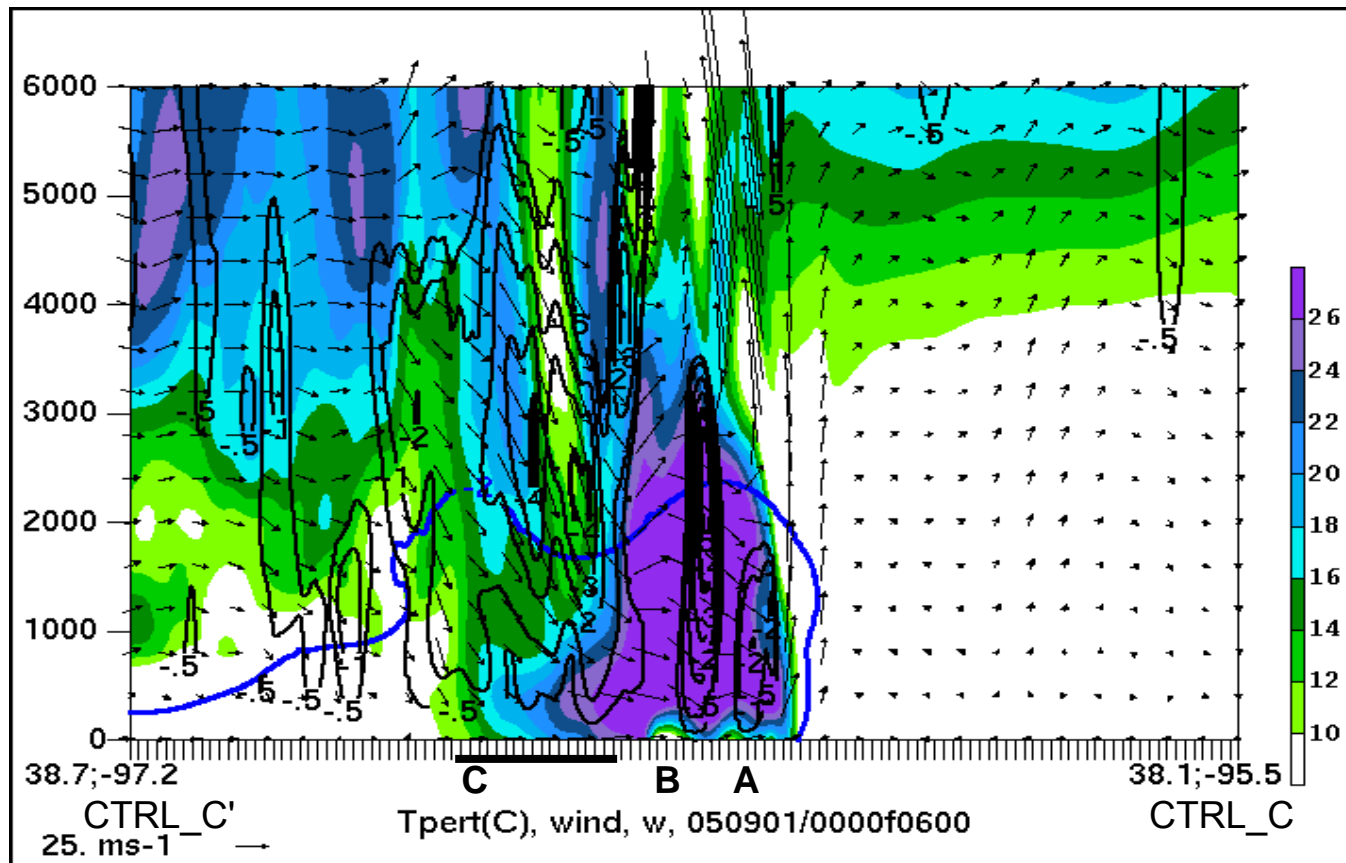


Figure 5.14: Total wind magnitude (ms^{-1} , shaded as indicated), cold pool ($T' = -2^\circ\text{C}$, black contour), and $w < 0$ (black contours, 0.5, -1, -2, -3, -4 and -5 ms^{-1}) at F06 along line CTRL_C – CTRL_C' in Fig. 5.13. A, B, and C denote specific downdrafts discussed in text.

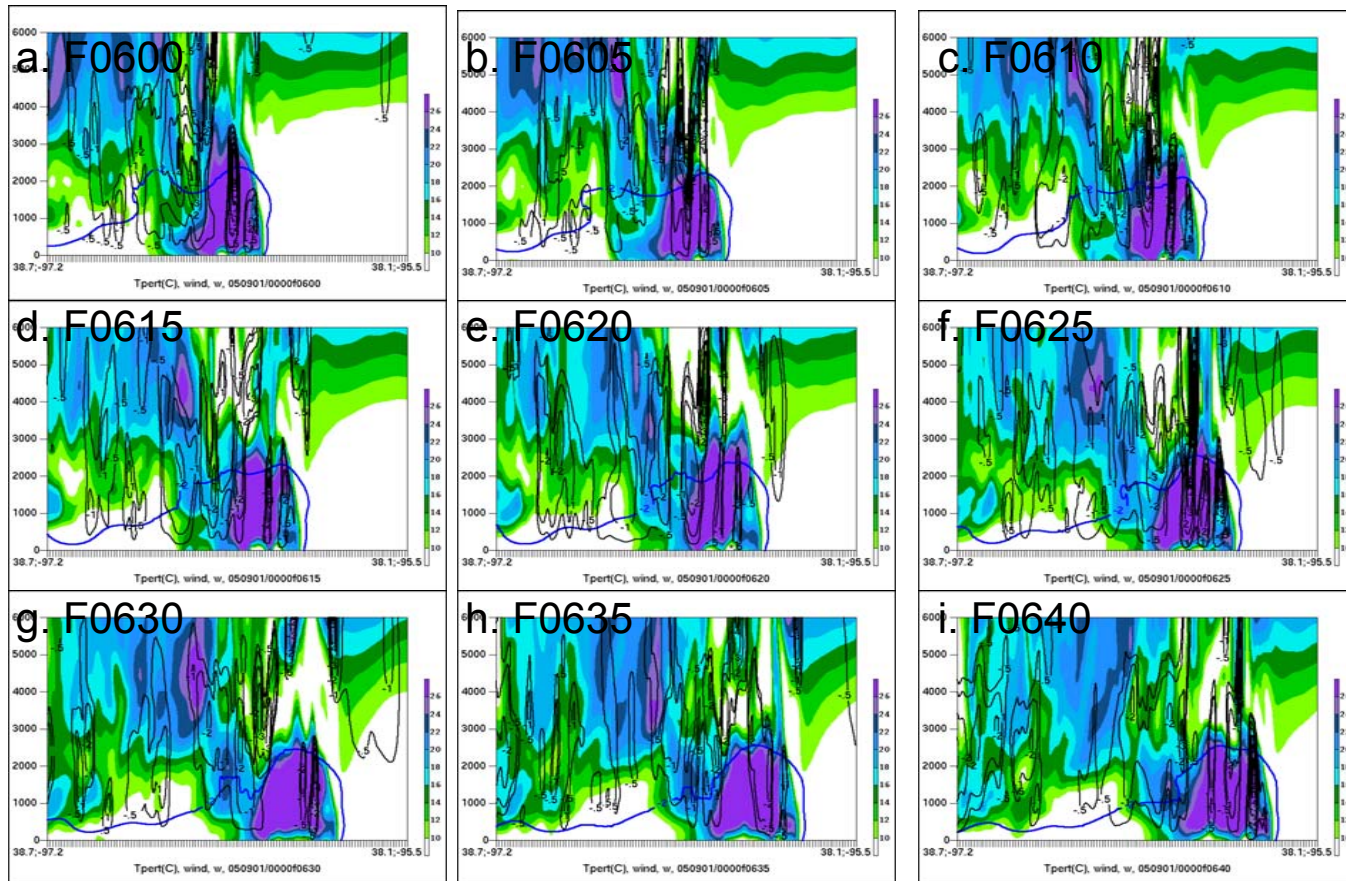


Figure 5.15: As in Fig. 5.14 except wind vectors omitted and times F0600 – F0640 shown as labeled.

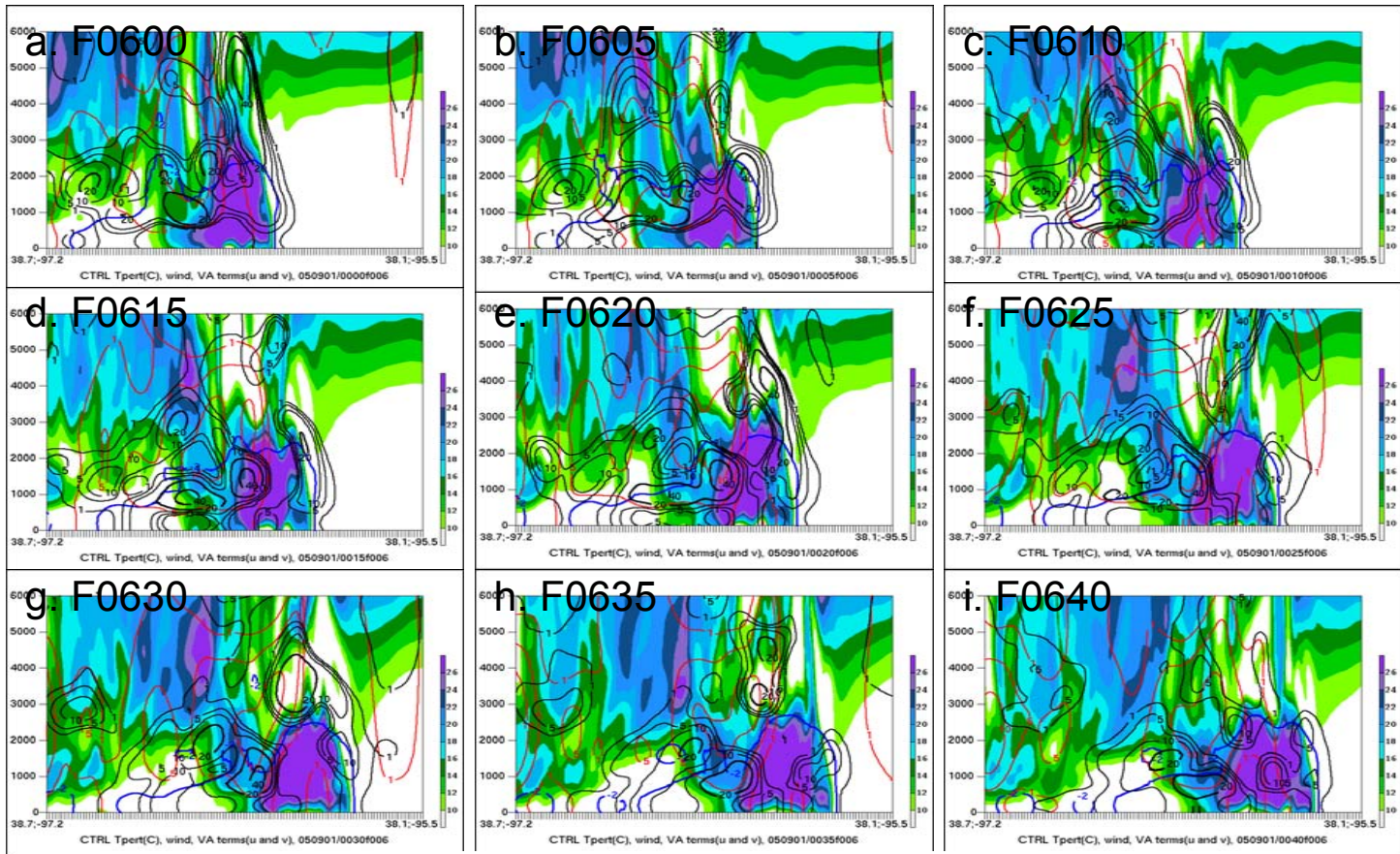


Fig. 5.16 As in Fig. 5.11 except along line CTRL_C – CTRL_C' for F0600 – F0640 as labeled.

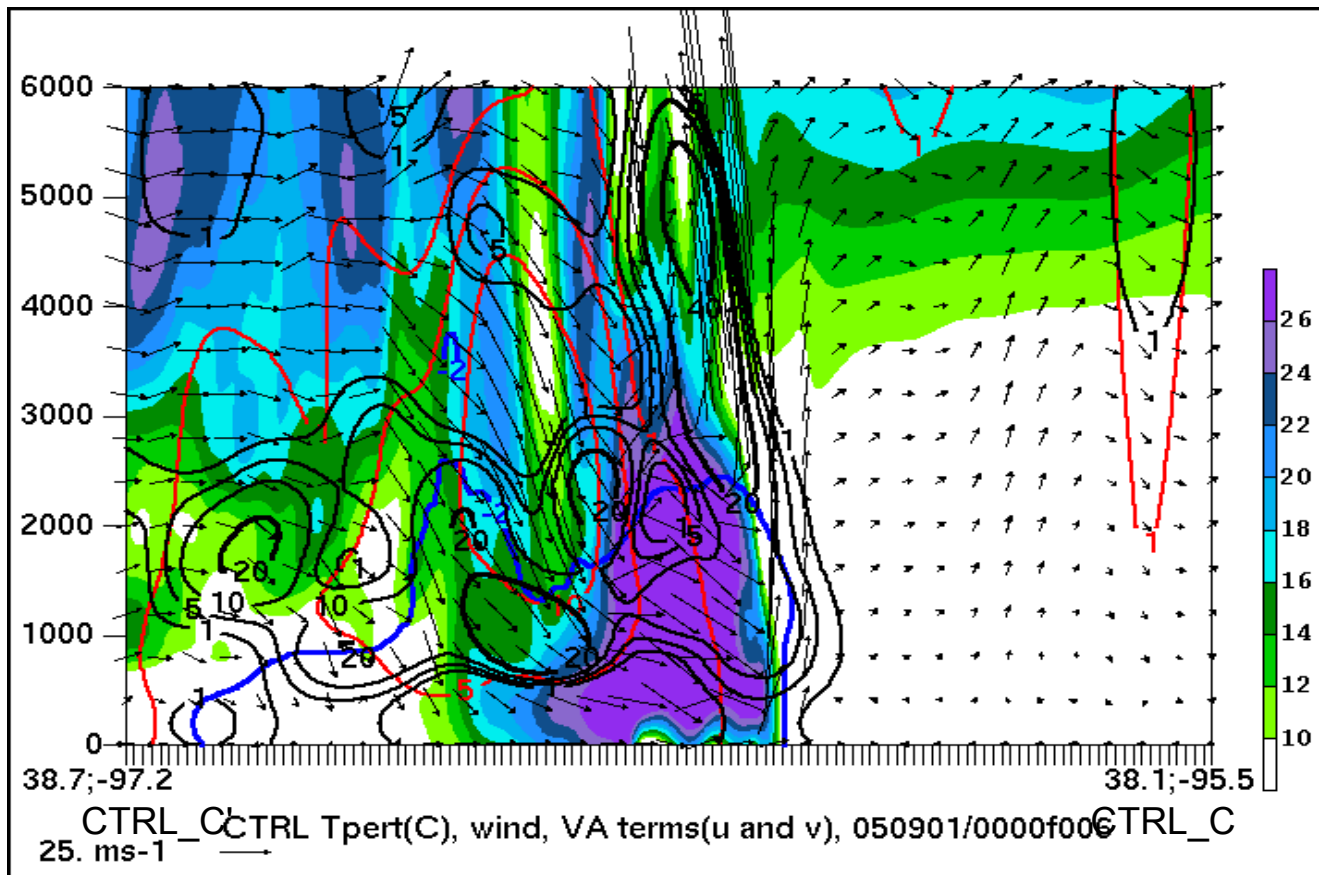


Figure 5.17: CTRL cold pool (blue contour, $T = -2^{\circ}\text{C}$), total wind magnitude (ms^{-1} , shaded as indicated, vectors according to reference vector in lower left), VAu' ($\text{ms}^{-1}\text{h}^{-1}$, black contours starting $1 \text{ ms}^{-1}\text{h}^{-1}$), $VA\bar{u}$ ($\text{ms}^{-1}\text{h}^{-1}$, red contours starting at $1 \text{ ms}^{-1}\text{h}^{-1}$).

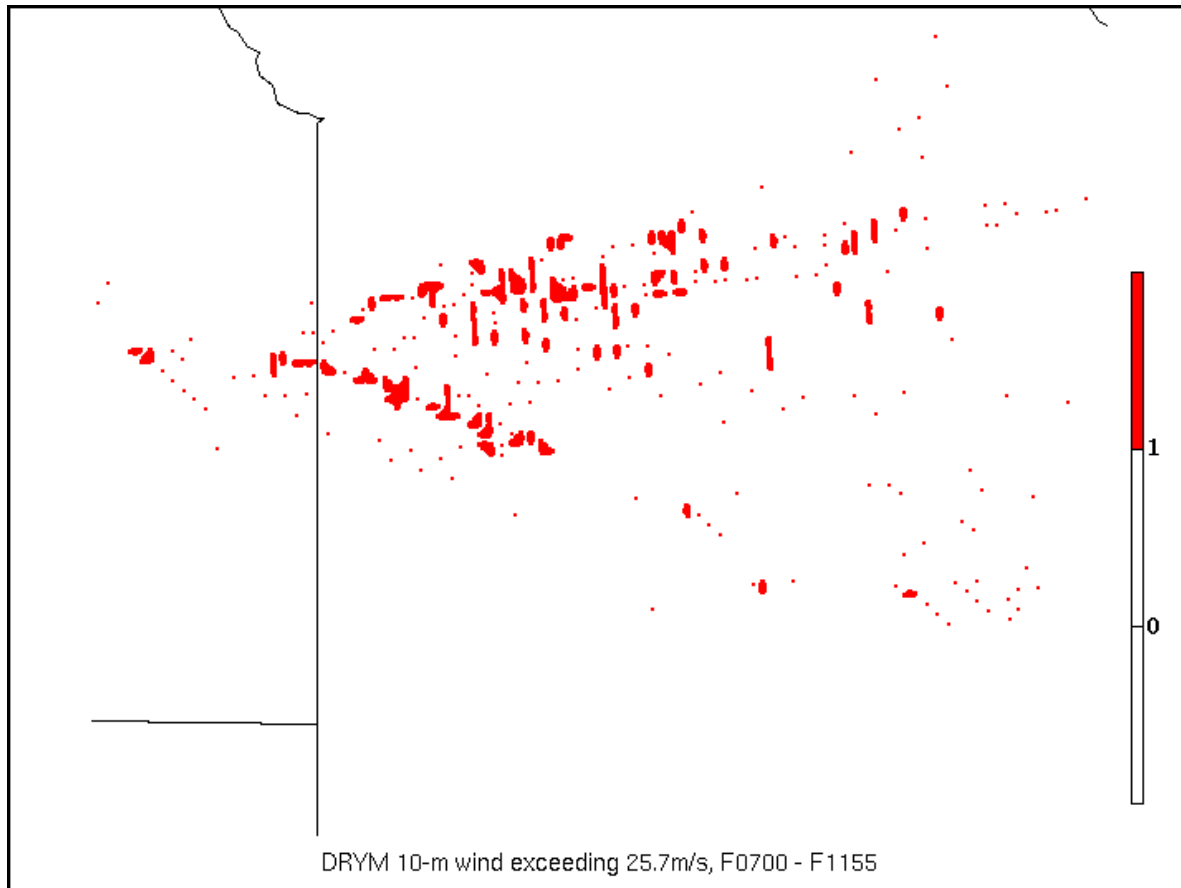


Figure 5.18: DRYM occurrences of grid cell 10-m wind magnitude $> 25.7\text{ms}^{-1}$ (red) for times F0700 – F1155.

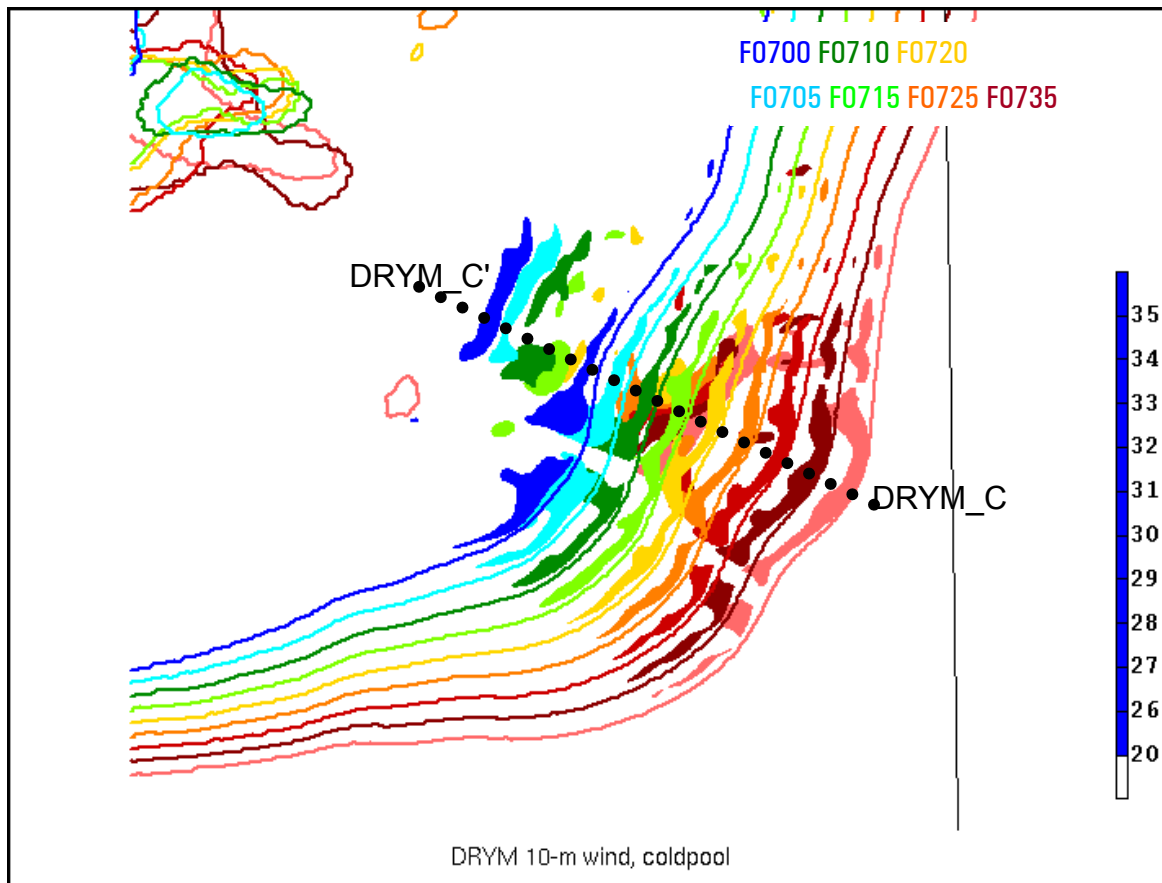


Figure 5.19: As in Fig. 5.13 except for DRYM from F0700 – F0740 as labeled in upper right.

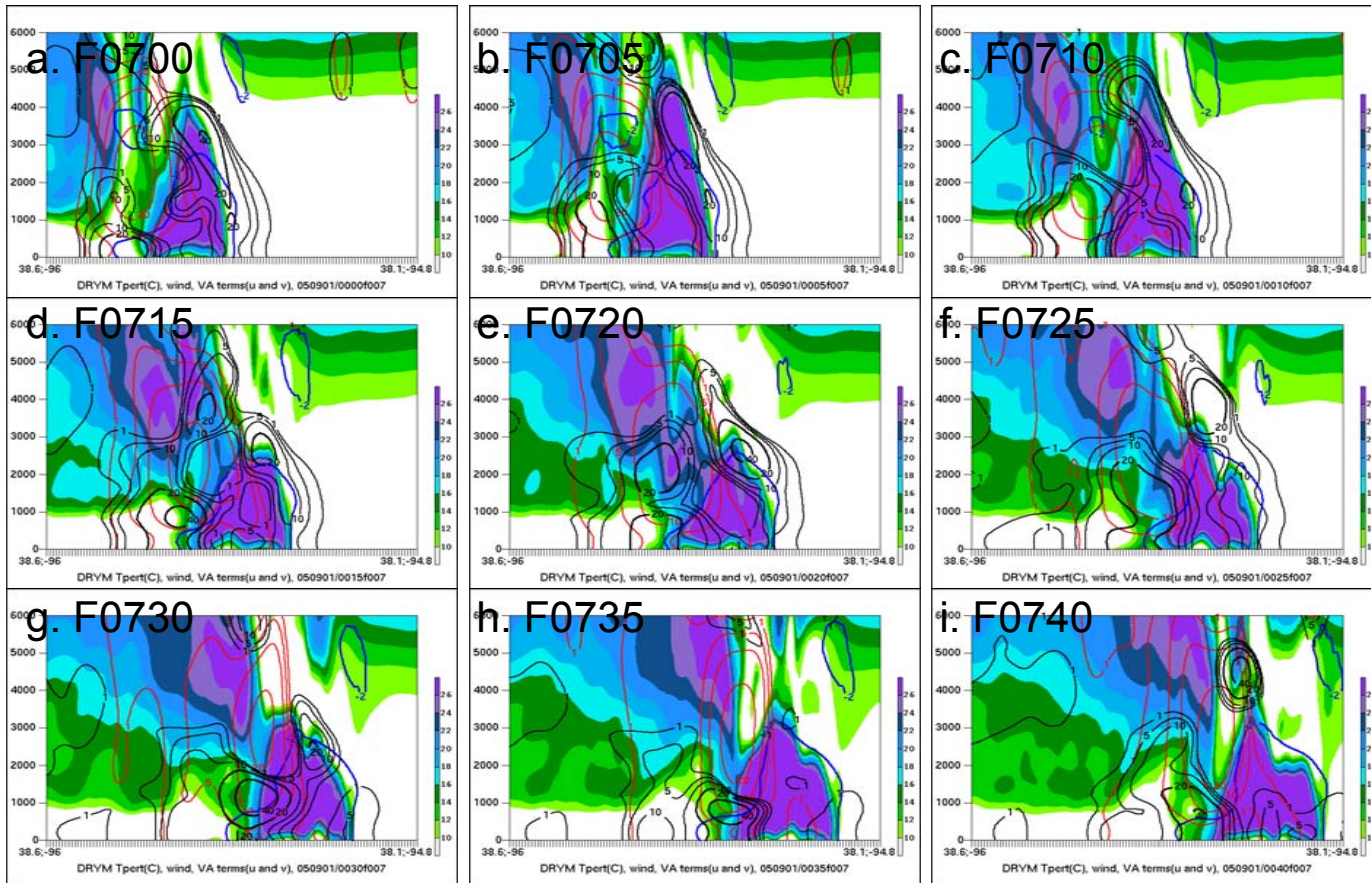


Fig. 5.20 As in Fig. 5.16 except along line DRYM_C – DRYM_C' and for F0700 – F0740 as labeled.

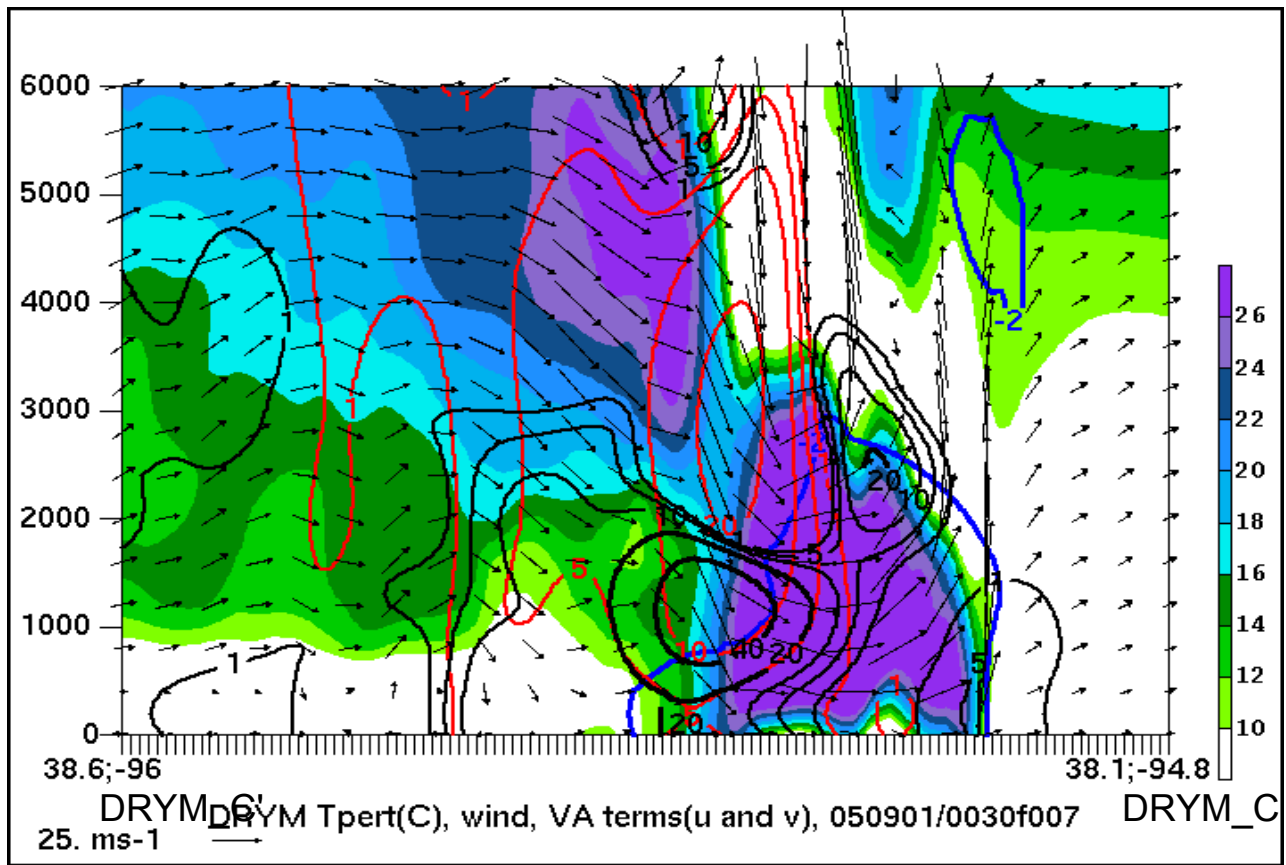


Figure 5.21: As in Fig. 5.17 except for DRYM at F0730.

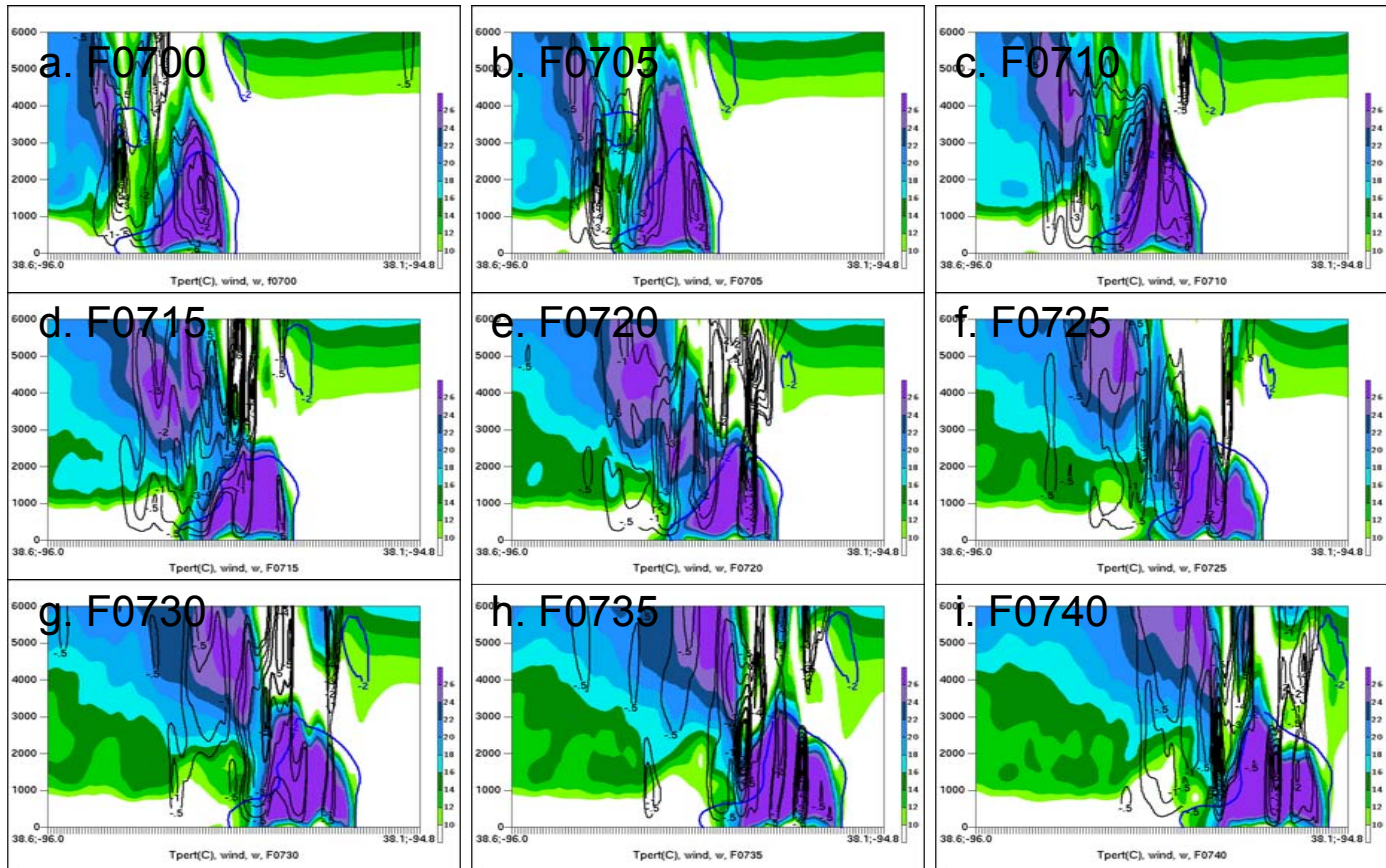


Figure 5.22: DRYM cold pool (blue contour, $T' = -2^\circ\text{C}$), total wind magnitude (ms^{-1} , shaded as indicated), $w < 0$ (ms^{-1} , black contours starting 0.5 ms^{-1}) along line DRYM_C – DRYM_C' from F0700 – F0740 as labeled.

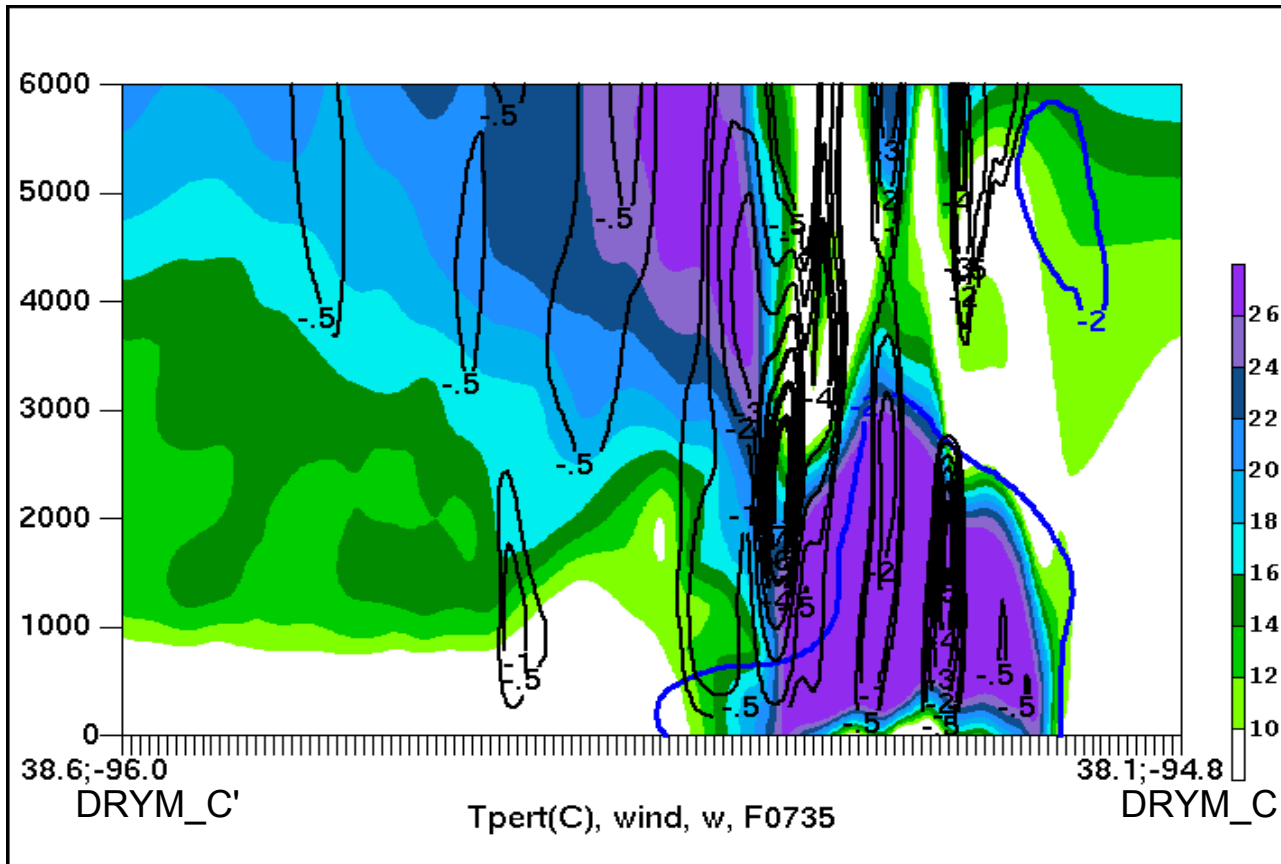


Figure 5.23: As in Fig. 5.22 except for F0735 only.

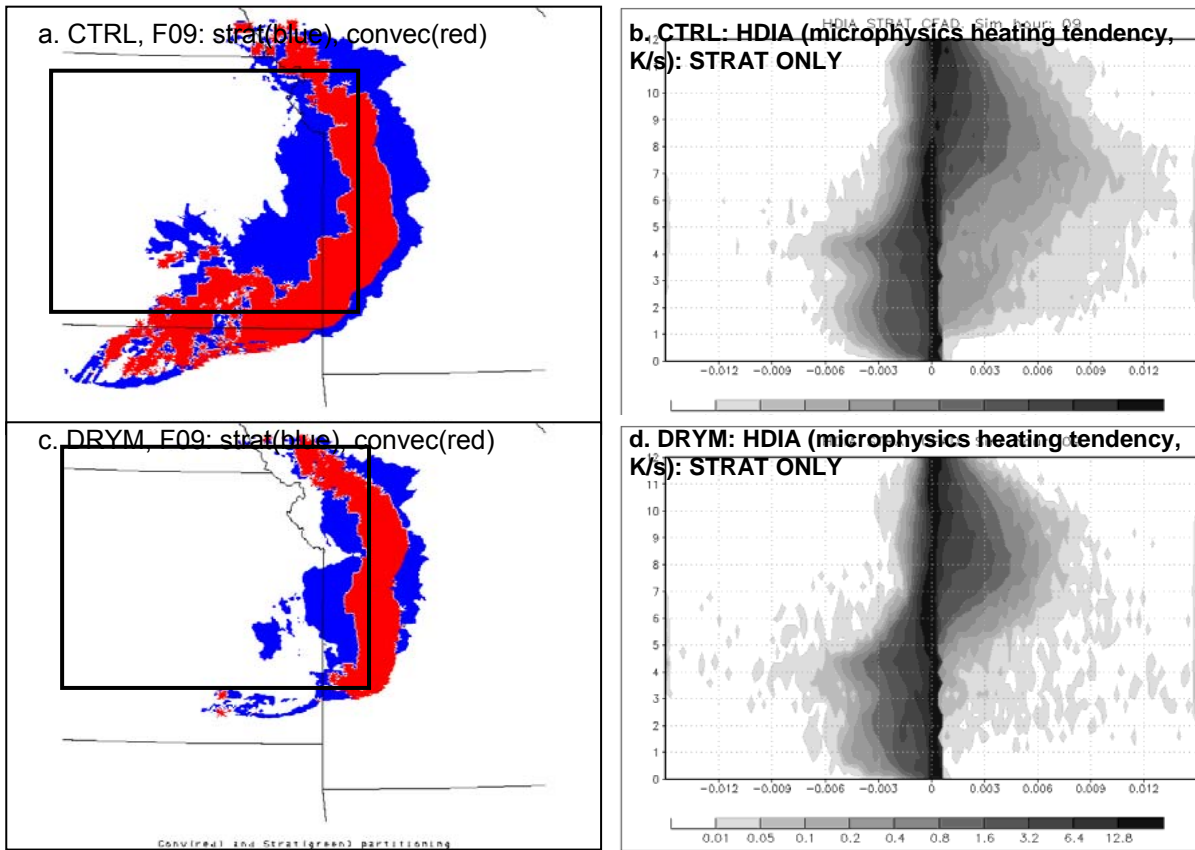


Figure 5.24: a) CTRL at F09: convective gridpoints (blue) and stratiform gridpoints (red) according to criteria described in text. Box denotes boundaries of areas in which stratiform gridcells are averaged within in images at right; b) CFAD of CTRL microphysical scheme heating tendency (Ks^{-1}) at F09 for boxed blue stratiform area in (a), c) as in a) except for DRYM simulation; d) as in d) except for DRYM simulation. Bin size $.00025 Ks^{-1}$.

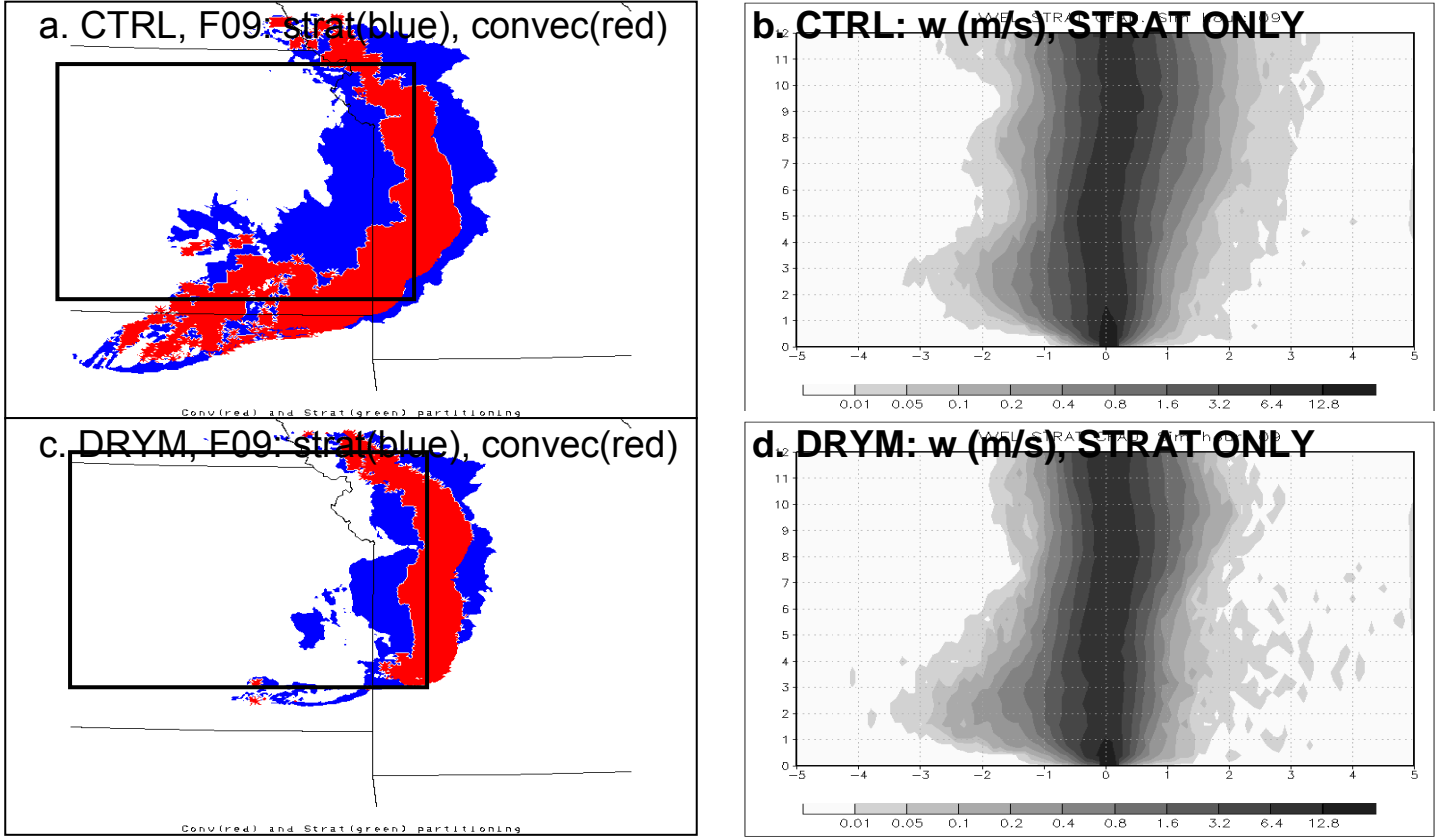
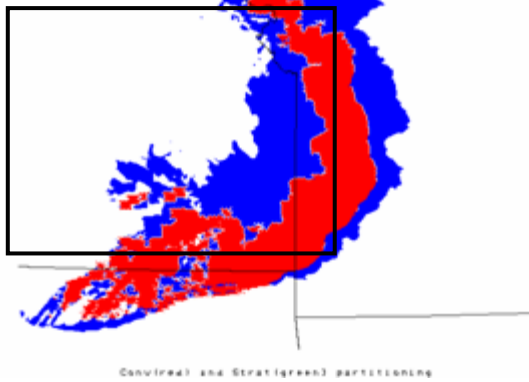
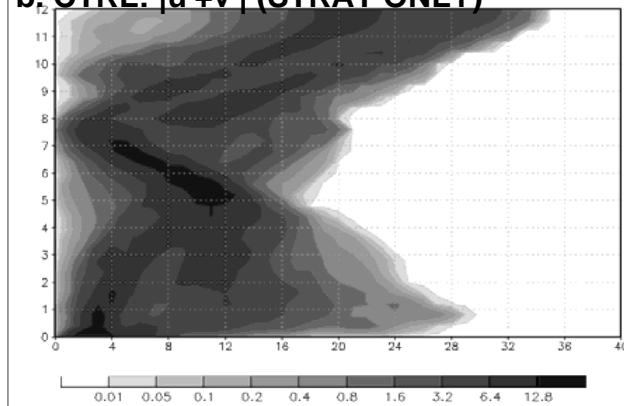


Figure 5.25: a) CTRL at F09: convective gridpoints (blue) and stratiform gridpoints (red) according to criteria described in text. Box denotes boundaries of areas in which stratiform gridcells are averaged within in images at right. (b); b) CFAD of CTRL vertical velocity w , at F09 for boxed blue stratiform area in (a). Bin size is 0.1 ms^{-1} and plot is contoured as indicated by shading and key at bottom; c) as in a) except for DRYM simulation; d) as in d) except for DRYM simulation.

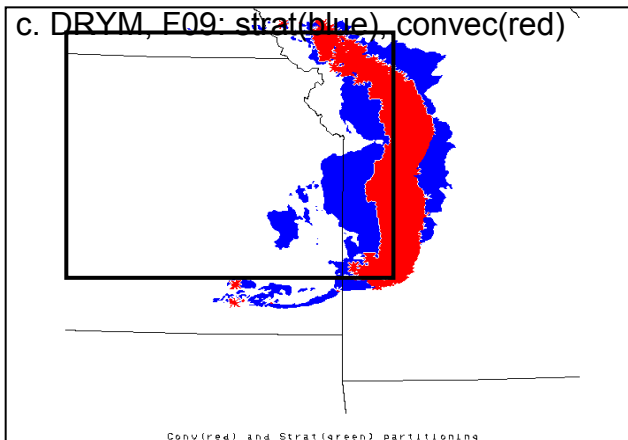
a. CTRL, F09: strat(blue), convec(red)



b. CTRL: $|u'+v'|$ (STRAT ONLY) 09



c. DRYM, F09: strat(blue), convec(red)



d. DRYM: $|u'+v'|$ (STRAT ONLY) 09

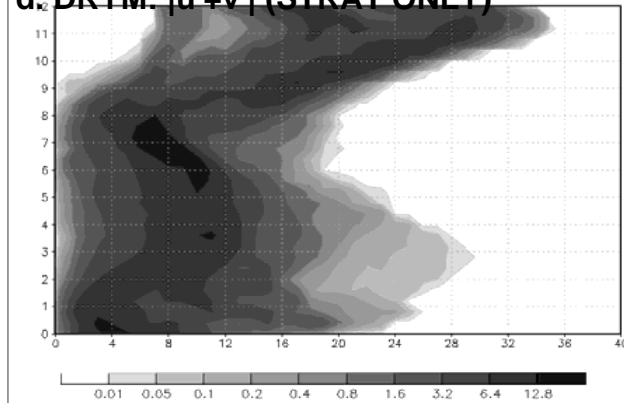


Figure 5.26: As in Fig. 5.25 except b) and d) display the magnitude of the perturbation wind speed $((u'^2 + v'^2)^{1/2}, \text{ms}^{-1})$, bin size 1ms^{-1} .

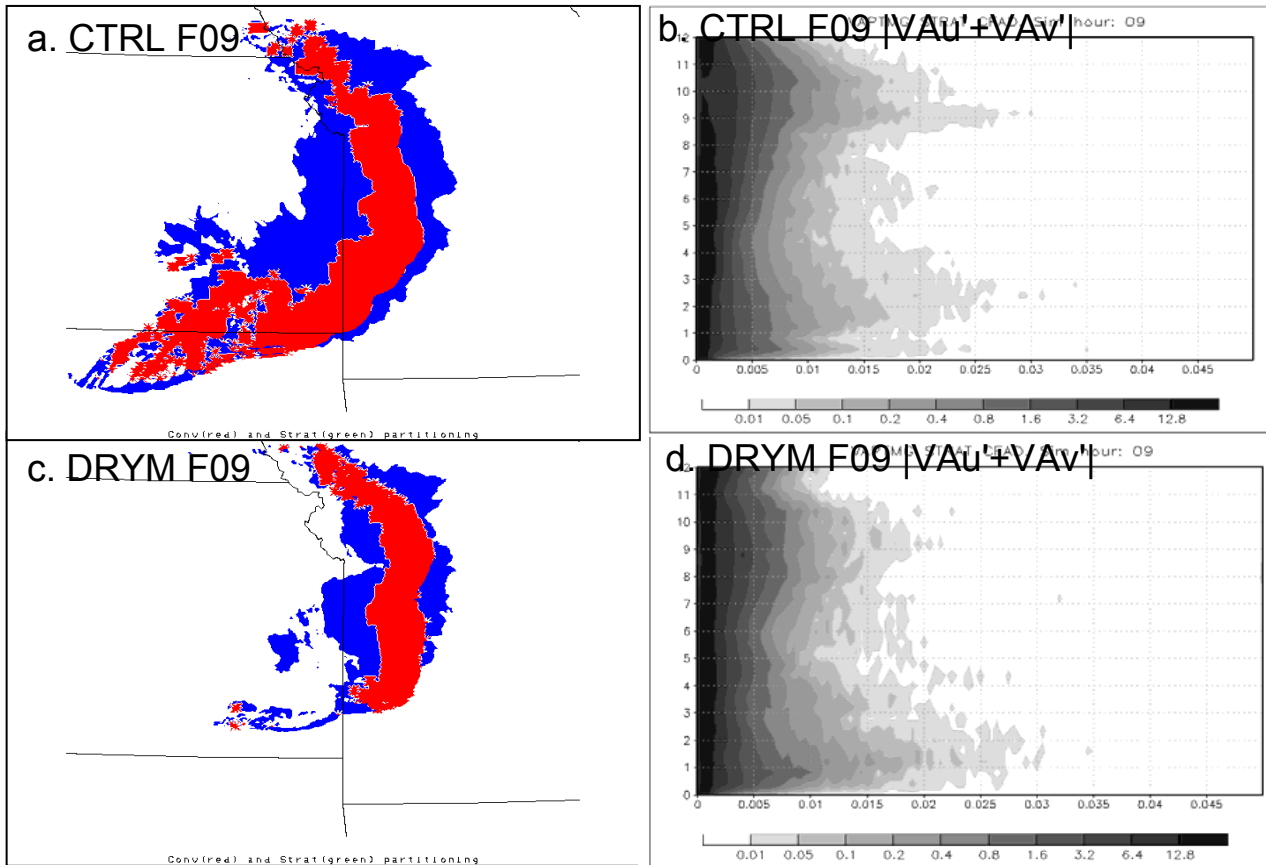


Figure 5.27: As in Fig. 5.25 except b) and d) display VAV' bin size $.01\text{ms}^{-1}\text{ s}^{-1}$.

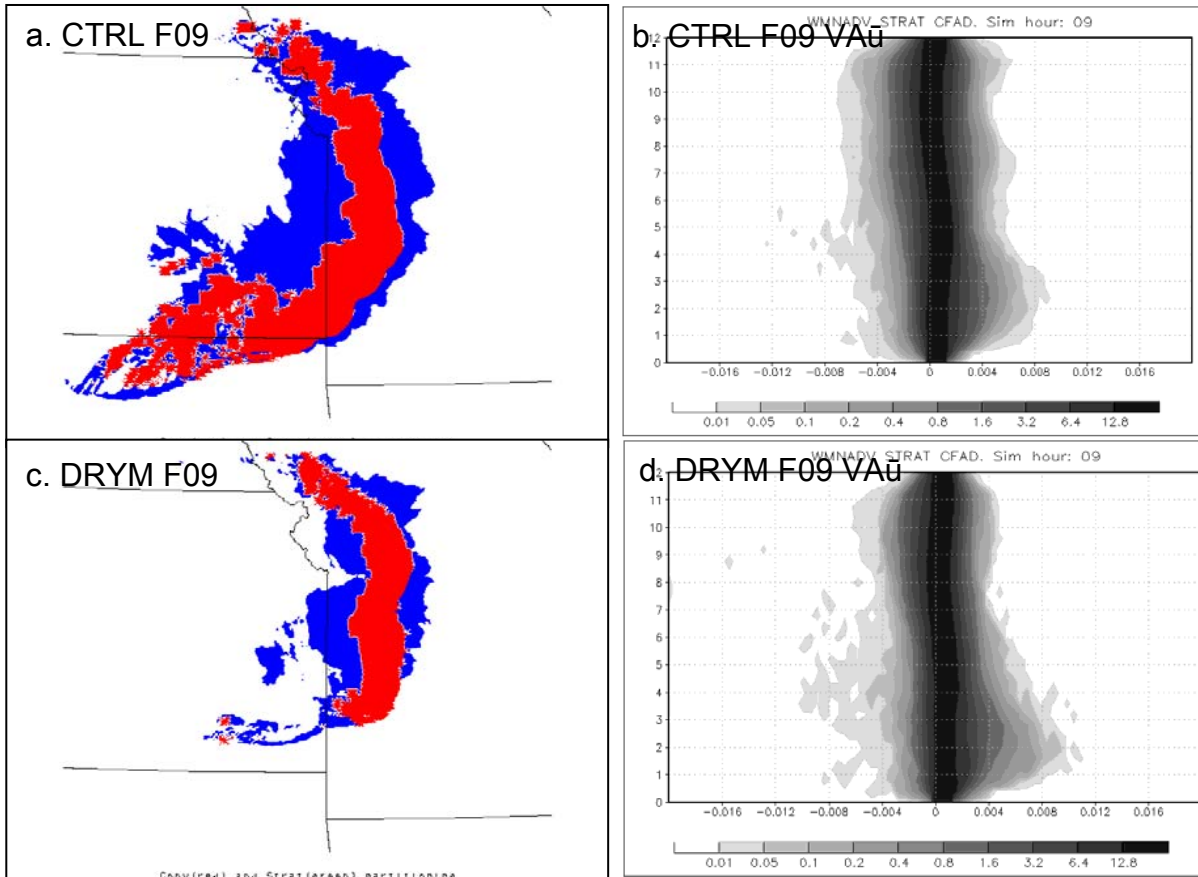


Figure 5.28: As in Fig. 5.25 except b) and d) display VAU bin size $.01\text{ms}^{-1} \text{ s}^{-1}$.

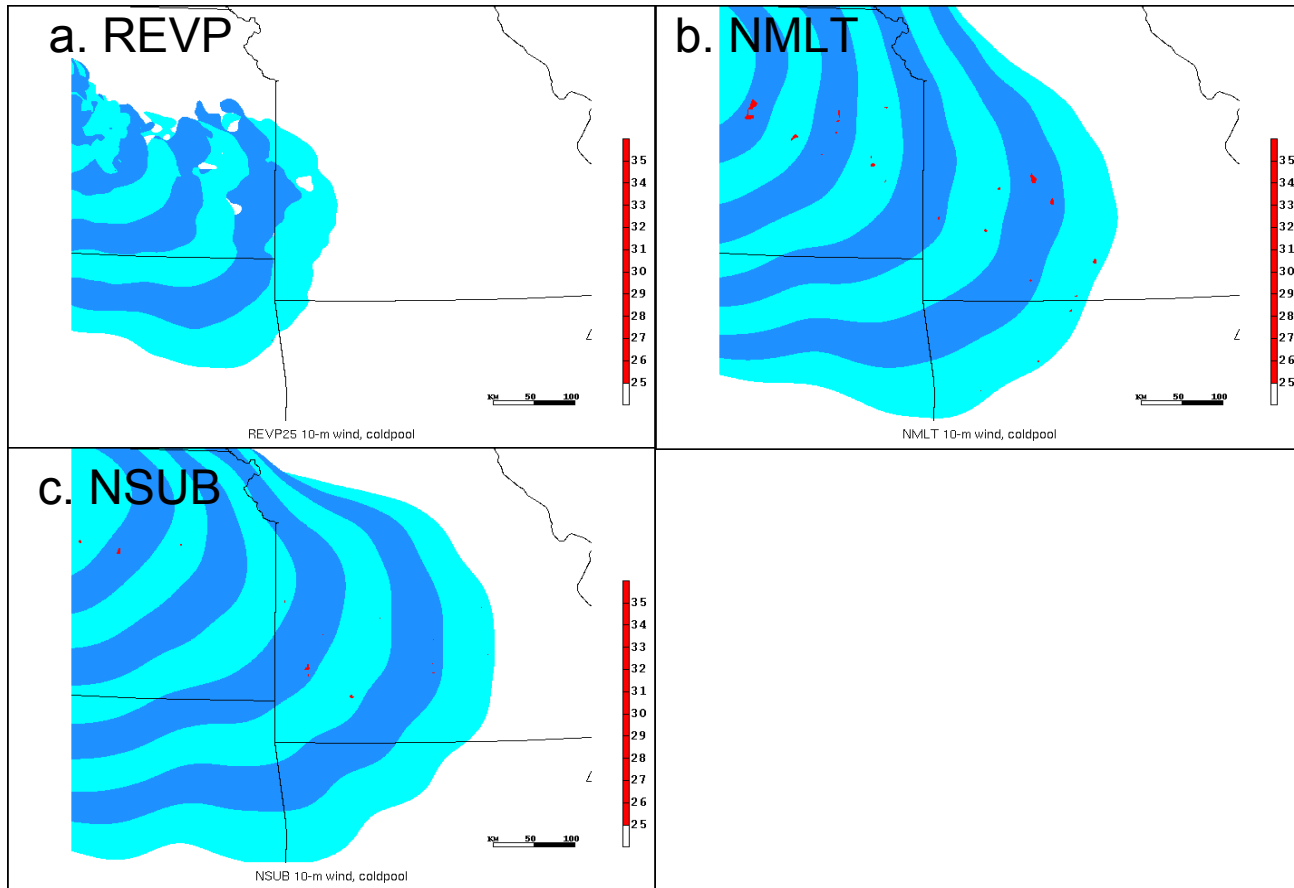


Figure 5.29: As in Fig. 5.2a,b except for a) REVP, b) NMLT, and c) NSUB.

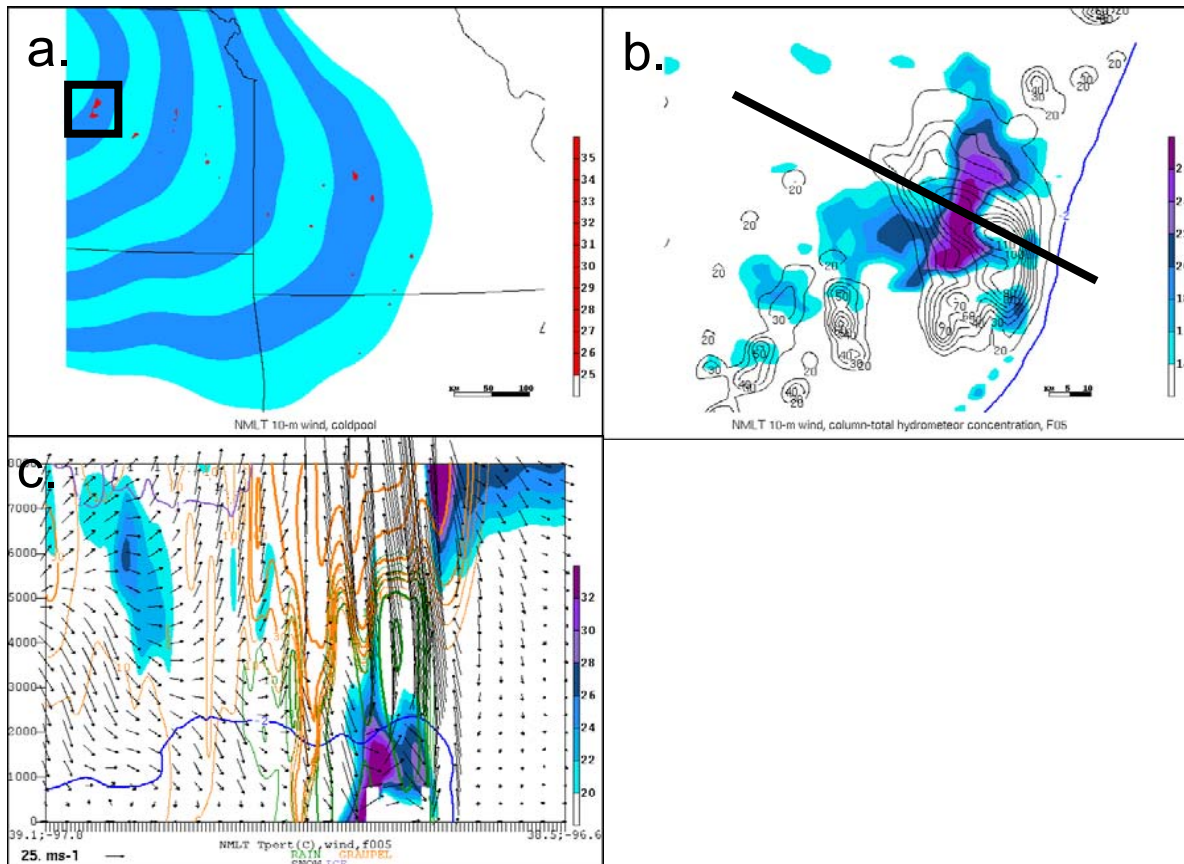


Figure 5.30 a) as in Fig. 5.29b, black box shows area of severe winds shown in b); b) 10-m AGL total wind magnitude (ms^{-1} , shaded as indicated), column-total hydrometeor concentration (black contours as labeled $\times 10^{-4}$, gkg^{-1}); c) vertical cross-section shown by black line in b), cold pool (blue contour, $T' = -2^\circ\text{C}$), total wind magnitude (ms^{-1} , shaded as indicated, vectors according to reference vector in lower left), and hydrometeor mixing ratios (contours as labeled $\times 10^{-4}$, gkg^{-1}) for graupel (orange), cloud ice (light purple), rain (green), and snow (pink).

Chapter 6

Concluding remarks

6.1 Summary of results

The work presented here investigates the vertical transport of horizontal momentum within quasi-idealized simulated MCSs, and evaluates the significance of this process with respect to both MCS motion and the evolution of the lower-tropospheric wind field. The analysis provided in Chapter 3 demonstrates that the motion of a numerically-simulated MCS is significantly impacted by CMT within the MCS. Lagrangian and Eulerian momentum budgets of a simulated mid-latitude MCS are computed and results show that the vertical advection of the perturbation wind (V_{Au}') is a primary contributor to the momentum field at the leading edge of the cold pool -- the region in which the resulting accelerated winds drive system motion. The momentum budgets also show that the pressure gradient acceleration (PGA) and, to a lesser degree the vertical advection of the background environmental wind ($V_{A\bar{u}}$), contribute to the acceleration of rear-to-front momentum in the middle- to rearward portions of the storm, serving to both generate and reinforce the perturbation flow transports into the cold pool and accelerate the MCS. The contribution of CMT to MCS speed in the simulation presented in Chapter 3 is significant: system acceleration during periods of large downward transport suggests a contribution to system acceleration from CMT on the order of up to $5 - 10 \text{ ms}^{-1}$ over a period of 3 – 4 hours (Figs. 3.5, 3.10). While previous studies have examined CMT from alternative angles such as its influence on the large-scale momentum budget, the process is rarely considered in the literature as one that significantly influences the speed at which MCSs move (as opposed to buoyancy effects in the cold pool, gravity-wave motion, etc). This initial portion of the investigation demonstrates the specific role of CMT in accelerating MCS motion using trajectories, momentum fluxes, and both Eulerian and Lagrangian momentum budgets to elucidate the significance of this contribution both qualitatively and quantitatively.

In Chapter 4, four sensitivity experiments are performed to assess the impact of a drier midlevel environment (DRYM), reduced evaporation (REVP), and the removal of melting and sublimation (NMLT and NSUB, respectively) on CMT and MCS motion. The results show that drier air at mid-levels slightly increases average MCS speed by $\sim 1 \text{ ms}^{-1}$ despite producing a smaller and somewhat weaker system. The drier air at mid-levels increases descent within the TSR and enhances CMT. Theoretical cold pool speed values account for the observed system speed reasonably well at later times in the simulation, but fail to do so during earlier stages of storm development. The initial phase of MCS acceleration in DRYM is actually marked by a decrease in surface cold pool intensity and theoretical cold pool speed, and CMT during this period is shown to be a probable contributor to system motion during a period that is evidently not completely determined by cold pool dynamics. With respect to the microphysics sensitivity tests, REVP shows the most marked decrease in MCS motion (average groundspeed 14 ms^{-1}), followed by NMLT (average groundspeed 17 ms^{-1}) and NSUB (average groundspeed 18 ms^{-1}). The changes in REVP are likely attributable to decreases in both c and CMT; the near lack of a surface cold pool clearly impedes MCS development and motion, and weakened downward motion throughout the system causes downdrafts themselves, as well as any horizontal momentum transported with them, to be less likely to reach the surface. NMLT shows a slowing of MCS groundspeed by $\sim 1 - 2 \text{ ms}^{-1}$ overall; this is consistent with the observations of Yang and Houze (1995). As the cold pool intensity and theoretical cold pool speeds of NMLT are generally equal to or even slightly greater than those found in CTRL, it is likely that this difference in motion is explained by decreased downward motion and decreased CMT, particularly in the TSR. Finally, NSUB reveals very little decrease in observed overall speed from CTRL, and few dynamical or structural differences overall. While the horizontal extent of the TSR is slightly greater relative to CTRL, it appears that the effects of NSUB are most pronounced in leading anvil, and are not as dynamically significant in rear of system where downward transports are most relevant to the CMT process of interest here.

The analyses of lower-tropospheric wind speeds in Chapter 5 illustrate the role of CMT in generating certain types of strong or severe surface winds. CMT is first examined with respect to a proposed mechanism for severe surface wind production in the vicinity of mesovortices. Several of the leading theories for mesovortex generation are directly linked to the descent of the RIJ and/or convective downdrafts; CMT is further shown to be a process that explains the occurrence of severe surface winds produced via the favorable superpositioning of a descending RIJ and the low-level circulation associated with a gust front mesovortex. The potential for a descending RIJ to cause strong surface winds at locations away from the leading edge of the gust front is also discussed. While this process may occur in a variety of storm environments, it is shown that the additional downward motion imparted by decreasing the relative humidity of the mid-levels affects CMT fields and contributes to an increase in the number of gridcell occurrences of strong to severe surface winds. The results presented add to a growing body of knowledge that improves our understanding of the specific processes that produce damaging surface winds, and may hold promise in updating both our conceptual models of convective windstorms as well as forecast strategies to improve prediction of such events.

The three most important findings of this work can be summarized by the following points: (i) CMT is a significant driver the MCS low level momentum field and impacts both MCS motion and the low-level wind field; (ii) its sensitivity to the microphysical processes altered here show less sensitivity than expected, but may have greater roles in other storm environments, and (iii) the sensitivity simulations produce changes in the surface wind field that are significant both in terms of the number of severe wind occurrences produced and the altered processes by which such surface winds are generated.

6.2 Potential for forecast application of findings

6.2.1 CP scheme implementation

Part of the initial motivation for this investigation was to evaluate whether the neglect or coarse representation of CMT in some convective parameterization (CP) schemes may have unfavorable effects on model forecasts of convective systems. Mahoney and Lackmann (2007) describe operational model forecasts of an observed MCS in which a CP scheme is employed that exhibit a negative bias in forecasted MCS speed, and hypothesize that the CP scheme's neglect of CMT may play a role in the error. It has long been recognized that CP schemes possess myriad problems in adequately representing organized convection, and a large body of research demonstrates the many shortcomings of CP schemes with specific regard to MCSs and MCS motion (e.g., Molinari and Dudek 1992; Done et al. 2004; Bukovsky et al. 2006; Correia et al. 2008). While such studies enumerate many challenges to successful numerical simulations of MCSs that use CP schemes (e.g., correct representation of the vertical heating profile, cold pool properties, etc.), neglecting or poorly representing CMT within an MCS is likely also detrimental to the representation and numerical prediction of MCSs and MCS motion.

In this study, the large contribution of CMT to the total lower-tropospheric MCS momentum field presented in Chapter 3 demonstrates that the omission of this process in many operational NWP model CP schemes is indeed questionable, and may conceivably contribute to a negative bias in numerical forecasts of MCS motion at grid lengths where CP schemes are needed. However, the synthesis of the results of all of the simulations presented here also underscores the complexity involved in parameterizing the effect in a physically realistic manner that would produce improvements across a spectrum of storm types. The finding that the vertical advection of the storm perturbation wind (V_{Au}' , V_{Av}') is the dominant process in the leading portion of the system reveals one of the main challenges to the successful implementation of CMT into a CP scheme: as perturbation winds are largely the product of subgridscale processes, they are therefore more difficult to parameterize relative to background/large-scale winds (i.e., \bar{u}). Thus, the perturbation flow induced by an MCS itself either needs to be resolved by the model dynamics [generally considered to be possible (if only in a coarse sense) when using grid spacing of ~ 12 km

or less (e.g., Weisman et al. 1997; Bryan et al. 2003; Correia et al. 2008)], or else be parameterized itself. In either case, accurate representation of the perturbation flow is only one part of adequately simulating the CMT process. Vertical motion is also clearly important, and is both variable between (and even within) storm regions and is also highly resolution-dependent in numerical models (e.g., Weisman et al. 1997; Bryan et al. 2003; Gentry and Lackmann 2009). Thus, in designing a CP scheme to improve MCS forecasts (and minimize the potential for worsening forecasts in other environments), several key factors should be first addressed, ideally with careful consideration of the needs of the end-user and the utility for which forecasts or simulations are intended.

The first such issue is model grid spacing, and the ability of a given model set-up to simulate specific scales of motion. That is, the treatment of convection and MCSs should be quite different between large-scale or global models (i.e., grid spacing $> \sim 50$ km) in which MCSs are not individually represented in any significant detail, and more intermediate grid spacings (e.g., 12 – 30 km) in which individual precipitation systems and some of their dynamical features may be resolved. For the former types of applications, existing CP schemes designed for large grid spacing (that do adjust momentum, albeit in a crude way) may be sufficient (e.g., Han and Pan 2006; Moncrieff and Liu 2006; Hogan and Pauley 2007). For grid spacings trending more toward the scale of current operational models (e.g., ~ 12 km), a simple vertical adjustment of the total wind field to match typical “before and after” momentum profiles may be possible, assuming that the full wind field adequately accounts for the perturbation wind induced by the MCS (e.g., Fig. 6.1). Generally speaking, however, the division of mesoscale vs. convective-scale processes will need to be considered as grid spacings reach values in which some storm-scale features such as the RIJ are resolved, but downdraft representation remains inadequate (e.g., Bryan et al. 2003). Molinari and Dudek (1992) describe this “in-between” range of grid spacings as being characterized by the “lack of an obvious solution” (with respect to how to best represent convection in a mesoscale model.) For example, Correia et al. (2008) found that simulations using 10-km grid spacing and a CP scheme indeed produced a RIJ (generally considered to be a mesoscale

feature), but that its features were distorted. The combination of the above concerns and known problems resulting from the omission of critical convective-scale processes (e.g., convective downdrafts, turbulent mixing) when using larger grid spacing and CP schemes (e.g., Weisman et al. 1997; Bryan et al. 2003), affirms that careful thought will need to be given regarding grid spacing and what parts of the CMT process can and should be parameterized.

A second concern is that of “representativeness” and ascertaining that the changes designed to improve the prediction of one type of system (e.g., an MCS) are not so mismatched with the dynamics of the rest of the model domain that the overall forecast worsens. The variability among different types of convective storms, and even within the sub-classification of MCSs, demonstrates that variability with respect to RIJ intensity, RIJ descent, extent of the TSR, orientation of the TSR, etc., presents a daunting challenge to treat using a simple adjustment in a series of larger model gridcells. It is conceivable that a system of “checks” should be implemented, in which the gridcell must “qualify” as being part of an MCS or otherwise appropriate system in which adding the momentum transport effect would be beneficial.

Finally, before an operational CMT parameterization can be refined, additional research should be performed using real MCSs and existing CP schemes that neglect the CMT process. Comparison over many MCSs of (i) average vertical profiles of the wind fields before and after the passage of an MCS as produced by a coarse-resolution model without CMT included with (ii) the same profiles produced by a high-resolution explicit numerical simulation, and (iii) observations will reveal important information regarding the magnitude of the error possible from CMT neglect, and also shed light on how to best make such adjustments.

As the approach to severe weather and convective forecasting trends toward high-resolution, explicit-convection modeling (e.g. Kain et al. 2008; Weisman et al. 2008; Coniglio et al. 2009), work on the development and improvement of CP schemes for this particular purpose has slowed. However, while increased computing power may eventually make CP schemes unnecessary for short- and medium-range operational

forecasting, they will likely remain essential for a number of other uses. Ensemble forecasts of all spatial and temporal scales, as well as global and regional climate models are all evolving areas in which the treatment of convection and precipitation continues to be the weakest forecast parameter (e.g., Fritsch and Carbone 2004; Trapp et al. 2007; James et al. 2009). Therefore, it is likely that improving CP schemes to include the effects of more realistic convective system dynamics will remain a valuable contribution, even after mesoscale operational models are run without them.

6.2.2 Corfidi vectors

Corfidi vectors are a forecast tool utilized by operational forecasters to predict MCS motion. The original method is outlined in Corfidi et al. (1996), and an update is provided in Corfidi (2003). The original Corfidi vector approach is presented as a simple technique designed to predict the short-term (3 – 6 h) motion of MCSs using the low-level jet to estimate storm propagation. In this formulation, MCS motion is predicted to be the sum of a vector that represents cell advection by the mean cloud-layer wind (\vec{V}_{CL}) and a vector that represents storm propagation (i.e., new cell development) that is equal in magnitude but directed opposite to the low-level jet, \vec{V}_{LLJ} :

$$\vec{V}_{MCS} = \vec{V}_{CL} - \vec{V}_{LLJ} \quad 6.1$$

The graphical representation of (6.1) is shown in Fig. 6.2a.

The updated technique described in Corfidi (2003) is largely designed to account for the presence of cold pools and the potential for system propagation away from the low-level flow. The new formulation uses the cloud-bearing wind to represent cold pool motion for MCSs that propagate downwind, stating that “a cold pool will elongate in the direction of the mean cloud-layer wind as a result of momentum transfer.” Thus, in a

coarse way, CMT is added to this conceptual model to predict MCS motion. For a downwind propagating system the modified expression becomes:

$$\vec{V}_{MCS} = \vec{V}_{CL} - \vec{V}_{LLJ} + \vec{V}_{CL} \quad 6.2$$

Further detail and justification for the updated technique is provided in Corfidi (2003), and the updated graphical representation for both upwind- and downwind-propagating systems is shown in Fig. 6.2b.

Comparison of the original and updated Corfidi vector approaches thus allows for a simple sensitivity test of the impact of (one way to incorporate) CMT on MCS motion forecasts. Using the CTRL simulation discussed in Chapters 4 and 5, both formulations of Corfidi vectors are calculated for F09 (Fig. 6.3). Vectors are shown for the entire domain, though the relevant areas to the MCS motion “forecast” are those along and ahead of the MCS leading edge (in practice, one uses a mean vector to estimate the motion of the MCS “centroid”). It is clear that the second addition of \vec{V}_{CL} according to the Corfidi (2003) update significantly increases predicted MCS speed overall, and more than doubles the speeds predicted by the Corfidi et al. (1996) formulation along the system’s leading edge. At F09, the MCS produced by the CTRL simulation is estimated to move at $\sim 25\text{ms}^{-1}$ at its bowing center point (e.g. Fig. 6.3). Thus, from this preliminary assessment, it appears that the updated Corfidi vector approach represents a significant improvement over the original for this particular type of MCS environment. However, as seen in Fig. 6.3 and noted by Corfidi (2003) and others, the method remains a rough estimate of overall MCS motion, and leaves significant room for improvement. It is also not entirely clear how such forecasts are actually used in practice in a variety of operational settings; information from forecasters regarding perceived strengths and weaknesses of the method would provide helpful guidance for any future attempts to refine or include CMT in MCS motion forecasts.

The foregoing discussion is not intended to prove or refute the utility of either Corfidi vector approach, but rather to illustrate one example of an effort to incorporate CMT into the forecast framework. Nevertheless, the results of Chapters 3 and 4 do suggest that future work to improve Corfidi vectors by attempting to incorporate a more physical treatment of the storm-induced perturbation wind [and/or thermodynamic information, as shown in Chapter 4 and also discussed by Corfidi (2003)] might lead to further improvement of the technique. As the method is often used on short timescales, it is possible that the inclusion of storm-induced dynamical features such as the RIJ might be more viably incorporated into this type of forecast process as opposed to proximity sounding-based or forecast model-based approaches. From the brief discussion here, it is evident that the effort by Corfidi (2003) to incorporate a simplified representation of the CMT process yields improvement over a past technique neglecting it, and that future attempts to more fully incorporate more detailed aspects of the process may thus be worth pursuing.

6.2.3 Potential incorporation of CMT into a surface wind gust forecast parameter

The analyses and discussion of CMT and surface wind speeds in Chapter 5 suggest that CMT may be an important mechanism in the generation of some types of thunderstorm wind gusts. While the majority of past studies investigating the causes of severe surface winds have focused on the classic downburst model largely driven by concentrated downdrafts and subsequent surface divergence (e.g., Fujita 1985; Wakimoto 2001), some studies have acknowledged the likely influence of the vertical transfer of horizontal momentum (e.g., Brandes 1977; Johns and Doswell 1992; Weisman 1992; Geerts 2001). However, the contribution of CMT to wind gusts beneath thunderstorms remains poorly understood.

Most forecast indices aimed at predicting the potential for strong surface winds are thermodynamically-based, and focus on the potential strength of the convective downdraft itself rather than the actual strength of the resulting surface wind. One example

of such a parameter is “downdraft convective available potential energy” [DCAPE; Emanuel (1994)]. This index, and various methods by which to calculate it, has been examined by several past studies, and investigations by Evans and Doswell (2001) and Kuchera and Parker (2006) find relatively high success rates using it to predict severe wind events. However, many have also noted its inherent weaknesses, such as the violation of parcel theory that occurs when the θ_e values of parcels change due to entrainment of environmental air and subsequent dilution of a downdraft (e.g., Gilmore and Wicker 1998). Moreover, Kuchera and Parker (2006) found that both CAPE and DCAPE were not as successful as ground-relative winds in the lowest several kilometers of the troposphere in predicting severe convective winds, and that including a parameter to account for ground-relative winds into a composite parameter produced the most skillful result.

As Geerts (2001) points out, the literature on strong, convectively-generated surface winds rarely mentions the downward transport of horizontal momentum as a contributing process, despite a number of studies that have found it to be a key driving mechanism (e.g., Eilts and Doviak 1987; Weisman 1992; Orf and Anderson 1999). It is thus conceivable that in many cases, strong surface winds may not necessitate an especially intense downdraft itself, provided that strong winds from aloft are brought far enough surface-ward by moderate or relatively weak downward motions.

One attempt to examine the forecast utility of CMT within the context of strong surface winds was performed by Geerts (2001). In this investigation, a simplified representation of the CMT of ambient winds (i.e., $VA\bar{u}$) is incorporated into an existing thermodynamically-based surface wind gust prediction index, WINDEX (WI ; McCann 1994). The modified index, GUSTEX (GU) uses a fraction of the original WINDEX value, and adds to it one-half of the 500-hPa wind magnitude:

$$GU = \alpha WI + 0.5U_{500} \tag{6.3}$$

where U_{500} is the magnitude of the 500-hPa wind vector, and α is a constant ($0 < \alpha < 1$, found to be ~ 0.60 for the particular dataset used). The factor of 0.5 is used to account for the conservation of horizontal momentum as momentum is transferred from 500 hPa to the surface ($\rho_{500}/\rho_{1000} \sim 0.5$, where ρ is air density). The overall results of the GUSTEX index on 467 MCS events show an improvement (correlation coefficient $r = 0.77$) over WINDEX ($r = 0.05$) for the particular dataset.

While the results of Geerts (2001) are encouraging, many of the dataset's strong wind events remain under-predicted. As discussed previously, the results found in this investigation show the transport of ambient momentum to be of secondary significance to the storm-induced perturbation flow; a similar analysis is made by Weisman (1992) as well. Thus, a more complete integration of the suite of CMT physical processes (i.e. pressure gradient acceleration of mid-level winds and the vertical advection of both the ambient and storm-induced winds) into the forecast framework may be beneficial, and may improve the under-prediction of the strongest wind events.

The results of the evaluation of the GUSTEX parameter also highlight the relative importance of CMT over thermodynamic quantities in moderate-to-strong shear environments (in which long-lived, more organized systems tend to exist). This finding is also emphasized by studies such as Weisman (1992), Evans and Doswell (2001) and Kuchera and Parker (2006), and underscores the necessity of future work to evaluate CMT in a variety of shear profiles (e.g., Appendix B).

While developing and testing an improved wind gust forecast index requires the analysis of many MCS events and thus a large and robust dataset of such cases, several ideas for the incorporation of CMT emerge from the findings discussed here. First, similar to the discussion of CP scheme CMT incorporation above, developing a method to estimate the potential strength of perturbation flow [e.g., from CAPE or related sounding-derived quantities, model forecasts (when applicable), etc.] is important, given that the vertical advection of this quantity is a first-order effect. Though the ambient wind field is certainly easier to incorporate into such a framework (i.e., it can usually be taken from proximity soundings that precede a potential event by several hours), the tendency

of the GUSTEX parameter to underestimate strong surface wind events may be at least partially due to only accounting for the advection of the ambient wind field, and not the accelerated perturbation flow. Second, accounting for vertical wind shear within the context of the potential for storm organization is important, as strong wind shear may favor longer-lived, intense systems (e.g., Rotunno et al. 1988). As noted by Kuchera and Parker (2006), fast environmental winds and high values of vertical wind shear are often linked, and each favor the development of damaging winds by both CMT of high momentum air to the surface, as well as faster system motion and faster-moving gust fronts. Therefore, accounting for shear magnitude is also important. Finally, the direction of the total wind flow relative to the line is another important component if CMT is to be added to a wind gust forecasting tool in a physically-realistic manner; flow perpendicular to the convective line is shown to be a characteristic that providing further useful differentiation in the cases examined by Parker and Kuchera (2006). The strength and direction of ambient flow is often related to the RIJ by increasing (decreasing) RIJ strength through favorable (unfavorable) alignment, as found by Smull and Houze (1987). Thus, it is possible that enhanced forecast utility may be gleaned from further consideration of the potential of the ambient wind field to affect RIJ orientation and intensity.

The incorporation of the abovementioned ideas into an improved wind gust forecast parameter are not trivial, and it may be difficult (if not impossible) to ultimately develop a tool that produces improvements across a spectrum of MCS events. A common theme to the potential for the incorporation of CMT into forecast applications is the need for an inclusive investigation of many MCS events. Such an approach is a likely direction of future research.

6.3 Summary of ideas for future work

The results of this investigation highlight several avenues for potential future work. One topic inviting further study and discussed above is the potential for the improved incorporation of CMT into CP schemes. A second area of potential future

research involves the analysis of a substantial dataset of observed MCS events with which to gauge the potential forecast improvement of MCS motion and severe surface wind gust potential by incorporation of CMT principles. The exploration of additional storm environments within the idealized modeling framework is also desirable in order to better understand the role of the background wind field and shear profile in determining the significance of CMT in a given storm environment (this is discussed briefly in Appendix B). Finally, within the field of MCS research in general, there remain outstanding research questions regarding the processes that dictate the intensity and descent of the RIJ, and also the challenges in adequate and realistic representation of the trailing stratiform region by numerical models. As both of these MCS features are critical to determining the ultimate impact of CMT to both system speed and surface wind generation, further research to better understand them is key. As previously noted, these features and other relevant CMT processes may also be quite sensitive to model grid spacing; future investigation should examine this sensitivity and consider using higher resolution simulations as computing capabilities advance. While the work described herein represents an important step in improving the understanding of the CMT process in MCSs, the optimal use of such results within an operational forecasting framework will require further study in the above areas.

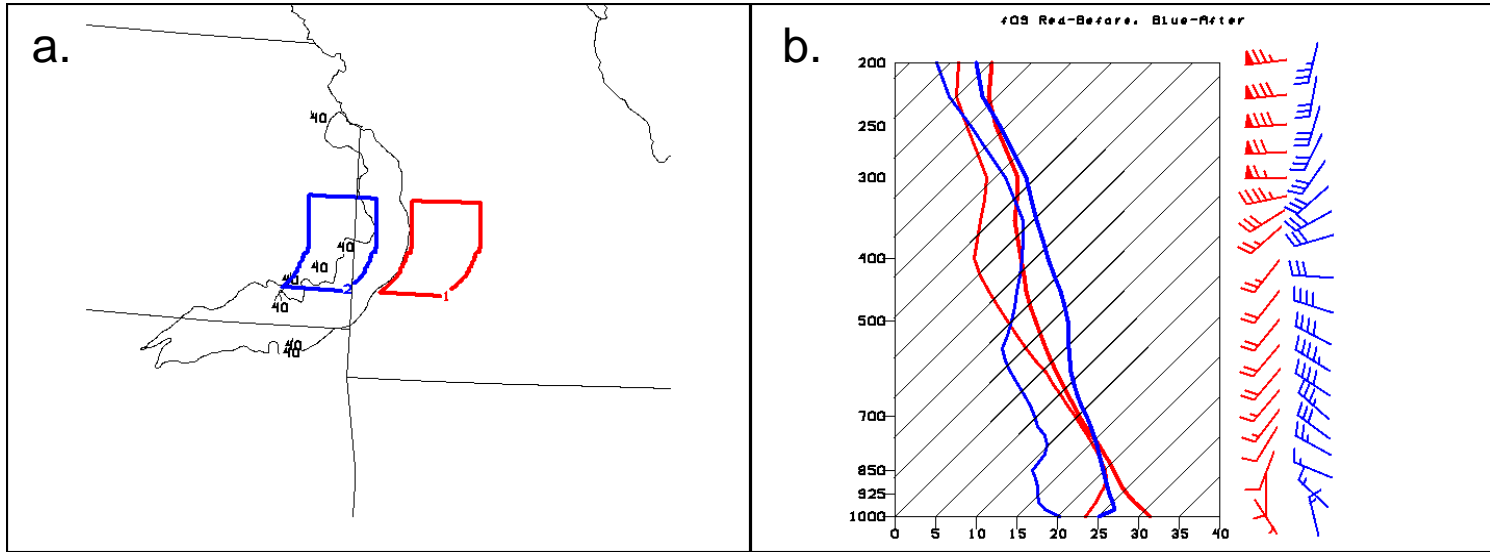


Figure 6.1: a) Schematic of “before”-MCS region (red) and “after”-MCS region (blue) used for averages shown in b); b) SKEW-T showing “before”-MCS area-averaged temperature and dewpoint profiles (red, right and left, respectively) and “after”-MCS area-averaged temperature and dewpoint profiles (red, right and left, respectively), with average wind fields shown at right in knots.

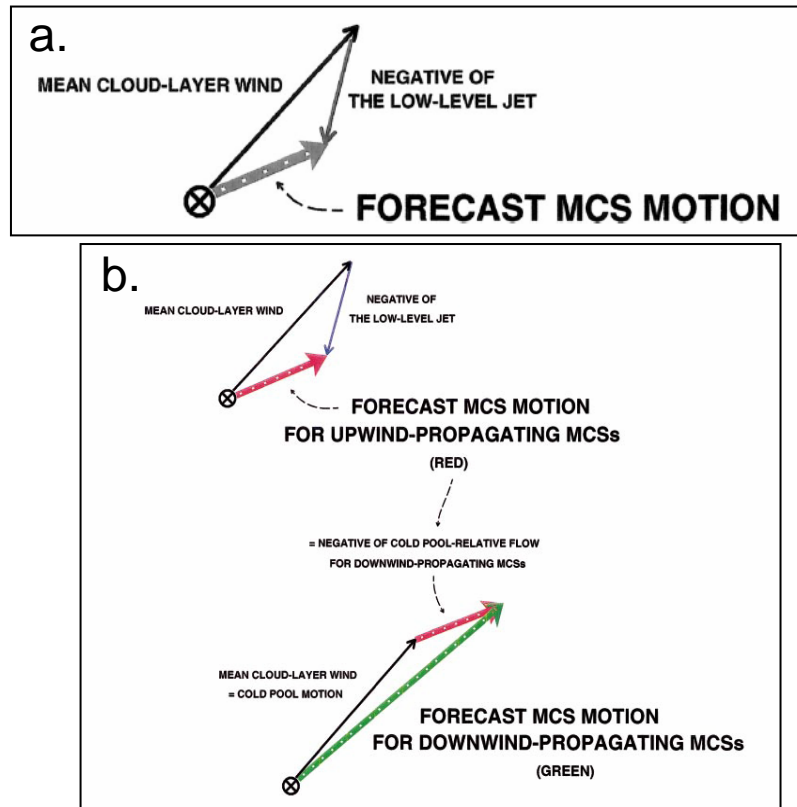


Figure 6.2: a) Original Corfidi vector technique, with MCS core motion (thick dotted arrow) expressed as the vector sum of 1) advection of cells by the mean cloud-layer wind (arrow pointing to upper right) and 2) cell propagation directed into the low-level jet (arrow pointing to bottom of page). MCS centroid is depicted by the cross symbol [from Corfidi (2003), after Corfidi et al. (1996)], and b) updated Corfidi technique showing (top) upwind and (bottom) downwind versions of the vector technique to forecast short-term motion of upwind-developing systems (MCS motion given by thick red arrows) and downwind-developing systems (MCS motion given by thick green arrow at bottom of figure), respectively. Vector lengths are proportional to wind speed; MCS centroids are denoted by the cross symbol [from Corfidi (2003)].

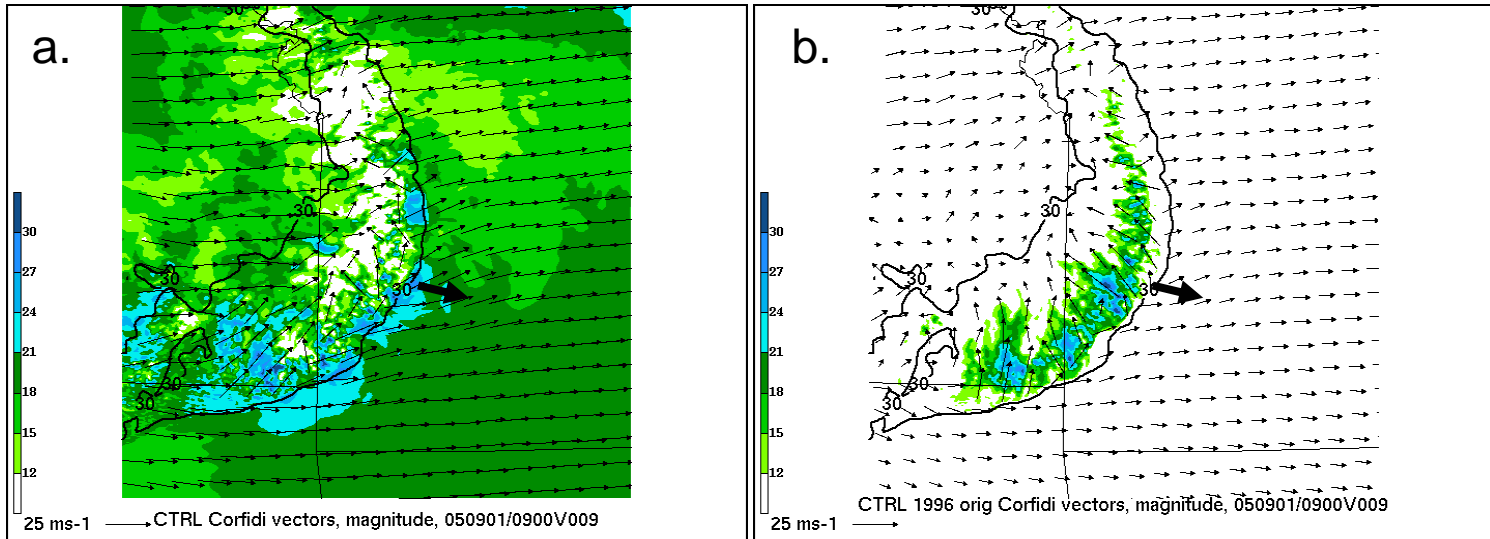


Figure 6.3: Corfidi vectors at F09 (vectors, reference vectors as indicated in lower left) and vector magnitude (ms^{-1} , shaded as indicated) calculated according to a) Corfidi (2003), and b) Corfidi et al. (1996). Single thick black arrow represents “observed” mean vector motion of CTRL MCS.

REFERENCES

- Ashley, W. S., and T.L. Mote, 2005: Derecho hazards in the United States. *Bull. Amer. Met. Soc.*, **86**, 1577–1592.
- Atkins, N. T., C. S. Bouchard, R. W. Przybylinski, R. J. Trapp, and G. Schmocker, 2005: Damaging surface wind mechanisms within the 10 June 2003 Saint Louis bow echo during BAMEX. *Mon. Wea. Rev.*, **133**, 2275–2296.
- , and M. St. Laurent, 2009a: Bow echo mesovortices. Part I: Processes that influence their damaging potential. *Mon. Wea. Rev.*, **137**, 1497–1513.
- , and ———, 2009b: Bow echo mesovortices. Part II: Their genesis. *Mon. Wea. Rev.*, **137**, 1514–1532.
- Betts, A. K., 1986: A new convective adjustment scheme. Part I: Observational and theoretical basis. *Quart. J. Roy. Meteor. Soc.*, **112**, 677–691.
- Bluestein, H. B., 1993: *Synoptic-Dynamic Meteorology in Midlatitudes. Vol. II: Observations and Theory of Weather Systems*. Oxford University Press, 594 pp.
- , and M. H. Jain, 1985: Formation of mesoscale lines of precipitation: Severe squall lines in Oklahoma during the spring. *J. Atmos. Sci.*, **42**, 1711–1732.
- Brandes, E. A., 1977: Gust front evolution and tornado genesis as viewed by Doppler radar. *J. Appl. Meteor.*, **16**, 333–338.
- Brasseur, O., 2001: Development and application of a physical approach to estimating wind gusts. *Mon. Wea. Rev.*, **129**, 5–25.

- Braun, S. A., and R. A. Houze, Jr., 1995: Melting and freezing in a mesoscale convective system. *Quart. J. Roy. Meteor. Soc.*, **121**, 55-77.
- , and ———, 1997: The evolution of the 10–11 June 1985 PRE-STORM squall line: Initiation, development of rear inflow, and dissipation. *Mon. Wea. Rev.*, **125**, 478–504.
- Bryan, G. H., and R. Rotunno, 2008: Gravity currents in a deep anelastic atmosphere. *J. Atmos. Sci.*, **65**, 536–556.
- , and M. L. Weisman, 2006: Mechanisms for the production of severe surface winds in a simulation of an elevated convective system. Preprints, *23rd Conf. on Severe Local Storms*, St. Louis, MO, Amer. Meteor. Soc., 7.5.
- , J. C. Wyngaard, and J. M. Fritsch, 2003: Resolution requirements for the simulation of deep moist convection. *Mon. Wea. Rev.*, **131**, 2394–2416.
- Bukovsky, M. S., J. S. Kain, and M. E. Baldwin, 2006: Bowing convective systems in a popular operational model: Are they for real? *Wea. Forecasting*, **21**, 307–324.
- Carr, M. T., and C. S. Bretherton, 2001: Convective momentum transport over the tropical Pacific: Budget estimates. *J. Atmos. Sci.*, **58**, 1673–1693.
- Charba, J., 1974: Application of gravity current model to analysis of squall-line gust front. *Mon. Wea. Rev.*, **102**, 140–156.
- Chen, S.-H., and W.-Y. Sun, 2002: A one-dimensional time dependent cloud model. *J. Meteor. Soc. Japan*, **80**, 99–118.

- Cohen, A. E., M. C. Coniglio, S. F. Corfidi, and S. J. Corfidi, 2007: Discrimination of mesoscale convective system environments using sounding observations. *Wea. Forecasting*, **22**, 1045–1062.
- Coniglio, M. C., D. J. Stensrud, and L. J. Wicker, 2006: Effects of upper-level shear on the structure and maintenance of strong quasi-linear mesoscale convective systems. *J. Atmos. Sci.*, **63**, 1231–1252.
- , K. L. Elmore, J. S. Kain, S. J. Weiss, M. Xue, 2009: Evaluation of WRF model output for severe-weather forecasting from the 2008 NOAA Hazardous Weather Testbed Spring Experiment. *Wea. Forecasting*. *In Press*.
- Corfidi, S. F., 2003: Cold pools and MCS propagation: Forecasting the motion of downwind-developing MCSs. *Wea. Forecasting*, **18**, 997–1017.
- , J. H. Meritt and J. M. Fritsch, 1996: Predicting the movement of mesoscale convective complexes. *Wea. Forecasting*, **11**, 41–46.
- Correia, J., R. W. Arritt, and C. J. Anderson, 2008: Idealized mesoscale convective system structure and propagation using convective parameterization. *Mon. Wea. Rev.*, **136**, 2422–2442.
- Done, J., C. Davis, and M. Weisman, 2004: The next generation of NWP: Explicit forecasts of convection using Weather Research and Forecasting (WRF) Model. *Atmos. Sci. Lett.*, DOI: 10.1002/asl.72.
- Eilts, M. D., and R. J. Doviak, 1987: Oklahoma downbursts and their asymmetry. *J. Appl. Meteor.*, **26**, 69–78.

- Emanuel, K. A., 1994: *Atmospheric Convection*. Oxford University Press, 883 pp.
- Engerer, N. A., D. J. Stensrud, and M. C. Coniglio, 2008: Surface characteristics of observed cold pools. *Mon. Wea. Rev.*, **136**, 4839–4849.
- Evans, J. S., and C. A. Doswell, 2001: Examination of derecho environments using proximity soundings. *Wea. Forecasting*, **16**, 329–342.
- Ferrier, B. S., W. K. Tao, and J. Simpson, 1995: A double-moment multiple-phase four-class bulk ice scheme. Part II: Simulations of convective storms in different large-scale environments and comparisons with other bulk parameterizations. *J. Atmos. Sci.*, **52**, 1001–1033.
- Forbes, G. S., and R. M. Wakimoto, 1983: A concentrated outbreak of tornadoes, downbursts and microbursts, and implications regarding vortex classification. *Mon. Wea. Rev.*, **111**, 220–236.
- Foster, D. S., 1958: Thunderstorm gusts compared with computed downdraft speeds. *Mon. Wea. Rev.*, **86**, 91–94.
- Fovell, R. G., and Y. Ogura, 1988: Numerical simulation of a midlatitude squall line in two dimensions. *J. Atmos. Sci.*, **45**, 3846–3879.
- , G. L. Mullendore, and S. H. Kim, 2006: Discrete propagation in numerically simulated nocturnal squall lines. *Mon. Wea. Rev.*, **134**, 3735–3752.
- Fritsch, J. M., and G. S. Forbes, 2001: Mesoscale convective systems. *Severe Convective Storms*, Meteor. Monogr., No. 50, Amer. Meteor. Soc., 323–357.

- , and R. E. Carbone, 2004: Improving quantitative precipitation forecasts in the warm season: A USWRP research and development strategy. *Bull. Amer. Meteor. Soc.*, **85**, 955–965.
- Fujita, T. T., 1978: Manual of downburst identification for project NIMROD. Satellite and Mesometeorology Res. Pap. No. 156, University of Chicago, Dept. of Geophysical Sciences, pp. 104.
- , 1985: The downburst. SMRP Res. Paper No. 210, NITIS PB 85-148880. 122 pp. [Available from the University of Chicago, Chicago, IL.]
- , and R.M. Wakimoto, 1981: Five scales of airflow associated with a series of downbursts on 16 July 1980. *Mon. Wea. Rev.*, **109**, 1438–1456.
- Gallus, W. A., and R. H. Johnson, 1992: The momentum budget of an intense midlatitude squall line. *J. Atmos. Sci.* **49**, 422–450.
- , and M. Pfeifer, 2008: Intercomparison of simulations using 5 WRF microphysical schemes with dual-Polarization data for a German squall line. *Advances in Geosciences*, **16**, 109-116.
- Gao, K., D-L Zhang, M. W. Moncrieff, and H-R Cho, 1990: Mesoscale momentum budget in a midlatitude squall line: A numerical case study. *Mon. Wea. Rev.*, **118**, 1011–1028.
- Geerts, B., 2001: Estimating downburst-related maximum surface wind speeds by means of proximity soundings in New South Wales, Australia. *Wea. Forecasting*, **16**, 261–269.

- Gentry, M. S., and G. M. Lackmann, 2009: Sensitivity of simulated tropical cyclone structure and intensity to horizontal resolution, *Mon. Wea. Rev.*, *submitted*.
- Gilmore, M. S., and L. J. Wicker, 1998: The influence of midtropospheric dryness on supercell morphology and evolution. *Mon. Wea. Rev.*, **126**, 943–958.
- Glickman T. S., Ed. 2000: *Glossary of Meteorology*. 2nd ed. Amer. Meteor. Soc., 855 pp.
- Goff, C. R., 1976: Vertical structure of thunderstorm outflows. *Mon. Wea. Rev.*, **104**, 1429–1440.
- Grell, G. A., 1993: Prognostic evaluation of assumptions used by cumulus parameterizations. *Mon. Wea. Rev.*, **121**, 764–787.
- Grim, J. A., R. M. Rauber, G. M. McFarquhar, B. F. Jewett, and D. P. Jorgensen, 2009a: Development and forcing of the rear inflow jet in a rapidly developing and decaying squall line during BAMEX. *Mon. Wea. Rev.*, **137**, 1206–1229.
- , G. M. McFarquhar, R. M. Rauber, A. M. Smith, and B. F. Jewett, 2009b: Microphysical and thermodynamic structure and evolution of the trailing stratiform regions of mesoscale convective systems during BAMEX. Part II: Column model simulations. *Mon. Wea. Rev.*, **137**, 1186–1205.
- Grubišić, V. and M. W. Moncrieff, 2000: Parameterization of convective momentum transport in highly baroclinic conditions. *J. Atmos. Sci.*, **57**, 3035–3049.
- Haertel, P. T., and R. H. Johnson, 2000: The linear dynamics of squall line mesohighs and wake lows. *J. Atmos. Sci.*, **57**, 93–107.

- Han, J., and H-L Pan, 2006: Sensitivity of hurricane intensity forecast to convective momentum transport parameterization. *Mon. Wea. Rev.*, **134**, 664–674.
- Hogan, T. F., and R. L. Pauley, 2007: The impact of convective momentum transport on tropical cyclone track forecasts using the Emanuel cumulus parameterization. *Mon. Wea. Rev.*, **135**, 1195–1207.
- Hong, S.-Y. and J.-O. Lim, 2006: The WRF single-moment 6-Class microphysics scheme (WSM6). *J. Korean Meteor. Soc.*, **42**, 129-151.
- , Y. Noh, and J. Dudhia, 2006: A new vertical diffusion package with an explicit treatment of entrainment processes. *Mon. Wea. Rev.*, **134**, 2318–2341.
- Houze, R. A., Jr., 1973: A climatological study of vertical transports by cumulus-scale convection. *J. Atmos. Sci.*, **30**, 1112-1123.
- , 2004: Mesoscale convective systems. *Rev. Geophys.*, **42**, 10.1029/2004RG000150, 43 pp.
- , S. A. Rutledge, M. I. Biggerstaff, and B. F. Smull, 1989: Interpretation of Doppler weather radar displays in midlatitude mesoscale convective systems. *Bull. Amer. Meteor. Soc.*, **70**, 608-619.
- , B. F. Smull, and P. Dodge, 1990: Mesoscale organization of springtime rainstorms in Oklahoma. *Mon. Wea. Rev.*, **118**, 613-654.
- , S. S. Chen, D. E. Kingsmill, Y. Serra, and S. E. Yuter, 2000: Convection over the Pacific warm pool in relation to the atmospheric Kelvin-Rossby wave. *J. Atmos.*

- Sci.*, **57**, 3058-3089.
- James, K. A., D. J. Stensrud, and N. Yussouf, 2009: Value of real-time vegetation fraction to forecasts of severe convection in high-resolution models. *Wea. Forecasting*, **24**, 187–210.
- James R. P., and P. M. Markowski, 2009: A numerical investigation of the effects of dry air aloft on deep convection. *Mon. Wea. Rev.*, In Press.
- Janjić, Z. I., 1994: The step-mountain eta coordinate model: Further developments of the convection, viscous sublayer, and turbulence closure schemes. *Mon. Wea. Rev.*, **122**, 927–945.
- Jankov, I., Bao J. W., Neiman P. J., Schultz P. J., Yuan H., 2009: Evaluation and comparison of microphysical algorithms in WRF-ARW: Model simulations of atmospheric river events affecting the California coast. *J. Hydromet.*, In Press.
- Jewett, B. F., and R. B. Wilhelmson, 2006: The role of forcing in cell morphology and evolution within midlatitude squall lines. *Mon. Wea. Rev.*, **134**, 3714–3734.
- Johns, R. H., and C. A. Doswell, 1992: Severe local storms forecasting. *Wea. Forecasting*, **7**, 588–612.
- , and W. D. Hirt, 1987: Derechos: Widespread convectively induced windstorms. *Wea. Forecasting*, **2**, 32–49.
- Johnson, R. H., and P. J. Hamilton, 1988: The relationship of surface pressure features to the precipitation and airflow structure of an intense midlatitude squall line. *Mon. Wea. Rev.*, **116**, 1444–1473.

- Kain, J. S., and J. M. Fritsch, 1993: Convective parameterization for mesoscale models: The Kain-Fritsch scheme. *The Representation of Cumulus Convection in Numerical Models*, Meteor. Monogr., No. 46, Amer. Meteor. Soc., 165–170.
- , S. J. Weiss, D. R. Bright, M. E. Baldwin, J. J. Levit, G. W. Carbin, C. S. Schwartz, M. L. Weisman, K. K. Droegemeier, D. B. Weber, and K. W. Thomas, 2008: Some practical considerations regarding horizontal resolution in the first generation of operational convection-allowing NWP. *Wea. Forecasting*, **23**, 931–952.
- Keyser, D., and L. W. Uccellini, 1987: Regional models: Emerging research tools for synoptic meteorologists. *Bull. Amer. Meteor. Soc.*, **68**, 306–320.
- Kingsmill, D. E., and R. M. Wakimoto, 1991: Kinematic, dynamic, and thermodynamic analysis of a weakly sheared severe thunderstorm over Northern Alabama. *Mon. Wea. Rev.*, **119**, 262–297.
- Klimowski, B. A., 1994: Initiation and development of rear inflow within the 28-29 June 1989 North Dakota mesoconvective system. *Mon. Wea. Rev.*, **122**, 765–779.
- Knupp, K. R., 1987: Downdrafts within High Plains cumulonimbi. Part I: General kinematic structure. *J. Atmos. Sci.*, **44**, 987–1008.
- , 1988: Downdrafts within High Plains cumulonimbi. Part II: Dynamics and thermodynamics. *J. Atmos. Sci.*, **45**, 3965–3982.
- Kuchera, E. L., and M. D. Parker, 2006: Severe convective wind environments. *Wea. Forecasting*, **21**, 595–612.

- Lafore, J. P., and M. W. Moncrieff, 1989: A numerical investigation of the organization and interaction of the convective and stratiform regions of tropical squall lines. *J. Atmos. Sci.*, **46**, 521–544.
- Lee, B. D., and R. B. Wilhelmson, 1997: The numerical simulation of non-supercell tornadogenesis. Part I: Initiation and evolution of pretornadic misocyclone circulations along a dry outflow boundary. *J. Atmos. Sci.*, **54**, 32–60.
- LeMone, M. A., 1983: Momentum transport by a line of cumulonimbus. *J. Atmos. Sci.*, **40**, 1815–1834.
- Lin, Y. L., R. D. Farley, and H. D. Orville, 1983: Bulk parameterization of the snow field in a cloud model. *J. Appl. Meteor.*, **22**, 1065–1092.
- Liu, C., and M.W. Moncrieff, 2007: Sensitivity of cloud-resolving simulations of warm-season convection to cloud microphysics parameterizations. *Mon. Wea. Rev.*, **135**, 2854–2868.
- Loehrer, S. M., and R. H. Johnson, 1995: Surface pressure and precipitation life cycle characteristics of PRE-STORM mesoscale convective systems. *Mon. Wea. Rev.*, **123**, 600-621
- Lynn, B. H., A. P. Khain, J. Dudhia, D. Rosenfeld, A. Pokrovsky, and A. Seifert, 2005: Spectral (bin) microphysics coupled with a mesoscale model (MM5). Part II: Simulation of a CaPE rain event with a squall line. *Mon. Wea. Rev.*, **133**, 59–71.
- Mahoney, K. M., and G. M. Lackmann, 2007: The effect of upstream convection on downstream precipitation. *Wea. Forecasting*, **22**, 255–277.

- McCann, D. W., 1994: WINDEX—A new index for forecasting microburst potential. *Wea. Forecasting*, **9**, 532–541.
- Mechem, D. B., S. S. Chen, and R. A. Houze, Jr., 2006: Momentum transport processes in the stratiform regions of mesoscale convective systems over the western Pacific warm pool. *Quart. J. Roy. Meteor. Soc.*, **132**, 709–736.
- Merritt, J. H., and J. M. Fritsch, 1984: On the movement of the heavy precipitation areas of mid-latitude mesoscale convective complexes. *Preprints*, 10th Conf. on Weather Analysis and Forecasting, Clearwater, Amer. Meteor. Soc., 529–536.
- Molinari, J. and M. Dudek, 1992: Parameterization of convective precipitation in mesoscale numerical models: A critical review. *Mon. Wea. Rev.*, **120**, 326–344.
- Moncrieff, M. W., and C. Liu, 2006: Representing convective organization in prediction models by a hybrid strategy. *J. Atmos. Sci.*, **63**, 3404–3420.
- Morrison, H., G. Thompson, and V. Tatarskii, 2009: Impact of cloud microphysics on the development of trailing stratiform precipitation in a simulated squall line: Comparison of one- and two-moment schemes. *Mon. Wea. Rev.*, **137**, 991–1007.
- Newton, C. W., 1950: Structure and mechanisms of the prefrontal squall line. *J. Meteor.*, **7**, 210–222.
- , and J. C. Fankhauser, 1964: On the movements of convective storms, with emphasis on size discrimination in relation to water-budget requirements. *J. Appl. Meteor.*, **3**, 651–668.

- , and H. R. Newton, 1959: Dynamical interactions between large convective clouds and environments with vertical shear. *J. Meteor.*, **16**, 483–496.
- Nicholls, M. E., R. H. Johnson, and W. R. Cotton, 1988: The sensitivity of two-dimensional simulations of tropical squall lines to environmental profiles. *J. Atmos. Sci.*, **45**, 3625–3649.
- Orf, L. G., and J. R. Anderson, 1999: A numerical study of traveling microbursts. *Mon. Wea. Rev.*, **127**, 1244–1258.
- Paluch, I. R., 1979: The entrainment mechanism in Colorado cumuli. *J. Atmos. Sci.*, **36**, 2467–2478.
- Pandya, R. E. and D. R. Durran, 1996: The influence of convectively generated thermal forcing on the mesoscale circulation around squall lines. *J. Atmos. Sci.*, **53**, 2924–2951.
- Parker, M.D., 2008: Response of simulated squall lines to low-level cooling. *J. Atmos. Sci.*, **65**, 1323–1341.
- , and R. H. Johnson, 2000: Organizational modes of midlatitude mesoscale convective systems. *Mon. Wea. Rev.*, **128**, 3413–3436.
- , and ———, 2004a: Simulated convective lines with leading precipitation. Part I: Governing dynamics. *J. Atmos. Sci.*, **61**, 1637–1655.
- , and ———, 2004b: Structures and dynamics of quasi-2D mesoscale convective systems. *J. Atmos. Sci.*, **61**, 545–567.

- Proctor, F. H., 1989: Numerical simulations of an isolated microburst. Part II: Sensitivity experiments. *J. Atmos. Sci.*, **46**, 2143–2165.
- Richardson, Y. P., K. K. Droegemeier, and R. P. Davies-Jones, 2007: The influence of horizontal environmental variability on numerically simulated convective storms. Part I: Variations in vertical shear. *Mon. Wea. Rev.*, **135**, 3429–3455.
- Rotunno R., J. B. Klemp, and M. L. Weisman, 1988: A theory for strong, long-lived squall lines. *J. Atmos. Sci.*, **45**, 463–485.
- Rutledge, S. A., R. A. Houze, M. I. Biggerstaff, and T. Matejka, 1988: The Oklahoma–Kansas mesoscale convective system of 10–11 June 1985: Precipitation structure and single-doppler radar analysis. *Mon. Wea. Rev.*, **116**, 1409–1430.
- Sanders, F., and K. A. Emanuel, 1977: The momentum budget and temporal evolution of a mesoscale convective system. *J. Atmos. Sci.*, **34**, 322–330.
- Skamarock, W. C., M. L. Weisman, and J. B. Klemp, 1994: Three-dimensional evolution of simulated long-lived squall lines. *J. Atmos. Sci.*, **51**, 2563–2584.
- , J. B. Klemp, J. Dudhia, D. O. Gill, D. M. Barker, W. Wang, and J. G. Powers, 2007: A description of the advanced research WRF Version 2. NCAR Technical Note.
- Smith, A. M., G. M. McFarquhar, R. M. Rauber, J. A. Grim, M. S. Timlin, B. F. Jewett, and D. P. Jorgensen, 2009: Microphysical and thermodynamic structure and evolution of the trailing stratiform regions of mesoscale convective systems during BAMEX. Part I: Observations. *Mon. Wea. Rev.*, **137**, 1165–1185.

- Smull, B. F., and R. A. Houze, Jr., 1987: Rear inflow in squall lines with trailing stratiform precipitation. *Mon. Wea. Rev.*, **115**, 2869-2889.
- Srivastava, R., 1985: A simple model of evaporatively driven downdraft: Application to microburst downdraft. *J. Atmos. Sci.*, **42**, 1004–1023.
- , 1987: A model of intense downdrafts driven by the melting and evaporation of precipitation. *J. Atmos. Sci.*, **44**, 1752–1774.
- Stein, U., and P. Alpert, 1993: Factor separation in numerical simulations. *J. Atmos. Sci.*, **50**, 2107–2115.
- Szeto, K. K., R. E. Stewart, and C. A. Lin, 1988: Mesoscale circulations forced by melting snow. Part II: Application to meteorological features. *J. Atmos. Sci.*, **45**, 1642–1650.
- Trapp, R. J., and M. L. Weisman, 2003: Low-Level Mesovortices within Squall Lines and Bow Echoes. Part II: Their Genesis and Implications. *Mon. Wea. Rev.*, **131**, 2804–2823.
- , D. M. Wheatley, N. T. Atkins, R. W. Przybylinski, and R. Wolf, 2006: Buyer beware: Some words of caution on the use of severe wind reports in postevent assessment and research. *Wea. Forecasting*, **21**, 408–415.
- , B. Halvorson, and N. S. Diffenbaugh, 2007: Telescoping, multimodel approaches to evaluate extreme convective weather under future climates, *Journal of Geophysical Research*, **112**, D20109, doi:10.1029/2006JD008345.

- Trier, S. B., M. A. LeMone, and W. C. Skamarock, 1998: Effect of three-dimensional structure on the stormwide horizontal accelerations and momentum budget of a simulated squall line. *Mon. Wea. Rev.*, **126**, 2580–2598.
- , C. A. Davis, D. A. Ahijevych, M. L. Weisman, and G. H. Bryan, 2006: Mechanisms supporting long-lived episodes of propagating nocturnal convection within a 7-day WRF model simulation. *J. Atmos. Sci.*, **63**, 2437–2461.
- van den Broeke, M. S., D. M. Schultz, R. H. Johns, J. S. Evans and J. E. Hales, 2005: Cloud-to-ground lightning production in strongly forced, low-instability convective lines associated with damaging wind. *Wea. Forecasting*, **20**, 517–530.
- Vescio, M. D., and R. H. Johnson, 1992: The surface-wind response to transient mesoscale pressure fields associated with squall lines. *Mon. Wea. Rev.*, **120**, 1837–1850.
- Wakimoto R. M., 2001: Convectively driven high wind events. *Severe Convective Storms, Meteor. Monogr.*, No. 50, Amer. Meteor. Soc., 255–298.
- , H. V. Murphey, C. A. Davis, and N. T. Atkins, 2006: High winds generated by bow echoes. Part II: The relationship between the mesovortices and damaging straight-line winds. *Mon. Wea. Rev.*, **134**, 2813–2829.
- Weisman, M. L., 1992: The role of convectively generated rear-inflow jets in the evolution of long-lived mesoconvective systems. *J. Atmos. Sci.*, **49**, 1826–1847.
- , 1993: The genesis of severe, long-lived bow echoes. *J. Atmos. Sci.*, **50**, 645–670.

- , and J. B. Klemp, 1982: The dependence of numerically simulated convective storms on vertical wind shear and buoyancy. *Mon. Wea. Rev.*, **110**, 504–520.
- and ———, 1986: Characteristics of Isolated Convective Storms. *Mesoscale Meteorology and Forecasting*, P. S. Ray, Ed., Amer. Meteor. Soc., 331–357.
- , and R. J. Trapp, 2003: Low-level mesovortices within squall lines and bow echoes. Part I: Overview and dependence on environmental shear. *Mon. Wea. Rev.*, **131**, 2779–2803.
- , W. C. Skamarock, and J. B. Klemp, 1997: The resolution dependence of explicitly modeled convective systems. *Mon. Wea. Rev.*, **125**, 527–548.
- , C. Davis, W. Wang, K. W. Manning, and J. B. Klemp, 2008: Experiences with 0–36-h explicit convective forecasts with the WRF-ARW model. *Wea. Forecasting*, **23**, 407–437.
- Wheatley, D. M., and R. J. Trapp, 2008: The effect of mesoscale heterogeneity on the genesis and structure of mesovortices within quasi-linear convective systems. *Mon. Wea. Rev.*, **136**, 4220–4241.
- Wheatley, D.M., R.J. Trapp, and N.T. Atkins, 2006: Radar and damage analysis of severe bow echoes observed during BAMEX. *Mon. Wea. Rev.*, **134**, 791–806.
- Wu, X., and M. Yanai, 1994: Effects of vertical wind shear on the cumulus transport of momentum: Observations and parameterization. *J. Atmos. Sci.*, **51**, 1640–1660.

- , L. Deng, X. Song, and G. J. Zhang, 2007: Coupling of convective momentum transport with convective heating in global climate simulations. *J. Atmos. Sci.*, **64**, 1334–1349.
- Xue, M., 2000: Density currents in two-layer shear flows. *Quart. J. Roy. Met. Soc.*, **126**, 1301-1320.
- Yang, M.-J., and R. A. Houze, Jr., 1995: Sensitivity of squall-line rear inflow to ice microphysics and environmental humidity. *Mon. Wea. Rev.*, **123**, 3175-3193.
- , and ——, 1996: Momentum budget of a squall line with trailing stratiform precipitation: Calculations with a high-resolution numerical model. *J. Atmos. Sci.*, **53**, 3629-3652.
- Yuter, S. E., and R. A. Houze, Jr., 1995a: Three-dimensional kinematic and microphysical evolution of Florida cumulonimbus. Part III: Vertical mass transport, mass divergence, and synthesis. *Mon. Wea. Rev.*, **123**, 1964-1983.
- , and ——, 1995b: Three-dimensional kinematic and microphysical evolution of Florida cumulonimbus, Part II: Frequency distributions of vertical velocity, reflectivity, and differential reflectivity. *Mon. Wea. Rev.*, **123**, 1941-1963.
- Zhang, D. L., and K. Gao, 1989: Numerical simulation of an intense squall line during 10–11 June 1985 PRE-STORM. Part II: Rear inflow, surface pressure perturbations and stratiform precipitation. *Mon. Wea. Rev.*, **117**, 2067–2094.
- , K. Gao, D. B. Parsons, 1989: Numerical simulation of an intense squall line during 10–11 June 1985 PRE-STORM. Part I: Model verification. *Mon. Wea. Rev.*, **117**, 960–994.

Zhang, Q. H., K. H. Lau, Y. H. Kuo, and S. J. Chen, 2003: A numerical study of a mesoscale convective system over the Taiwan Strait. *Mon. Wea. Rev.*, **131**, 1150–1170.

Zipser, E., 1977: Mesoscale and convective-scale downdrafts as distinct components of squall-line structure. *Mon. Wea. Rev.*, **105**, 1568–1589.

Appendices

Appendix A

Model framework: “Idealized” vs. “quasi-idealized”

Significant consideration was given to performing this investigation of CMT in MCSs using a more traditional idealized MCS model methodology in which a horizontally homogeneous initial sounding is used, and both thermal wind balance and the Coriolis force are omitted. For reasons detailed in Chapter 2, the “quasi-idealized” methodology was instead selected after methodically comparing the two frameworks. Some of those comparisons are detailed briefly here.

The most comprehensive comparison of model set-up was done with two simulations with identical parameterizations but different initial conditions as detailed in Table A.1. The runs will be referred to as “idealized” and “quasi-idealized,” (Q-I) despite the fact that the “idealized” run is quite different from the more traditional 2-D idealized squall line studies such as those in Rotunno et al. (1988). Skamarock et al. (1994) discuss the differences that emerge when transitioning from a 2-D to 3-D framework in squall line simulations, and further emphasize differences in MCS symmetry, line-end vortices, and mesoscale convective vortex (MCV) generation revealed by sensitivity studies that both include and omit the Coriolis force.

The two simulations to be compared here begin with the same initial sounding shape (Fig. A.1), but the Q-I simulation includes a north-south thermal gradient and a corresponding jet stream and Coriolis effects as before, while the Idealized simulation remains horizontally homogeneous and omits Coriolis effects. Figures A.2 and A.3 depict the evolution of each simulation, illustrating many of the same differences noted by Skamarock et al. (1994). That is, the Q-I run both develops and moves preferentially toward the southeast, likely due to both enhanced CAPE to the south as well as the rightward torque on cold pool winds provided by the inclusion of the Coriolis force. In contrast, the Idealized simulation maintains nearly perfect symmetry across its leading edge and line-end features.

Pressure perturbation features are qualitatively similar between the simulations, but a more intense mid-level mesolow and upper-level mesohigh are generated earlier in the Idealized simulation (Fig. A.4). However, while the Idealized run intensifies quickly but becomes fairly steady-state, the Q-I run intensifies after F06 and reveals more intense pressure perturbation features (as shown in Chapter 3). A comparison of relevant momentum budget terms shows qualitative similarities between the two runs as well, with a marked increase in magnitude for the terms in the Idealized simulation at F06 (Fig. A.5), while the Q-I simulation terms increase as the system, becoming as large or larger than the Idealized values ~F08 (Fig. A.6).

MCS motion between the simulations is of interest as well. While the Q-I simulation accelerates in a similar manner to CTRL, the Idealized simulation maintains a constant speed throughout the simulation (Fig. A.7). A possible explanation for this difference may be the effect of the CAPE gradient – that is, as the Q-I system moves southward and into a higher-CAPE environment, the intensification of the system likely affects both the cold pool intensity and the strength of the RIJ and CMT processes. It is beyond the scope of this study to determine the exact cause(s), but implications may be important due to large number of previous MCS studies that use a 2-D, idealized, Coriolis-omitting set-up. More completely assessing the cause of any dynamical differences between the two simulations is a potential area of future study.

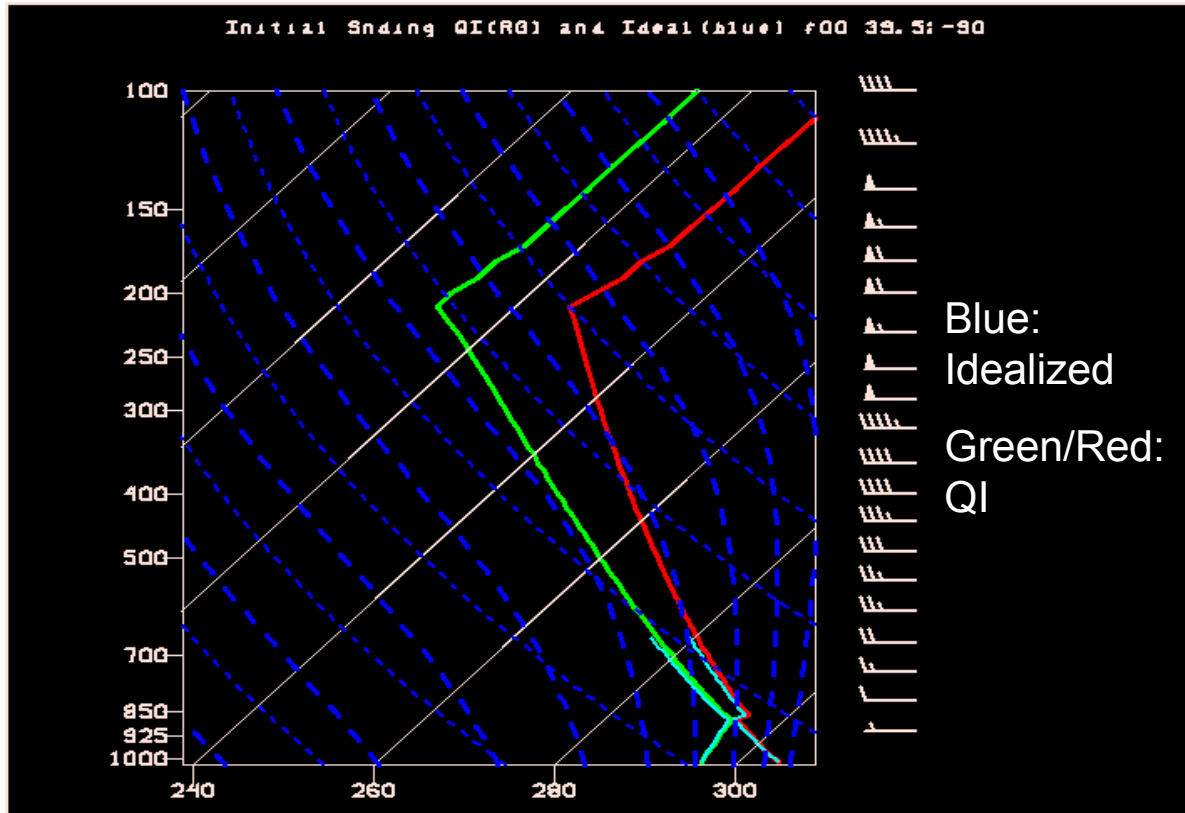


Figure A.1: Initial soundings for Q-I (red and green lines) and Idealized simulation (blue lines, plotted underneath red/green) taken near center of domain near trigger.

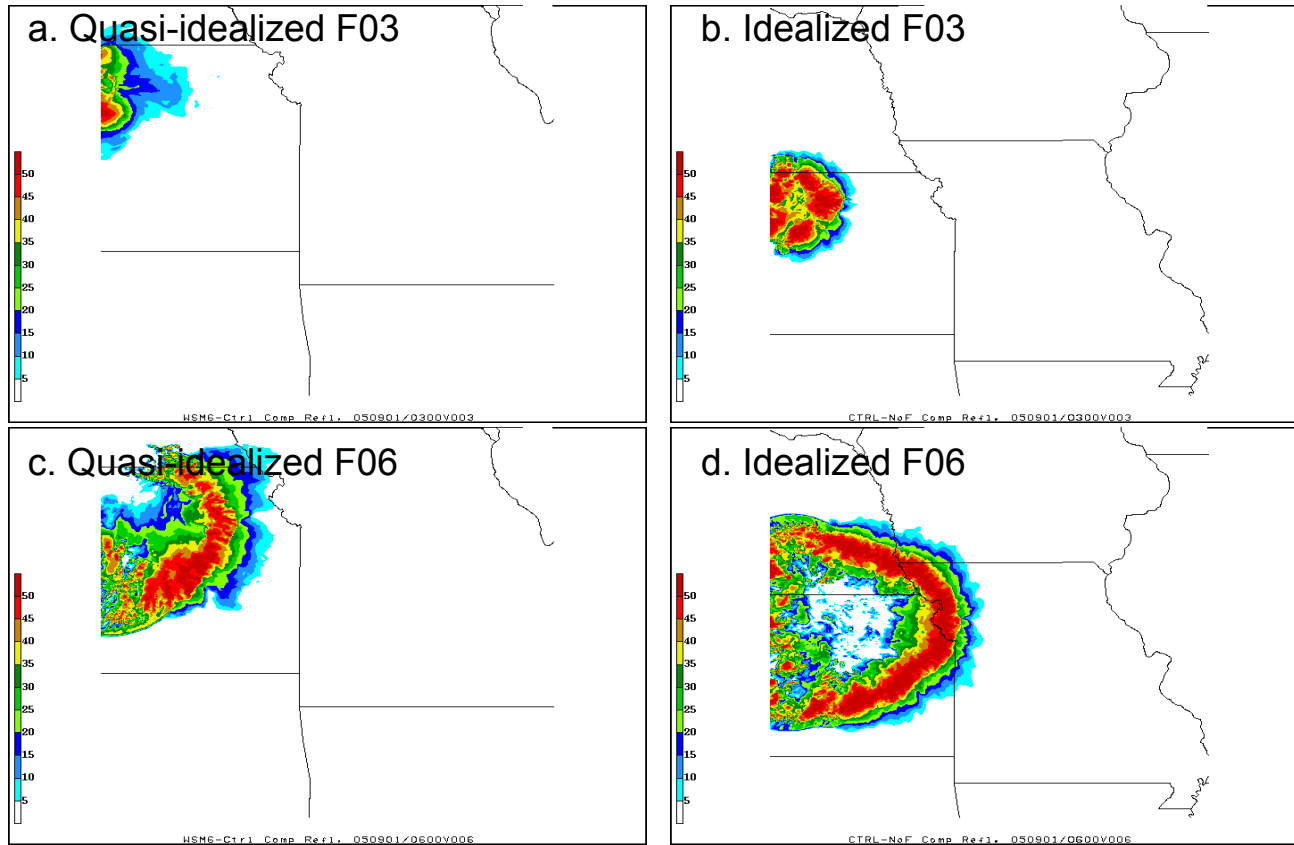


Figure A.2: Simulated composite reflectivity (dBZ, shaded as indicated) for a) Quasi-idealized simulation at F03; b) Idealized simulation at F03; c) as in a) except at F06; d) as in b) except at F06.

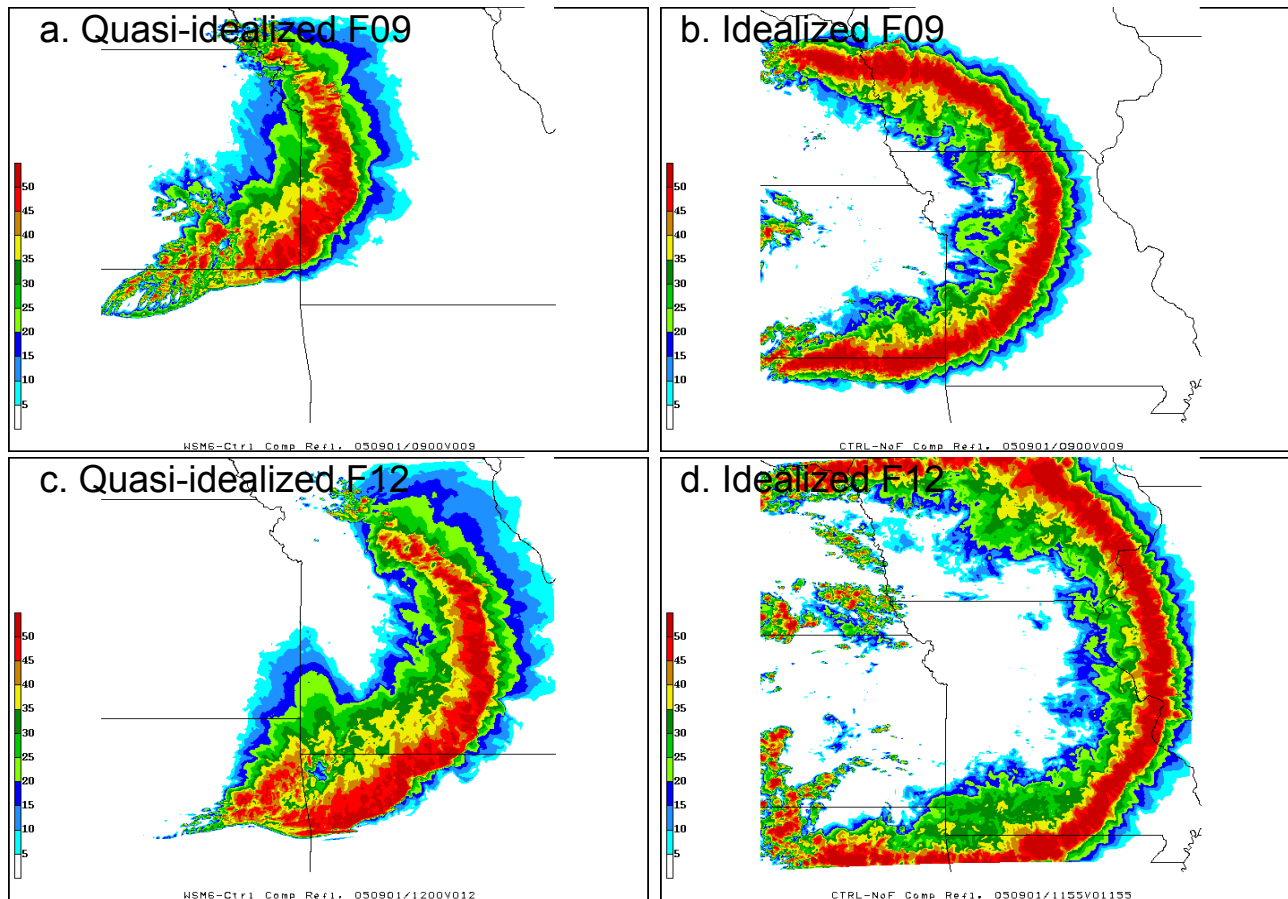


Figure A.3: As in A.2 except at F09 in a) and b) and at F12 in c) and d).

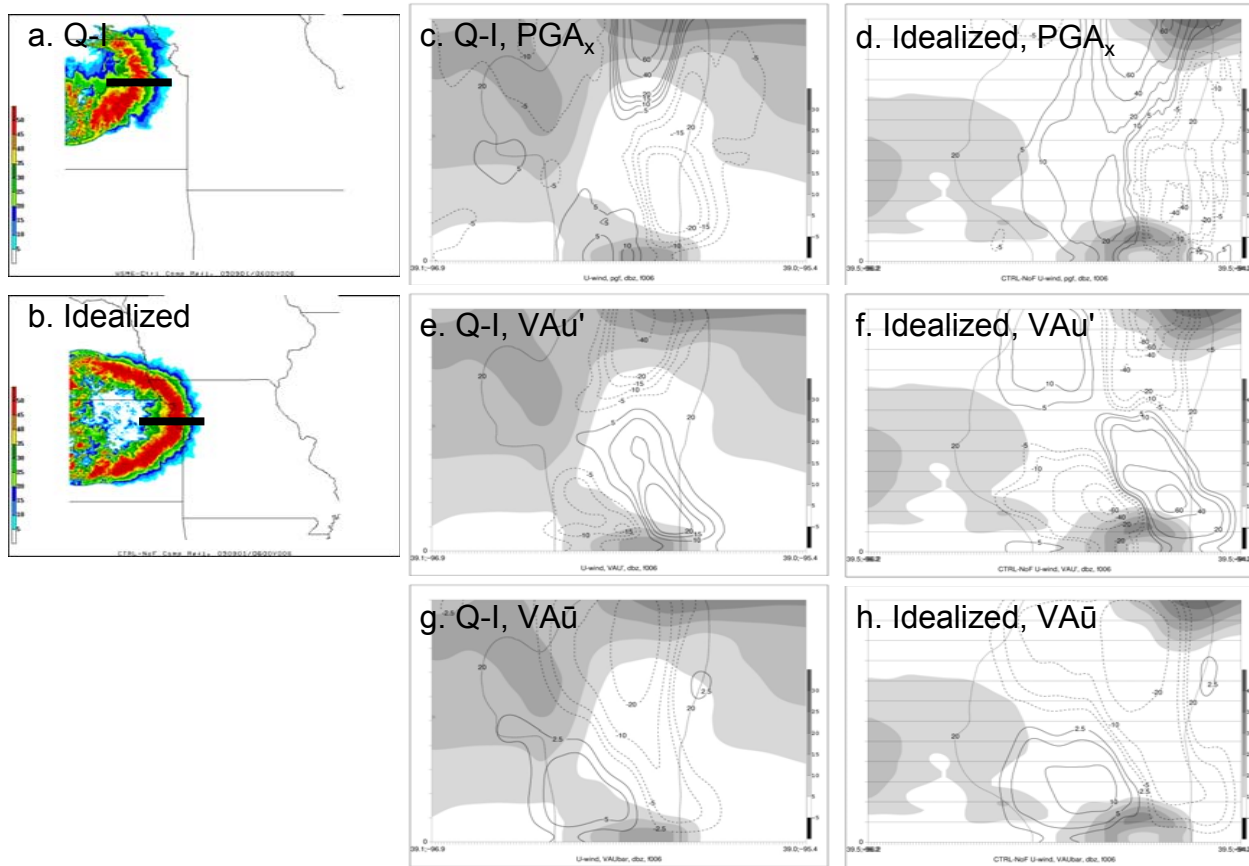
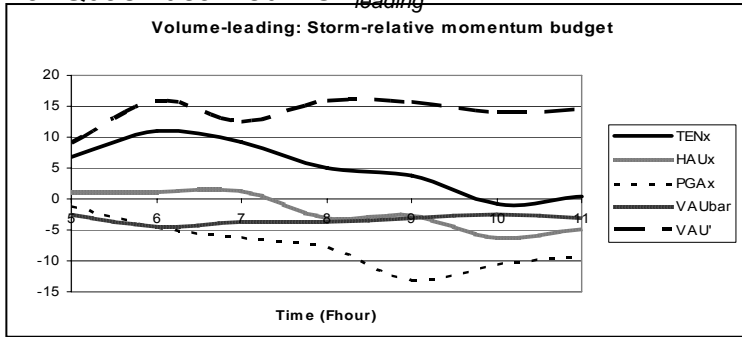
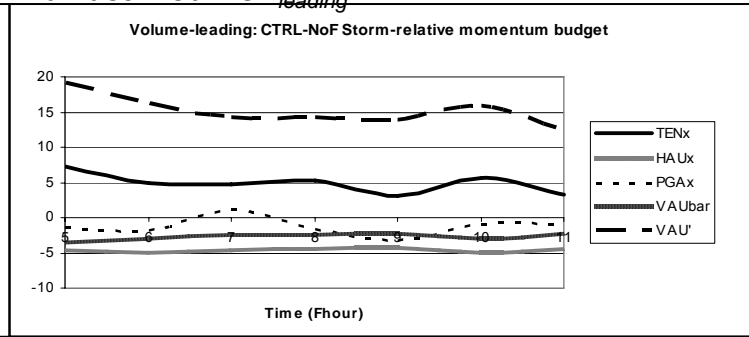


Figure A.5: a) Quasi-idealized simulated reflectivity at F06 with black line indicating cross-section in other panels; b) as in a) except for Idealized simulation; c) cold pool shaded as shown, simulated reflectivity (black contours), and PGA_x from Eqn 2.2 ($ms^{-1}h^{-1}$, positive (negative) values in purple solid (pink dashed) contours), d) as in c) except for Idealized; e) as in c) except VAU' ; f) as in e) except for Idealized; g) as in c) except $VA\bar{u}$; h) as in g) except for Idealized.

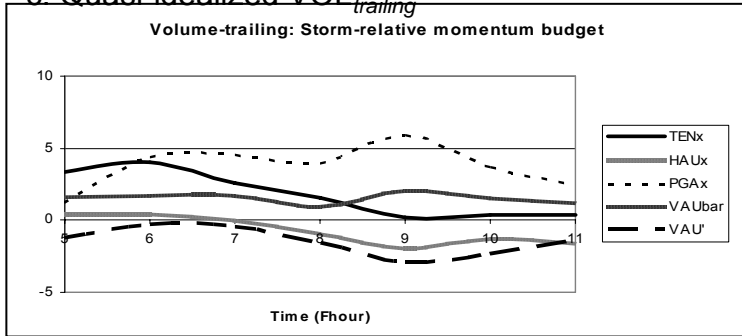
a. Quasi-idealized VOL_{loading}



b. Idealized VOL_{loading}



c. Quasi-idealized VOL_{trailing}



d. Idealized VOL_{trailing}

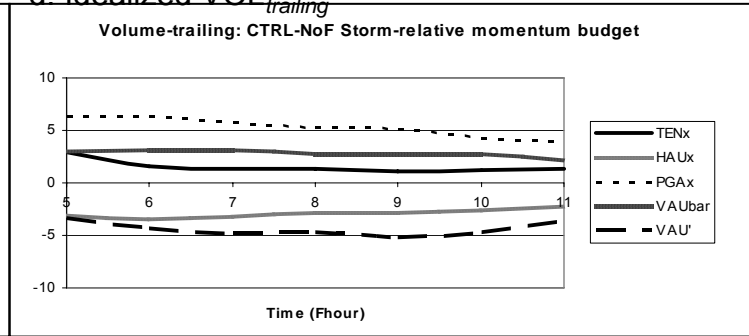


Figure A.6: Volume-averaged momentum budget terms as labeled in key for times F05 – F11 for the a) quasi-idealized leading volume and b) idealized simulation leading volume; c) as in a) except for trailing volume (*note different scales of y-axes*); d) as in c) except for idealized simulation.

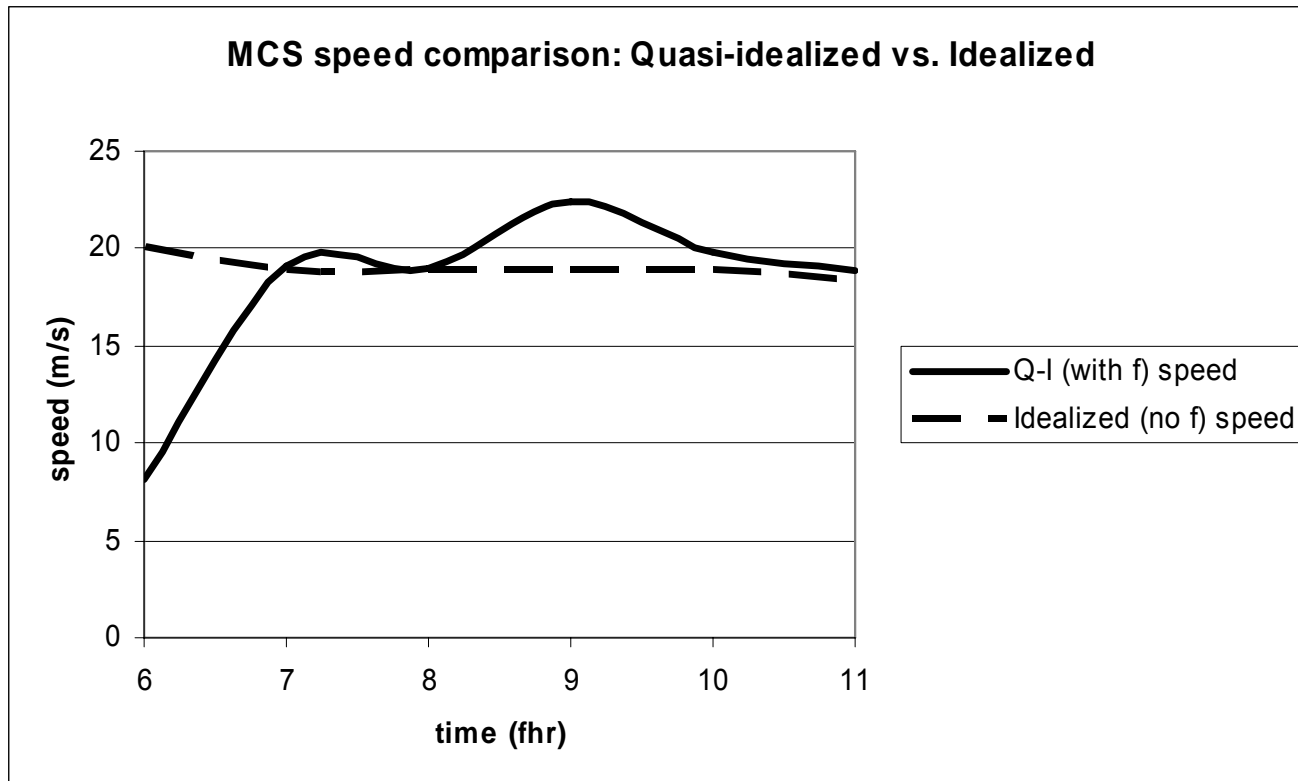


Figure A.7: Speed of MCS (ms^{-1}) from quasi-idealized simulation (solid) and idealized simulation (dashed).

Table A.1 Summary of Quasi-idealized and Idealized simulations

Quasi-idealized	Idealized
1-km grid spacing	1-km grid spacing
Jet stream included	Jet stream not included
Coriolis effects included	No Coriolis effects
CAPE variable $\sim 1200 - 2800$ Jkg^{-1} [heterogeneous initial sounding (T, T_d)]	CAPE fixed ~ 2000 Jkg^{-1} [homogeneous initial sounding (T, T_d)]
Other parameterizations as in Table 2.1	Other parameterizations as in Table 2.1

Appendix B

Sensitivity of CMT and MCS motion to shear and wind profile modification: Early model simulations and preliminary analyses

As discussed briefly in Chapter 4, variation of the initial condition kinematic profile and background environment (i.e., the magnitude, direction, and shear of the wind field) may also be explored in order to assess the significance of CMT in a variety of MCS environments. As noted in Appendix A, the most appropriate way to address these experiments in the idealized framework, so that thermal wind balance and Coriolis effects may be omitted. Toward this end, a set of preliminary experiments were conducted and results are shown here.

First, a run was performed in which wind speeds were uniformly increased at every vertical level by 10ms^{-1} (“FAST”). Thus, wind shear remains unchanged, but the mean cloud bearing wind increases. System structure remains similar between the “FAST” MCS and that of a control run using the same parameterizations but weaker initial condition windspeeds (CTRL) (Figs. B.1, B.2). The speed of the “FAST” system is 10ms^{-1} greater than CTRL, indicating that MCS groundspeed differences of 10ms^{-1} are likely due to a simple increase in horizontal advection via the mean cloud-bearing wind (also increased by 10ms^{-1}) (Fig. B.3).

Next, winds at upper levels only (300 – 150 hPa) were increased (“FAST-ULJ”) according to the sounding shown in Fig. B.4b. This simulation was contrasted in more detail to a run in which wind speeds were increased at low-levels (800-600 hPa) only (“FAST-LLJ”; Fig. B.4c). All three simulations [FAST-ULJ, FAST-LLJ, and a control simulation (CTRL)] reveal remarkably constant MCS speed, and very similar to one another in value (Fig. B.5d). The groundspeed of FAST-ULJ is slightly greater than FAST-LLJ, and both are only slightly greater than CTRL. System organization remains overall similar between these three simulations, with slightly more stratiform precipitation found in FAST-LLJ and slightly less found in FAST-ULJ. Differences in

RIJ strength and CMT can also be noted in Fig. B.6, but a more complete analysis using both more times and spatial averaging is required before stating systematic differences.

Finally, two simulations were performed to examine MCS motion and CMT when the direction of low-level flow is changed. A southerly component was added in one simulation (S-LLJ), while weak front-to-rear flow was incorporated into another (FtR-LLJ) (Fig. B.7). Both changes produce slight differences in the northern half of the MCS in particular, producing more of an eastward bulge in this region (Figs. B.8, B.9). Thus, both simulations deviate from the CTRL simulation with respect to the nearly perfect system symmetry in CTRL. Enhanced stratiform precipitation is also found along the southern (northern) flank of the MCS in S-LLJ (FtR-LLJ). It is likely that this is at least partially attributable to enhanced updraft tilt in areas where the low-level inflow is more perpendicular to cold pool motion (e.g., Rotunno et al. 1988).

Complete analysis of the simulations presented here is beyond the scope of this study, but these preliminary analyses offer considerable potential for future work. Variation of the kinematic profile of the background environment may be particularly worthy of future investigation given its facility to more closely examine the variability of the role of $VA\bar{u}$ – a parameter that may be of particular potential usefulness to the forecast process as discussed in Chapter 6. The simulations are shown here as a step in the direction of such potential future work.

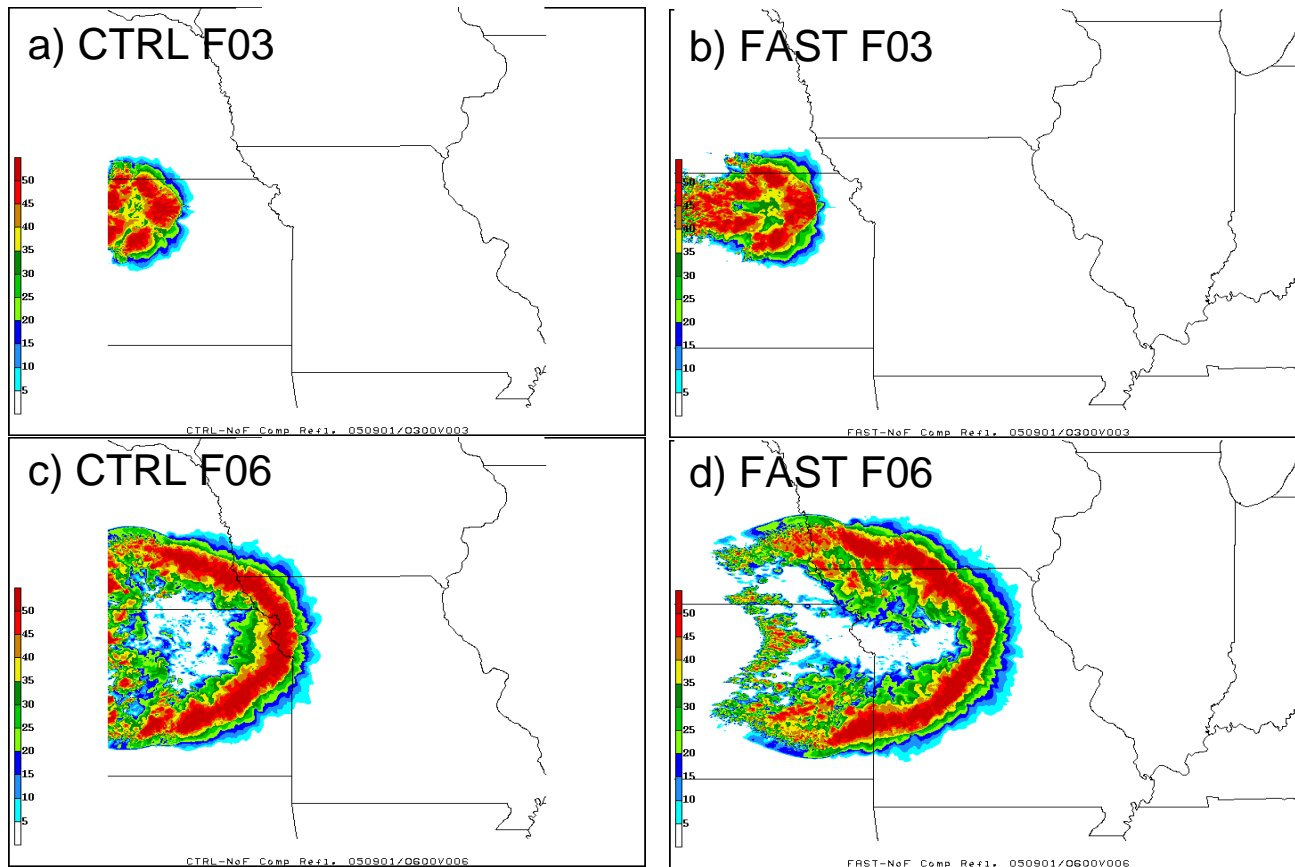


Figure B.1: Simulated composite reflectivity (dBZ, shaded as indicated at left) for a) CTRL at F03, b) FAST at F03, c) CTRL at F06, and d) FAST at F06.

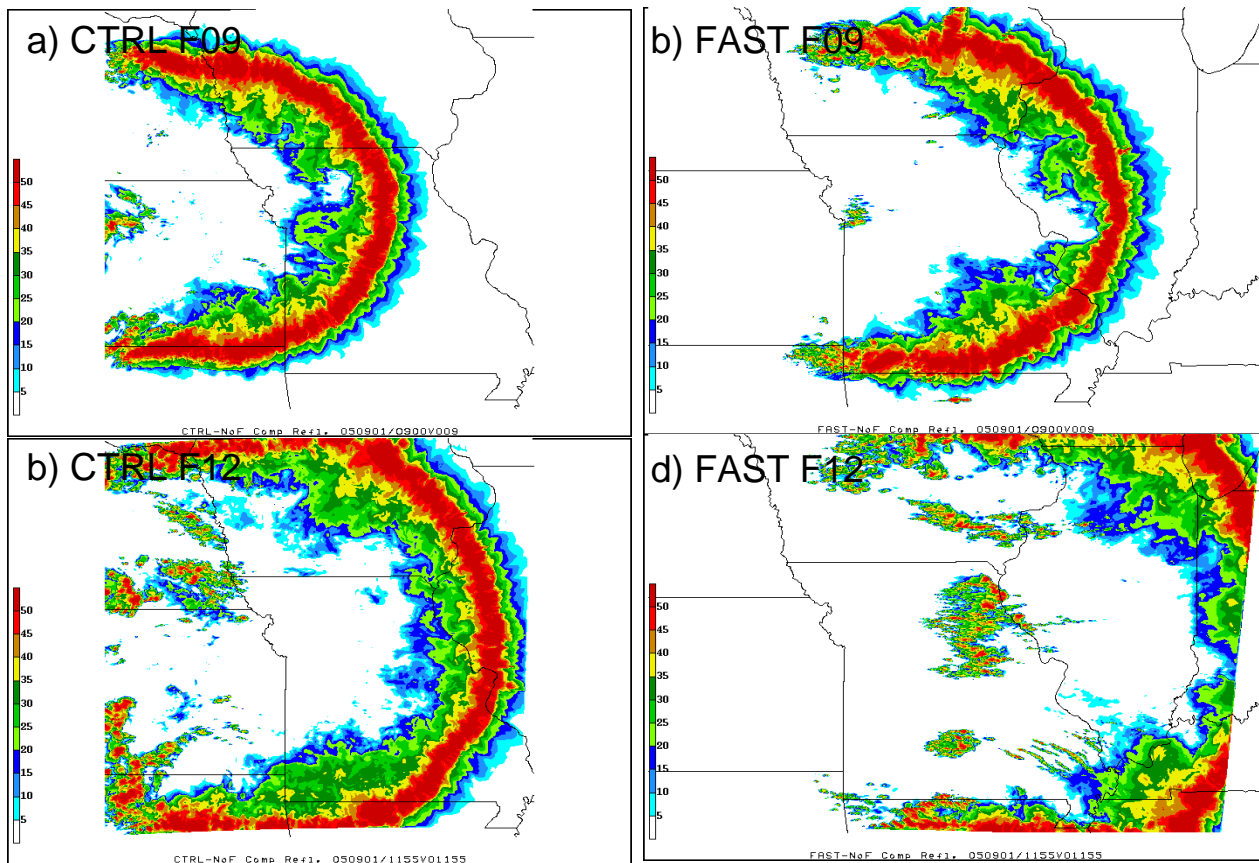
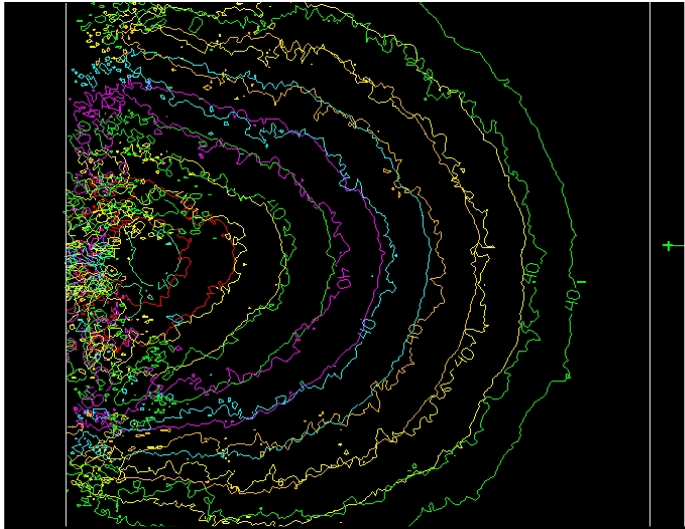
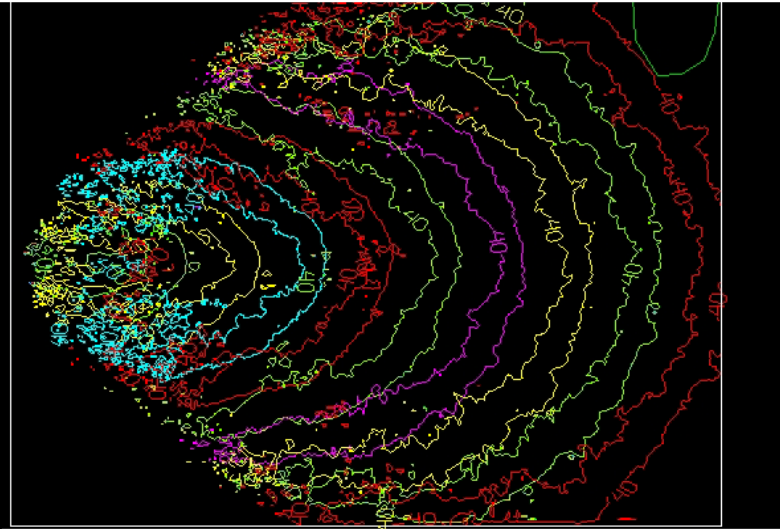


Figure B.2: Simulated composite reflectivity (dBZ, shaded as indicated at left) for a) CTRL at F09, b) FAST at F09, c) CTRL at F12, and d) FAST at F12.

a. CTRL



b. FAST



c.	Translational speed at apex (manual method)
CTRL	~19m/s
FAST	~29m/s

Figure B.3: a) Outline of 30-dBZ simulated composite reflectivity at each hour in different color for a) CTRL, and b) FAST. c) Table comparing average speed of CTRL and FAST.

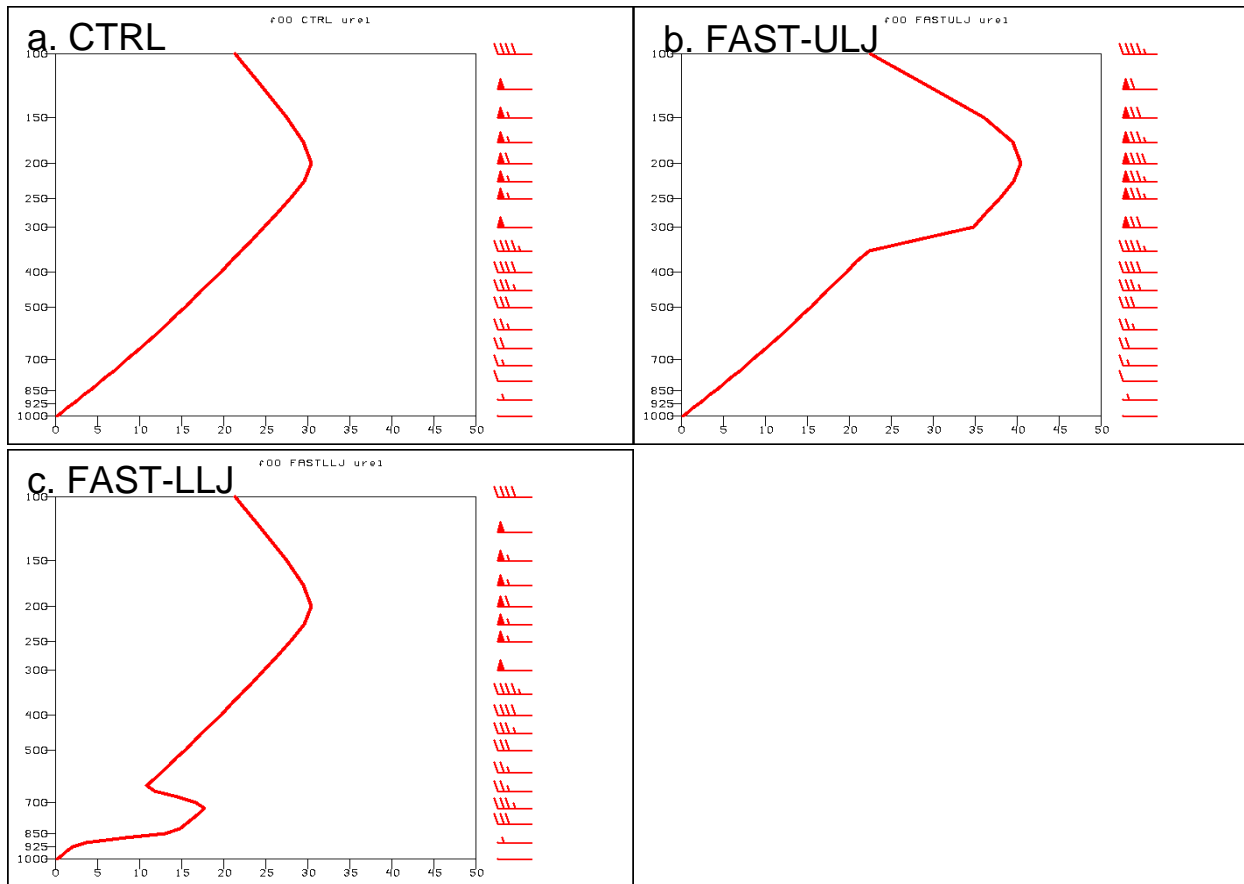


Figure B.4: Initial u-wind profiles (ms⁻¹) for a) CTRL, b) FAST-ULJ, and c) FAST-LLJ.

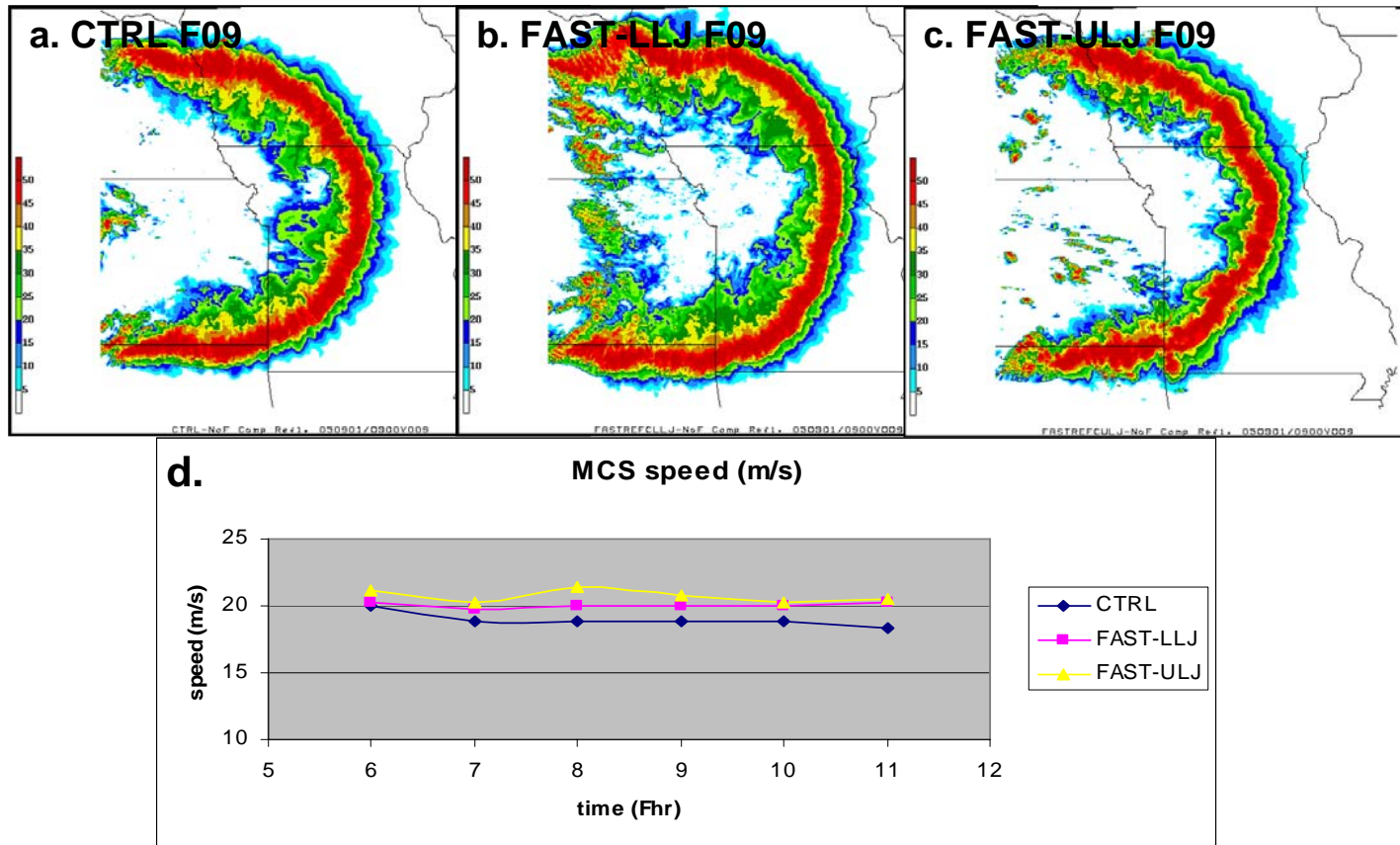


Figure B.5: Simulated composite reflectivity (dBZ, shaded as indicated at left) at F09 for a) CTRL, b) FAST-LLJ, c) FAST-ULJ. d) Comparison of system groundspeeds (ms^{-1}) as labeled.

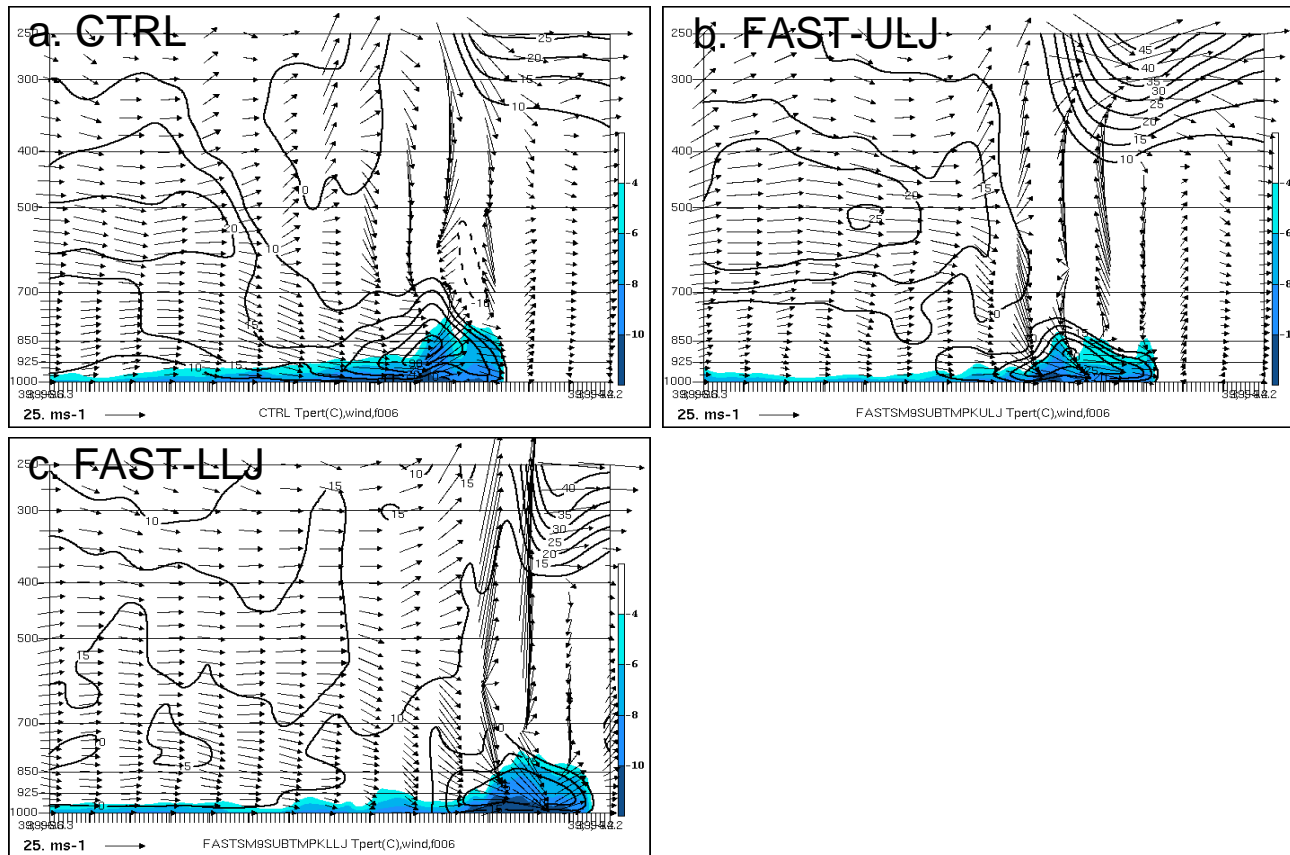


Figure B.6: (a) East-west cross-section taken in center of MCS apex at F06 showing cold pool (shaded as shown beginning at $T' = -4^{\circ}\text{C}$) and magnitude of total perturbation wind ($(u'^2 + v'^2)^{1/2}$, ms^{-1} , black contours) for a) CTRL, b) FAST-ULJ, and c) FAST-LLJ. Black arrows show ground-relative flow in the x - z plane scaled as shown by reference vector in lower left corner.

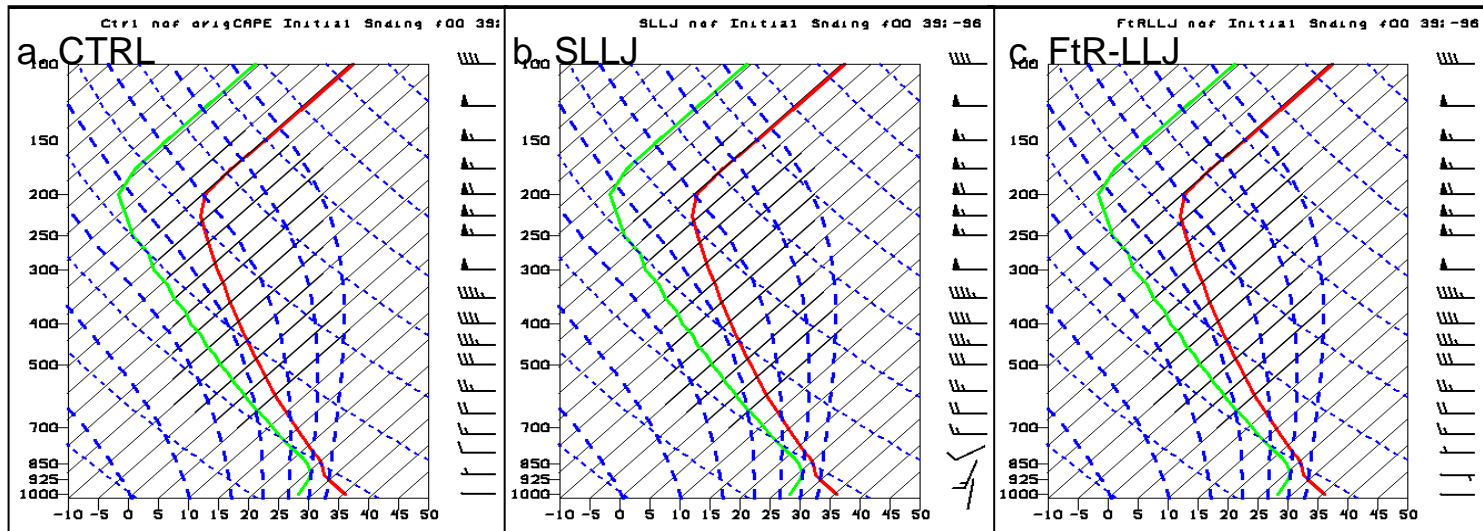


Figure B.7: Initial soundings for a) CTRL, b) SLLJ, and c) FtR-LLJ.

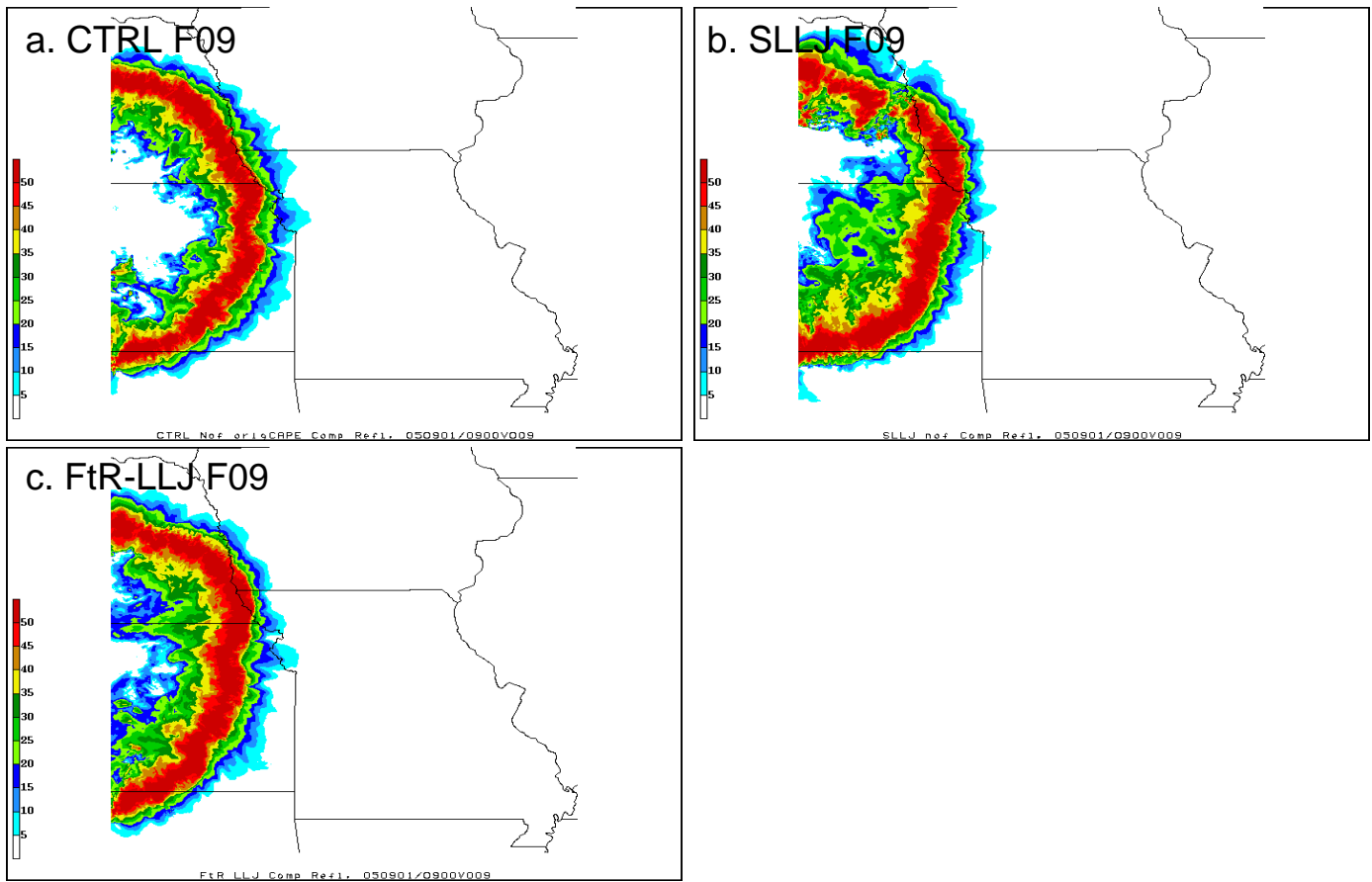


Figure B.8: Simulated composite reflectivity (dBZ, shaded as indicated at left) for at F09 for a) CTRL, b) SLLJ, and c) FtR-LLJ.

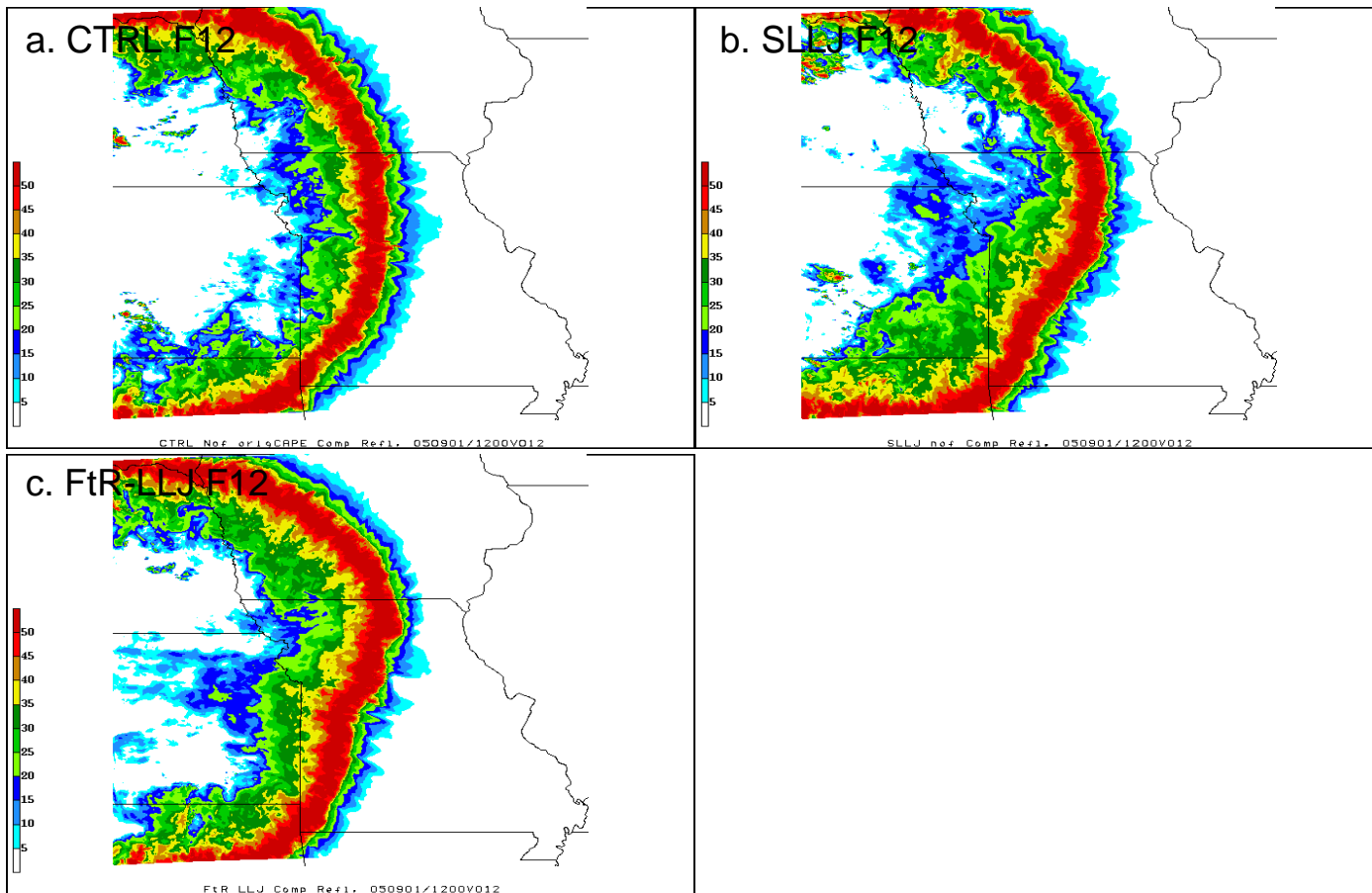


Figure B.9: As in Fig. B.8 except at F12.

Appendix C

Additional sensitivity simulations: Increased-evaporation, increased midlevel relative humidity

The sensitivity simulations presented in Chapters 4 and 5 generally change the environment or microphysical processes in one direction, i.e., *decreasing* relative humidity, and *decreasing* cooling due to microphysics. In order to provide greater assurance of the results from such tests, two additional simulations are performed to adjust these same parameters in the opposite direction, i.e., *increase* the mid-level relative humidity and evaporation.

Thus, as an analogue to REVP, the increased evaporation (IEVP) simulation alters the WSM6 microphysics scheme to increase evaporation rates by 75%. Results are shown in Figs. C.1 – C.4 and indeed appear to agree with the conclusions from the REVP simulation that increased evaporation leads to a stronger cold pool, stronger descent, and faster MCS motion. A more complete analysis will examine this simulation with respect to CMT, as well as how it compares with the DRYM simulation, in which it was assumed that increased evaporation would also occur, but may also introduce some ambiguities in interpretation (e.g., James and Markowski 2009).

As a comparison to the DRYM simulation, a moist mid-levels simulation was also performed, with relative humidity increased by 25% at ~600hPa and blended as shown in Fig. C.5. Figs. C.6 – C.9 illustrate the increase in convective intensity that results from increased midlevel moisture, as well as enhanced MCS speed and TSR extent. As above however, a more robust future analysis will focus on which processes are most responsible for these changes, particularly in MCS motion and TSR processes, and also investigate topics related to severe wind generation as well.

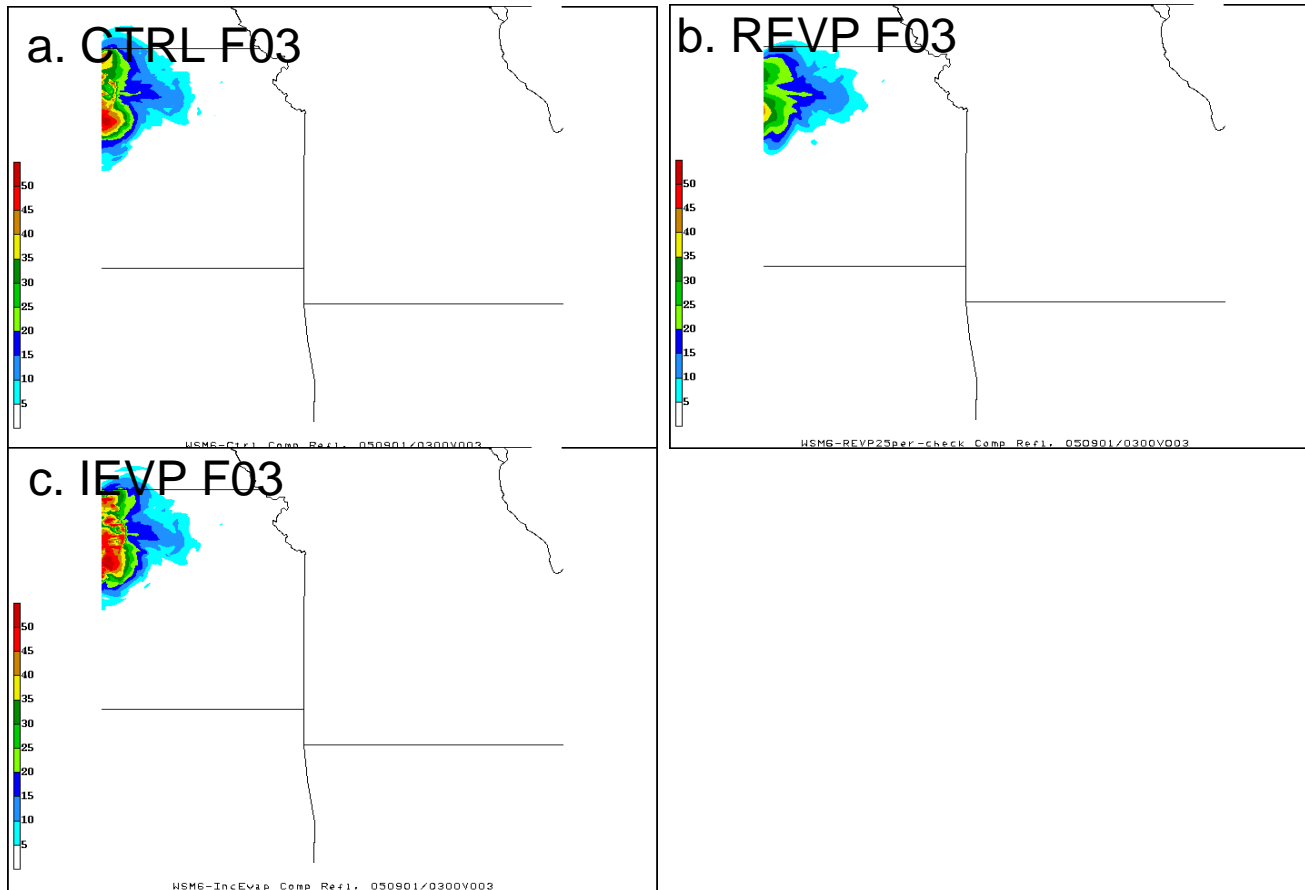


Figure C.1: Simulated composite reflectivity (dBZ, shaded as indicated at right) at F03 for (a) CTRL run (b) REVP, and (c) IEVP

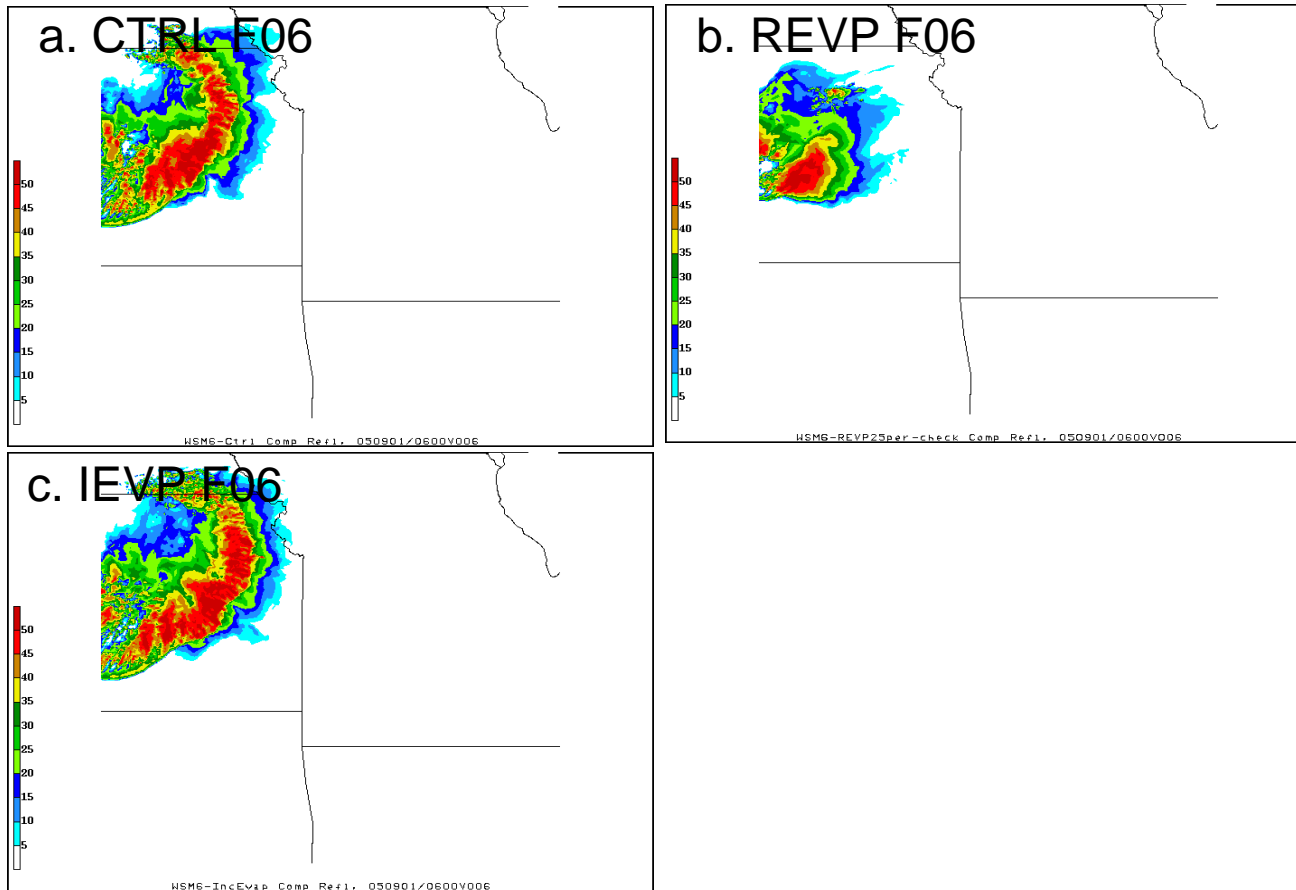


Figure C.2: As in Fig. C.1 except at F06.

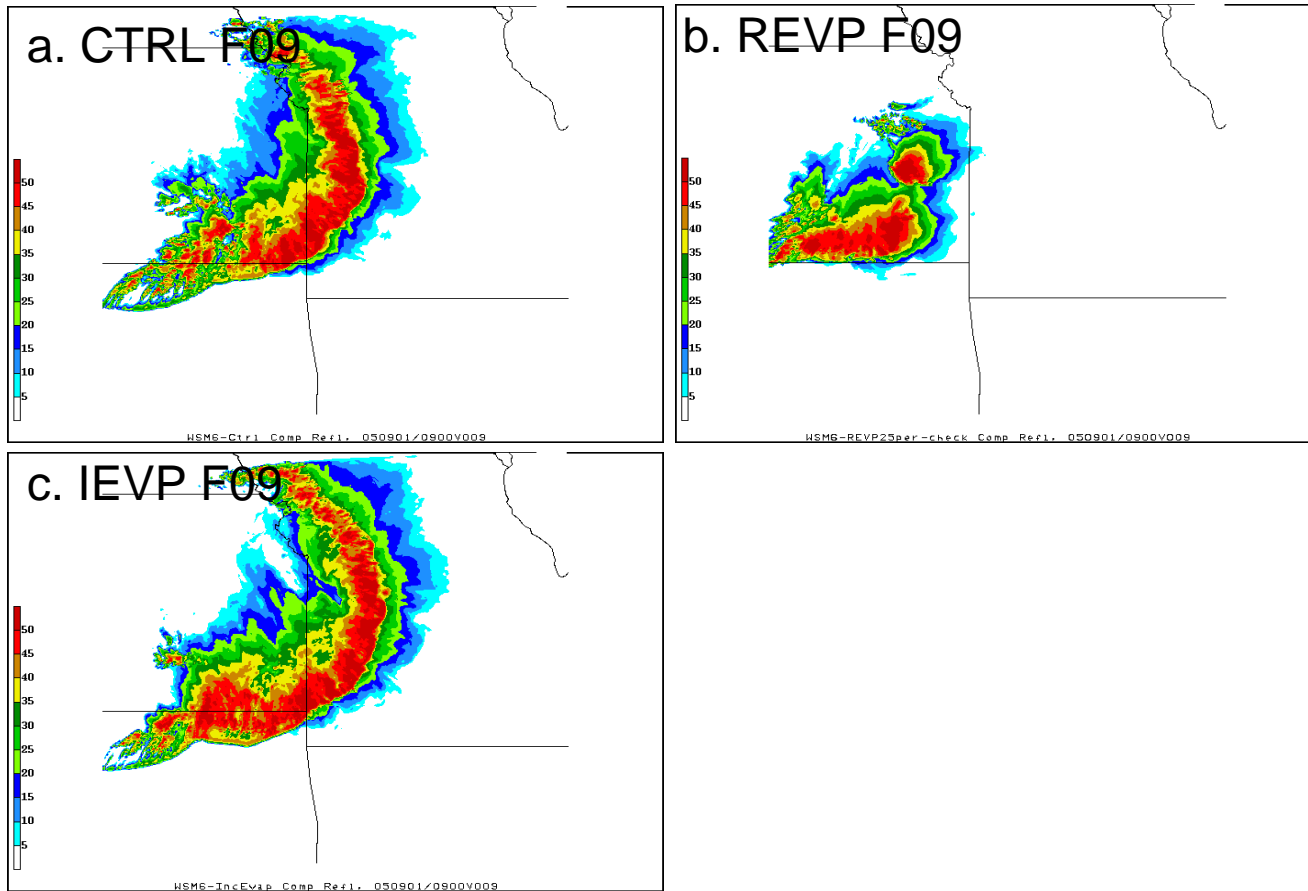


Figure C.3: As in Fig. C.1 except at F09

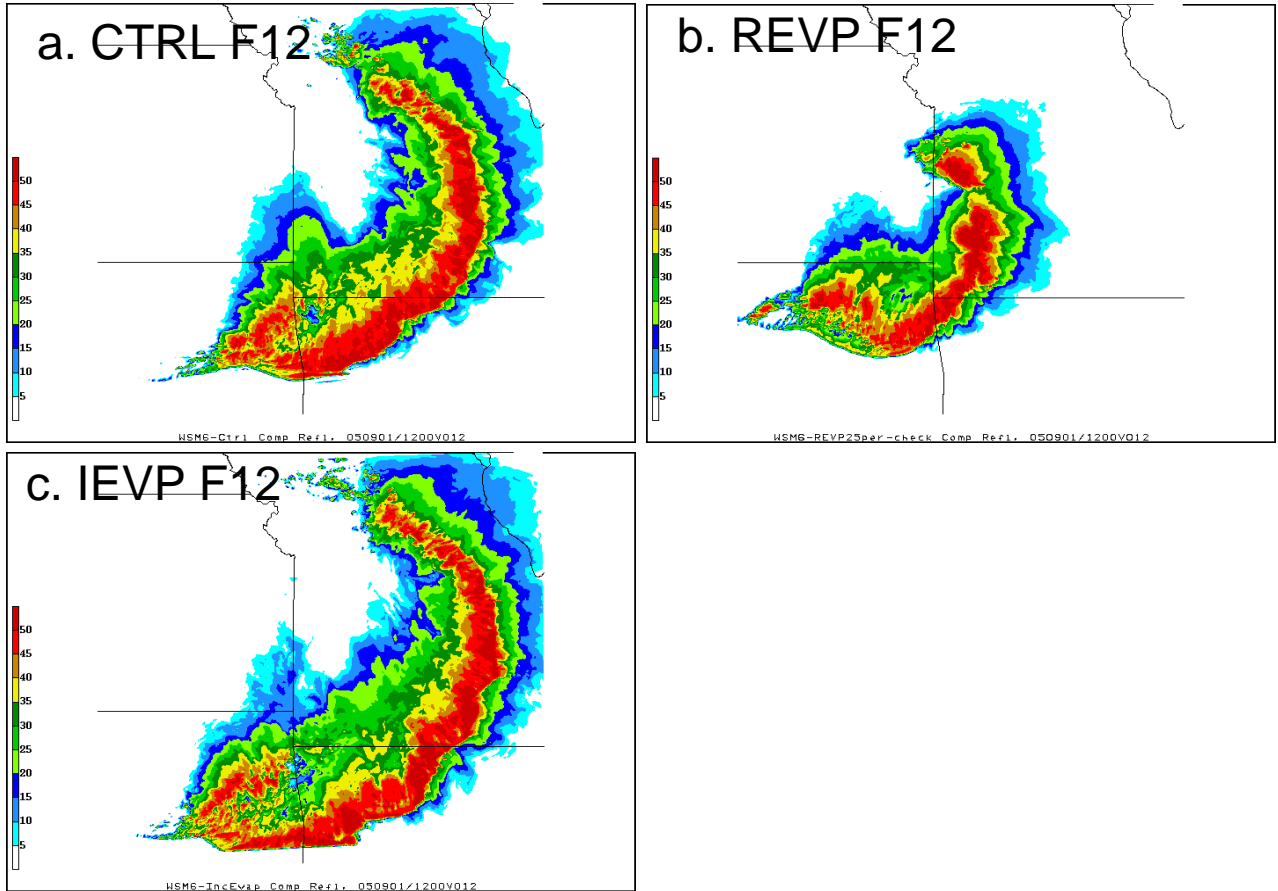


Figure C.4: As in Fig. C.1 except at F12

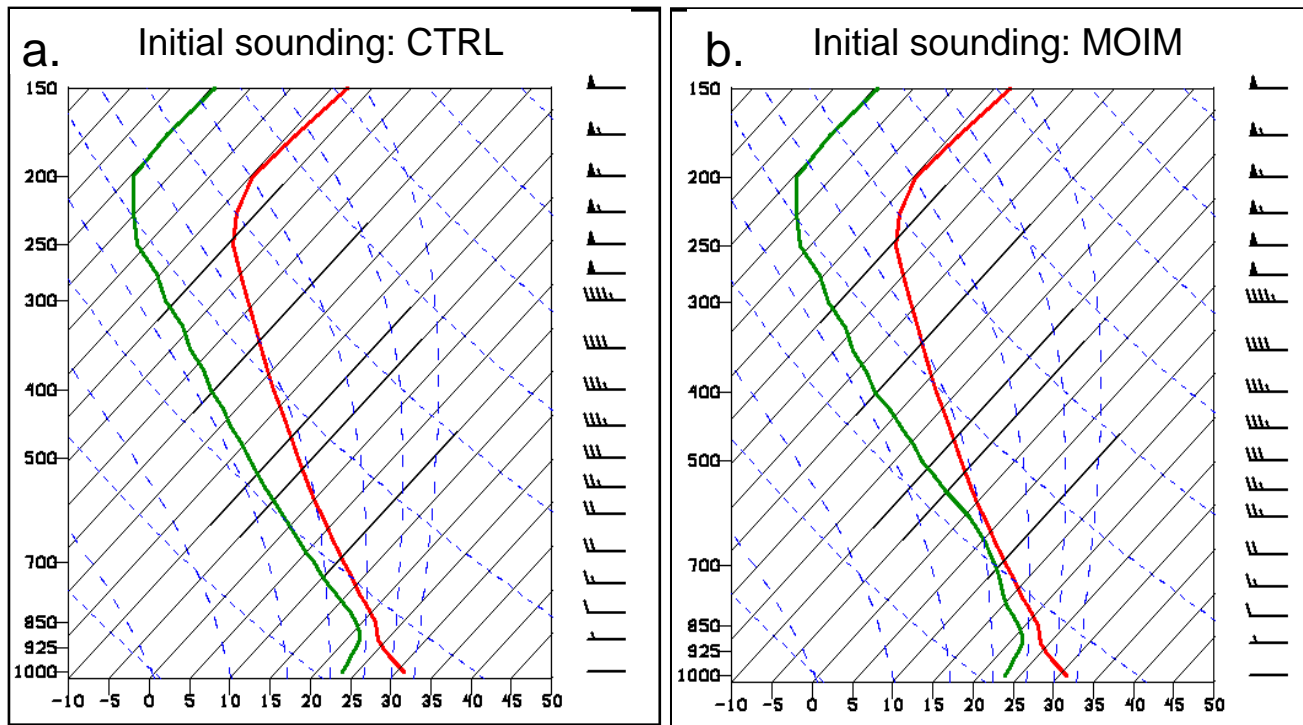


Figure C.5: Comparison of initial sounding shape used to initialize the quasi-idealized MCS simulation (at $(35^{\circ}\text{lat}; -95^{\circ}\text{lon})$) for (a) CTRL simulation, and (b) MOIM (moist mid-levels) simulation. Temperature ($^{\circ}\text{C}$, solid line), dewpoint ($^{\circ}\text{C}$, dashed line), wind barbs in knots at right.

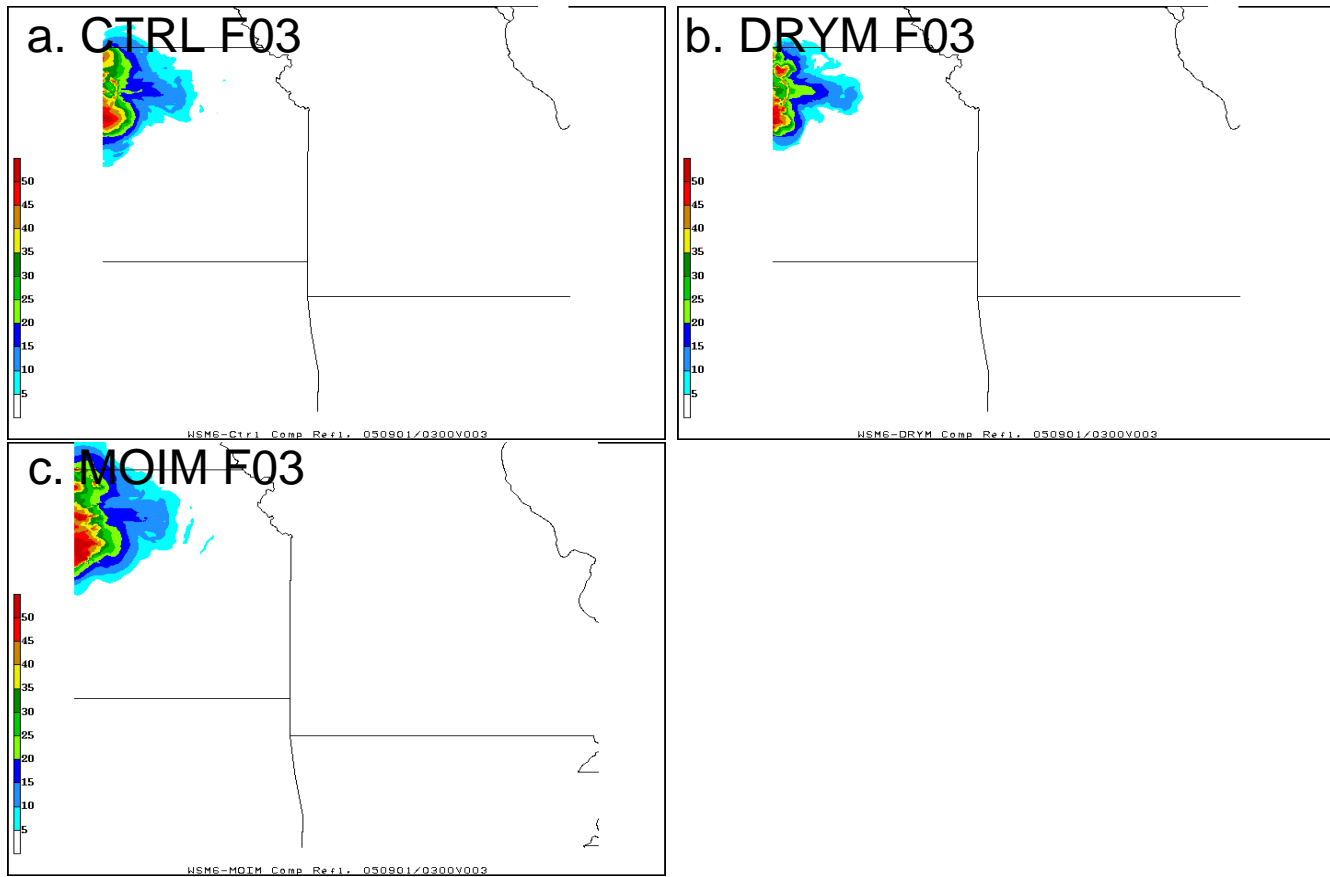


Figure C.6: Simulated composite reflectivity (dBZ, shaded as indicated at right) at F03 for (a) CTRL run (b) DRYM, and (c) MOIM.

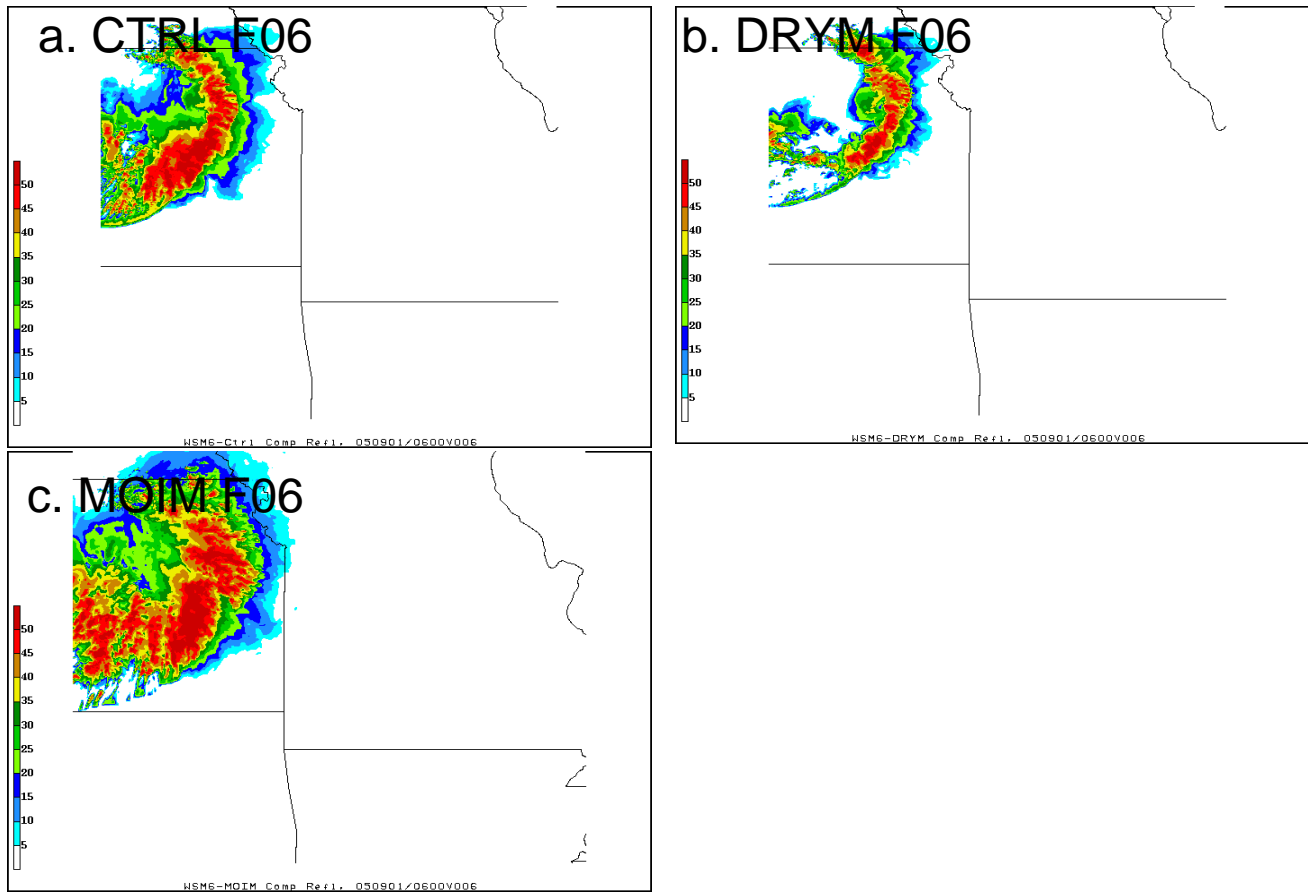


Figure C.7: As in Fig. C.6 except at F06

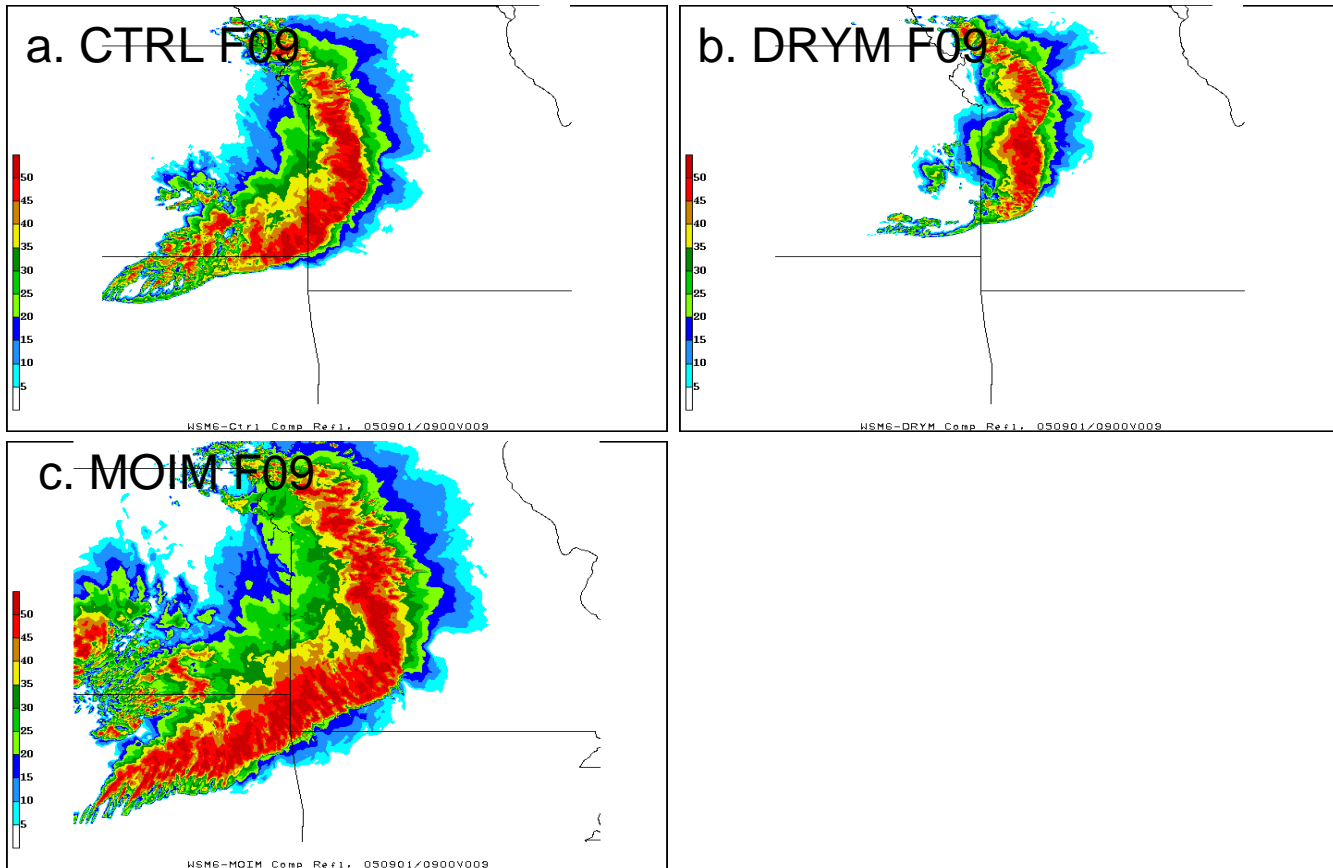


Figure C.8: As in Fig. C.6 except at F09

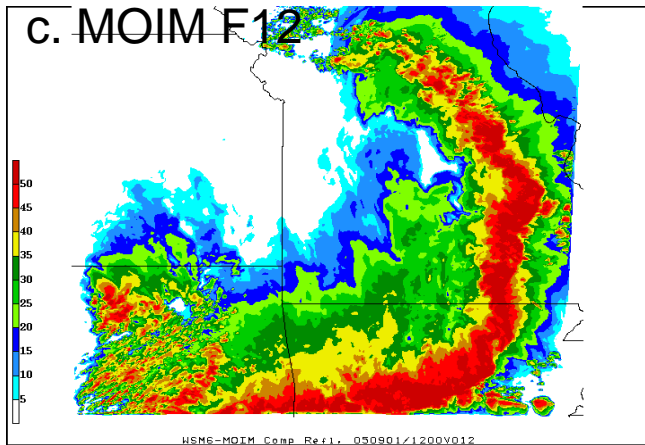
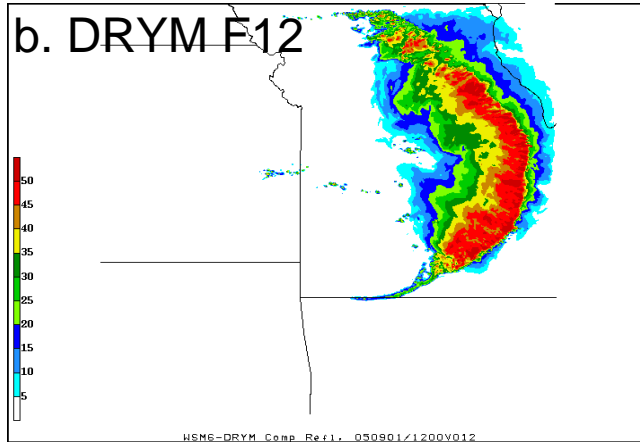
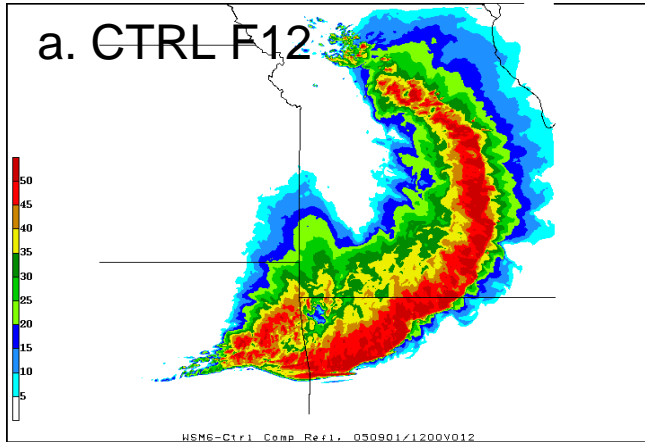


Figure C.9: As in Fig. C.6 except at F12